The Dissertation Committee for Jisuk Yoon Certifies that this is the approved version of the following dissertation:

Application of Pore Fluid Engineering for Improving the Hydraulic Performance of Granular Soils

Committee:

Chadi S. El Mohtar, Supervisor

Robert B. Gilbert

Jorge G. Zornberg

Raissa D. Ferron

Matthew T. Balhoff

Application of Pore Fluid Engineering for Improving the Hydraulic Performance of Granular Soils

by

Jisuk Yoon, B.E.; M.S.C.E.

Dissertation

Presented to the Faculty of the Graduate School of

The University of Texas at Austin

in Partial Fulfillment

of the Requirements

for the Degree of

Doctor of Philosophy

The University of Texas at Austin

December 2011

Dedication

To the most loving my wife,

In Jung Choi

To my most loving parents,

Soo Kil Yoon and Jung Sook Choi, Jae Bum Choi and Hwa Sook Jung

Acknowledgements

I would like to express my sincere gratitude to Professor Chadi S. El Mohtar for his valuable guidance, continuing encouragement, and substantial support throughout my doctoral study. I would also like to express my deep appreciation to Professor Robert B. Gilbert for his continuing support and valuable comments throughout the course of my study. Sincere thanks and appreciations are also expressed to Professor Jorge G. Zornberg for his support, valuable contribution, and guidance during this project. Deep appreciation to Professors Matthew Balhoff and Raissa P. Ferron for their interest in this project, their willingness to serve on my dissertation committee, and their valuable discussions and comments.

I would like to thank my colleagues Hansic Hwang and Dennis Rugg for their assistance and valuable contributions throughout the first stage of this research. Sincere gratitude is also expressed to other friends in geotechnical engineering group at the University of Texas at Austin.

Finally, I would like to express my deep and sincere gratitude to my wife In Jung Choi for her great sacrifice during this work, and my lovely parents Soo Kil Yoon and Jung Sook Choi, Jae Bum Choi and Hwa Sook Jung for their patience, encouragement, and their continuous love and support throughout the course of this work.

Jisuk Yoon

The University of Texas at Austin

December, 2011

Application of Pore Fluid Engineering for Improving the Hydraulic Performance of Granular Soils

Publication No._____

Jisuk Yoon, Ph.D.

The University of Texas at Austin, 2011

Supervisor: Chadi S. El Mohtar

Over the past years, levee failures during floods have caused significant losses of lives and properties in the nation. Majority of these failures were induced by seepage through granular foundation soils underneath the top soil on which the levees were built. One of methods to mitigate this phenomenon includes the treatment of the granular soil deposits with an engineered fluid delivered by permeation (permeation grouting), resulting in a less pervious deposit. Since the conventional cement-based suspensions and chemical solutions may cause groundwater contamination due to long term reaction with groundwater, clay suspension such as bentonite suspension can be an alternative in terms of environmental friendliness and long-term safety. Moreover, the suspensions, after being permeated, are expected to be stable in the pore space due to the thixotropic nature of bentonite. The main challenge in this approach is being able to permeate a concentrated suspension through the pores of a granular material. To achieve a significant reduction in the hydraulic conductivity, concentrated bentonite suspensions

should be used; however, concentrated suspensions can have low mobility, resulting in a low penetration depth and little practical application.

The main objective of this study is to investigate the permeation of concentrated bentonite suspensions by controlling their rheological properties. The first portion of this research focuses on measuring the rheological properties of the various engineered bentonite suspensions over time. The second point of focus of this research is the parameters affecting the flow of the bentonite suspensions through granular soils, and the final focal area is determining the hydraulic performance of the grouted granular soils.

In order to achieve these objectives, an experimental program was developed in this research. First, rheological tests were performed with the bentonite suspensions with and without various concentrations of sodium pyrophosphate (SPP); SPP is an ionic additive that is used to reduce the initial yield stress and viscosity of bentonite suspensions. A stress controlled test with the vane geometry produced rheological parameters with a minimal disturbance. Suspensions were stored in sealed cups and tested at various times to measure the long term thixotropic changes in yield stress and viscosity. Second, the various concentrations of the bentonite suspensions were injected at a constant pressure through clean sands which were prepared at various conditions (relative density, fine contents, and grain size) in order to investigate soil and suspension parameters affecting the flow of the bentonite suspensions. The results from these experimental tests were utilized to develop a groutability criterion of bentonite suspensions for practical purposes. Finally, the saturated hydraulic conductivity of the treated soils was measured using falling and rising head method. The traditional concept of "clay void ratio" was re-examined. The results from this study showed that the modified bentonite suspensions could be used as an alternative grout in permeation grouting to improve hydraulic performance of the permeable granular soils.

List of Contents

List of Tables

List of Figures

CHAPTER 1: INTRODUCTION

1.1. Problem statement

Over the past years, levee failures and subsequent floods have threatened life and property in the United States. During the 1993 flood, known as the great flood, 36 levees were overtopped or failed causing over 10 billion dollars in damages. In August 2005, Hurricane Katrina produced a widespread damage in New Orleans, Louisiana. About 1,800 people were killed and over 100 billion dollars of property was damaged due to the flooding. There were 50 major breaches in the Hurricane Protection System during Katrina. Moreover, the Sacramento-San Joaquin Delta and Suisan Marsh have experienced over 160 levee failures during the last century. Most recently, the Upper Jones track failure, which occurred in June, 2004, caused the inundation of 16,000 acres and approximately 90 million dollars in repair costs only. Historically, repairing levee failures in the Delta had required 8 to 10 million dollars per a single levee failure According to the Delta Risk Management Strategy Phase 1 report (DWR, 2007), 80 percent of the past levee failures are believed to be caused by underseepage-induced failures in the Sacramento-San Joaquin Delta and Suisan Marsh. The remaining 20 percent of failures were attributed to overtopping. Moreover, 4 levees which failed during the 1993 flood in the Midwest were also caused by seepage through the foundations of the levees. Table 1.1 summarizes the locations of levee failures and the properties of foundation soils in some of the documented levee failures in the United States. Overall, the distribution of the failure modes indicates that underseepage is the major cause of levee failures in the United States.

Table 1.1 Location and foundation soils of levees failed by underseepage (GAO, 2006; CDWR, 2007; Seed et al., 2008; Rogers and Meehan, 2008)

Levee	Area	Date of Failure	Permeable layer	Hydraulic Conductivity (cm/sec)
Upper Jones Tract*	Sacramento-Suisan Marsh, CA	June 2004	Sand	N/A
Marysville	Yuba and Sutter County, CA	Feb 1986	Gravel	2×10^{-1}
Linda				
Arboga				
Kaskaskia Island	Mississippi River, IL	July 1993	Sand	3.5×10^{-2} - 1.2×10^{-1}
Bois Brule		July 1993	Sand	3.5×10^{-2} - 1.2×10^{-1}
Sny Island		July 1993	Sand	3.5×10^{-2} - 1.2×10^{-1}
London Avenue	New Orleans, LA	Aug 2005	Sand	3×10^{-2}

* The most recent levee failure in the Delta and Suisan Marsh.

Underseepage is a phenomenon that occurs when water flow through granular sub-layers underneath the top soil increases due to an increase in the river water level (Figure 1.1). As the river level increases, a higher hydraulic gradient is induced between the riverside and the landside of a levee and seepage emerges at the landside (or the toe) of levees through the top soil. The concentrated seepage delivers sand/silt up to the surface (sand boils), and creates open channels through eroding the foundation soils (piping), which leads to levee failures.

One method to mitigate this phenomenon includes the treatment of the granular soil deposits with an engineered fluid delivered by permeation (permeation grouting), resulting in a less permeable deposit. While cement suspensions and chemical solutions have been widely utilized as grouts for many decades, they may cause groundwater

contamination due to long term reaction with groundwater. As an alternative, clay suspension, such as bentonite suspension, can be a more environmentally friendly solution. Moreover, due to the thixotropic nature of bentonite, the permeated suspensions will become more stable in the pore space over time.

The main challenge in using this approach is being able to permeate a concentrated suspension through the pores of granular soils. To achieve a significant reduction in the hydraulic conductivity, concentrated bentonite suspensions should be used. However, concentrated suspensions can have very low mobility, resulting in a low penetration depth and little practical application. Therefore, there is a need to engineer the optimal bentonite grout that can have both, a high concentration and reasonable penetration depth to achieve the desired reduction in underseepage.

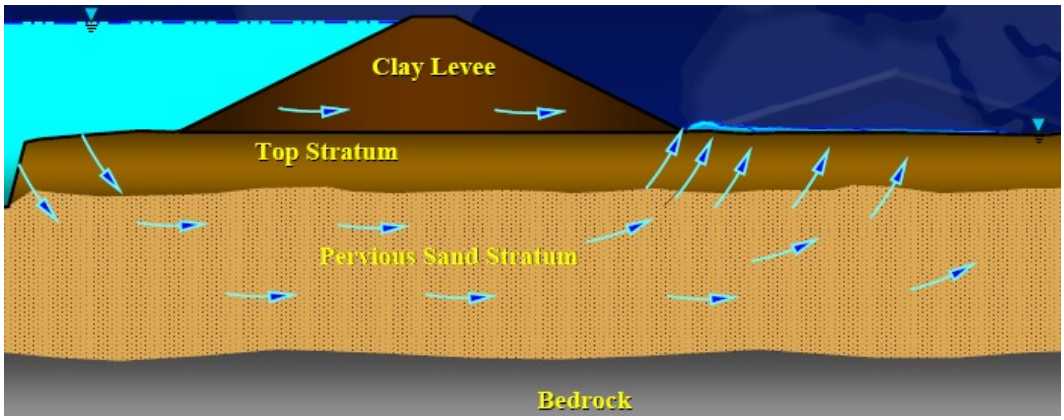

Figure 1.1 Underseepage through pervious foundation sand. (McCaskie, 2008)

1.2. Research objectives

The overall objective of this research is to investigate the permeation of concentrated bentonite suspensions by controlling their rheological properties using an ionic additive (sodium pyrophosphate), and evaluate the change in hydraulic conductivity

of the grouted soils. This objective includes measuring the rheological properties of bentonite suspensions with various bentonite fractions and sodium pyrophosphate concentrations over time, investigating the parameters affecting the flow of the bentonite suspensions through granular soils and measuring the change in the hydraulic conductivity of the permeated sands. Finally, the research will lead to the development of a new groutability criteria and penetration depth model that can be used to evaluate the applicability of a specific grout though a certain soil, and more importantly, help identify how to better engineer the grouts (in terms of controlling their rheological properties) to achieve the optimum results in the field.

1.3. Organization of the thesis

The thesis consists of eight chapters. Chapter 1 is an introduction that includes the problem statement and objective of this study along with the dissertation organization. Chapter 2 presents background of underseepage and permeation grouting. The chapter is divided into two parts: 1) general background such as mechanisms and countermeasures of underseepage, and 2) technical issues such as behavior of bentonite clay in aqueous medium, rheology, groutability and hydraulic conductivity.

Chapter 3 introduces a detailed description of the testing equipment and properties of material used in this study. This chapter includes general index tests of materials and the physical and chemical properties of the bentonite used. Details on rheometry and measurements of yield stress and apparent viscosity in the modified and unmodified bentonite suspensions are presented as well. Moreover, constant pressure and flow rate injection technique are described. Finally, the hydraulic conductivity test equipment and testing procedures for determining bentonite content of permeated specimens are presented.

Chapter 4 covers the rheological properties of bentonite suspensions focusing on the effect of SPP on yield stress, apparent viscosity and their time dependent behavior. The results from stress ramp and oscillatory shear tests are presented. Based on the results, an optimal dosage of SPP is recommended. In addition, the disturbance effect which typically occurs in time-dependent yield stress measurements is discussed with the experimental data obtained from the different rheometries (cone and plate and vane and cup).

Chapter 5 includes injection tests using constant pressure and constant flow rate techniques. The parameters affecting grout flow such as bentonite fraction, relative density, effective grain size, fines content and the injection pressures are investigated.

Chapter 6 describes the hydraulic conductivity of the grouted sands. The effect of bentonite content, relative density and fines content is studied and a normalized pore property, BC/BCmax is utilized along with the clay void ratios to explain water flow through the grouted sand.

Chapter 7 presents a comprehensive analysis of the relationship between rheological parameters and suspension flow through sand. The stoppage mechanism of the suspension flow is discussed and empirical correlations to predict the penetration distance and groutability using the modified bentonite suspensions are proposed. A numerical approach using the concept of filtration is presented to estimate groutability of bentonite grouts under 1-D injection. Different propagation mode of the suspension flow is investigated to link 1-D with the 3-D injection under constant flow rate condition. Finally, the post grouting stability of the placed bentonite suspensions with time is covered.

The main conclusions drawn from the analyses of the results are presented in Chapter 8 along with recommendations for future work.

CHAPTER 2: BACKGROUND AND LITERAURE REVIEW

2.1. Introduction

This chapter divided into two parts: 1) general background of underseepage and 2) technical background and related literature reviews. The first part focuses on the mechanism and case histories of underseepage induced levee failures, underseepage countermeasures and the concept of permeation grouting. The second part presents the detailed theoretical and experimental issues on permeation grouting using SPP modified bentonite suspensions such as rheology, structural kinetics of bentonite suspensions, groutability of granular soil deposits and their hydraulic performance after treatment.

2.2. Mechanism of underseepage

Underseepage occurs due to a differential hydrostatic head of water when the river level is higher than the adjacent land, creating a hydraulic gradient in the granular deposits under the levee. The seepage occurs (from river bed or top stratum on the riverside) beneath the levee, producing excess pressures landward.

Once the excess pressures exceeds the submerged unit weight of the top soil on the landside, heaving or rupture (sand boils) of the top soil occurs due to the concentration of seepage flow. Prior to levee failures, sand boils are typically observed as an apparent evidence of underseepage. Sand boils occur when vertical seepage forces exerted by the upward flow of water are greater than the vertical downward weight of the submerged soil. The flowing water through a sand boil carries the eroded soil particles along the water and deposits them on the soil surface, forming a cone around the sand boil (Ozkan, 2003). Heave and piping are the main mechanisms involved in creating a

pipe that leads to sand boils. Heaving occurs when seepage forces push the substrata upward. Piping is the phenomenon where seeping water progressively erodes and washes away soil particles, leaving large voids through the substrata. Loss of soil through sand boils by piping or internal erosion weakens both levees and their foundations, leading to settlement and catastrophic failures of levees.

Figure 2.1 shows formation of sand boils due to underseepage. The critical gradient required causing sand boils or heaving is approximately 0.85 for silty sands and silts, and 0.80 for silty clay and clay (Turnbull and Mansur, 1959). In the field, the critical gradient required to cause sand boils can best be determined by measuring the hydrostatic head beneath the top stratum at the time a sand boil starts (Ozkan, 2003).

Figure 2.1 Photograph of sand boils (from http://centrallapolitics.blogspot.com)

2.3. Case history of underseepage induced levee failures

Over the past century, about 160 levees failures have occurred in Sacramento-Suisun Marsh Area, California. The large portion of seepage induced failures in the Delta levees came from their generic material properties in levees and foundations. Delta levees were commonly 15 to 20 feet high, protecting island interiors that are 10 to 15 feet below sea level. However, they started out as 3 to 5 feet high dikes of peat, and over the last 150 years, were continuously raised and widened with either dredged, clean permeable river sand or interbeded layers of organic and mineral soils. Over time, the weight of the levees compressed and displaced the soft, organic soils beneath them, resulting in the land surface significantly subsiding. The foundations of these levees consisted of river sediments and organic materials, ranging from coarse-grained sediments, including gravel and loose, clean sands to soft fine grained materials such as silts, clays, and organics including fibrous peat. Hydraulic conductivity of the sand layer was estimated to be 10^{-3} cm/sec based on the preliminary seepage analysis on Terminous Tract (CDWR, 2007). High level of flood and subsidence of interior land made both the levees and their foundations very susceptible to have seepage distress and internal erosion.

Similar seepage induced levee failures have occurred in Yuba and Sutter County which are located in north of Sacramento, California. The Yuba City Basin, called the Sutter Basin, is a flat plain with lower elevation than the surrounding Sacramento, Feather, Yuba and Bear Rivers. Levees failed in 1955, 1986 and 1997 in this area. Especially, the flood in 1955 resulted in over 40 lives lost and approximately $65 million dollars of damage, which was approximately one-third of the total assessed properties in the region (Sutter Butte Flood Control Agency, 2007). In February, 1986, Linda levee along the south side of Yuba River failed at 74.3 feet of the water elevation which was

8.4 feet below the elevation of the levee crest. This levee, which was originally constructed with mine slickens in 1904, was underlain by a thick layer of porous and unstable gravel. In 1934, the levee was heightened up to 80.7 feet using borrow material from the river side of the embankment; the Corps of engineers then raised the levee to 82.7 feet of the crest in 1940. The width of the levee crest was approximately 10ft. After the levee failure, pump tests in the Dhillon Orchard next to the failure site were performed in 1990; the results showed that the hydraulic conductivity of the gravel layer was 0.2 cm/sec. During the flooding, the water seeped through the gravel layer and emerged from the surface where the upper layer had been disturbed. Historically, this region had experienced sand boils which resulted in the undermining and collapse of the levees.

Several seepage induced levee failures occurred during the 1993 Midwest flood, called "the Great Flood of 1993." It was the largest flood measured at St. Louis. Nine Midwestern states were damaged by the flood. In Illinois, 39 counties were declared federal and state disaster areas, and another five counties were declared state disaster areas (Chrzastowski, 1994). Because of this catastrophic flood, 38 people died and estimates of the damage have ranged from $12 to $16 billion (GAO, 1995). In July, 1993, Kaskakia Island, Bois Brule, and Sny levee which were located along the Mississippi River, failed by excessive underseepage and internal erosion. Water pressure from the Mississippi River caused a large sand boil, resulting in opening 600 to 1500 feet long breach. Water height was still in the freeboard of 1 to 2 feet below the crest of the levee. These levees were typically constructed of sediments dredged from the river channels or excavated from the flood plains and built on similar foundation condition. The top layer consists of alluvium layer with thickness of 10 to 25 feet underlain by coarser sands and gravels. The substratum sands varied in thickness from

100 to 150 feet and were highly pervious with hydraulic conductivity ranging from 3.5×10^{-2} cm/sec to 1.2×10^{-1} cm/sec (Turnbull and Mansur, 1959).

Foundation condition of Sny Island levee was a little different from other levees along the Mississippi River. The thickness of surface layer ranged from 5 to 10 feet and generally consisted of 2 to 4 feet of lean clay overlying the silt zone that was underlain by silty sand. The bedrock was the Ordovician formation with elevation significantly higher than the regional elevations. Therefore, the thickness of the sand stratum was approximately 35 feet, which was lower than the thickness of sand in the surrounding regions of 100 feet. The height of the levee was approximately 15 feet. Hydraulic conductivity of the sand layer ranged from 1×10^{-2} cm/sec to 2×10^{-2} cm/sec. Mansur et al. (2000) reviewed studies carried out since the 1940's on underseepage, piping, and sand boil formation in the Mississippi River Valley. They gathered sand boil information for seven levee districts after the 1993 high water. Uplift gradients calculated from existing piezometers showed that significant sand boils were observed when uplift gradients were in the range of 0.58 to 0.84.

In August 2005, Hurricane Katrina produced widespread damage in New Orleans, Louisiana. About 1,800 people were killed and over 100 billion dollars of property damage resulted due to the flooding. There were 50 major breaches in the Hurricane Protection System during Katrina (Seed et al., 2008a and USACE, 2008). Levees failed south of London Avenue canal because water seeped through foundation soil, thus increasing the hydraulic gradient enough to initiate the piping. The site investigation was performed by the Interagency Performance Evaluation Taskforce (IPET) which was in charge of an intense performance evaluation of the New Orleans and Southeast Louisiana Hurricane Protection System during Hurricane Katrina. The levee beneath the I-wall was approximately 15 feet in height and 10 feet in width. The levee

foundation consisted of a Swamp-Marsh unit which is represented as organic clay (usually CH) and a peat underlined by Holocene beach. Swamp-Marsh has a hydraulic conductivity of 2×10^{-6} cm/sec to 2×10^{-4} cm/sec. Holocene beach is a loose to medium dense sand layer with a hydraulic conductivity of 3×10^{-2} cm/sec.

The historic underseepage induced levee failures shown above indicate that levees located on the pervious granular deposits are highly subject to underseepage, thus subsequent failures so that they need to be mitigated.

2.4. Mitigation of underseepage

The amount of underseepage and uplift hydraulic pressure vary with the river stage, location of seepage entrance, thickness and perviousness of the substratum and of the landside top stratum, underground seepage, and geological features (Turnbull and Mansur 1959). However, underseepage control measures are typically required or extended if the exit hydraulic gradient measured in the vertical direction exceeded an allowable range of 0.6 to 1.1 (Wolff, 2002). In order to control the seepage induced levee failure, various seepage control measures can be used such as riverside blankets, relief wells, seepage berms and cutoffs.

2.4.1. Riverside blankets

Riverside blankets consist of relatively impervious soils to prevent water from seeping into a borrow pit or thin top stratum, resulting in reducing landward pressure and seepage. The blanket should be wide enough to cover the width of borrows pits, typically 1000 to 1500 feet, and its thickness ranges from 3 to 5 feet. The hydraulic conductivity of blankets is typically on the order of 0.01 to 0.1×10^{-4} cm/s (Kolb, 1976).

However, the required thickness and length of a blanket are determined based on the hydraulic conductivity of the blanketing material, the stratification and thickness of the foundation, and the depth of reservoir (Sherard et al., 1963). Riverside blankets can be constructed after levee construction is completed. However, the blanket material should satisfy the filter criteria. If it is constructed on a sloped area, it should have protection against wave attack and erosion from runoff. Moreover, an upstream blanket will be less effective as seepage goes through the upstream portion of the embankment and into the foundation (Wolff, 1987). Based on the piezometer data obtained at the crest of Mississippi river levees during 1950's high water, the average hydraulic conductivity of the silty blanket was reported about 2.5×10^{-4} cm/sec and silty sand blankets up to 10 feet thick averaged about 6.0×10^{-4} cm/sec (USACE, 1956).

2.4.2. Relief wells

Using relief wells is one of seepage control methods to relieve uplift pressures beneath the levee. Typically, the wells spaced 75 to 375 feet apart on the landward sides of levee (Kolb, 1976). It is recommended that the wells have depths of 60 to 120 feet with screens 40 to 80 feet in length (USACE, 1956). However, the relief wells should penetrate through the full depth of the pervious layer. Otherwise, the effectiveness of the wells is reduced significantly. Relief wells require low right-of-way for construction. In addition, the well system is so flexible that intermediate wells can be added later if necessary to keep the pressure below any desired value (Sherard et al., 1963). However, relief wells require periodic inspection and maintenance since the efficiency of the wells is reduced with time. A filter screen should be maintained to protect from back-flooding due to clogging. Moreover, seepage quantity needs to be controlled since it increases about 20 to 40% depending on the site conditions (Kolb,

1976). If no collection and disposal measures are provided for well effluent, it can cause damage during normal spring high water (Wolff, 2002). Finally, if high uplift is present, boring and installation may be difficult requiring extra measures to keep the hole open and stable until the screen and filter are installed (Wolff, 1987).

2.4.3. Seepage berms

Seepage berms provide additional weight to balance upward seepage forces and proved a longer path of seepage flow, resulting in preventing ground heaving near the levee. The thickness of the berms at the toe of levees ranges from 3 to 10 feet and their width ranges from 100 to 400 feet (Kolb, 1976). There are four types of seepage berms: impervious berms, semi-pervious berms, sand berms, and free-draining berms. The selection of type of berm depends on the availability of fill materials, landside space of the levee, and the relative costs. Advantages of constructing seepage berms include the protection against sloughing of the landside levee slope, easy to build and require low maintenance. Disadvantages of seepage berms include the space required for construction and the cost and availability of borrow materials. In addition, it is not efficient where the top stratum is relatively thick and high uplift pressure develops. Moreover, the berms would not provide mitigation for foundation seepage. If berms have low hydraulic conductivity, they will reduce seepage, but increase uplift pressure beneath the downstream toe of the levee since they force seepage to exit further downstream of the levee. If pervious, they must be designed as a filter or with an underlying filter to prevent upward migration of particles from the foundation materials beneath them (Wolff, 1987). No field data is available, but seepage berms have been typically designed to have the permeability of 1×10^{-4} cm/s for impervious berms and 1.0×10^{-2} cm/s for pervious berms in Mississippi river levees (USACE, 1956).

2.4.4. Cutoff walls

Cutoff walls reduce the quantity of underseepage by lengthening the seepage path. The cutoff should penetrate at least 95% of the full depth of the pervious foundation (USACE, 1956). However, partial seepage barriers are applicable to the sites where the average hydraulic conductivity of the foundation soil decreases with depth or where there is a single continuous impervious layer into which the cutoff can be connected (Sherard et al., 1963). Cutoff walls can be constructed with sheet piling, grouting and slurry.

2.4.4.1. Sheet piling

Sheet piling is a seepage control measure using steel sheet piles as a seepage barrier. Steel sheet piles which are driven by hammer forms a continuous wall. Sheet piles have a limited penetration depth of approximately 100 to 150 feet depending on soil type and drilling equipment (Smyth et al., 1995). Sheet piling is very strong and successful in containing both soil and water. It can resist chemical attacks and show consistent hydraulic conductivity. Its construction does not require excavation; therefore, the disposed wastes can be minimized. Installation procedures are well established and it is possible to construct with irregularly shaped barriers in confined areas. However, sheet piles tend to be relatively expensive and can not guarantee the perfect cutoff of seepage flow as leakage occurs through interlocks, at splices, and through torn interlocks (USACE, 1956). Piling can potentially corrode if used for long-term containment (Rumer et al., 1996). Moreover, it is difficult to install in hard, rocky soil sites and installation can cause significant noise and vibrations.

2.4.4.2. Slurry wall

Slurry wall is a common type of subsurface wall to prevent ground water flow and is considered a baseline barrier technology (Heiser and Dwyer, 1997). Slurry wall is constructed by using slurry trench technique (Figure 2.2). The bentonite slurry is used to support the trench and forms a filter cake on the trench sidewalls plugging the soils. The excavation under a slurry filled trench provides stability and prevents the trench from collapsing. After excavation, the permanent wall is formed by replacing the slurry with the engineered low permeability backfill such as cement, bentonite, fly ash, ground-blasted furnace slag, and clay. There are different types of materials, and combinations of materials that can be used to construct slurry cutoff wall: soil-bentonite, cement-bentonite, and plastic concrete. The limit of wall depth is approximately 200 feet (Pearlman, 1999).

The construction of slurry walls has been well understood, practiced and accepted. Installation is quick (Heiser and Dwyer, 1997) and can be used with other remediation technologies such as pressure relief wells and riverside blankets. If cement-soil is used for wall material, they will provide more strength than soil-based walls. Additionally, they do not require backfilling since cement-bentonite is self-hardening slurries with little or no displacement. Slurry wall does not require wide access areas. However, installation of slurry wall requires excavation, produces large amount of disposals and needs a space for mixing. Slurry level should be above the groundwater table and the orientation of wall is limited to the vertical direction. In addition, it is difficult to assess proper emplacement. Cracking due to shrinkage, thermal stress, and wet/dry cycling can increase hydraulic conductivity of the wall (Heiser and Dwyer, 1997).

Figure 2.2 Construction of slurry wall in Yuba County, CA, (taken from www. sierratestinglaboratories.com)

2.4.4.3. Deep soil mixing (DSM)

Deep soil mixing (DSM) is a technique where an additive is mixed with the soil to produce a hard mass that acts as a barrier. An auger with a mixing shaft simultaneously drills and injects the desired material, resulting in a column of soil and material. Continuous walls can be constructed by overlapping individual columns (Mutch et al., 1997). Possible slurry materials include bentonite, cement, lime, and additives such as fly ash and slag. Walls can be constructed up to 100 feet in depth. Since deep soil mixing is non-displacement technique, disposal costs and labor work can be minimized. Moreover, walls can be installed in small areas with less danger of collapse because they are constructed in small sections. However, it is difficult to verify continuity so that gaps between walls are minimized. During installation, verticality is very important and rock mixed into the slurry can cause construction problems and limit drilling ability.

2.5. Permeation grouting

For levees located near urban areas, one method to mitigate underseepage includes the treatment of the granular soil deposits with an engineered fluid delivered by permeation (permeation grouting), resulting in a less permeable deposit. Various grouts are filled into the soil void spaces by pressure injection through boreholes. Some additives can be used to control the grout set time. Contrast to the slurry wall, permeation grouting does not destruct the original soil structure in the process and the grouting operation creates minimal ground disturbance and can be used for in situ remediation to existing structures. Since the permeation grouting is an in-place technique, disposal costs and labor work can be reduced. However, the technique is limited to use in some formations depending on the types of grouts. In addition, it is difficult to predict the grout penetration radius and the flow of grout in heterogeneous soils (because the grout tends to follow the path of least resistance), and ensure continuity of grouting.

The disadvantages of a single grouting may be overcome by performing a sequence of overlapped grouting. Grout curtain wall is a horizontally extended seepage barrier which is constructed by permeation grouting technique. The grout curtain is formed by one or more interlocking rows of grouted soil or rock cylinders. Laboratory works by Karol (2003) showed that a minimum of three rows of holes are required to approach complete cutoff. In order to secure homogeneity of the individual hole, it is desired to grout with short sections. The distance between individual holes are determined by economics, but typically 1 to 5 feet. The success of this seepage wall is highly dependant on types of treated soils and compatibility between soil matrix and grouts. This type of cutoff has been successfully installed in Serre Pocon, Sylbentein, FR Germany, and Mattmark dam (Karol, 2003).

There are two types of permeation grouting based on injection materials: particulate (bentonite and cement) and chemical grouting (resins or other polymers). Particulate grouts, mainly cement grouts, are composed of water and Portland cement, and the properties of grouts vary with the water to cement ratio (W/C). Moreover, the blending with an additive, such as bentonite and sodium silicate, changes grout properties. Similar to the particulate grouts, the chemical grouts penetrate into the soil by permeation. However, chemical grouts can penetrate into finer grained soils which are inaccessible to particulate grouts. While cement suspensions and chemical solutions have been widely utilized as grouts for many decades, they may cause groundwater contamination due to long term reaction with groundwater (Metcalfe and Walker, 2004). This implies that bentonite can be an alternative in terms of environmental friendliness and long term safety.

Based on the injection method, permeation grouting is classified as two main methods: point injection and sleeve pipe injection (Tube-A'-Manchette). In the point injection method, the casing is installed to the full depth and grout is injected as the casing is withdrawn (Rumer et al., 1995). As shown in Figure 2.3, the Tube-A'-Manchette method involves grouting a sleeve pipe in the grout hole and injecting grout through holes in the pipe (Rumer et al., 1995). The holes are covered and placed at 1 foot intervals along the pipe and the grout is injected under a constant pressure or flow rate into the soil. The determination of the injection pressure or flow rate highly depends on type of soil, depth of injection, confining soil and structural pressure. The advantage of the Tube-A'-Manchette method is that different grouts can be injected into different holes, and grout can be re-injected if there is a problem (Pearlman, 1999).

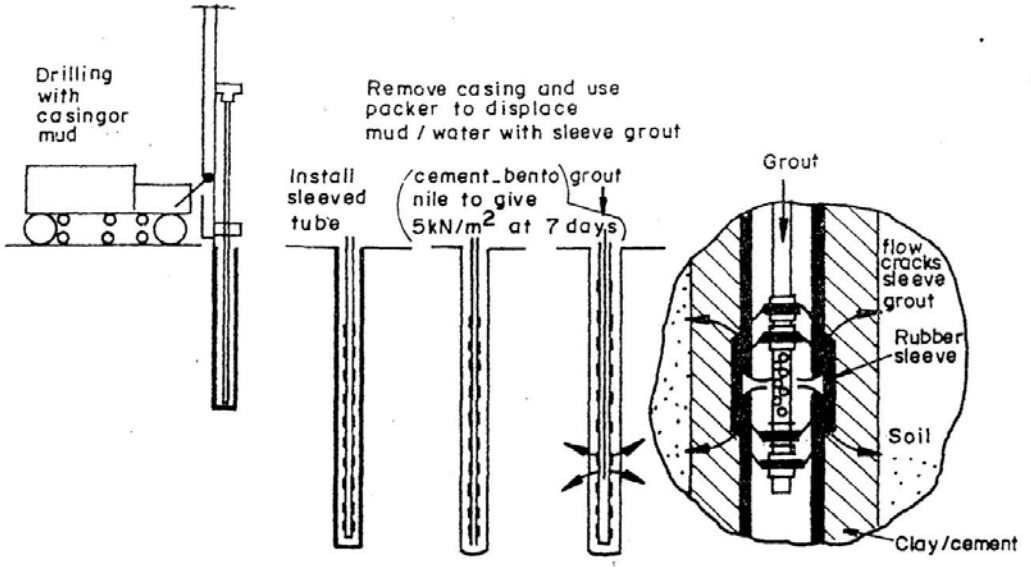

Figure 2.3 Schematic of permeation grouting procedures using Tube-A'-Manchette (from http://www.ce.metu.edu.tr)

2.6. Rheological properties of bentonite grouts

The permeation of a grout through porous medium is significantly affected by both, rheological property of the grout and properties of the porous medium. In addition, the addition of an ionic additive greatly changes rheological property of bentonite grout, producing different permeation character. From this section, theoretical and experimental backgrounds for this study are presented including rheology, structural kinetics of bentonite-additive system, groutability and hydraulic conductivity of the grouted sand.

2.6.1. Introduction to rheology

Rheology is a study of deformation and flow of matters. Two constitutive relations have been used to approximate the material behavior: Hooke's law of elasticity and Newton's law for viscous fluids. Hooke's law relates the stresses to strains linearly

within elastic materials to the constant proportionality (elastic modulus), which is considered as a material property. However, the relationship is only valid within the range where the stresses are directly proportional to the strains; not showing any strain softening or hardening.

$$\sigma = E\varepsilon \quad \text{or} \quad \tau = G\gamma \tag{2.1}$$

Where σ is the tensile stress, τ is the shear stress, ε is the tensile strain, γ is the shear strain, E is the Young's modulus and G is the shear modulus. While Hooke's law represents an elastic solid behavior, Newton's law explains the viscous behavior of fluids. This constitutive relationship relates the shear strain rates to the applied shear stresses with the constant proportionality (viscosity). Similar to the elastic modulus, viscosity is a material property which is a measure of the resistance to shear flow.

$$\tau = \eta \dot{\gamma} \tag{2.2}$$

Where τ is the shear stress, $\dot{\gamma}$ is the shear rate and η is the viscosity of fluids. However, the common material behavior can not be fully explained with the single relationship mentioned above, since they show both elastic and viscous behavior known as viscoelasticity. The material behavior is time dependent so the response depends on observation time or duration of experiments (Barnes et al., 1989). Once a strain is applied to a solid material, the applied strain energy is stored in the material up to rupture (solid like behavior), but it can be dissipated almost instantaneously in a liquid (liquid like behavior). In viscoelastic materials, some portion of energy can be stored, followed by energy dissipation. The time of energy dissipation known as relaxation time varies with the type of material; the more a material is solid like, the slower the energy is dissipated. The types of behavior are distinguished using the Deborah number which is a ratio of a materials relaxation time to the experimental or observation time of the

material. A material with Deborah number greater than 1, equal to 1 and less than 1 shows elastic, viscoelastic and viscous behavior respectively.

When the Deborah numbers are greater than or equal to 1, there are no significant changes in the internal structure so that the behavior is independent of the applied shear rate. This flow characteristic is tested by performing stress relaxation, creep and recovery and oscillatory shear test. This study focuses on oscillatory shear tests since these tests provide information on the transition from a sol to a gel in bentonite suspensions where the weak liquid-like dispersions transformed to strong solid-like gels. In addition, the dynamic properties of bentonite suspensions measured from the test may be useful properties to investigate the stability of bentonite suspensions under seismic loading condition (El Mohtar et al., 2008). The oscillatory tests are performed by applying oscillatory stains or stresses at a constant frequency and materials are deformed sinusoidally. The more common approach is that the sinusoidal strains are applied and the corresponding sinusoidal stresses and shear rates are monitored (Clarke, 2008).

$$\gamma = \gamma_o \sin(\omega t) \tag{2.3}$$

$$\tau = \tau_o \sin(\omega t + (\delta + \Phi)) = \tau_o' \sin(\omega t) + \tau_o'' \cos(\omega t) \tag{2.4}$$

$$\dot{\gamma} = \gamma_o \omega \cos(\omega t) = \dot{\gamma}_o \cos(\omega t) \tag{2.5}$$

Where γ_o is the amplitude of strain, τ_o is the amplitude of stress, τ_o' is the amplitude of elastic component stress, τ_o'' is the amplitude of viscous component stress $\dot{\gamma}$ is the amplitude of shear rate, ω is the angular frequency, t is the time, and δ and Φ are the phase angles (in phase with the strain and strain rate). The applied sinusoidal strain is 90 degrees out-of-phase with the measured sinusoidal shear rate based on the summation of phase angle δ and Φ. The measured sinusoidal stress is divided into two components: in phase with the applied strains and in phase with the measured shear rate.

In purely elastic materials, the stress and strain occur in phase so that the response of one occurs simultaneously with the other. In purely viscous materials, there is a phase difference between stress and strain where strain lags stress by a 90 degree. Therefore, materials subjected to oscillatory shear displays elastic like behavior and viscous like behavior when the phase angles for the measured sinusoidal stresses are 0< Φ+ δ <45 degrees and 45< Φ+ δ<90 degrees, respectively. When Φ+ δ is 45 degrees the material behaves like a viscoelastic fluid. Instead of using the measured sinusoidal stress, material functions such as the in-phase or elastic modulus (storage modulus), G', the out-of-phase, viscous modulus (loss modulus), G", and complex modulus G*, along with phase angle are defined as:

$$G' = \frac{\tau_o'}{\gamma_o} = \frac{\tau_o}{\gamma_o}\cos(\Phi') \tag{2.6}$$

$$G'' = \frac{\tau_o''}{\gamma_o} = \frac{\tau_o}{\gamma_o}\sin(\Phi') \tag{2.7}$$

$$\tan(\Phi') = \frac{G''}{G'} \tag{2.8}$$

$$G^* = \frac{\tau_o}{\gamma_o} = G' + iG'' \tag{2.9}$$

On the other hand, the flow behavior becomes shear rate dependent when the Deborah numbers are less than 1, which indicates significant changes in the internal structures of the material. In this case, the fluid initially shows a liner behavior, followed by a non-linear behavior. Due to the shear rate dependency, two types of flow behavior are generated within a fluid or in different fluids: Newtonian and non-Newtonian. Figure 2.4 shows various flow response based on shear rates. The observed flow behaviors are typically described by constitutive models.

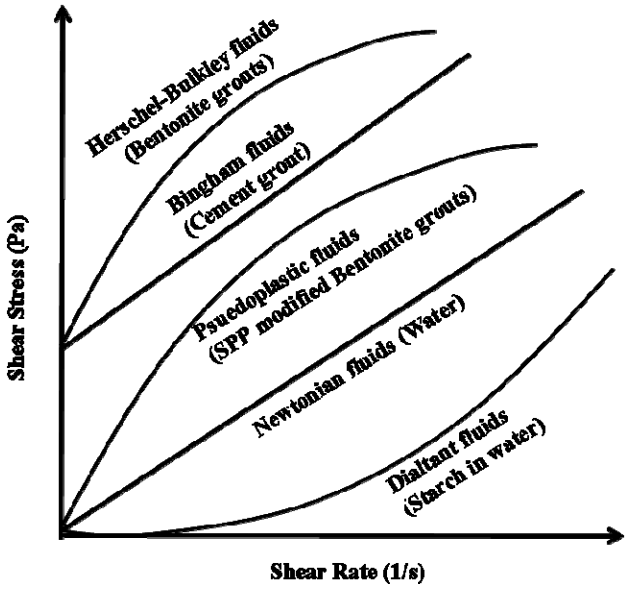

Figure 2.4 Flow behaviors of different materials

The Newtonian fluids such as water strictly obey the Newton's law for viscous fluid at constant temperature and pressure (Barnes, 1999). A change in temperature and/or pressure will cause a change in the Newtonian viscosity. Since the applied shear rate is directly proportional to the stress, the flow curve is a straight line passing through the origin.

However, fluids that deviate from Newtonian fluid displays various types of flow behaviors. Fluids which are represented by pseudo-plastic and dilatant flow display a shear thinning or thickening behavior respectively. Shear thinning is a phenomenon that the internal structure of fluids breaks continuously due to an increase in shearing. This phenomenon typically occurs in particulate suspensions and long chained polymer due to 1) alignment of the particles with respect to the flow direction and 2) rearrangement of the internal structures and breakdown flocs, decreasing the viscosity of fluids. The pseudo-plastic flow can be modeled with a power law equation

$$\tau = K\dot{\gamma}^{n} \tag{2.10}$$

Where K is the flow consistency index and n is the flow behavior index. The relative value of K refers to viscous behavior of fluids and n indicates a deviation of the fluid behavior from Newtonian behavior. More complex models based on the power-law model have been proposed to improve the description of pseudo-plastic fluid behavior. The models are based on the observation that a fluid shows two different behaviors depending on the range of shear rates applied: shear-thinning at low to medium shear rates, followed by Newtonian behavior at high shear rates. The Carreau model incorporates two terms of η_o and η_∞ which correspond to the viscosity at very low and high shear rate.

$$\frac{\eta_o - \eta}{\eta_o - \eta_\infty} = (1 + (K\dot{\gamma})^2)^{(n-1)/2} \tag{2.11}$$

On the other hand, shear thickening occurs due to the buildup of the internal structure with the increase in shearing. Although the pure shear thickening behavior is extremely rare, it can be represented with the power low model having n greater than 1.

Some fluids show yield stress, which is a minimum stress to initiate flow. Below this stress, a material shows solid-like behavior with an infinite viscosity. Above the yield stress, the material behaves like liquid and the viscosity changes with the applied shear rates. If the power-law fluids have a yield stress, it is expressed with Herschel-Bulkley model, incorporating the yield stress term to the power law equation

$$\tau = \tau_y + K\dot{\gamma}^{n} \tag{2.12}$$

For the materials represented by Bingham model such as cement based grouts, the initiation of flow take places when the applied stress exceeds yield stress, then the flow

becomes Newtonian at large shear rates. The model is expressed as the following relationships:

$$\tau = G\gamma \qquad (\tau<\tau_y) \qquad (2.13)$$

$$\tau = \tau_y + \eta_{pl}\dot{\gamma} \qquad (\tau>\tau_y) \qquad (2.14)$$

The bentonite suspensions show various flow behaviors depending on bentonite fractions and testing conditions. According to Kasperski et al. (1986), diluted aqueous suspensions of Na-montmorillonite (up to 1%) show low viscosity similar to water. Moreover, Bandenburg and Lagaly (1988) reported that the influence of Na-montmorillonite concentration on the viscosity of suspensions depends on particle size of Na-montmorillonite, but the flow is Newtonian up to about 5% solid concentration below the shear rate of 200 s^{-1}. Even though the bentonite suspensions show a Newtonian behavior at the low concentration, the flow behavior is also affected by pH. Above 5% of solid concentration, the suspensions behave as non-Newtonian fluid having a yield stress and also show shear thinning behavior, resulting in a flow behavior that can be modeled by the Herschel-Bulkley model (Bekkour et al., 2005 and Kelessidis et al., 2007). However, the addition of electrolyte changes the type of flow behavior to pseudo-plastic flow which is modeled by power low equation depending on the amount of electrolyte introduced.

2.6.2. Yield stress

There is still no consensus as to the existence and definition of the yield stress (Cheng, 1986; Barnes, 1999; Barnes and Nguyen, 2001; Uhlherr et al., 2005) and its measurement is challenging because it highly depends on the measuring systems used, the testing programs, and the interpretation methods (Nguyen et al., 2006). However,

the general belief is that the yield stress is created by an internal structure of a fluid that is able to resist a certain amount of stress prior to flow. Steffe (1992) explained that a variation in yield stress measurement depending on the rest time, the shear rate and type of test performed was attributed to the presence of a dominant time dependent microstructure in a liquid based on a two-structural theory proposed by Cheng (1986). Despite of the debatable nature of yield stress, it is still a useful parameter, especially in bentonite suspensions since it is an indicator to the information of micro-structures in the suspensions. Bentonite particles in aqueous medium interact with each other, creating a continuous network with a flocculated structure. The suspensions flow only when the applied stress is large enough to break down the network structure and the yield stress represents the strength of network structure (Uhlherr et al., 2005). In addition, yield stress becomes a useful parameter in grouting applications since it is related to stoppage of grout flow through a porous medium and the post grouting performance after a certain resting period (Cambefort, 1964; Gustafson and Stille, 1996; Axelsson, 2006; Liu and Neretnieks, 2006; Axelsson and Gustafson, 2007; Axelsson et al., 2009). Details are presented in Chapter 7.

2.6.3. Rheometry

Based on the principles of drag flow, several common geometries such as parallel plates, cone and plate and bob and cup are used in shear rheometry for the investigation of the rheological behavior of suspensions. Among them, the cone and plate is the most widely using geometry. As shown in Figure 2.5, the geometry consists of a rotating truncated cone and a fixed base plate.

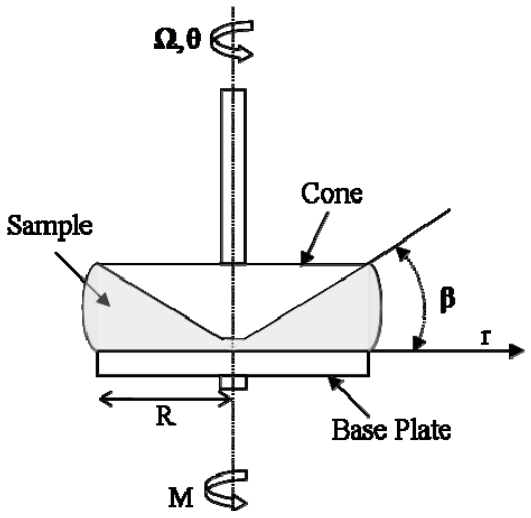

Figure 2.5 Schematic of cone and plate geometry

The cone is rotated at a speed generated by the applied torque. The angular deflections and velocities generated by the applied torque are measured, and then shear stresses, shear strains and shear rates are calculated based on the following relationships:

$$\tau = \frac{3M}{2\pi r^3} \tag{2.15}$$

$$\gamma = \frac{\theta}{\beta} \tag{2.16}$$

$$\dot{\gamma} = \frac{\Omega}{\beta} \tag{2.17}$$

Where M is the applied torque, r is the diameter of the cone, θ is the deflection angle of the cone, Ω is the rotation velocity of the cone, and β is the angle of the cone. The angle of the cone is determined such that the change in the gap size generates constant shear rate along the radius, thus producing a homogenous flow. However, it is challenging to maintain an intact initial structural state of fluids using this geometry because the structural fluids are susceptible to be disturbed during the setup for testing. Therefore, a preshearing should be applied prior to any measurement to provide a

consistent initial condition. This geometry is also susceptible to the artifact known as wall slip which is caused by the depletion of particles near the surface of the cone and the plate. Due to this effect, a low-stress Newtonian plateau is created in a stress versus viscosity plot (Buscall et al., 1993), and the measured rheological properties are significantly underestimated. Moreover, the particles can be easily trapped in the small gap between the cone and plate, significantly increasing torque (or interpreted shear stress). Thus, the size of particles limits the usage of this geometry.

Vane geometry has become popular for measuring yield stress of thixotropic fluids such as bentonite suspensions (Benna et al., 1999; Coussot et al., 2002, 2006; Mahaut et al., 2008), food systems, bioengineering systems, and various types of dispersions (Barnes and Nguyen, 2001) over the past 30 years. The vane is rotated in a cup and the shear stress and shear rate are determined from the measured torque and rotational speed as shown in Figure 2.6.

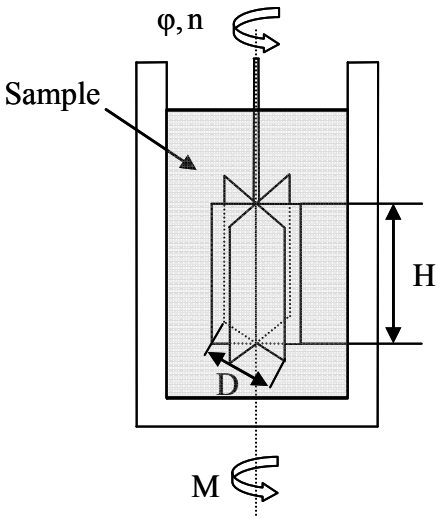

Figure 2.6 Schematic of vane geometry

This geometry assumes that the fluid between the vane blades act as part of the vane and the diameter of the vane is described as a cylinderical shape and the shearing of

fluids occurs at the boundary of the cylinder. Similar to cone and plate, the vane is rotated at a speed generated by the applied torque. The angular deflections (φ) and speed (n) generated by the applied torque (M) are measured, and then shear stresses, shear strains and shear rates are calculated. In vane geometry, disturbance can be minimized by inserting thin blades into the sample (Cheng, 1986; Barnes and Carnali, 1990; Barnes and Nguyen, 2001). In addition, the measurement is less affected by large particles. Because the shearing plane occurs only within the sample itself, wall slip can be avoided (Keentok, 1982 and Stokes and Telford, 2004). However, the application of the vane is limited to the yield stress fluids which are not highly influenced by inertia effects. In this method, the secondary flow and end effect are typically assumed to be negligible for all practical purposes (Barnes and Carnali, 1990).

2.6.4. Determination of yield stress

The yield stress is evaluated by either indirect or direct method. The indirect method typically determines yield stress by fitting constitutive models to the flow curve. The flow curve is a plot of shear stresses versus shear rates obtained from various rheometries. Along with the artifact such as wall slip mentioned in the previous section, the yield stress obtained from the constitutive models may not have any physical meanings (Zhu et al., 2001), and tend to overestimate the actual yield stress (Coussot, 2005). In addition, the yield stress should be determined by an extrapolation since the lowest shear measurement is finite.

As an alternative, the yield stress can be graphically determined from the shear stress-shear strain curve obtained from the stress ramp technique (details for this technique will be presented in Chapter 3). Initially, the shear strain increases linearly with shear stress at a slow rate; this rate increases significantly when the shear stress

reaches sufficiently large values and the slope of the stress-strain curve becomes close to zero (Figure 2.7). For this approach, the plots can be either τ-log γ or log τ-log γ plots. Two straight lines are extended from the solid-like and liquid like regimes; the shear stress value at the intersection between these two lines is determined as the yield stress (Zhu et al., 2001 and Clarke, 2008).

With the vane geometry, yield stress can be directly measured (Nguyen and Boger, 1985). The vane is fully inserted into the sample and a torque is applied at a constant but sufficiently slow rate; the change in torque is monitored with time as shown in Figure 2.8. The yield stress is then calculated using the maximum torque and the dimensions of the vane such as diameter and length of the blades. The yield stress is calculated by the following equation

$$\tau_y = \frac{2}{\pi D^2}\left(\frac{H}{D}+\frac{1}{3}\right)^{-1} T_{\max} \tag{2.18}$$

Where τ_y is the yield stress, T_{max} is the maximum torque, D is the diameter of the vane, and H is the length of the blades. The comparison of different yield stress measurements will be presented in Chapter 3.

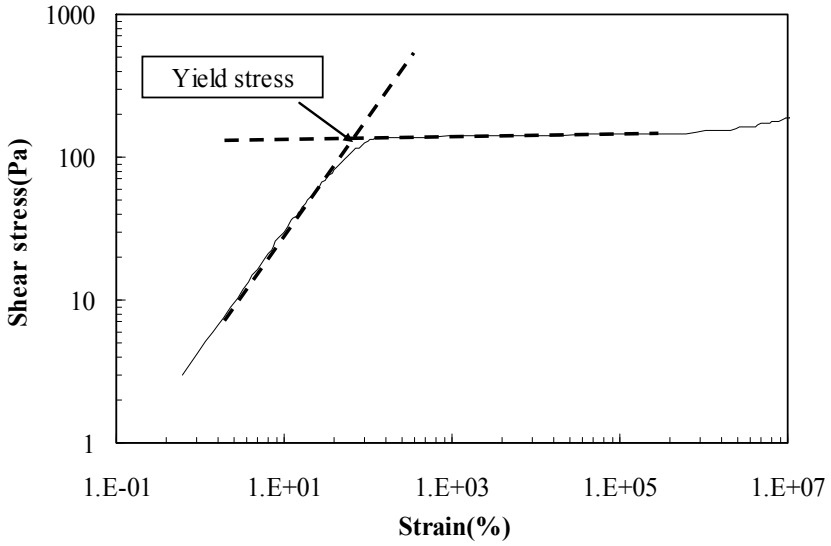

Figure 2.7 Schematic of the determination of yield stress using log τ-log γ plot

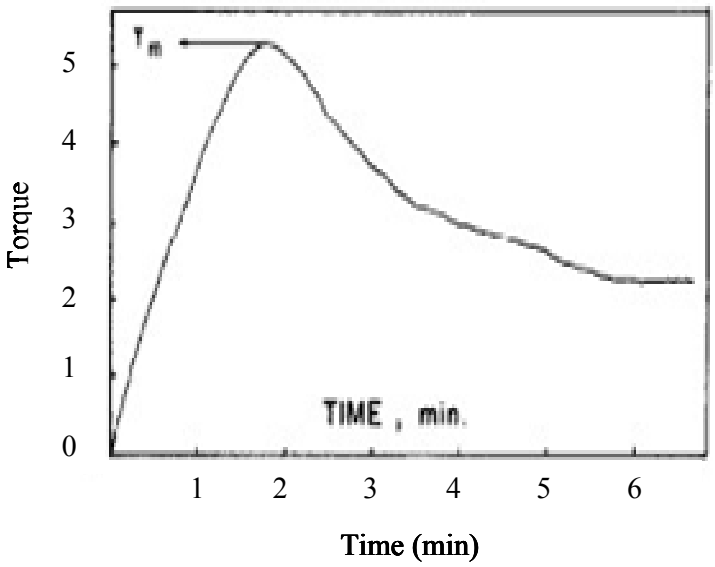

Figure 2.8 Schematic of the determination of yield stress using direct method (Adapted from Nguyen and Boger, 1985)

2.6.5. Time-dependent yield stress measurement

Bentonite suspensions are well known thixotropic materials. Under shearing, the bentonite suspensions lose their strength, but it gradually increases at rest condition. This is a desirable property in the grouting application, but it is challenging to maintain an intact initial structural state of fluids for time dependent measurements because they are subject to disturbance during the setup for testing when using the conventional geometries (cone and plate, plate and plate, and bob and cup). In order to eliminate the disturbance and provide consistent initial condition, preshearing is typically applied prior to yield stress measurement (Ketz et al., 1988; Bekkour et al., 2005; Coussot et al., 2002, 2006; Uhlherr et al., 2005; Mahaut et al., 2008). The preshearing technique provides consistency in the initial yield stress measurements under flow conditions; this measurement is desirable for the initial grout yield stress (immediately after mixing) since the grouts will be flowing during the grouting process. However, for the post grouting analysis where the grout is not mobile inside the soil/rock, the measurement of yield stress after a long resting period under no flow conditions is more representative. The samples should remain in the rheometer for the entire resting time (a few days to months) after preshearing to achieve long term measurements with minimal disturbance. This becomes impractical in terms of equipment management and testing efficiency. More importantly, it will be practically impossible to prevent evaporation of such a small amount of sample for a long time. The evaporation is a larger source of error in the cone and plate measurements due to the small sample size; the vane is inserted deep into the suspension and surface evaporation is less critical on the measured yield stress. Vane geometry has been considered a good practice for the measurement of thixotropic fluids and by resting samples in separate cups for the desired resting times (as being

proposed in this research in Chapter 4), disturbance during sample loading can be minimized.

2.7. Structural kinetics of bentonite suspensions

2.7.1. Bentonite

The bentonite clay is derived from volcanic ash, having high plasticity and swelling potential and primarily formed from the mineral montmorillonite. The minerals consist of a 2:1 structure formed with an octahedral (Alumina) layer between two tetrahedral (Silica) layers. Figure 2.9 shows an atomic structure of the montmorillonite.

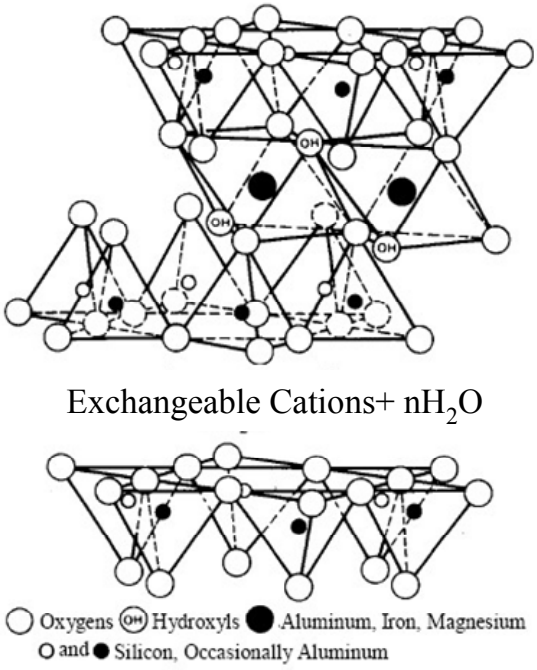

Figure 2.9 Atomic structure of montmorillonite (Adapted from Mitchell, 1993; after Grim, 1959)

The octahedral layer (sheet) includes aluminum, iron or magnesium atoms in octahedral coordination which is closely packed with oxygen and hydroxyls, resulting in equidistance from six oxygen or hydroxyls. The tetrahedral sheet includes a silicon atom (or aluminum) which is equidistant from four oxygen atoms. The two sheets are symmetric and similar in dimensions so that oxygen atoms are shared between the two sheets, forming a unit layer. The unit layers in a clay mineral are stacked parallel to each other and it repeats itself in a lateral direction as well (referred as to Hofmann structure), producing a unit cell. Moreover, a crystal lattice is produced by a stack (face to face) of the unit cell. While bonds in the unit layers are stable due to covalent bonds, the layers in lattice layer are relatively unstable since they are held by Van der Waals forces so that the lattice breaks along the basal surfaces, producing tiny mica flakes. These unit layers can be separated by adsorption of water and other polar molecules, resulting in high swelling potential (van Olphen, 1977).

Because of isomorphic substitutions (e.g. cation replacement of Si^{4+} in octahedral layer and Al^{3+} in tetrahedral layer by Al^{3+} and Mg^{2+} respectively), the surface of the layers are always negatively charged. At the edge of the particles, which is relatively small in area, the continuous crystal lattices are disrupted and bonds are broken in the silica and alumina sheets (van Olphen, 1977). The edge surface (mainly octahedral Al-OH and tetrahedral Si-OH groups) behaves as an oxide surface (Rand and Melton, 1977 and Johnston and Tombácz, 2002).

2.7.2. Bentonite in aqueous medium

The clay has a constant negative charge since the charge is determined by the lattice substitution. In aqueous environment, the negative charges on the clay surface

are compensated by counter ions attracted to the clay surface, developing diffuse double layers as shown in Figure 2.10.

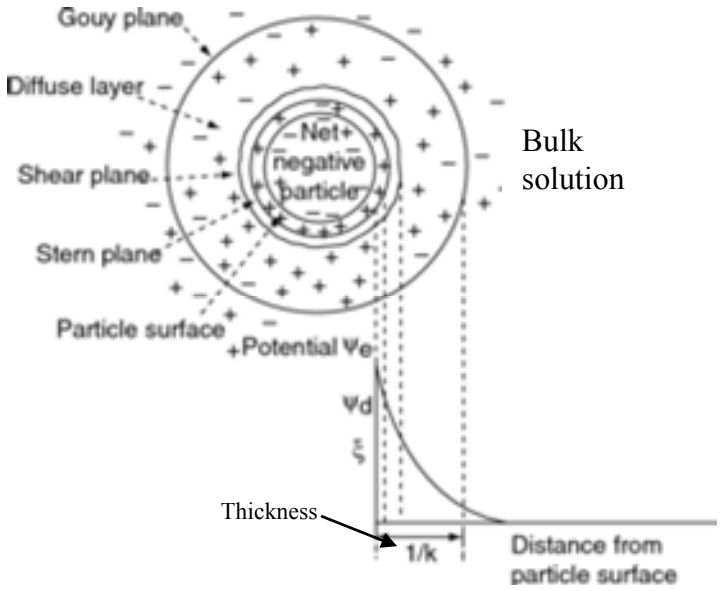

Figure 2.10 Distribution of ions near clay particles and potentials (Adapted from Li and Thin, 2006)

These ions have a tendency to diffuse away from the surface to the bulk solution where the concentration is lower (Luckham and Rossi, 1999). The ions are located both on the exterior surfaces and between unit layers in the stack (van Olphen, 1977). According to Gouy and Chapman theory, the electrical potential ψ of the solution shows an exponential decay with the distance x from the plane surface. This expressed by the following equation:

$$\psi = \psi_o \exp(-\kappa x) \tag{2.19}$$

Where $1/\kappa$ is the thickness of double layer and ψ_o is the surface potential and the x is the distance from clay surface. This expression is valid for a certain distance from the charged surface, where the potential is relatively low and decreases exponentially

$$\frac{1}{k} = \sqrt{\frac{\varepsilon_o RT}{F^2 \sum_{i=n} c_i z_i^2}} \tag{2.20}$$

Where, F is the Faraday constant, c_i the electrolyte concentration, z_i the valence of the ion, ε_o the dielectric constant of the medium, R the gas constant (1 atm/mol·K) and T the absolute temperature (K). However, this theory results in unrealistically high ion concentrations at high potentials due to the assumption of point charge (counter ions). In order to correct for this, Stern (1924) postulated the existence of an adsorbed layer of counter ions adjacent to the particle surface. The potential in the Stern layer decreases linearly from its surface value to the Stern potential, followed by decaying exponentially (Luckham and Rossi 1999).

On the other hands, charges at edge are determined by direct transportation of H^+ and OH^- from aqueous medium depending on pH conditions. While the edges are positively charged at pH values less than the isoelectric point (pH of the dispersions where the edges have zero charge (van Olphen, 1977)), they becomes negative at pH values greater than the isoelectric point. The exact value of the isoelectric point is not well known (Kelessdis et al., 2007), but many researchers reported the range of the isoelectric point from 5 to 8 (Anderson and Sposito, 1991; de Krester et al., 1998; Benna et al., 1999, Missana and Adell., 2000; Abend and Legaly, 2000; Duran et al., 2000; Ramos-Tejada et al., 2001; Legaly and Ziesmer, 2003; Tombácz and Szekeres, 2004). The chemical reactions can be expressed as follows (Tombácz and Szekeres, 2004)

$$\underline{Al}\text{-}OH + H^+ \leftrightarrow \underline{Al}\text{-}OH_2^+ \text{ (Positive edge)}$$

$$\underline{Al}\text{-}OH + OH^- \leftrightarrow \underline{Al}\text{-}O^- \text{ (Negative edge)}$$

$$\underline{Si}\text{-}OH + OH^- \leftrightarrow \underline{Si}\text{-}O^- \text{ (Negative edge)}$$

The zeta potential (the potential at "plane of shear" or boundary between the fixed and mobile part of the diffuse double layer), is important to determine the stability of the colloidal systems. The zeta potential indicates the degree of repulsion between adjacent, similarly charged particles in dispersion. For molecules and particles that are small enough, a high zeta potential will confer stability, i.e., the solution or dispersion will resist aggregation. When the potential is low, attraction exceeds repulsion and the dispersion will break and flocculate. Therefore, colloids with high zeta potential (negative or positive) are electrically stabilized while colloids with low zeta potentials tend to coagulate or flocculate. The zeta potential in sodium bentonite slurry tends to decrease with decrease in pH, but relatively insensitive (Callaghan and Ottewill, 1974; Niriella and Carnahan, 2006; Goh et al., 2011). In addition, Callaghan and Ottewill (1974) reported that the calculated (negative) zeta potential increases in magnitude with ionic strength.

The stability of colloidal system may be explained with the superposition of electrical forces between particles. DLVO theory, developed by Derjaguin and Landau (1941) and Verwey and Overbeek (1948), states that the interaction between colloidal particles is determined by a combination of the interparticle double layer repulsion energy (V_R) and the Van der Waals attractive energy (V_A) as shown in Figure 2.11.

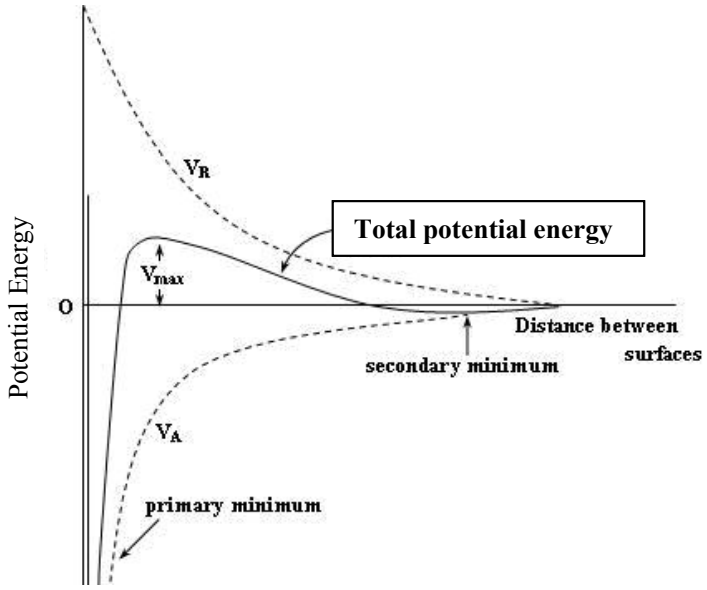

Figure 2.11 DLVO theory: total interaction energy for parallel flat plates as a function of particle separation (Adapted from Luckham and Rossi, 1999)

The inter-particle double layer repulsion (electrostatic) is created by interference of diffuse double layers when two particles approach each other in suspensions due to Brownian motion. Even though there are three types of intermolecular attraction (dipole-dipole, induced dipole-dipole interactions and attractive forces between non-polar molecules (London dispersion forces)), the London dispersion forces, which are due to the polarization of one molecule by fluctuations in the charge distribution in the second molecule, account for nearly all of the Van der Waals attraction in colloidal systems (Luckham and Rossi, 1999). The total interaction energy existing in system can be expressed as:

$$V_T = V_A + V_R \tag{2.21}$$

Because of the presence of electrolyte, particles approach and aggregate each other. The diffuse double layer and DLVO theory are generally utilized to explain the association of bentonite particles in water system since particle association depends on the thickness of double layer and forces between particles which vary with pH, the type

and concentration of ions. For instance, the thickness of diffuse double layer decreases and attractive forces between two plates increase with the increase of cations. On the other hand, the anions increase repulsion between two particles by increasing electro-negativity of particles.

2.7.3. Association of bentonite particles

The delaminated particles, which are surrounded by the diffuse double layers of counter ions, form stable sol by repulsive (electrostatic) forces in the diluted suspensions (<1%). As the particle contents increase (≥1%), the surrounding diffuse double layer restricts rotational and translational motion of particles, producing a certain degree of parallel orientations of particles which tend to be oriented towards positions of minimum free energy under the influence of Brownian motion. Further increase in particle contents (>3%) stiffens dispersions, forming a gel (Luckham and Rossi, 1999 and Abend and Lagaly, 2000).

Due to the charge heterogeneity of bentonite particles, three types of particle association: edge-edge (EE), edge-face (EF) and face-face (FF) may be formed in bentonite suspensions depending on pH. In acidic environment (pH<isoelectric point), the edges of particles are positively charged by adsorption of hydrogen to the broken edge, forming edge (+) to face (-) association under strong attraction. In addition, the dissolved aluminum ions and the partial exchange of Na^+ by H^+ in Stern layer due to the higher adsorption effectiveness of H^+ than that of Na^+ (Hauser and Reed, 1937; Lagaly, 1989; Permien and Lagaly, 1994; Palomino and Santamarina, 2005) may reduce face-face (FF) repulsion. This produces 'card-house' structure in bentonite dispersions (van Olphen, 1977). However, the more addition of H^+ causes strong edge to face contacts promote aggregation of particles to clusters of finite size which move independently

under applied stress. In less acidic media, the card-house breaks down due to low positive charge density of edge, forming unstable edge-edge contracts. The net charge of the edges will be low and the Van der Walls forces can create an attractive potential (Lagaly, 1989).

On the other hand, the edges are negatively charged in the alkaline medium (pH>isoelectric point) by adsorption of OH^-. Because of absence of different charges, the total forces become repulsive, dispersing the particles in the diluted suspensions. In the concentrated suspensions, the diffuse double layers are lager than the half distance between particles which then arrange in a way that repulsion is reduced as much as possible, restricting rotational and transitional movement of particles. Due to the constrained particle motion, the particles are held at a distance with a parallel orientation. Stress is required to shift the particles out of the position. This produces 'band-like' or 'zig-zag' structure in bentonite dispersions (Norrish, 1954 and Fukushima, 1984). Once two particles closely approach each other, Ca^{2+} ions not only reduce the thickness of the diffuse layer but promote quasicrystalline structures with a central layer of the ions and attractive electrostatic potentials. In addition, partial overlapping of the platelets builds up voluminous networks (increases in yield stress and viscosity by increasing the attraction at edge (-) to edge (-) and edge (-) to face (-)) (Lagaly 1989). But, they will produce less network than face (-) to face (-) contacts due to small contact area (Callaghn and Osttewill, 1974). This also produces thicker particles formed by face (-) to face (-) association because the distance between Ca^{2+}-rich regions of two approaching lamellae cannot exceed 10Å (Shomer and Mingelgri, 1978 and Schramm and Kwak, 1982).

As stated, the concentration of salt significantly affects aggregation of bentonite particles, but the degree of effect depends on pH conditions. The addition of Na^+ ions increases attractive forces by contracting the thickness of double layer. In acidic media,

this increased attractive force either increases the stability of card-house structure (acidic medium) or cause the formation of particle aggregates (very acidic medium). Further addition of the Na^+ ions (high salt concentration) promotes the aggregates because the potential between lower charged faces of approaching particles or between regions of low charge density becomes attractive and promote face to face attractions. The enhanced face to face contacts decreases the stability of the structure. In addition, the electrostatic attraction at face/face defects which are created by Ca^{2+} ions increased. In alkaline solution, there still exist face to face contacts by Ca^{2+} ions. The addition of small amount of Na^+ ions enhance the attraction in the contact region, but further addition (high salt concentration) cause particle aggregation between two faces and Ca^{2+} ions, weakening the band-like structures. Furthermore, the face to face aggregation by Na^+ ions can occur when two regions of appropriate charge density approach. The network then consists of thicker particles which are separated by shearing more easily than thin platelets with extended regions of superposition.

2.7.4. Effect of ionic additives on bentonite suspensions

The effect of ionic additives on stability of bentonite suspensions varies with physical and chemical properties of bentonite particles such as particle size, shape, surface charge, cation exchange capacity, type of exchangeable cations, edge charge density (Brandenburg and Lagaly, 1988 and Goh et al., 2011). Previous researchers have widely studied the effects of the various ionic additives on the yield stress and viscosity of bentonite suspensions. Introducing ionic additives such as sodium hydroxide, sodium silicate, and poly-phosphate can reduce the viscosity and yield stress of bentonite suspensions resulting in increased mobility (Abend and Lagaly, 2000; Gonzales and Martin-Vivaldi, 1963; Jessen and Turan, 1961). Among the various

anions, polyphosphate has been known for a pronounced dispersing ability compared to other ionic additives such as sodium hydroxide and sodium silicate (Ford et al., 1940; Tchillingarian, 1953; Penner and Lagaly, 2001; Goh et al. 2011); the anion effectively reduces yield stress and viscosity of bentonite suspensions.

While most of ionic additives tend to decrease the yield stress and viscosity of the bentonite suspensions, the time dependent behavior of the treated suspensions varies with the type of the additive. Bentonite suspensions treated with sodium hydroxide produced substantially lower yield stress and viscosity compared to the untreated suspensions tested after 24 hours (Gonzales and Martin-Vivaldi, 1963). On the other hand, Tchillingarian (1952) observed complete flocculation in clay suspensions treated with sodium hexametaphosphate after 3 days, indicating that the reduction in yield stress and viscosity is tentative. The following sections will explain the mechanism of adsorption of phosphate anions on bentonite particles and effects of cations in alkaline suspensions since bentonite typically produces alkaline suspensions by releasing NaOH (Ford et al., 1940).

2.7.4.1. Adsorption mechanism of sodium pyrophosphate

It is well known that bentonite suspensions become dispersed and their yield stress and viscosity are reduced by the addition of polyphosphates. This phenomenon is attributed to the attachment of phosphate ions to the edges or their adsorption at the edges by exchanging structural OH^- groups, increasing repulsion between particles. The increased negative charge and repulsion between particles result in reduced yield stress and viscosity of bentonite suspensions (Ford et al., 1940 and Penner and Largaly, 2001). Although the adsorption of phosphate anions at the edge sites of bentonite particles in alkaline medium has been questioned due to the presence of the negatively charged edges

by the adsorption of OH^- (Kelessdis et al., 2007) and the relatively small area, the attachment of anions to the edges may be still possible due to the presence of a considerable portion of the exchangeable cations formed by the spilled double layer into the edges, providing a weak positive charge (Abend and Lagaly, 2000 and Tombácz and Szekeres, 2004). Moreover, Goh et al. (2011) reported that yield stress of 7% (wt/wt) bentonite suspensions increases with an increase of the squared value of zeta potential at a certain pH levels (pH>7). This attributed to the existence of positive-negative charge attraction between the bentonite particles. Furthermore, Kelessidis et al. (2007) observed a dominant edge to face association in 6.42% (wt/wt) suspensions (no electrolyte addition) at alkaline ranges of pH (pH = 9.1) by using scanning electron microscope.

2.7.4.2. Hydrolysis of sodium pyrophosphate

The sodium pyrophosphate hydrolyzed slowly in solution (Michaels, 1958; Ahmad and Kelso, 2001). According to Bailey and Webb (1944), sodium pyrophosphate hydrolyzed as the following:

$$Na_4P_2O_7 + H_2O \rightarrow 2Na_2HPO_4$$

or

$$HP_2O_7^{3-} + H_2O \rightarrow 2HPO_4^{2-} + H^+$$

However, the presence of clay significantly promotes this process. Michaels (1958) reported that the hydrolysis of sodium tetraphosphate reached a limiting value after 7 days, and sodium tripolyphosphate hydrolyzed even faster then tetraphsphate (6 hours) in kaolinite suspensions. In addition, this process is accelerated with decreased pH and increased ionic strength, cations (Na^+ and Ca^{2+}) and water-insoluble hydroxides of many metals (e.g Al-OH^-) (Michaels, 1958; Ryden and Syers, 1975; Gonzáles et al.,

1992). However, the process is self-limited and the influence Ca^{2+}/Na^{+} on hydrolysis occurs during the first 40 hours (Michaels, 1958 and Ryden and Syers, 1975). By this process, the cation exchange capacity increases due to partial replacement of Ca^{2+} and/or Mg^{2+} by Na^{+}, increasing cation concentration in suspensions (Michaels, 1958).

The adsorption of the anions on bentonite particles also can be affected by pH, the concentration of cations, and ionic strength (Gonzáles et al., 1992). In alkaline media, the negatively charged phosphate ions may be disrupted by the increased negative electrostatic potential. This causes lower degree of adsorption of phosphate ions than that in low pH conditions (Parfitt, 1978 and Ioannou and Dimirkou, 1997). However, the presence of cations in suspensions increases the adsorption of phosphate ions by reducing the thickness of diffuse double layer followed by increasing anion concentrations in the double layer. Especially, Ca^{2+} ions can form a linkage between particles and phosphate ions, increasing the adsorption of phosphate ions.

2.7.4.3. Association of bentonite particles with sodium pyrophosphate

Although the phosphate ions disperse bentonite suspensions, the particles may approach each other due to the presence of the exchangeable cations and Brownian motion of particles, leading to coagulation. Due to the competing effect of the coagulating cations and liquefying anions, initially anions induce the acidic hydrolysis of alumina (attach to edges) and then cations affect the diffuse double layer (Ford et al., 1940). Coagulation by the latter occurs at the critical concentration of electrolyte known as the critical coagulation concentration as the concentration of the additive increases. In diluted suspensions, the increased negative edge charge density in the presence of phosphate requires a higher salt concentration. This indicates that the bentonite-phosphate system may not be significantly affected by the external saline

water. The coagulation is initiated by edge (-) to face (-) contacts when the force between the edges (-) and faces (-) becomes attractive by the addition of salt (DLVO theory; Sposito and Grasso, 1999). However, the coagulation occurs when the salt concentration reaches the critical coagulation concentration for face (-) to face (-) coagulation due to the relatively small area of the edge (-) to face (-) contacts (Abend and Lagaly, 2000). As far as the repulsion from face (-) to face (-) exists, the coagulation of edge (-) to face (-) is disrupted. In concentrated suspensions, the strong repulsion between the faces aligns the particles into parallel orientation (Fukushima, 1984; Ramsay et al., 1990; Mourchid et al., 1995), forming edge(-) to edge(-) coagulation; the interaction between the negative edges becomes attractive (Penner and Lagaly, 2001). In addition, this process may also include a certain overlapping of the particles, forming band type structures. Due to the small area of edges, the process requires smaller phosphate concentrations than face (-) to face (-) coagulation in the dilute dispersions. As stated, the hydrolysis of SPP increases the concentration of cations such as Na^{+} and Ca^{2+} and the increased cations play an important role to coagulate particles in bentonite suspensions. Once two particles closely approach each other, the increased cations reduce the thickness of the diffuse layer, increasing the attraction at edge (-) to edge (-) and edge (-) to face (-) (Brandenburg and Lagaly, 1988). This causes a faster buildup of network compared to pure bentonite suspensions and strengthens the bonds between particles. This effect is more pronounced at the less concentrated suspensions.

In fact, the gelation in the concentrated bentonite suspensions are more complicated than the diluted suspensions since they probably have more complex interaction of particles and network formations. Therefore, there is a controversy on the type of aggregation. Although face (-) to face (-) association in alkaline bentonite suspensions caused by strong repulsion between particles has been widely adopted

(Norrish, 1954; Fukushima, 1984; Ramsay et al., 1990; Mourchid et al., 1995; Luckham and Rossi, 1999; Abend and Lagaly, 2000), more recent studies showed the possible presence of edge (-) to face (-) association formed by attraction between edge (-) and face (-) (Kelessdis et al., 2007 and Goh et al., 2011).

2.8. Groutability

2.8.1. Introduction

Although both bentonite and cement based grouts are similar in that they are both particulate suspensions, the application of the existing groutability to bentonite suspensions may cause inaccurate prediction of groutability in granular soils because they differ in their particle size and shape as well as their rheological properties such as yield stress and viscosity. This section describes the existing groutability for cement based grouts and limitations in the existing groutability. In addition, a background to link rheology to grout flow is presented through stop mechanism, grout flow through porous medium and post grouting stability.

2.8.2. Existing groutability criteria

The groutability of granular soils with cement based grouts has been studied based on the groutability parameter, N using grain size of soils and cements (Burwell, 1958; Bell, 1993; Incecik and Ceren, 1995). Since pressure filtration takes place due to the presence of large particles in grout during injection process, the size of voids in grouted soils and particle size in grout controls a success of grouting. Burwell (1958) suggested the following simple equation for the particulate grouting.

$$N = \frac{d_{15}(soil)}{d_{85}(grout)} \tag{2.22}$$

Where N is the groutability of soil, d_{15} is the diameter of soil passing 15% of total soil mass, d_{85} is the diameter of grout passing 85% of total grout mass. In accordance with the equation, a soil is groutable when N is greater than 25, and ungroutable if N is less than 11. However, Burwell found that another criterion should be satisfied even with the soil has N greater than 25.

$$N = \frac{d_{10}(soil)}{d_{95}(grout)} \tag{2.23}$$

Where N is the groutability of soil, d_{10} is the diameter of soil passing 10% of total soil mass, d_{95} is the diameter of grout passing 95% of total grout mass. He suggested that if N is greater than 11, a soil can be successfully grouted, but a soil can not be grouted if N is less than 5. Similar approach was proposed in Incecik and Ceren (1995), which used d_{90} of grout with d_{10} of sand. Based on their equation, a soil is groutable when N is greater than 11.

Other criteria were suggested by Karol (2003) based on the hydraulic conductivity of the base soils. Table 2.1 describes approximated relationship between hydraulic conductivity and groutability. Based on this relationship, the suspension grouts require base soils having the hydraulic conductivity of greater than 0.1 cm/sec. Since the groutability is strongly dependent on hydraulic conductivity and hydraulic conductivity is a function of grain size, grain size distribution becomes a useful indicator of groutability. Figure 2.12 shows a generalized relationship between groutability and the range of grain size. By comparing grain size distribution of a target soil with the chart, groutability of a soil is determined.

Table 2.1 Approximate relationship between hydraulic conductivity and groutability (Adapted from Karol, 2003)

Permeability (cm/sec)	Groutability (Ability of the soil to receive grout)
$\leq 10^{-6}$	Ungroutable
10^{-5} to 10^{-6}	Groutable with difficulty by grouts with viscosity < 5 mPa • s and ungroutable with grouts having a viscosity > 5 mPa • s
10^{-3} to 10^{-5}	Groutable with low viscosity grouts but difficult with grouts with a viscosity greater than 10 mPa • s
10^{-1} to 10^{-3}	Groutable with all commonly used chemical grouts
$\geq 10^{-1}$	Requires suspension grouts or chemical grouts containing a filler material

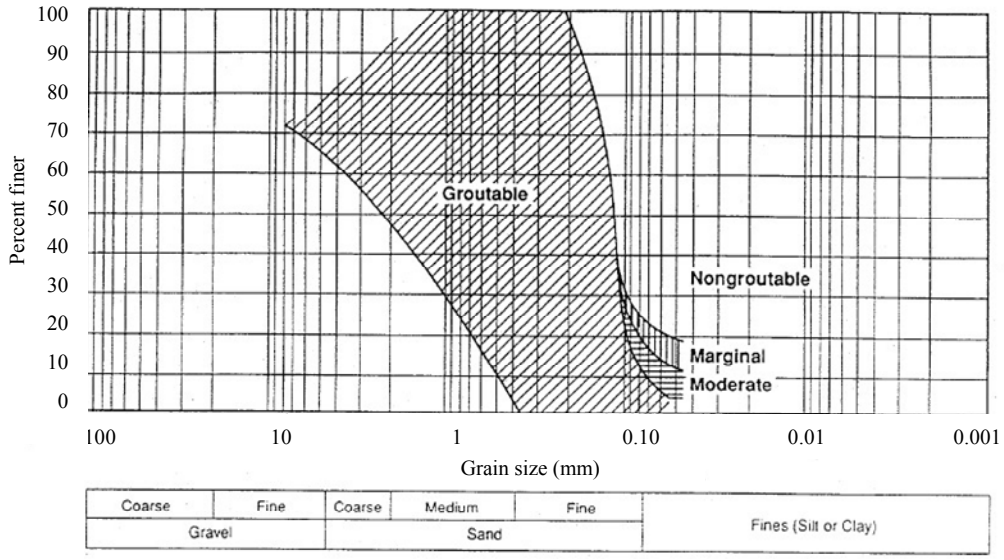

Figure 2.12 Range of grain size suitable for grouting (Adapted from Karol, 2003)

More advanced groutability criteria has been developed by Akabulut and Saglamer (2002) considering other parameters which were not included in the previous criteria. Akabulut and Saglamer (2002) showed that different parameters of soils and grouts (such as fine contents (FC), grouting pressure (P), relative density (Dr), and water cement ratios (W/C)) can affect the groutability of granular soils, especially in large scale tests. They performed extensive injection tests with Portland cement grouts at the range

of 0<FC<6%, 0.8<w/c<2:1, and 50<P<200kPa, and proposed the following equation as a new groutability criterion of granular soils.

$$N = \frac{d_{10}(soil)}{d_{90}(grout)} + k_1 \frac{w/c}{FC} + k_2 \frac{P}{Dr} \tag{2.24}$$

Where N is the groutability of soil, d_{10} is the diameter of soil passing 10% of total soil mass, d_{90} is the diameter of grout passing 90% of total grout mass, k_1 and k_2 are the empirical constants equal to 0.5 (unitless) and 0.01 (1/kPa), respectively, w/c is the water-cement ratio, FC is the fine contents, P is the injection pressure, and Dr is the relative density. They recommended that if N is greater than 28, a soil is groutable. The groutability of a soil should still be investigated in the lab when N is less than 28. However, the existing groutability criteria for cement grouts do not provide either the quantity or the penetration depth of the injected grouts leaving the meaning of a successful grouting ambiguous.

The parameters affecting the groutability of granular soils also affect the penetration distance. Santagata and Santagata (2003) showed that the penetration distance of micro-fine cement grouts varied with the water-cement (W/C) ratio of the grouts, the effective grain size (or hydraulic conductivity) of the sand, the injection pressures, and the amount of super-plasticizers. Moreover, they observed that grouts with the same w/c ratios but varying viscosity, due to the addition of super-plasticizers, resulted in different penetration distances. This study implies that the rheological parameters of the grouts should be incorporated in the groutability criteria of granular soils rather than the weight ratios. Furthermore, Perret et al. (2000) reported that penetrability of grouts is a function of the degree of saturation of granular soils; partially saturated sands showed faster grout propagation compared to that in fully saturated sands due to the suction created by negative pore water pressure.

2.8.3. Stoppage of grout flow

The different groutability of soils results from different stoppage mechanisms of grout flow. If the injection pressure is equilibrated with the resistance to grout flow, the grout cannot flow any more. In this case, yield stress, which represents a resistance to flow, contributes to the stoppage of grout flow.

However, the stoppage of grout through a soil is also affected by the physical configurations of the soil and grout referred to as clogging and filtration. According to Axelsson et al. (2009), clogging occurs when the grain size of particles in the grout is approximately one third (or greater than) the size of the pore where the particles are not able to enter the pores. Well dispersed (i.e. high W/C ratio) grouts have lower risk of stoppage due to this type of mechanism. On the other hand, filtration allows particles in the grout to settle in the pores of the sand, gradually blocking the flow path. At the close to limit of penetrability, there is filtration of grout particles and the voids filling efficiency increases. Herzig et al. (1970) reported that this phenomenon governed the stoppage of grout flow depending on the grain size of sand (typically grout particle size of 3 to 30 microns), resulting in different penetration distances. More details on the stoppage of suspensions flow through sand are presented in Chapter 7.

2.8.4. Grout flow through porous medium

As mentioned in section 2.8.3, the flow of particulate grout through a soil can be controlled by filtration, which is a phenomenon that particles are filtered from a liquid grout by soil grains, retarding grout flow. In the past, most of the theoretical and numerical works related to filtration phenomenon have been made for water treatment with diluted suspensions (referred to as deep bed filtration) (Herzig et al., 1970 and Ghidaglia, 1994). In order to model this phenomenon, four different approaches have

been used as summarized in Saada et al. (2005). Phenomenological model uses a macroscopic model based on mass balance equations. This model based on the resolution of mass balance equations by using phenomenological law of filtration and the pressure evolution (Herzig et al., 1970). Trajectory analysis models (Rege and Fogler, 1988 and Mackie, 1989) utilize a microscopic approach so that the porous medium is modeled as collector elements of different geometrical shapes and transport of individual particles under driving forces. Stochastic models (Tarafda et al., 1992) are based on the global probability approach of deep filtration, describing the progressive clogging of the porous medium. The filtration is considered as birth and death, which are represented blocking of the initially open pores and opening of the initially blocked pores. Network models (Bouchelaghem and Vulliet, 2001; Saada et al., 2005; Kim and Whittle, 2009) generally consist in modeling the porous space of the matrix by a network of cylindrical canals with random sizes. Then the flow rate in each pore throat is calculated by solving the mass balance equation at each node of the network. The probability of a particle to be transported in a canal is proportional to the flow rate and the particles have a probability of capture which is a function of the canal radius.

However, all of the models were based on constant flow rate conditions and practical application is challenging since they do not provide any information of groutability so that it is required to perform further experimental and theoretical studies. Instead of these approaches, Kim et al. (2009) proposed a 3-D step-wise solution for compaction grouting under constant pressure condition. The model correlates a lump parameter which controls particle entrapments in grout flow through porous medium to groutability of soil with microfine cement grout. Darcy's law and Kozey-Carman equation are introduced to consider the change in porosity along with 3-D filtration law derived from the governing equation. The major advantage of this model is that

groutability can be estimated based on one model parameter along with capturing the volumetric flow behavior of grouts under filtration condition. Details for this model will be presented in Chapter 7.

2.8.5. Post grouting stability

After being permeated, the grout should be stable in-place under gravity settling and hydraulic gradient. A simple approach to evaluate grout stability under an external pressure was proposed by Cambefort (1964). He assumed that the minimum pressure gradient to mobilize the grout placed in a soil is proportional to yield stress of grout. The pressure gradient is calculated by the following relationship

$$\frac{P}{L} = \tau_O \cdot S \cdot (1 - n) \tag{2.25}$$

Where, τ_o is the yield stress of grout (Pa), P is the pressure (Pa), L is the length of grouted zone (m), S is the specific surface area of soil (1/m), and n is the porosity of soil. Moreover, Axelsson et al. (2008) performed erosion tests with a Bingham fluid (Myanit) at different water pressures through rock fracture replica (380-410 μm). The general conclusion drawn was that the fluids having higher ratio between yield stress of fluid and hydraulic stress remained in the pipe, but the fluids with low ratio was totally washed out. Similar tests were performed with un-gelling and gelling silica sol. While the un-gelling silica sol and the gelling silica sol rested half of the gelling time were washed out, the gelling silica soil rested three quarter of the gelling time remained in the pipe. The observations imply that the post grouting stability is closely related to the yield stress of grout.

2.9. Hydraulic performance of grouted sand

2.9.1. Introduction

One of the objectives in permeation grouting is to improve hydraulic performance of the permeable granular soils so that low enough hydraulic conductivity after permeation should be secured. Figure 2.13 shows residual hydraulic conductivity after treatment along with an approximated relationship between hydraulic conductivity of soils and penetrability of various grouts reported by Karol (2003). This approach may provide first hand information to determine applicability of a certain type of grout with conservatism. Based on this chart, the hydraulic conductivity of soils having the hydraulic conductivity of 0.1 to 1 cm/sec decreases by two orders of magnitude using chemically treated bentonite grout.

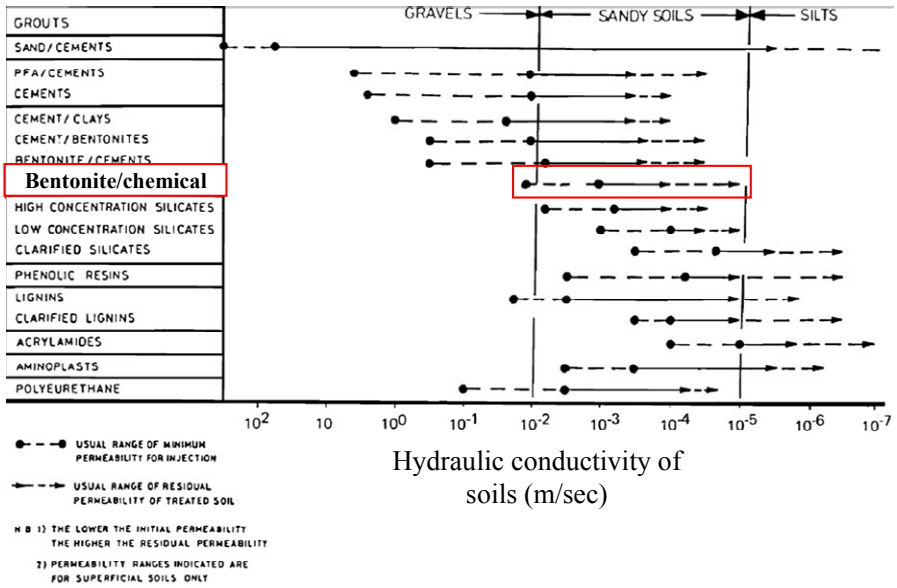

Figure 2.13 Indicative range of grout treatment (Adapted from Karol, 2003)

2.9.2. Hydraulic conductivity of SBMs

Although the hydraulic conductivity of bentonite grouted sands has not been studied extensively, previous researches on Sand-Bentonite Mixtures (SBMs) showed the effectiveness of bentonite in reducing the hydraulic conductivity of clean sand. Chapuis (2002) showed that the hydraulic conductivity of sand (10^{-2} cm/sec) was reduced to 10^{-6} cm/s when mixed with 5% dry bentonite (by mass of sand). Abichou et al. (2000) conducted hydraulic conductivity test with compacted SBMs, a mixture of foundry sand and bentonite (bentonite content of 5 to 16%), and reported that the hydraulic conductivity of compacted sand bentonite mixture was up to 6 orders of magnitude less than that of clean sand as shown in Figure 2.14. Hwang (2010) reported that the hydraulic conductivity of SBMs was reduced up to 10^{-9} cm/sec with 8% bentonite contents. Castelbaum and Shakelford (2009) used bentonite suspension for the treatment of chlorine contaminated zone and reported that the hydraulic conductivity ranged from 10^{-7} to 10^{-4} cm/s.

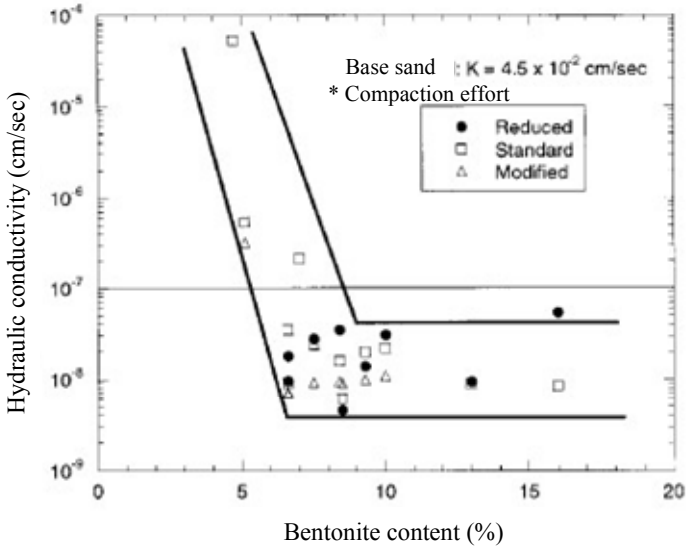

Figure 2.14 Range of hydraulic conductivity of SBMs (Adapted from Abichou et al., 2000)

2.9.3. Laboratory factors affecting hydraulic conductivity measurement

The measurement of hydraulic conductivity in SBMs is influenced by not only the properties of materials such as bentonite content and distribution, but also experimental conditions such as degree of saturation and hydraulic gradient. Therefore, this section covers the issues on the measurement of hydraulic conductivity. It is well known that a low degree of saturation reduces hydraulic conductivity due to the blockage of flow path by occluded air bubbles. Although hydraulic conductivity is measured until the amount of inflow and outflow reaches a steady state, this does not ensure fully saturated condition (Chapuis, 1990b). It is difficult to obtain 100% saturation since specimens prepared in laboratory possibly exposed to air even with deaired water since testing equipments are usually watertight but not airtight (Hwang, 2010). The most common approach is to circulate carbon dioxide gas through the specimen before flushing with water. This method increases the degree of saturation since carbon dioxide (CO_2) gas is much more soluble in water than air. When a flexible wall permeameter is used, a backpressure can be applied to increase the degree of saturation of specimens. In a rigid wall permeameter, vacuum can be applied with the dry state specimens during flushing water upward. According to Chapuis (1990b and 2004a), all the three methods are reliable to achieve the degree of saturation close to unity. However, there are not many options for a rigid wall test with a permeant such as grout which initially include air, resulting in the use of backpressure.

Since the water flow through the SBMs is assumed to follow Darcy's law, the hydraulic gradient is linearly proportional to the flow rate when the water flow is laminar. However, the application of an excessive gradient may cause non-Darcian flow resulting in particle migration especially when the teested soil includes some fines (Olson and Daniel, 1981; Beven and Germann, 1982). The excessive hydraulic gradients induces

washing of fines, significantly increasing hydraulic conductivity (Marcotte et al., 1994 and Kaoser et al., 2006). The hydraulic gradients ranging from 10 to 50 have been used for SBMs in laboratory (Haug and Wong, 1991; Kenny et al., 1992; Mollins et al., 1996) and ASTM D5084 recommends using an appropriate range of hydraulic gradients depending on the estimated hydraulic conductivity of specimens as presented in Table 2.2.

Table 2.2 Recommended hydraulic gradient (from ASTM D 5084)

Hydraulic conductivity(m/s)	Hydraulic gradient in Rigid wall permeameter
10^{-5} to 10^{-6}	2
10^{-6} to 10^{-7}	5
10^{-7} to 10^{-8}	10
10^{-8} to 10^{-9}	20
$< 10^{-9}$	30

The bentonite content, which expressed as a ratio between bentonite and sand by dry mass, is one of the important parameters affecting hydraulic conductivity of sand bentonite mixtures because it determines the portion of pores plugged with bentonite (Kenney et al., 1992). However, water flows through clay voids even after the bentonite blocks all the sand pores, causing a low hydraulic conductivity. With a low bentonite content, washing of bentonite or internal erosion has been observed during permeability tests on SBMs, causing an irreversible change in hydraulic conductivity (Hoeks et al., 1987; Chapuis, 1990b and 2002; Fernuik and Haug, 1990; Marcotte et al., 1994; Kaoser et al., 2006). However, an excessive addition of bentonite beyond the amount needed to fill the sand voids will produce a smaller and more tortuous flow path, but the effects on the hydraulic conductivity of SBMs is minimal (Chapuis, 2002).

The distribution of bentonite content may affect hydraulic conductivity of the mixtures. The homogeneity of specimen increases with bentonite content (Borgesson et al., 2003). As a result, a linear relationship between logarithm of hydraulic conductivity and logarithm of clay void ratio (see details in section 2.9.4) is produced (Terzaghi and Peck, 1967; Olson and Daniel, 1981; Yang and Barbour, 1992; Pandian et al., 1995; Mollins et al., 1996; Sivapullaiah et al., 2000) as shown in Figure 2.15. However, this is not the case in heterogeneous specimens, especially at very low bentonite content (Mollins et al. 1996 and Castelbaum and Shackelford 2009). Hwang (2010) reported that this linear trend of the hydraulic conductivity is true up to certain bentonite content, which is enough to fill all the pore spaces of the sand used. For lower bentonite contents, the bentonite does not fill all the pore space, and the hydraulic conductivity is governed by the flow through the unfilled pore space.

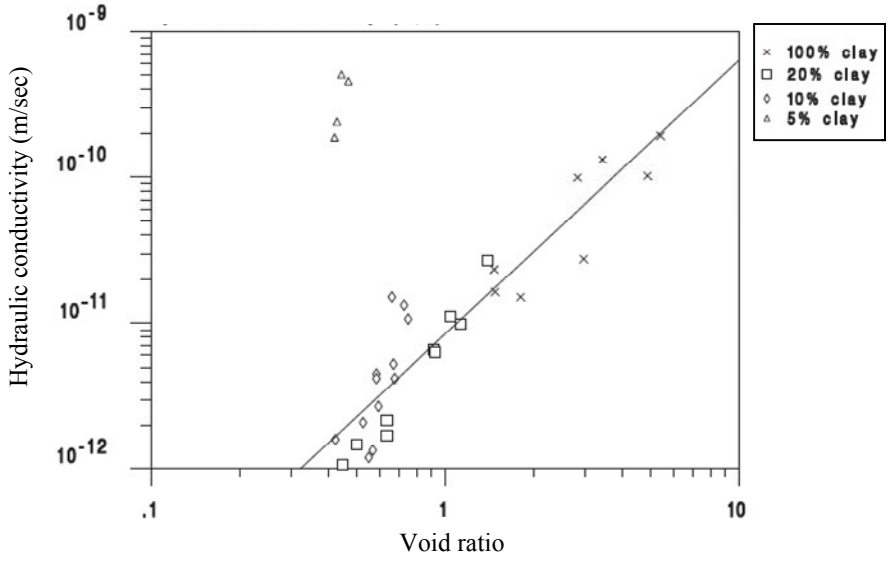

Figure 2.15 Hydraulic conductivity of SBMs based on clay void ratio (Adapted from Mollins et al. 1996)

2.9.4. Characterization of void ratio

An appropriate estimation of void ratio has been an issue on the study of liquefaction phenomenon of sands with fines (Kuerbis and Vaid, 1988; Mitchell, 1993; Salgado et al., 2000). Since hydraulic conductivity of a sand-fine mixture is also strongly dependent on void ratio of the mixture, it is required to evaluate an appropriate void ratio for sample preparation and analysis. In addition, a consistent definition of void ratio should be utilized when the mixture is prepared for permeation tests.

Conventionally, the void ratio is defined as the ratio of volume of voids (air and water) to volume of solids, usually referred as to global or bulk void ratio. When a mixture includes a portion of fines in the sand, the volume of fines is considered as a portion of the total volume of solids in the mixture. However, the fines should be included in a portion of the volume of voids because permeation grouting utilizes a suspension form, which occupies a pore volume. This allows us to use the concept of skeletal void ratio which is calculated based on the assumption that the volume occupied by the fines is a part of volume of pore. The skeletal void ratio is defined as follows (Mitchell, 1993 and Kuerbis and Vaid, 1988):

$$e_G = G_S \frac{\frac{\mathrm{W}}{100} + \frac{FC_C}{100G_{sC}}}{1 - \frac{FC_C}{100}} \tag{2.26}$$

Where W is the water content (%), FC_c is the percentage of clay to total solids by dry weight (%), Gs_C and Gs_G are the specific gravities of the clay and granular particles respectively. When the specific gravity of sand and fines are equal, the equation (2.26) is reduced to

$$e_G = \frac{\mathrm{e} + \frac{FC}{100}}{1 - \frac{FC}{100}} \tag{2.27}$$

Where e is the global (bulk) void ratio, FC is the dry weight of the fines to the dry weight of solids (%). Since water flows through clay voids rather than skeletal voids if the skeletal pores are fully blocked with a large portion of bentonite (Kenny et al., 1992 and Castelbaum and Shakelford, 2009), the concept of clay void ratio is introduced. The clay void ratio is defined as the volume of voids attributed to the bentonite divided by the volume of solid bentonite in mixture (Kenny et al., 1992). The clay void ratio (e_b) is expressed as follows:

$$e_b = G_{sb}\left[\left(1 + \frac{1}{r}\right)\frac{\rho_w}{\rho_{dm}} - \frac{1}{rG_{ss}}\right] - 1 \tag{2.28}$$

Where G_{sb} is the specific gravity of bentonite, G_{ss} is the specific gravity of sand, r is the ratio of dry sand and bentonite, ρ_w is the density of water, and ρ_{dm} is the dry density of the mixture.

2.10. Shear strength of bentonite grouted sand

The major assumption of permeation grouting using bentonite grout is that the permeation of the bentonite grout should have a little effect on the shearing strength of the original soil matrix. Rugg et al. (2011) performed a series of consolidated-undrained tests with the modified bentonite suspensions (10% bentonite suspensions with 2% SPP) and showed that the friction angle of the permeated sand, at both critical state (CS) and undrained instability state (UIS), did not change significantly compared to that of clean

sand (Figure 2.16). Based on this observation, the change in shearing strength due to permeation was reasonably assumed to be minimal through this study.

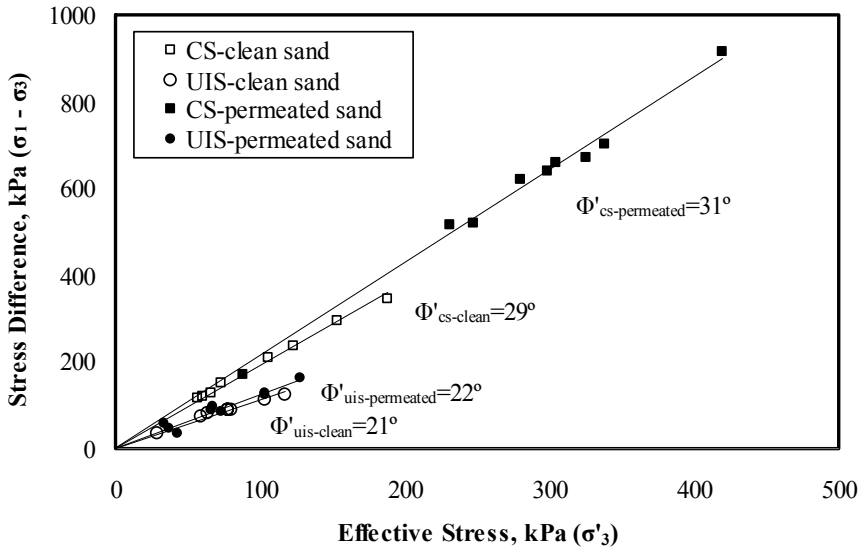

Figure 2.16 Modified Mohr-Coulomb plot for sand and permeated specimens (Adapted from Rugg et al., 2011)

2.11. Conclusions

The literature reviews provide that underseepage accompanies an excessive ground deformation through heaving or formation of large holes by sand boiling (piping), leading to levee failures, which have caused significant loss of lives and properties in US for several decades. Most of countermeasures showed relative advantages and disadvantages in terms of their performance and cost-effectiveness. Among them, permeation grouting (grout curtain) could be one of the methods to mitigate underseepage problems, especially for the levees located near urban area. In addition, the high hydraulic conductivity (10^{-1} to 10^{-2} cm/sec) in the failed levee foundations suggested that permeation grouting will be possibly applied as a countermeasure of seepage problems.

Since the conventional cement-based grouts may cause long term ground contamination, bentonite can be an alternative due to its environmental friendliness.

In permeation grouting, the property of grout (rheology) is of vital importance since it affects the penetration and post grouting stability. The rheological properties of bentonite suspensions are affected by pH, amount of cations and type of ionic additives; bentonite suspensions treated with sodium pyrophosphate appeared to have the most appropriate rheological properties for grouting applications due to the low initial viscosity, yield stress and their gradual buildup with time. The studies on the interaction of bentonite particles in aqueous medium revealed that the sodium pyrophosphate ions attach to the edge of the bentonite particles (even at the alkaline condition), increasing the electro-negativity of the particles. As a result, the suspensions are dispersed, reducing yield stress and viscosity. As time elapses, the dispersed particles become close to each other under Brownian motion of particles, forming network structures which causes the increase in the rheological properties.

The variation of the rheological properties of bentonite suspensions due to the addition of ionic additives will change its penetration through porous media. However, the previous researches did not account for this phenomenon by estimating groutability only based on the physical size of grout particles and sand grains. Once the bentonite suspensions are permeated into sand, its hydraulic conductivity significantly decreased without causing any significant change in shearing property of the soil deposit. This indicates that bentonite treatment of sand deposit can be effective to control seepage problem.

CHAPTER 3: EXPERIMENTAL PROGRAM

3.1. Introduction

This chapter is divided into two parts: material properties and experimental program. Index tests such as Atterberg limits, grain size distribution, specific gravity, and maximum and minimum void ratio have been conducted using ASTM standards. Some of the conventional standards have been slightly modified to suit the type of bentonite clay used in this study based on thorough studies published in the literature. In addition, X-ray diffraction, methylene blue (MB) adsorption and Energy dispersive X-ray spectroscopy (EDX) tests were conducted to characterize the physicochemical properties of the bentonite along with measuring pH, electrical conductivity and hardness of water. Experimental setups for rheological tests, constant pressure and constant flow rate permeation tests and hydraulic conductivity tests are presented. Moreover, the details of specimen preparation, testing procedures, acquiring data, modifications to meet a specific need for this study are listed. The test to determine bentonite contents is also described.

3.2. Material properties

3.2.1. Sand

In order to study the penetration of bentonite suspensions through highly permeable sand deposits with different grain size and the effect of bentonite for hydraulic performance of sand, well characterized and clean sands were used. Four different sands are utilized: Ottawa (ASTM graded C778), Monterey #0/30, Aggregate and Nevada sand. Grain size distribution was determined by sieve analysis based on ASTM D422-

63. Specific gravity and maximum and minimum void ratio were determined in accordance with ASTM D854-02, ASTM D4253 and D4254, respectively. Figure 3.1 depicts grain size distribution curves for the tested sands. All sands were classified as a SP based on a USCS classification with little to no fines. Table 3.1 summarizes properties of tested sands.

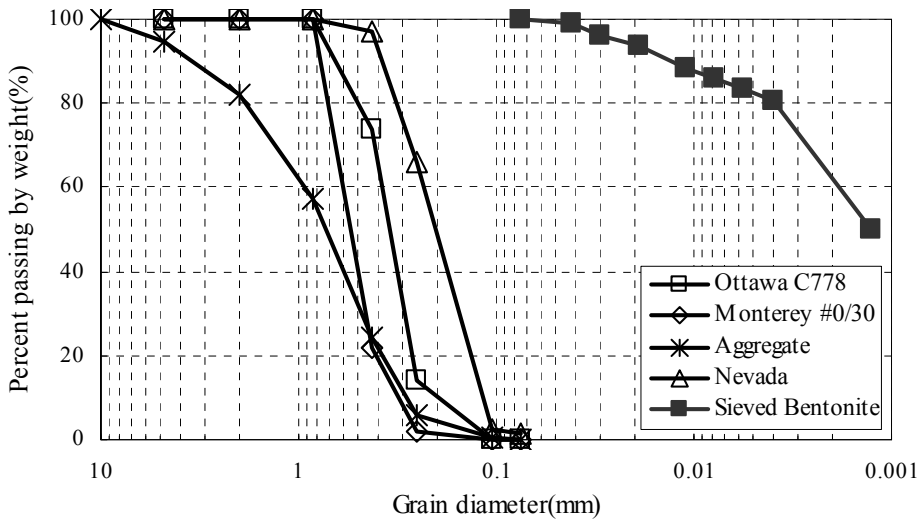

Figure 3.1 Grain size distribution curves for the tested sands

Table 3.1 Index properties of the tested sands

Sand	Gs	e_{max}	e_{min}	D_{10} (mm)	D_{30} (mm)	D_{60} (mm)	Cu	Cc	USCS
Ottawa (C778)	2.65	0.76	0.50	0.20	0.32	0.40	1.94	1.28	SP
Monterey #0/30	2.64	0.85	0.57	0.31	0.46	0.59	1.92	1.13	SP
Aggregate	2.68	0.64	0.43	0.28	0.48	0.94	3.36	0.88	SP
Nevada	2.67*	0.89*	0.51*	0.12	0.16	0.23	1.97	0.89	SP

* Gajan et al. (2006)

3.2.2. Non plastic Silt

The silty sands were formed with a fraction of non plastic silt to investigate the effect of fine contents on the penetration of bentonite suspensions. The soil has been used by Hazirbaba (2005) to study the effect of non plastic fines on cyclic behavior of sand. According to his study, the soil has a maximum grain size of 0.074 mm and a minimum grain size of less than 0.002 mm. The median grain size, D_{50}, is 0.0135 mm. The silt is white in color and has a specific gravity of 2.65. To confirm the plasticity of the soil, Atterberg limit tests were performed in accordance with ASTM D4318. Figure 3.2 shows the plasticity chart of the tested soil, classifying the soil as non plastic silt (ML).

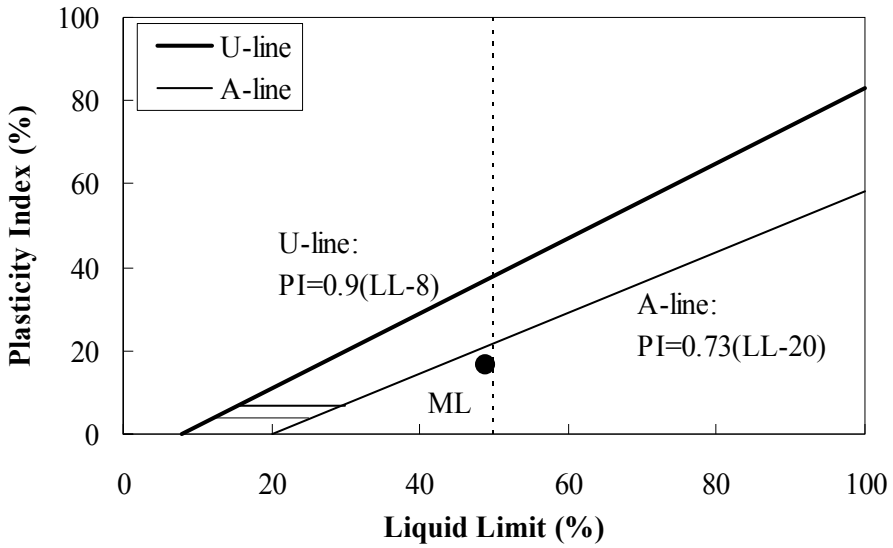

Figure 3.2 Atterberg limit of low plastic silt

3.2.3. Bentonite

3.2.3.1. Origin of bentonite

High swelling Wyoming bentonite powder (Volclay CP-200) obtained from CETCO has been used in this study. This bentonite meets API specification 13A for

drilling fluid materials and is being commercially used for the construction of soil/bentonite liner and slurry trenching. It provides a maximum filtrate loss of 18 ml and a barrel yield of 90 minutes based on API 13A. It swells freely up to 16 ml/2 g, when it is fully hydrated (ACC 1010).

3.2.3.2. X-ray diffraction

X-ray diffraction (XRD) is a common method used in mineralogy, especially for fine-grained material study. XRD provides the information of the proportion of the different materials present in the sample and the identification of crystalline structure of the minerals. Since the small particle size of soil prevents the investigation of one single crystal, the XRD technique requires placing a powdered sample of the material (power method) in holder. By placing a very large number of particles, it is insured that some number of the particles will be properly oriented to produce a reflection. As shown in Figure 3.3, X-rays of a fixed wave length (typically 1.54 Å from Copper radiation) strikes the sample and the intensity of the reflected radiation is then recorded. Based on the data for the diffraction angle (2θ), the inter-atomic spacing is calculated by applying Bragg's law and the composition of minerals in the specimen is determined.

$$n\lambda = 2d \sin \theta \tag{3.1}$$

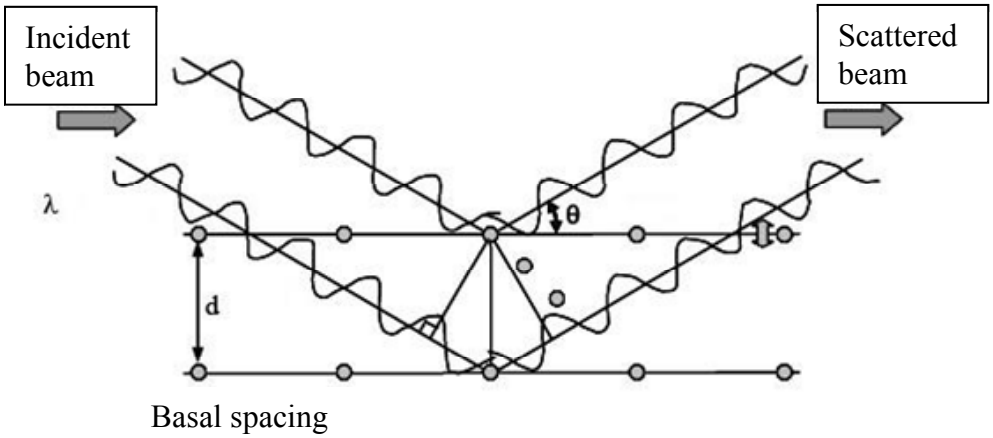

Figure 3.3 Concept of X-ray diffraction (Adapted from Muhammad, 2004)

Where, n is the order of the diffracted beam, λ is the wave length of the incident X-ray beam, d is the distance between adjacent planes of atoms (the d-spacing), and θ is the angle of incidence of the X-ray beam. With the known λ and measuring θ, the d-spacing is calculated and compared with standard references to identify the minerals (each mineral has a characteristic set of reflections at values of θ corresponding to the spacing between the different planes). XRD tests were performed at the Texas Material Institute (TMI) at the University of Texas at Austin using Scintag X1 theta-theta diffractometer. All tests were performed at room temperature using a Cu K-alpha x-ray source (λ≈ 1.5405 Å) and a solid state detector. Three types of tests were performed on 1) sieved bentonite; 2) air-dried flakes formed by sedimentation method and 3) saturated flakes with glycol to investigate the swelling of bentonite particles. Figure 3.4 shows the X-ray pattern of the sieved bentonite with the deflection angles (2θ). Based on the pattern, quartz, feldspar, mica and montmorillonite which are common minerals in bentonite were identified. A spurious peak was also observed due to large particle size. Figure 3.5 shows the X-ray pattern of the bentonite flakes with the deflection angles (2θ). The peak intensity appeared at approximately 2θ of 7.4 °, producing the first order reflection

($d_{(001)}$) of 11.9 Å. This is the typical basal spacing of montmorillonite when air-dried. When oven-dried, $d_{(001)}$ drops to about 10 Å due to the absence of interlayer water (Mitchell, 1993). However, small peaks were also observed at 24.5 and 50 °, identifying as mica. This was attributed to the insufficient removal of all impurities when preparing the flakes.

Figure 3.6 depicts the X-ray pattern of the glycol saturated bentonite flake with the deflection angles (2θ). The peak intensity was appeared at approximately 2θ of 4.9 °, resulting in the first order reflection ($d_{(001)}$) of 18 Å.

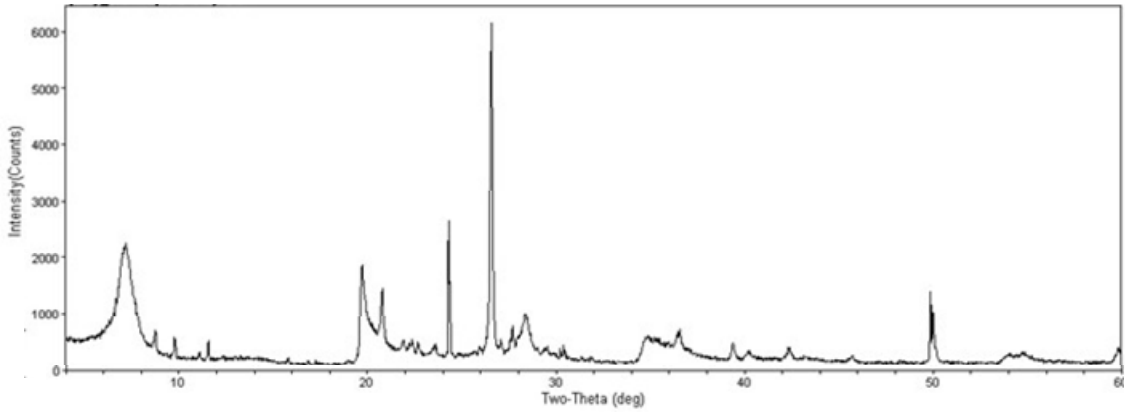

Figure 3.4 X-ray patterns for the sieved bentonite

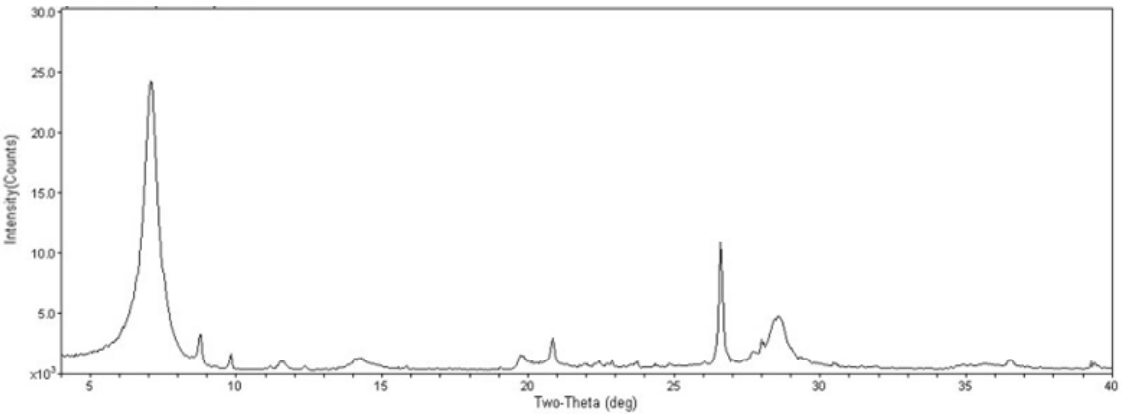

Figure 3.5 X-ray patterns for the bentonite flakes

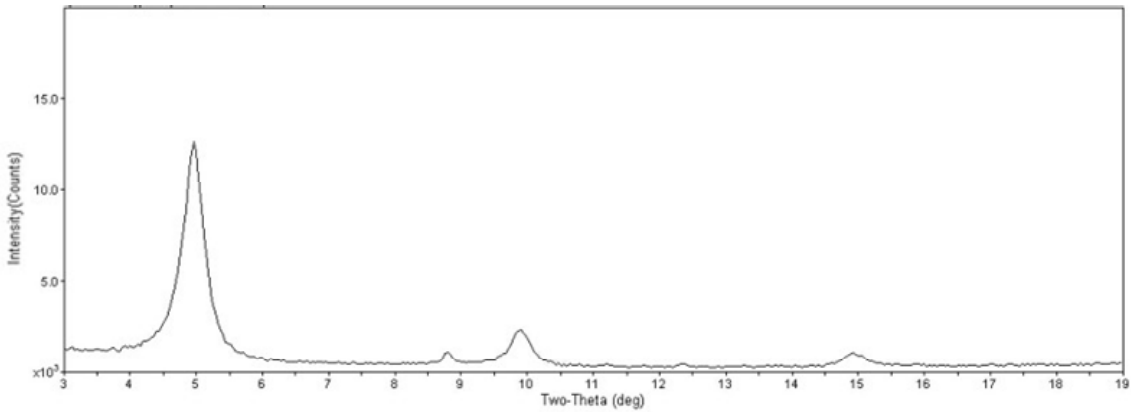

Figure 3.6 X-ray patterns for the bentonite flakes saturated with glycol

3.2.3.3. Atterberg limit

Atterberg limits of soils also identify the mineral contents of the soil materials using plasticity chart developed by Casagrande (1948) shown in Figure 3.7. If the sample has Atterberg limits high above the A line, near the U line, it may contain a lot of active clay minerals such as montmorillonite. Such clays would have very high liquid limits compared to other clay minerals because it adsorbs a tremendous amount of water on large surface areas. While the liquid limit of bentonite varies with the thickness of diffuse double layer, which is affected by dielectric constant, electrolyte concentration, valence of the electrolyte and temperature in pore fluid, it is also affected by the type of exchangeable interlayer cations present in bentonite. With the bentonite carrying the monovalent cations such as Na^+ or Li^+, the liquid limit increases significantly compared to that including polyvalent cations such as Ca^{2+}. (Luckham and Rossi, 1999). This behavior is attributed to the repulsive force between platelets is compensated by the attractive force exerted by polyvalent cations, causing less expansion of an interlayer separation. Therefore, a much smaller amount of water molecules can be adsorbed in the interlayer space when a large amount of polyvalent cations exists in the interlayer. In this study, Atterberg limit tests were performed in accordance with ASTM D4318.

Figure 3.8 shows Atterberg limits of the sieved bentonite tested in this study. The liquid limit of the sieved bentonite was found to be about 440% with plastic limit of 40% which plotted slightly above U-line. This deviation of PI was also reported in other studies (Malusis and Shackelford, 2002 and Muhammad, 2004) and attributed to the fact that the theoretical U-line might be drawn arbitrarily, especially at high PI region. The typical ranges of liquid limits from 100 to 950% and the plastic limits from 50 to 100% have been reported in literatures (Mitchell, 1993 and Santamarina et al., 2002).

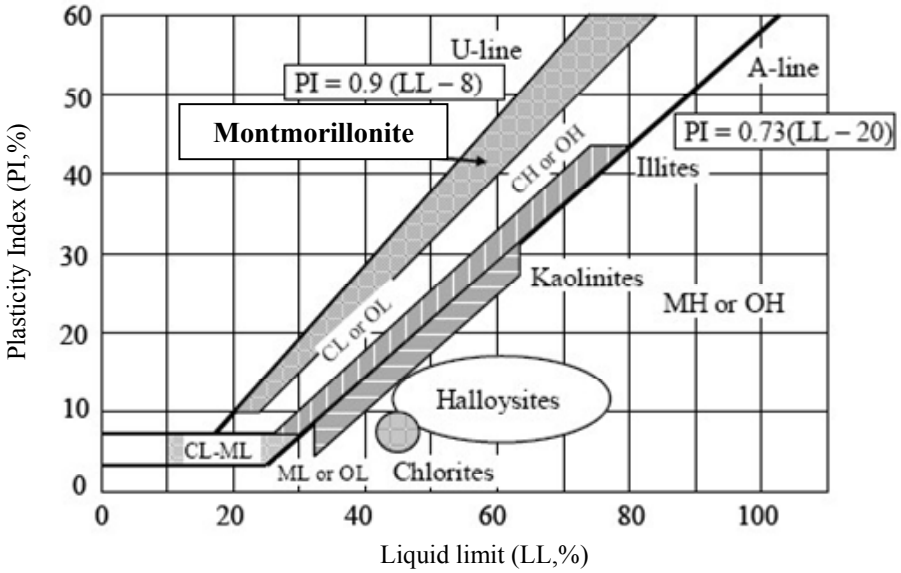

Figure 3.7 Plasticity chart (Adapted from Muhammad, 2004; after Holtz and Kovacs, 1981)

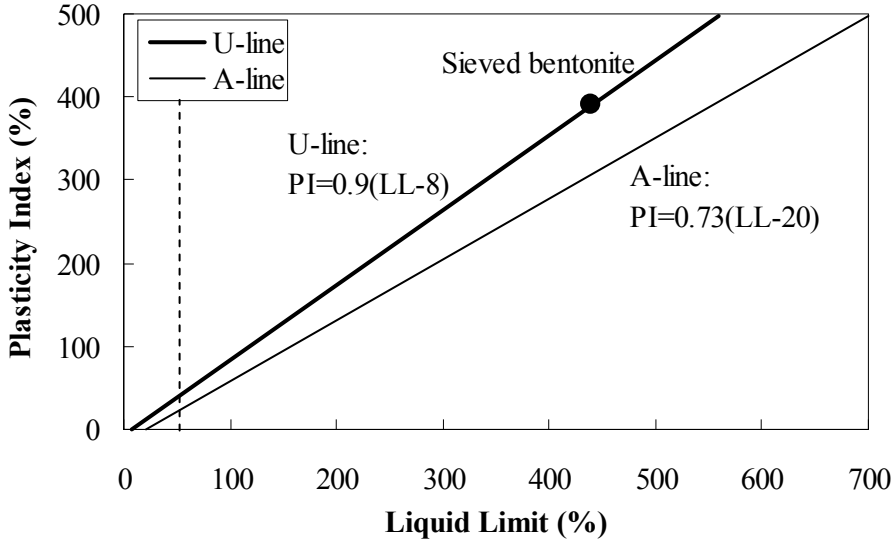

Figure 3.8 Plasticity chart of the sieved bentonite

3.2.3.4. Particle size

The bentonite particles have a platy shape and a long axis of particle usually less than 1 or 2 μm. The range of particle thickness is from 10 Å unit layers upward to about 1/100 of the width (Mitchell, 1993 and Luckham and Rossi, 1999). However, the raw bentonite initially included impurities such as plagioclase feldspar, orthoclase, and muscovite minerals and large particles (>75 μm) so that it was screened through a No.200 sieve to minimize the impurities and their effects on the results (Abend and Lagaly, 2000 and Clarke, 2008). No further purification and gradation was applied for mass production of material and field application. The particle size is important in permeation grouting since the penetrability of grout is mainly controlled by particle size of sand and grout. In order to characterize particle size of the sieved bentonite, hydrometer tests were performed in accordance with ASTM D422. Because of high tendency of flocculation between bentonite particles due to their high surface charges, the tests were conducted with a dispersing agent (sodium hexametaphosphate, 10% by dry

weight of bentonite) in deionized water. In addition, the suspensions were premixed with using high shear mixer before testing to ensure complete deflocculation of particles. Figure 3.9 shows grain size distribution curve for the sieved bentonite. This process produced approximately 95% of particles less than 25 μm, 60% of particles less than 2 μm and 50% of particles less than 1 μm.

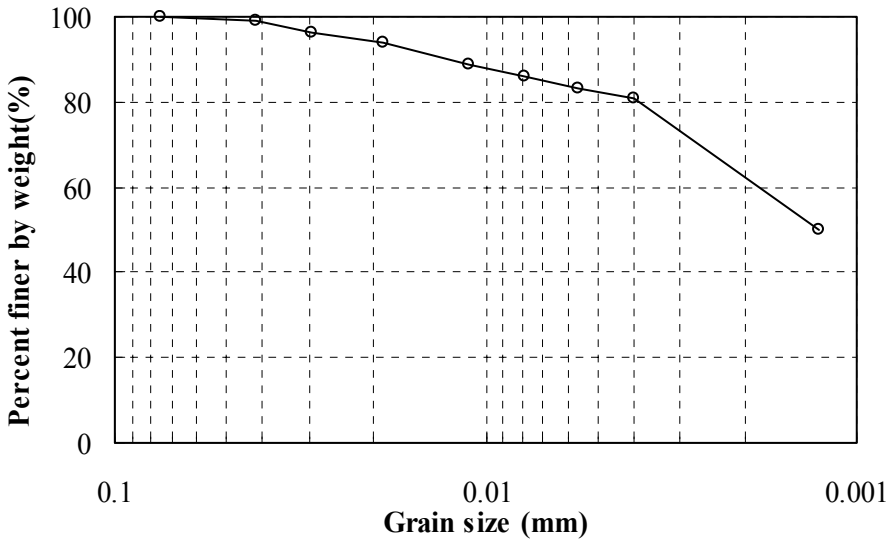

Figure 3.9 Grain size distribution curves for the sieved bentonite

3.2.3.5. Activity

Activity is a property considering the effect of an amount of clay size fraction in soils and defined as

$$A = \frac{PI}{\text{clay fraction}} \tag{3.1}$$

Where A is the activity of minerals, PI is the plasticity index and clay fraction is a percentage by weight of particle less than 2 μm. The higher activity means that the clay properties are more influenced by the physicochemical factors such as exchangeable cations and pore-fluid compositions. In addition, this property is well correlated to the

types of clay mineral (Holtz and Kovacs, 1981). Table 3.2 presents activities of various minerals. In this study, the activity of the sieved bentonite was found to be 4.8.

Table 3.2 Activities of various minerals (After Holtz and Kovacs, 1981)

Mineral	Activity
Na-Montmorillonite	4-7
Ca-Montmorillonite	1.5
Illite	0.5-1.3
Kaolinite	0.3-1.5
Halloysite(dehydrated)	0.5
Halloysite(hydrated)	0.1
Attapulgite	0.5-1.2
Allophane	0.5-1.2
Mica(muscovite)	0.2
Calcite	0.2
Quartz	0

3.2.3.6. Specific gravity (Gs)

Specific Gravity (Gs) of the sieved bentonite was measured in accordance with ASTM D- 854-02 (2002) using a 250 ml volumetric flask. The sieved bentonite was air-dried and soaked in de-ionized water for at least 24 hours under vacuum to expel air bubbles entrapped in the fine pores from the water-clay solution. The specific gravity may vary with impurities included in the bentonite. Previous researches have reported the specific gravity values within a range of 2.35 to 2.88 (Mitchell, 1993, Studds et al., 1998; Komine and Ogata, 2003; Kaoser et al., 2006). In this study, three tests were performed with the sieved bentonite in accordance with ASTM D854 as shown in Figure 3.10. The average specific gravity of the sieved bentonite was found to be 2.64 (±0.03).

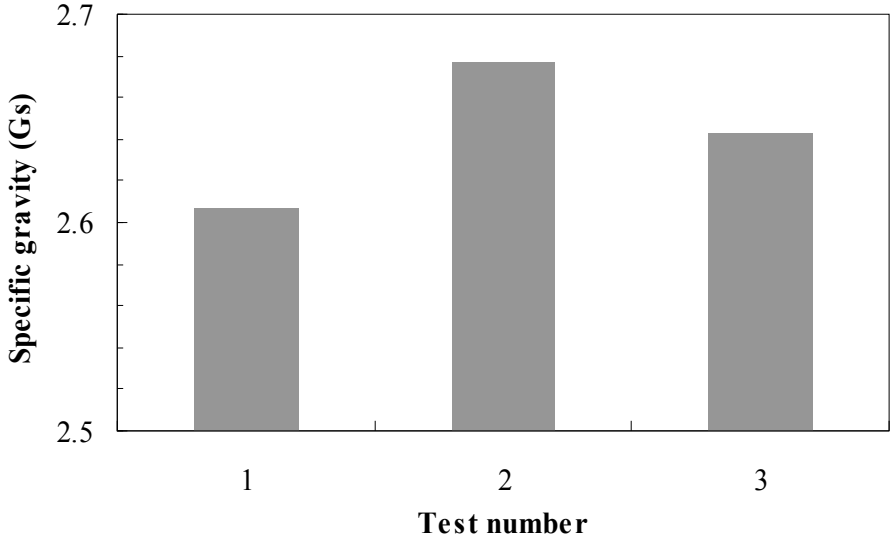

Figure 3.10 Specific gravity of the sieved bentonite

3.2.3.7. Cation exchange capacity (CEC)

Cation exchange capacity and specific surface area are important properties to study chemical adsorption of SPP onto bentonite particles. In this study, methylene blue (MB) adsorption tests were performed in accordance with ASTM-C837, API 13B-2009 and Santamarina et al. (2002). Methylene blue, which is the dissociated cationic dye ($C_{16}H_{18}ClN_3S^+$) in aqueous solution, replaces base cations (Na^+, K^+, Ca^{++} and Mg^{++}) of clay minerals in an irreversible manner and covers the particle surfaces so that both cation exchange capacity and specific surface area can be estimated based on the amount of adsorbed methylene blue dye. The chemical formula and molecular weight of methylene blue was $C_{16}H_{18}ClN_3S.3H_2O$ and 373.90, respectively. The chemical structure of methylene blue is shown in Figure 3.11.

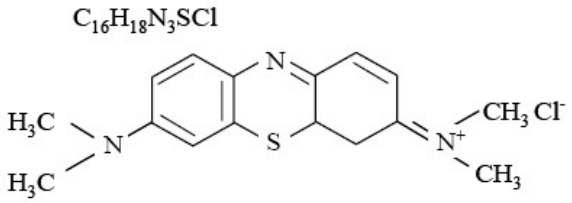

Figure 3.11 Chemical structure of Methylene blue

The step by step procedures are as follows: 1) the methylene blue solutions are prepared by mixing 3.2 g of dry powder to 1000 ml of de-ionized water, producing the methylene blue concentration of 0.01N, 2) the methylene blue solution was added at an increment of 5 ml into 0.5% bentonite suspensions (2 g of dry bentonite with 400 ml), which was stored overnight, 3) for each addition of methylene blue solution, the suspensions were mixed for 1 min with a glass rod, and then a small drop of the suspensions were removed and placed onto the filter paper (HM-4189.25), 4) if the unabsorbed methylene blue forms a permanent light blue halo around the clay spot, the end point has been reached, 5) cation exchange capacity was determined by the amount of methylene blue solution to reach the end point as follow:

$$\mathrm{CEC(meq/100g)} = \frac{\mathrm{E} \times \mathrm{V}}{\mathrm{W}} \times 100 \tag{3.2}$$

Where, CEC is the cation exchange capacity (meq /100 g), E is the milliequivalents of methylene blue per milliliter (0.01N), V is the milliliter of methylene blue solution required for the titration and W is the grams of dry material. In this study, the cation exchange capacity was found to be 91 meq/100 g which falls into the typical range from 80 to 150 meq /100 g (Mitchell, 1993).

3.2.3.8. Specific surface area

The specific area can be determined with the same technique as CEC. Since the technique is performed in aqueous suspensions and the expansive characteristic of bentonite, methylene blue may cover all available exposed area. The methylene blue molecule is rectangular in shape with dimension of approximately 17×7.6×3.3 Å. Due to the different dimensions in directions, the adsorption of this mineral has three possible orientations, resulting in different area covered by one methylene blue molecule:

1) The molecule is attached with its largest face on the clay surface, the covered area is about 130 Å per molecule,
2) The molecule may be tilted in the angle of 65 to 70˚ respect to the clay surface, the covered area is about 66 Å per molecule; and
3) If the longest axis is oriented to perpendicular to the surface, the covered area becomes about 24.7 Å per molecule.

The most common assumption is that the methylene blue molecule lies flat on the mineral surface with the largest surface (Santamarina et al., 2002 and Karim and Salem, 2011). Therefore, the surface area covered by methylene blue molecule was assumed to be 130 Å. The surface area of bentonite was calculated with the following relationship:

$$S = \frac{1}{319.87} \cdot \frac{3.2}{1000} \cdot (0.5n) A_V A_{MB} \tag{3.3}$$

Where, S is the specific surface area (m^2/g), Av is the Avogadro number ($6.02*10^{23}$/mole), A_{MB} is the surface area covered by MB molecules and n is the number of increment of MB addition. In this study, the specific surface area was found to be 712.5 m^2/g. The typical range of specific area of bentonite has been reported from 400 to 800 m^2/g (Mitchell, 1993 and Santamarina et al., 2002).

3.2.3.9. Energy Dispersive X-ray Spectroscopy (EDX)

Rheological behavior of bentonite suspensions are significantly affected by the chemical elements in bentonite, especially Na/Ca ratios (Lagaly, 1989). In this study, chemical analysis was conducted by Energy Dispersive X-ray Spectroscopy (EDX) to obtain chemical components in the tested bentonite.

This analytical technique uses the focused or scanning electron beam in the electron microscope to excite the atoms in a sample and discriminates the characteristic x-rays emitted. During the analysis, the specimen is bombarded with an electron beam of a scanning electron microscope (SEM). The electrons collide with the atoms comprising the specimen and a vacancy is created by ejecting an inner shell electron. An electron from an outer shell is then transferred into the vacancy in the inner shell to return the atom to its balanced state. This occupation accompanies the loss of energy in outer the shell electron by emitting an X-ray. The amount of energy released by the transferring electron varies with the location of the vacancy and the replacing or transferring electrons. Since the level of X-ray energy released by the atom of every element is unique, the type of the atom from which the X-ray was emitted can be identified by measuring the amounts of energy present in the X-rays being released by a specimen during electron beam bombardment. The EDX spectrum is a plot of frequency in X-rays received for each energy level. It displays peaks corresponding to the energy levels for which the most X-rays had been received. Each of these peaks is unique to an atom or a single element.

In this study, EDX characterization of the sieved bentonite powder was performed using a Philips/FEI XL30 Environmental Scanning Electron Microscope (ESEM) equipped with EDAX located at the Department of Geosciences at the University of Texas at Austin (Figure 3.12). A Gaseous Secondary Electron (GSE)

detector was utilized with frame and spot mode of EDAX. In addition, ESEM pictures were taken during the chemical analysis. Figure 3.13 shows an ESEM photograph of the sieved bentonite powder. Since the raw bentonite initially includes some water, partially hydrated bentonite consisting of aggregated bentonite particles were observed up to about 20 μm in scale. Energy peaks for various elements for a bentonite specimen are shown in Figure 3.14, which shows the major elements derived from EDX. The main chemical elements in the composition of bentonite are found to be oxygen, chlorine, silicon, aluminum, calcium, sodium, iron, sulfur, magnesium and some other trace metals. This clay has the Na/Ca ratio of 1.9. Table 3.3 shows the quantitative chemical composition of all the elements and trace metals derived from EDX. The information on the chemical compounds that constitute the raw bentonite was also obtained from the manufacturer. Table 3.4 presents the quantitative chemical compounds from X-ray fluorescence (XRF), showing it mainly consists of SiO_2, Al_2O_3, Fe_2O_3, Na_2O, MgO, CaO, TiO_2, K_2O, MnO, and some other trace metal oxides. Moreover, the loss of ignition which indicates the portion of organic material was about 12%.

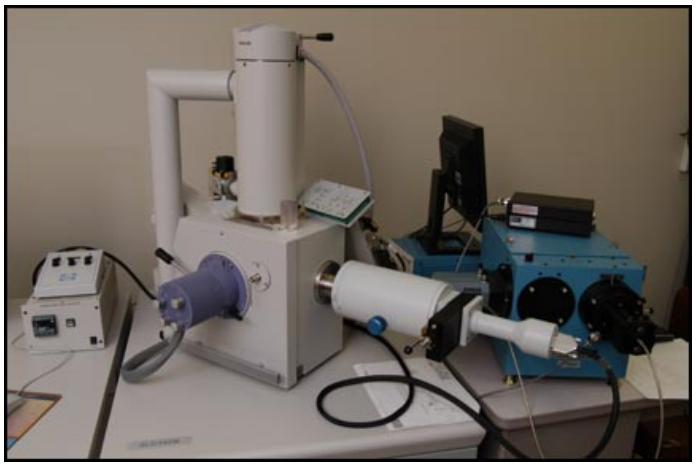

Figure 3.12 Philips/FEI XL30 Environmental Scanning Electron Microscope (ESEM) equipped with EDAX (http://www.geo.utexas.edu)

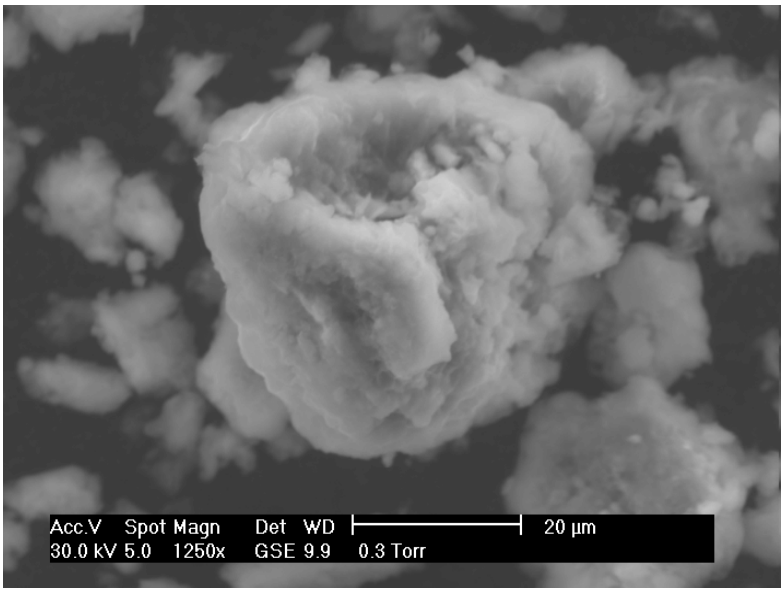

Figure 3.13 ESEM photograph of the sieved bentonite (partially hydrated)

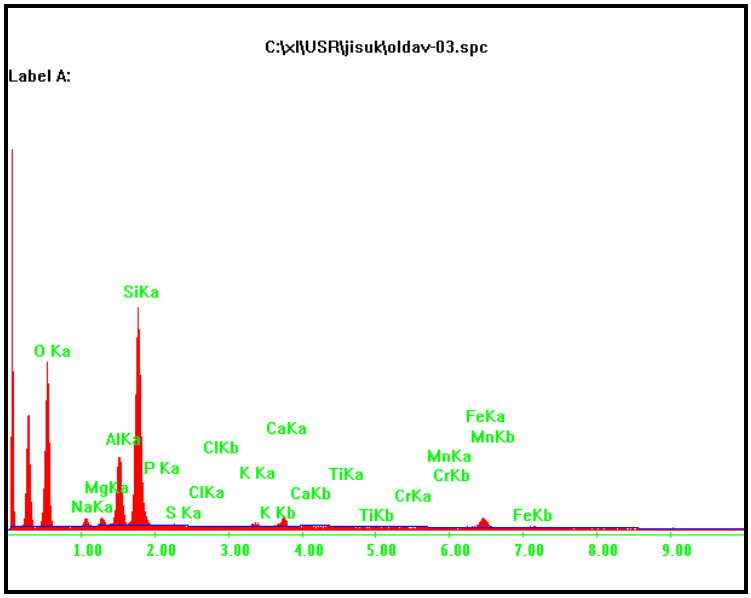

Figure 3.14 EDX Spectrum for the sieved bentonite (frame mode)

Table 3.3 EDX result of the sieved bentonite, wt%

O	53.05	K	0.52
Na	2.27	Ca	1.2
Mg	1.52	Ti	0.15
Al	9.07	Cr	0.11
Si	28.77	Mn	0.2
P	0.46	Fe	2.31
S	0.43	Total	100
Cl	0.09	Na/Ca	1.89

Table 3.4 Chemical compounds of raw bentonite (CECTCO), wt%

SiO_2	60.89	MnO	0.11
Al_2O_3	17.27	Na_2O	2.15
CaO	1.12	P_2O_5	0.04
Cl	0.03	SO_3	0.27
Cr_2O_3	0.02	TiO_2	0.21
Fe_2O_3	3.56	LOI	11.72
K_2O	0.62	Total	100
MgO	2.01	Na/Ca	1.92

3.2.3.10. pH measurement

In aqueous system, the bentonite dispersions have the pH of alkaline due to hydrolysis (Barr and Guth, 1950). Since the clay mineral includes chiefly silicate having the dominant exchangeable cation as sodium, the process of hydrolysis can be expressed as:

$$Na_2SiO_2+2H_2O\leftrightarrow H_2SiO_2+2NaOH$$

The silicate acid has little effect on pH due to weak ionization, but NaOH is almost completely ionized, resulting in alkaline solution. (Barr and Guth, 1950). The pH of bentonite suspensions decreases with an increase of solid contents possibly due to the effect of electrolyte, but the detailed mechanisms are still obscure (Barr and Guth, 1950). The pH condition in bentonite suspensions is important since it is related to

particle associations (van Olphen, 1977; Lagaly, 1989; Abend and Lagaly, 2000; Kelessidis et al., 2007), causing a variation in flow behavior of bentonite suspensions. In addition, the pH changes with time due to the hydration of bentonite as well as the mixing fluids such as water (tap and deionized) and SPP solution. The pH of the bentonite suspensions and various mixing fluids were measured using a JENCO 60 portable digital pH meter, which was calibrated with buffer solutions of pH 4.01, 7.00 and 10.01. Figure 3.15 shows the pH values of the unmodified bentonite suspensions and mixing fluids. The pH measurement of the modified suspensions is presented in Chapter 4. The bentonite suspensions showed a consistent alkalinity with an average of 9.33 and a standard deviation and C.O.V. of 0.21 and 0.02, respectively. The natural pH of bentonite has been reported within a range of 8.5 to 10 (Kaoser et al., 2006; Kelessidis et al., 2007; Clarke, 2008). In addition, the pH values of the mixing fluids were 6 and 8.9 for de-ionized water and tap water, respectively.

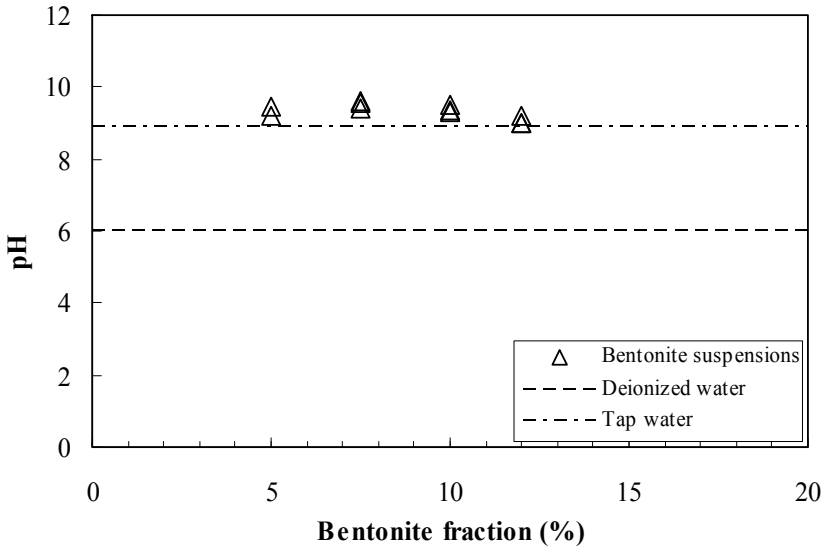

Figure 3.15 pH measurement of bentonite suspensions

3.2.4. Water

The ionic strength of the mixing water has a large effect on the rheological behavior of the bentonite suspensions because the ions included in water may react with bentonite, disrupting the reaction between bentonite and SPP. In order to characterize the amount of ions in the water, the electrical conductivity was measured using a CDM230 conductivity meter owned by the environmental group at the University of Texas at Austin and converted to ionic strength. Table 3.5 summarizes ionic strength of the used water.

Table 3.5 Ionic strength of water

Water type	μm/cm	mM
Tap	336.3	4.6×10^{-3}
Pure	0.83	1.1×10^{-5}
*De-ionized	0.96-1.56	$1.3\text{-}2.2\times10^{-5}$

* The water mainly used through this study.

However, it is not practical to use de-ionized water in the field and the cations, mainly Ca^{2+} and Mg^{2+} included in tap water, can affect the reaction between SPP and bentonite. In order to characterize the amount of cations included in tap water, water hardness tests were performed with tap water (taken from ECJ basement at the University of Texas at Austin) in accordance with ASTM D1126-02 (reapproved in 2007). During these tests, calcium and magnesium included in tap water were sequestered by the addition of disodium ethylenediamine tetraacetate. The step by step procedures are as follows:

1) Adjust the pH of the sample from 7 to 10 by adding NH_4OH solution (prepared by mixing one volume of NH_4OH with four volumes of water)

2) Add 0.5 ml of buffer solution, and approximately 0.2 g of hardness or calcium hardness indicator powder. The buffer solution was prepared by mixing 5% sodium tetraborate ($Na_2B_4O_7 \cdot 10H_2O$) solution and a solution including 10 g of sodium hydroxide (NaOH), sodium sulfide ($Na_2S \cdot 9H_2O$) and potassium sodium tartrate ($KNaC_4O_6 \cdot 4H_2O$) in 100 ml of water. 1 g of magnesium disodium ethylenediamine tetraacetate, having a magnesium-to-EDTA mole ratio of 1 to 1, was added to make up to 1 L with water, and

3) Standard Na_2H_2EDTA solution was added slowly from a burette with continuous stirring until the color changes from red to blue. The standard disodium ethylenediamine tetraacetate (Na_2H_2 EDTA) solution was prepared by dissolving 3.8 g of disodium ethylenediamine tetraacetate dihydrate in approximately 800 ml of water, and then the pH of the solution was adjusted to 10.5 with NaOH solution (50 g/L). Complete the titration within 5 min after the buffer addition. If the titration requires more than 20 ml of the titrating solution, dilute the sample and repeat the test.

The hardness of the water is calculated by the following relationship:

$$\text{Total Hardness, epm} = \frac{20C}{S} \tag{3.4}$$

$$\text{Calcium Hardness, epm} = \frac{20D}{S} \tag{3.5}$$

$$\text{Magnesium hardness= total hardness-calcium hardness} \tag{3.6}$$

Where epm is the equivalent parts per million or milliequivalents per liter, C is the standard Na_2H_2EDTA solution added in titrating hardness (ml), D is the standard Na_2H_2EDTA solution added in titrating calcium hardness (ml) and S is the sample taken for test (ml). As presented in Table 3.6, the tap water includes magnesium and calcium ions, which were not detected in deionized water, and the concentration of magnesium

ions were approximately 13 times higher than that of calcium ions in the tested water sample.

Table 3.6 Hardness of tap water (ECJ)

Total hardness (meq/l)	5.68
Calcium hardness (meq/l)	0.4
Magnesium hardness (meq/l)	5.28

3.2.5. Sodium pyrophosphate decahydrate

Sodium pyrophosphate (SPP) decahydrate ($Na_4P_2O_7 \cdot 10H_2O$) with 99% purity was purchased from Sigma-Aldrich Inc. Figure 3.16 shows the chemical structure of sodium pyrophosphate, which consists of a negatively-charged-chain phosphate. The chemical is a white, odorless, and crystalline material, which has a solubility of 62 g/l at 20˚C. Specific gravity and molecular weight of SPP are 1.82 and 446.06, respectively. According to material safety data sheet, this material is considered as a nontoxic chemical which is not listed on most of environmental regulations such as Clean water act, SARA, CERCLA, OSHA, and TSCA. The pH in a form of solution (1 to 5%) has been reported ranging from 9.5 to 10 (MSDS, 2001 and Clarke, 2008). In this study, 5% SPP solution was mainly used and the pH of the solution was 9.5.

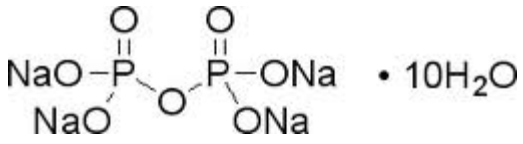

Figure 3.16 Chemical structure of sodium pyrophosphate decahydrate

3.2.6. Filter materials

In order to help uniform distribution of bentonite suspensions during permeation, the fine aggregate (pea gravel) and coarse sand were used as filter materials (either for penetrability tests or for sample preparation in hydraulic conductivity tests). The pea gravel was sieved through the No. 4 sieve prior to use (Diameter > 4.75 mm) and the coarse sand was sieved through the No. 10 and retained on the No. 16 sieves prior to use (1.2 mm < Diameter < 1.75 mm). Each material was washed to remove any fines that may have been present.

3.3. Experimental program

3.3.1. Rheological test

3.3.1.1. Rheometer

Figure 3.17 shows the rheological testing setup. The Physica MCR 301 rheometer, which is an air bearing device manufactured by Anton Paar, is used in this study. A variety of oscillatory and monotonic, stress-controlled, and strain-rate controlled tests including strain sweeps and stress ramps tests can be performed with the various measuring system such as parallel plate, cone and plate, bob and cup, and vane. The automated computer software, Rheoplus, programmed the testing variables. The dimensions of the rheometer (H×W×D) were 62.1 cm×48.5 cm×60.3 cm.

In this study, two types of geometries were utilized: cone and plate and vane and cup. While vane geometry was mainly utilized through this study to obtain the undisturbed rheological properties, especially for the samples rested for an extended time, cone and plate was also utilized to conduct preliminary tests as well as investigate

disturbance effect. A detailed discussion of the disturbance effect is presented in Chapter 4. The vane is six-bladed, with each blade having a 1 mm thickness and a length of 16 mm. The vane radius is 11 mm and the cup used has an internal diameter of 29 mm, resulting in a 3.5 mm measuring gap. Additional cups were manufactured for this research for long-term testing; the manufactured cups are 80 mm in length and 29 mm in internal diameter. The cone and plate has a diameter of 50 mm and an angle of 1º. No surface treatment on cone, plate, vane and cup such as sand blasting, was applied.

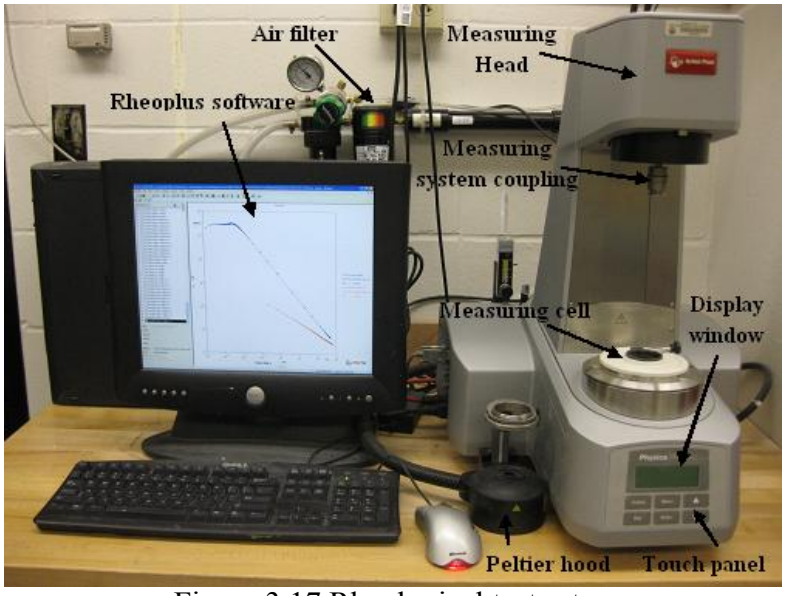

Figure 3.17 Rheological test setup

3.3.1.2. Preparation of the sodium pyrophosphate solution

Since the amount of SPP needed for each batch was very small, a 5% SPP solution was prepared in advance and the appropriate amount of solution was added to the water and bentonite to increase the accuracy of the measurement. The step by step procedures are as follows:

1) Place the appropriate amount of de-ionized water in mixing cup to make the 500 mL of 5% SPP solutions (i.e. 25 grams of SPP solids to 475 grams of water,
2) On weighing paper, measure the proper amount of SPP solids by weight to make the solutions,
3) Place the mixing cup in high shear mixer,
4) Turn on the high shear mixer and slowly add small amounts of SPP at a time until completely dissolves (approximately 15 minutes). For the initial addition, an extreme care was taken not to lose SPP solids by high shear mixing. This process should take 1 to 1.5 hours, and
5) Place both solutions in sealed containers and label them appropriately.

3.3.1.3. Preparation of the unmodified bentonite suspensions

In order to compare flow behavior of the unmodified and modified bentonite suspensions, the unmodified suspensions are also prepared. The preparation of the unmodified suspensions was based on the weight fraction of dry bentonite by total weight of suspension. Since the raw bentonite was delivered with an initial water contents which may vary during sieving and storing, the initial water contents (8.1 to 8.5%) were measured after sieving and taken into account in the calculation of the weight fraction of bentonite in suspensions. The step by step procedures for preparing the unmodified bentonite suspensions are as follows:

1) Place a mixing cup on a weighing scale and tare to the zero reading,
2) Add half the amount of de-ionized water needed for the suspensions to the mixing cup,
3) Obtain the needed amount of the sieved bentonite add to the mixing cup,
4) Add the remaining amount of water to the mix,

5) The mixing process of bentonite suspensions included three steps; each step consisted of 5 minutes of high shear mixing of the suspension followed by manual scraping of the sides and base of the mixing cup to remove attached bentonite flocs.

3.3.1.4. Preparation of the SPP modified bentonite suspensions

The rheological properties of the bentonite suspensions significantly vary with the sample preparation method, especially when ionic additives are introduced during the suspension preparation procedures. The effect of different mixing methods on rheological properties of bentonite suspensions will be discussed in chapter 4. The step by step procedures for preparing the modified bentonite suspensions are as follows:

1) Place the amount of de-ionized water needed for suspensions to the mixing cup,
2) Add the amount of SPP solution to the mixing cup by using an eye dropper and mix with the high shear mixer,
3) Add the desired amount of sieved bentonite to the mixing cup which has a half amount of desired SPP solution and water mixture to achieve the desired concentration,
4) In a separate mixing cup, mix the same amount of water and SPP solution as step 1 and 2 and mix with the high shear mixer. Add half of this mixture to the original mixing cup, and
5) The mixing process of bentonite suspensions is the same as that for the unmodified suspensions.

The contents of each ingredient were calculated based on the weight ratios. For example, the contents for a 1% SPP by 10% bentonite fraction were calculated as follows:

1. Desired total weight of suspension = 500 grams
2. Required bentonite mass = 50 grams
3. Required actual bentonite (considering 8% of the initial water content) = 54 grams
3. Weight of SPP solid = 0.5 grams
4. SPP Solution (i.e. amount from the 5% solution equivalent to required SPP solid mass) = 10 grams
5. Amount of additional water = 436 grams

3.3.1.5. Storage of the materials

Special care was taken in storing both the raw materials and the suspensions prepared for long term tests throughout this study. Following sieving, the sieved bentonite was stored in a tightly sealed chemical container in order to minimize any changes in water contents due to adsorbing moisture from room humidity. In order to achieve long term measurements with minimal disturbance to the structure of the bentonite suspensions, separate storage cups (Figure 3.18) were specially manufactured for this study in order to test the suspensions at different resting times.

Figure 3.18 Manufactured storage cup for long term tests

The cups were designed to fit in the rheometer without the need to scoop out any of the suspension and the only disturbance to the suspensions occurred from inserting the vane. Sample volume at each cup was maintained at 37 ml, which allowed the vane to penetrate approximately twice the length of its blades. For samples rested for extended periods of time, the cups were tightly sealed, after mineral oil was added on top of the bentonite suspensions, to prevent any evaporation from the samples. In addition, the cups were placed in a location where sample disturbance from vibration and shaking in the laboratory was minimal.

For cone and plate, a small amount of sample was carefully scooped from the top of the sample in the storage cup after removing the mineral oils and tested prior to the vane tests for comparison purposes. However, this sampling was only applied for relatively short range of resting times (a day to less than a month) due to a concern about the sedimentation of bentonite particles. For the short term measurements, the bentonite

suspensions were stored in the mixing cup with a wet cover to prevent evaporation of the suspensions.

3.3.1.6. Initialization of device and sample setup

The initializing process of the MCR 301 rheometer takes a few minutes. Since the device is air bearing device, a pressure level (approximately 80 psig) is required to be supplied, and is automatically checked from an external barometer prior to tests. After the display monitor shows "O.K", the gap and rotor sensors are checked by moving the measuring head to the top position of 140 mm and the measuring system coupling revolves at a high speed. The device utilizes the Peltier temperature control system, which maintains the temperature of the specimens using a water bath which connected to the back of the rheometer. The temperature in rheometer is adjusted through Rheoplus software (22 ºC was used in this study to shorten the time for equilibrium). Then a measuring system is connected to the motor coupling and the system automatically identifies the type of measuring system through a smart chip system. When the cone and plate is utilized, the gaps for a correct measuring and trimming position are set by adjusting the gap between the cone and the plate to a reference value (zero gap setting).

Following initialization of the rheometer, samples are mounted on the plate or in the cup for testing. For the cone and plate, a small amount of sample was scooped out from the storage vessel (or mixing cup) at the time of testing, and placed on the plate with extreme care. After that, the cone was lowered to the "trimming" position (to a gap of 0.103 mm) with a velocity of 8 mm/s; this process caused a small extrusion of the suspension. Since the extruded portion may affect the reproducibility and reliability of the results (Anton Paar Germany 2006), the extruded portion was carefully trimmed with a flat-bladed spatula; during this processes, the cone is locked in place to prevent it from

rotating and thus shearing the samples during trimming. Finally, the cone was moved to the "measuring" position (to a gap of 0.093 mm) with a much slower velocity of 5 μm/s. The maximum normal force was set to 50 N.

With the vane geometry, the prepared suspensions were poured immediately after mixing into the cup, followed by placing the cup right into the rheometer. For the samples rested for a designated time, the mineral oil on the top of the storage cup was carefully removed using an eye dropper at the time of testing, and then the cup was placed in the rheometer. The vane was inserted with the same velocity as 8 mm/s until the vane is completely immersed in the suspension.

3.3.1.7. Experimental program

In this study, several types of experimental program were utilized depending on loading conditions (drag shear and oscillatory shear) and material functions (yield stress and storage/loss modulus) which are studied. This section also addresses experimental procedures and issues on each type of experimental program.

Constant shear rate technique

This is the typical method, with vane geometry, that directly estimates the yield stress as the peak stress in the torque-time response at a constant shear rate. The vane is fully inserted into the sample and a torque is applied at a constant but sufficiently slow rate; the change in torque is monitored with time. The yield stress is then calculated using the maximum torque (M_{max}) and the dimensions of the vane such as diameter (D) and length (L) of the blades based on the equation provided in Chapter 2.

However, it is well known that the yield stress determined by this method is highly dependent on the applied shear rates. In addition, an apparent viscosity is

obtained only at a specific shear rate so that large numbers of tests are required to achieve apparent viscosities through a wide range of shear rates. As a preliminary test, constant shear rate tests were conducted with 10% bentonite suspensions at a range of low shear rates (0.05, 0.08, 0.1 and 0.5 s^{-1}) to confirm shear rate dependency of the measured yield stress. Suspensions were rested for 24 hours to remove any effect from bentonite hydration. Preshearing of 500 s^{-1} for 1 min was applied to provide a consistent initial condition prior to the measurements. Figure 3.19 shows the results of constant shear rate tests at four different shear rates. As can be seen, the peak stresses were 105, 110, 115 and 135 Pa at the shear rate of 0.05, 0.08, 0.1, and 0.5 s^{-1}, showing that the higher shear rates produced higher peak shear stresses. This result is compatible with data published in the literature; for example, Bekkour et al. (2005) conducted constant shear rate tests with 6, 8, and 10% bentonite suspensions at the shear rates of 0.03 to 2 s^{-1} and reported that the peak stress increases as shear rates increase. Saak et el. (2001) observed similar phenomena in cement pastes.

Determining a correct shear rate is very challenging since it varies with the bentonite fractions of suspensions. Previous studies (Dzuy and Boger, 1983 and Barnes and Nguyen, 2001) suggested establishing a suitable range of shear rates which produce essentially constant maximum shear stress and the shear rate should be slow enough to avoid viscous resistance and insufficient damping. In this study, the shear rate may be suitable up to 0.08 s^{-1} since the difference in peak values was very small (less then 5%). However, the lowest shear rate of 0.05 s^{-1} was selected to consistently capture yield stress from the diluted to the concentrated suspensions and avoid unforeseen errors in measurements. Nevertheless, peak stress did not appear at 5% suspensions (Figure 3.20), indicating that the shear rate of 0.05 s^{-1} is not sufficiently slow for 5% suspensions. In addition, the bentonite suspensions with a high percentage of SPP, tested at the shear

rates, showed continuous increase in shear stress and viscosity with time without displaying any peak stress. Barnes and Nguyen (2001) also suggested that this method is the most appropriate for yield stresses greater than 10 Pa.

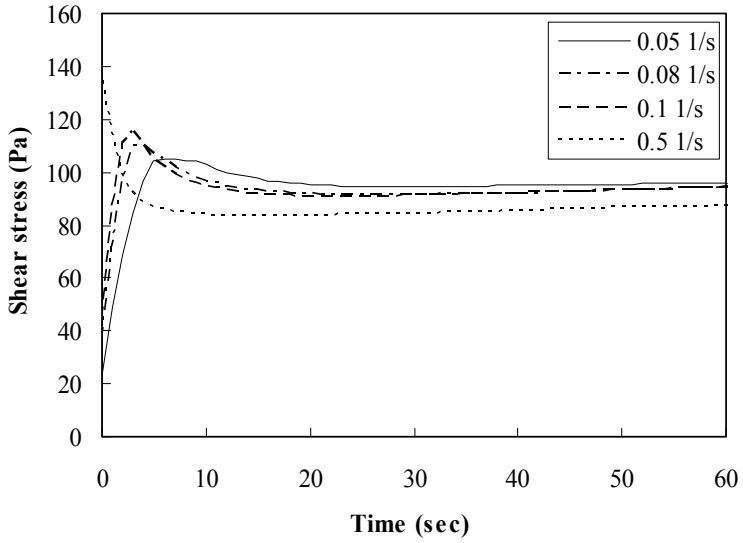

Figure 3.19 Shear stress - time curves: shear rate dependency in peak stress (10% suspensions at constant shear rates of 0.05, 0.08, 0.1, and 0.5s^{-1})

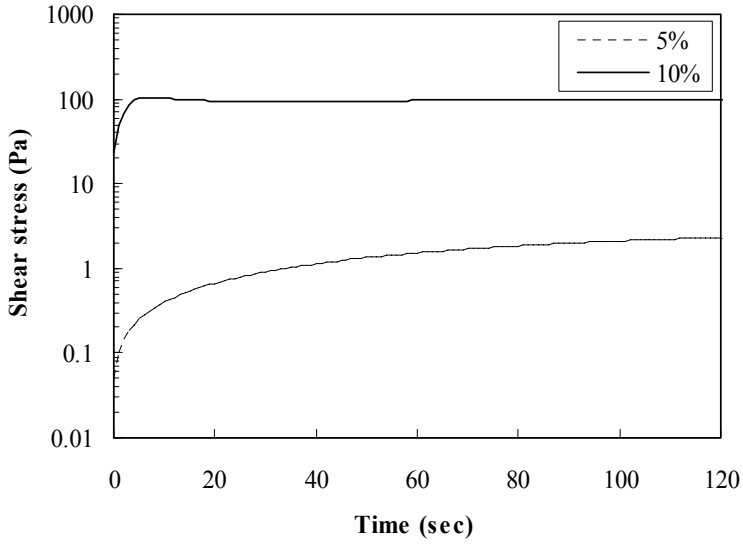

Figure 3.20 Shear stress - time curves: peak stress dependency on bentonite fractions (5 and 10% suspensions at constant shear rates of 0.05 s^{-1})

Stress ramp technique

Since the tested suspensions with low fractions of bentonite and/or high percentages of SPP have yield stresses lower than 10 Pa, the stress ramp, a stress controlled technique, was selected for this study over the constant shear rate method. The stress ramp method can be used to measure yield stresses below 10 Pa, and was considered to be a consistent way of measuring low and high yield stresses. Moreover, this technique allows us to estimate yield stress, and apparent viscosities through a wide range of shear rates so that the number of tests required could be reduced; the constant shear rate technique utilizes a slow shear rate to determine yield stress. In this method, the applied shear stress is increased in a stepwise function at a constant rate, resulting in a flow curve. Figure 3.21 shows a schematic of loading function used in this study. Each stress level is maintained for 12 sec and the data is recorded at the end of the interval. The tests were programmed such that samples rested for 2 min after placing the measuring system in the testing position to provide a consistent initial condition for all stress ramp tests (both, the cone and plate and the vane tests).

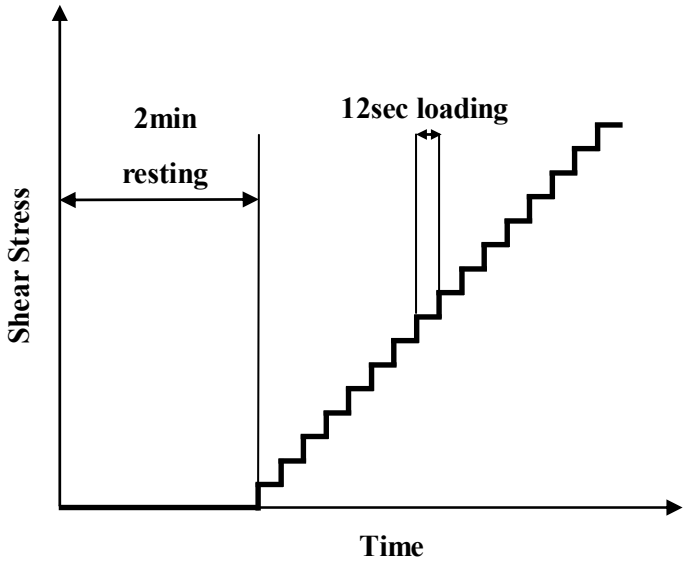

Figure 3.21 Schematic of loading steps in stress ramp technique

As stated in Chapter 2, the yield stress was determined by a log τ-log γ plot (Figure 2.7). However, the ramp rate is one of the important factors affecting yield stress measurement using the stress ramp technique. Zhu et al. (2001) suggested that slow enough ramp rates should be used in this technique and reported a little difference (5%) in yield stress measurement of 60% TiO_2 suspensions with three different rates of 0.063, 0.1 and 0.13 $Pa \cdot s^{-1}$. In addition, Besq et al. (2003) utilized a very small ramp rate of 0.016 $Pa \cdot s^{-1}$ for 2, 4, and 6% bentonite suspensions. However, applying too slow of ramp rate becomes impractical due to evaporation from sample surface (vane) and edge (cone), especially when a fluid has a large yield stress. The evaporation is a larger source of error in the cone and plate measurements due to the small sample size; the vane is inserted deep into the suspension and surface evaporation is less critical on the measured yield stress. In order to investigate the effect of ramp rate on the flow behavior of bentonite suspensions, two sets of stress ramp tests with 5 and 7.5% suspensions was performed with vane geometry at the ramp rates of 1, 2 and 3 Pa/step

(0.083, 0.167 and 0.25 $Pa \cdot s^{-1}$) immediately after mixing. As shown in Figure 3.22, 5% suspensions produced higher yield stresses at the shear rate of 3 Pa/step (0.25 Pas^{-1}), while the ramp rates of 0.5 and 1 Pa/step (0.042 and 0.083 $Pa \cdot s^{-1}$) exhibited similar yield stresses. This result suggested that the diluted suspensions should be tested less than 1 Pa/step to obtain consistent results. Figure 3.23 shows the effect of ramp rate on 7.5% suspensions. Three different ramp rates of 0.083 0.167 and 0.25 $Pa \cdot s^{-1}$ produced the average yield stress of 27.9 Pa (±0.3 Pa), indicating that the differences in these rates are small enough to ignore. This effect was also confirmed by performing a series of stress ramp tests with 8, 9, 10, 11 and 12% bentonite suspensions, immediately after mixing, using cone and plate geometry at two ramp rates. Figure 3.24 displays the comparison of yield stresses from two ramp rates. There was a good agreement between the yield stresses at the two ramp rates. Similar tests were conducted with 5% suspensions at three ramp rates of 0.5, 1 and 3 Pa/step to confirm the effect of ramp rates on the diluted suspensions. Based on the observations, the ramp rate of 1 Pa/step (0.083 $Pa \cdot s^{-1}$) was used for lower strength suspensions (either lower bentonite concentration, higher SPP content, and/or at early times) to improve the accuracy of measured yield stresses; and 3 Pa/step (0.25 $Pa \cdot s^{-1}$) was used for stronger suspensions to decrease the time required to reach the yield stress and minimize sample evaporation during the tests.

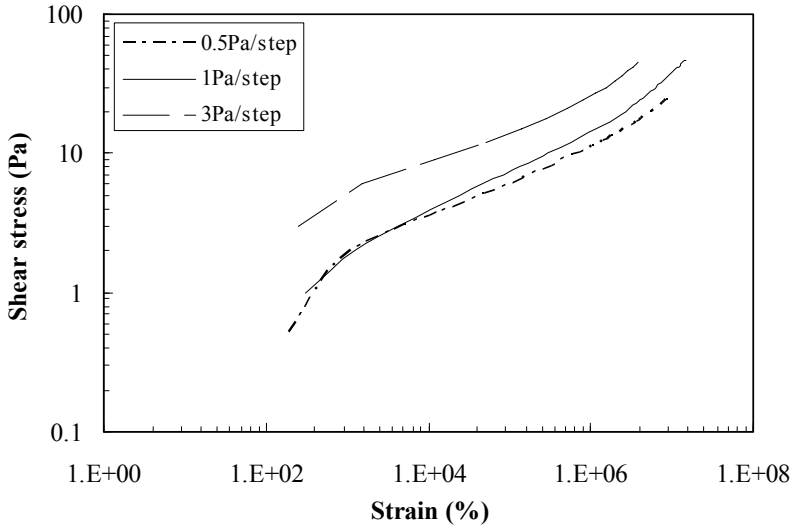

Figure 3.22 Comparison of different ramp rates of 5 % bentonite suspensions (Vane)

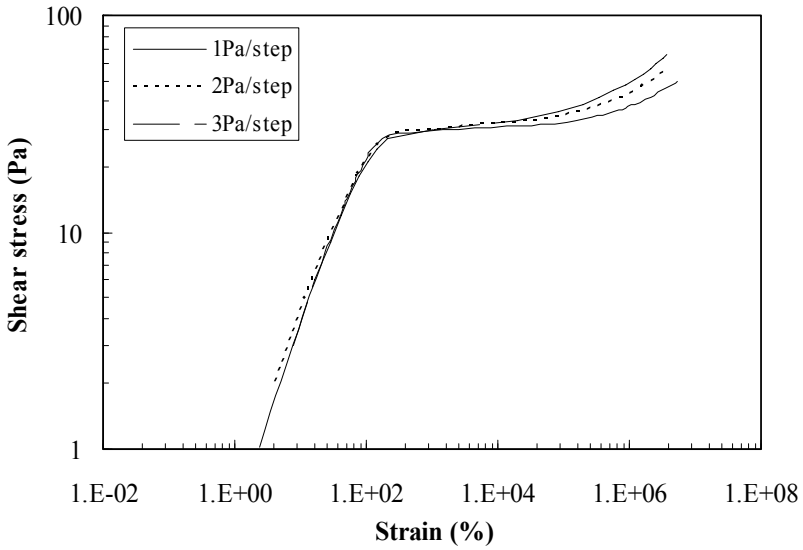

Figure 3.23 Comparison of different ramp rates at 7.5 % bentonite suspensions (Vane)

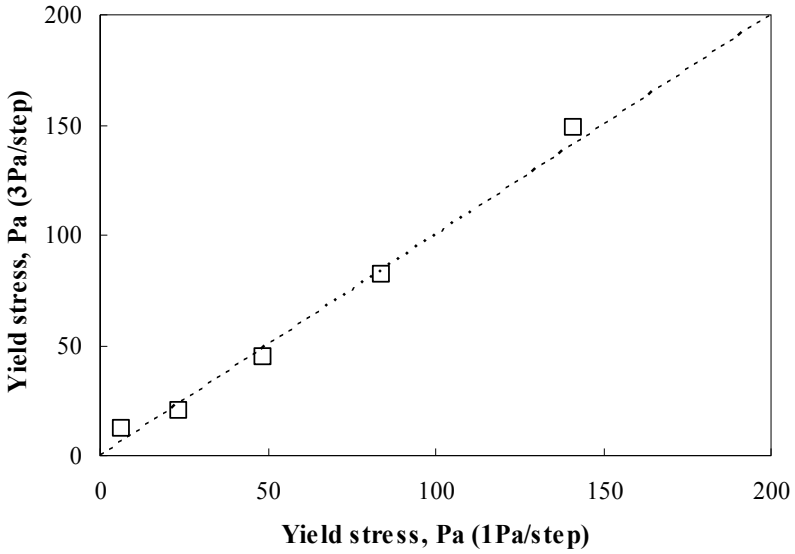

Figure 3.24 Comparison of different ramp rates by cone and plate (The dashed line is 45 ° line)

Comparison of constant shear rate and stress ramp

Peak stresses obtained from constant shear rate tests were compared to yield stresses from stress ramp tests immediately after mixing. Figure 3.25 displays the yield stresses obtained from the two methods for 6 to 18% bentonite suspensions (with 1% increment). Both methods provided well agreed yield stresses, indicating stress ramp technique can accurately estimate the yield stress.

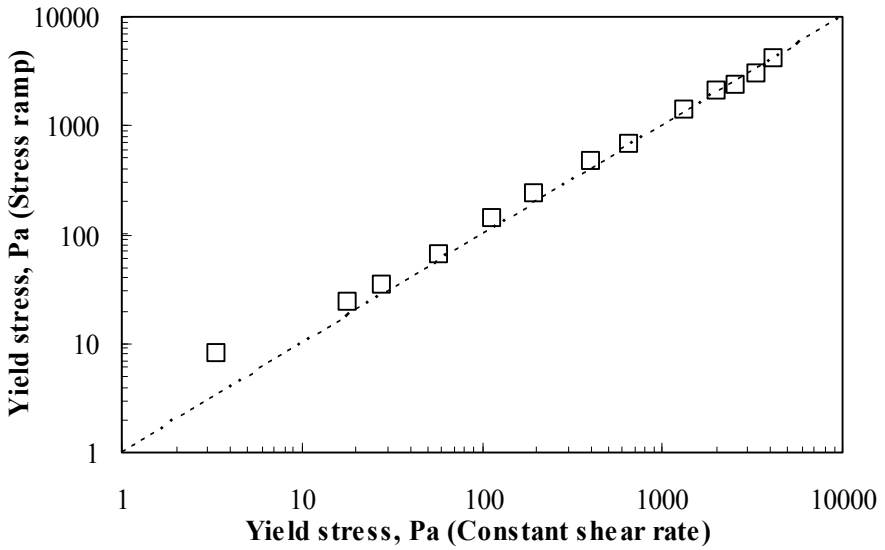

Figure 3.25 Comparison of yield stress from stress ramp and constant shear rate tests with vane geometry (6 to 8% of bentonite suspensions)

Oscillatory shear

The post grouting stability of bentonite suspensions under a dynamic loading can be evaluated by performing oscillatory shear test. This test applies oscillatory strains by increasing amplitudes at a constant level of frequency, providing the linear and non-linear behavior of the suspensions. The shear stress is shifted by a phase angle δ with respect to the applied strain so that it can be expressed as the sum of an elastic component (in-phase, G') and a viscous component (out-of-phase, G") with the applied strain as shown in Chapter 2.

In this study, oscillatory shear tests were conducted at a constant oscillation rate of 1Hz over the range of strains from 0.01 to 1000%. This method was slightly modified to obtain relatively constant value of critical storage modulus (G') by eliminating disturbance which occurred during inserting vane and avoid effect of structural buildup at the small strain range. The oscillatory shear stress at the strain of

0.01% was applied for 2 min before testing, followed by increasing strain on a log scale, recording 6 points per 10 digits. This modification could provide consistent initial state in sample prior to the measurement. As shown in Figure 3.26, storage modulus (G') and strain were not significantly changed by the method compared to the unmodified method. Storage modulus (G') did not show a significant change until it reaches a level of strain. The critical storage modulus is determined as small strain plateau where G' is constant, and then intersection between two straight lines extended from this plateau and larger strain region where describing the nonlinear behavior after flow are determined as critical strain as shown in Figure 3.27. At the small stain range, the suspensions display linear elastic response. Beyond this range, the non linear viscoelastic responses are observed; storage modulus is degraded, followed by an increase in loss modulus (G") and phase angle (δ).

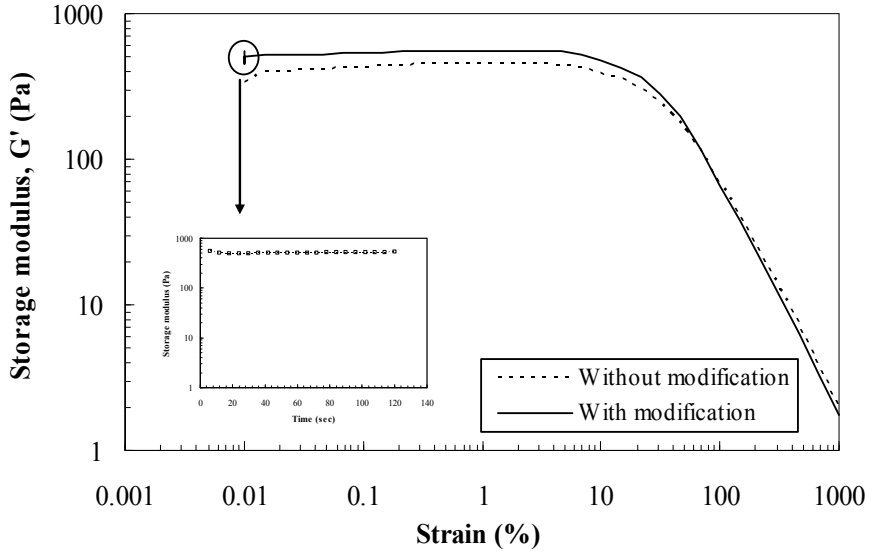

Figure 3.26 Modified strain sweep result of 10% bentonite suspensions at zero resting time.

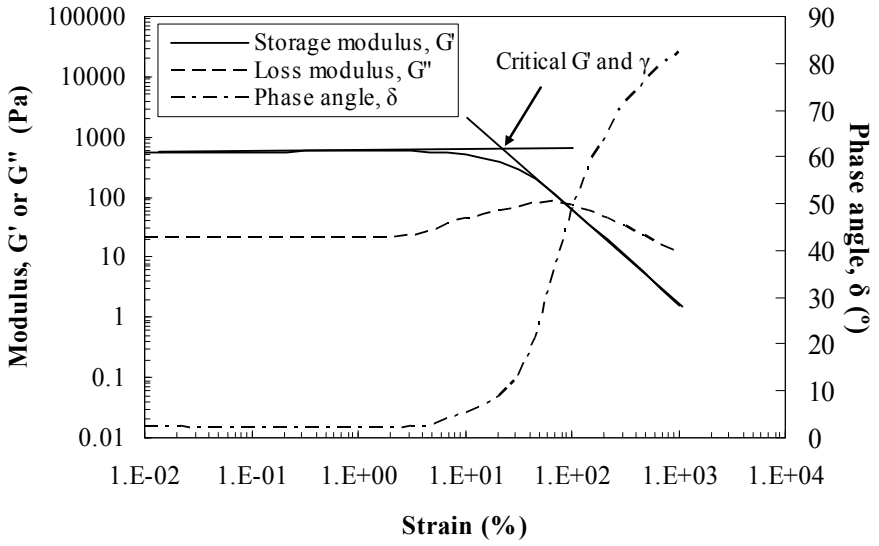

Figure 3.27 Determination of critical storage modulus and strain

The important issue for this test is the frequency dependency of storage modulus. Moreover, this test reveals whether the response of the suspensions to cyclic loading is independent or dependent on frequency when a selected constant shear strain within the linear elastic range. Frequency sweep tests were performed at different bentonite suspensions (5, 7.5, 10 and 12%) using the cone and plate geometry. Figure 3.28 shows storage modulus at various frequencies ranging from 0.1 to 10 Hz at 0.5% strain. As can be seen, no significant change in storage modulus at different frequencies was observed; indicating that strain sweep tests performed in this study as well as the cyclic behavior of the bentonite suspensions are independent of frequency. Geier (2004) also reported the frequency independent behavior of bentonite suspensions and Clake (2008) observed similar phenomenon with the SPP modified suspensions.

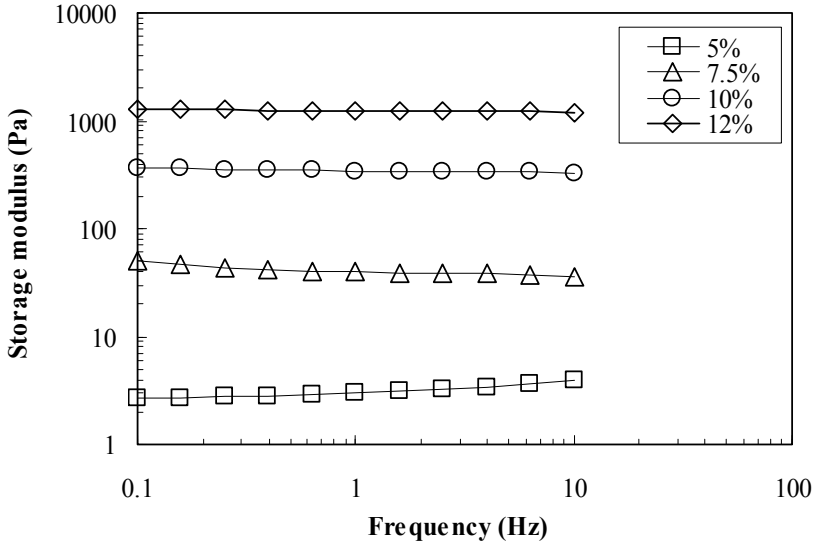

Figure 3.28 Frequency dependency of storage modulus at different bentonite fractions (5, 7.5, 10 and 12%)

3.3.2. Permeation setups

3.3.2.1. Constant pressure setup

Constant pressure injection tests were conducted to evaluate the parameters affecting the penetrability and groutability of the modified bentonite suspensions. Based on these tests, penetration distance and injected pore volume of the suspensions through various sand columns were estimated. Figure 3.29 and Figure 3.30 show the 1-D constant pressure injection testing setup. A pressure cell having a 6.3 cm diameter and a 17 cm in height connected to a Trautwein pressure panel from the top was connected to the permeation cell. The permeation cell was made of a transparent cylinder and had a 3.8 cm diameter and a height of 21 cm. For the permeation cell required for the longer penetration, two separate cells were connected using a clamping ring and rubber gaskets (0.4 mm in thickness), resulting in a length of 51 cm. A balance

is placed to measure the weight of the effluents during testing. The precision of the balance was ±0.2 g.

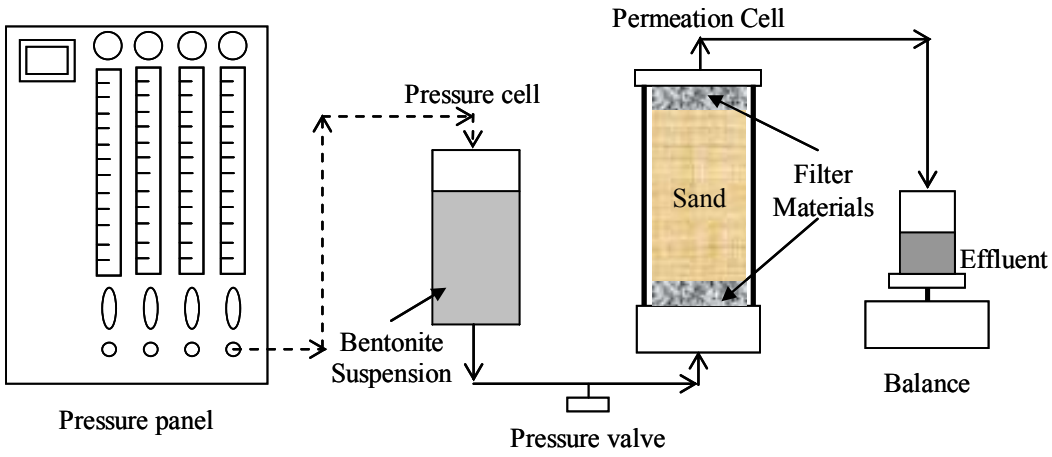

Figure 3.29 Schematic of 1-D constant pressure injection setup

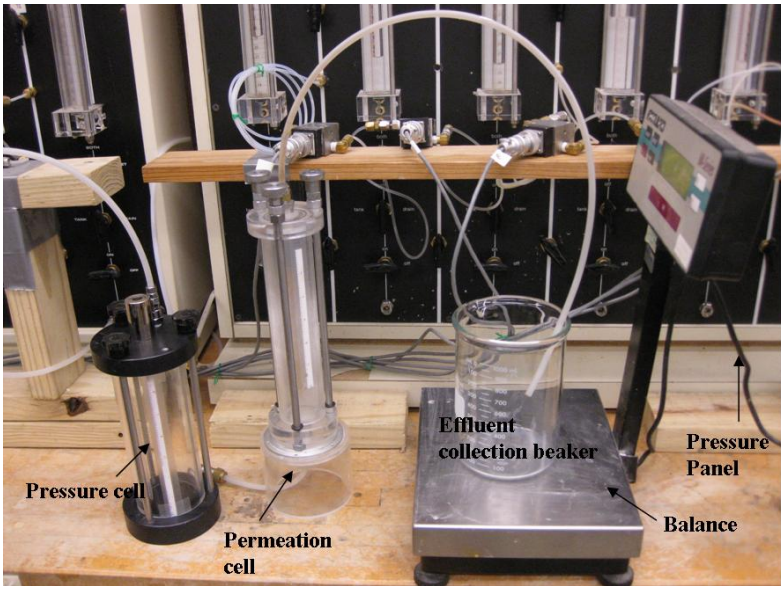

Figure 3.30 Photograph of constant pressure test setup (21cm permeation cell)

Sand was air pluviated with a funnel into the permeation cell and initially saturated with slow flushing of de-aired water (at least 3 pore volumes) from bottom to top, and then more pore volume of water (at least 3 pore volumes) was flushed with the

pressure of 35 kPa to expel entrapped air bubbles in the specimen (ASTM D4320/D4320M-09). For specimens prepared with silty sands, the moist tamping method was used to prepare the specimens. The specimens were then saturated slowly with low gradient flow to reduce/eliminate any fines washing through the specimen. A filter material, consisting of a layer of coarse sand (1.2 mm < D < 1.75 mm) and a layer of pea gravel (D>4.75 mm), was placed on the top and bottom of the sand column (with a total thickness of 25 mm) to help in providing a uniform distribution of the suspension throughout cross-section of the sand column and prevent sand washing into the tubes.

Bentonite suspensions were prepared in the same way to that for the rheological tests and placed in the pressure cell within 2 minutes after mixing for consistency with the rheological tests. The bentonite suspensions were injected into the sand column from the bottom at a constant pressure of 35 or 140 kPa. 5, 7.5, 10, and 12% bentonite suspensions mixed with 0 to 4% of SPP were injected into various sand columns. The four different sands are prepared at a relative density of 30 or 80%, had an effective grain size of 0.12, 0.20, 0.28, and 0.31 mm, and were mixed with 0 to 15% non-plastic fines. The weight of the effluent was monitored until there are no more effluents (for 10 minutes) to confirm completion of the permeation. In this study, the effect of the degree of saturation was not considered by assuming the flushing of the large pore volumes (over 6 pore volumes) of water to sand columns (close to full saturation).

3.3.2.2. Constant flow rate setup

Figure 3.31 and Figure 3.32 display the injection setup for the constant flow rate tests. A transparent cylinder (7cm in diameter and a 21.6 cm to 100 cm in height) was used as the permeation cell. A peristaltic pump was utilized for permeating the bentonite suspensions through the permeation cell; the pump was manufactured by

Stenner Pump Company (model 85MHP22). This model has an adjustable output pump that could apply flow rates between 5 and 100 ml/min with a maximum pressure of 700 kPa. A pressure sensor (manufactured by GEOTAC with a maximum pressure of 1400 kPa) was connected to the injection line between the pump and the grout injection inlet at the base of the permeation setup. The pump inlet line was connected to a bentonite suspension tank in which the bentonite was subjected to continuous shearing to prevent any yield stress or viscosity buildup. A balance is placed to monitor the amount of effluent during testing.

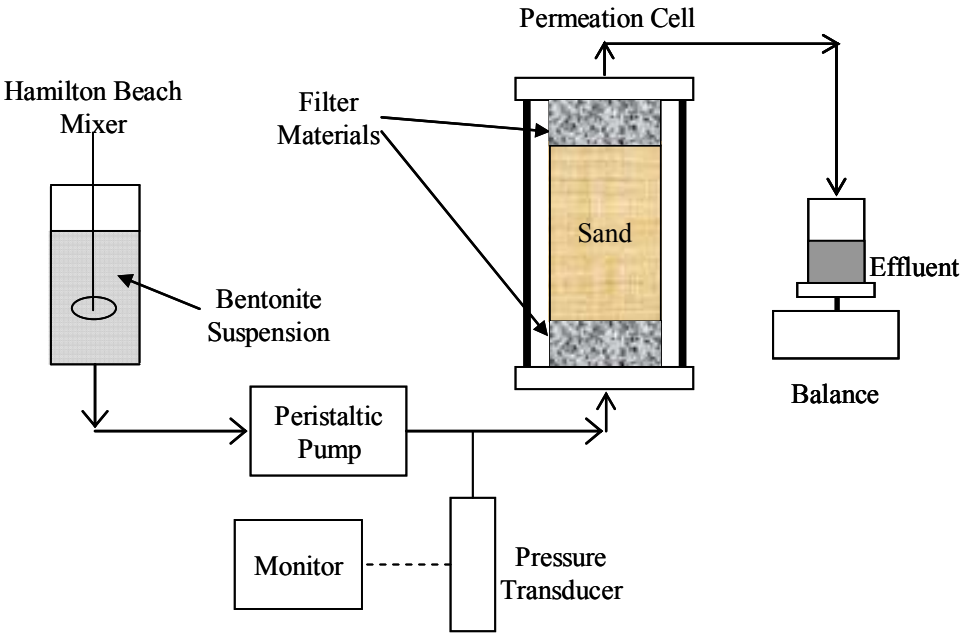

Figure 3.31 Schematic of constant flow rate test setup.

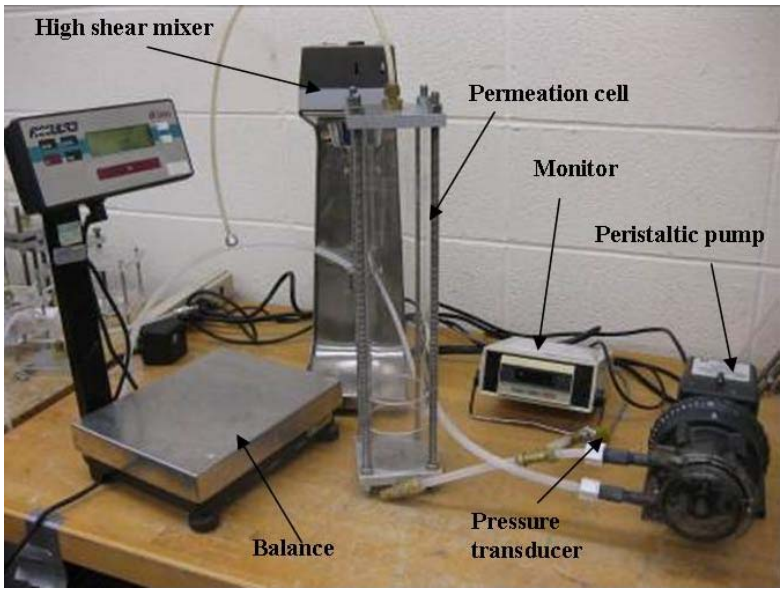

Figure 3.32 Photograph of constant flow rate test setup (40 cm permeation cell)

The specimen preparation (sand and filter material) was similar to that of the constant pressure tests. The specimen was first connected to a pressure panel (similar to the setup in Figure 3.30) and the permeation cell is flushed with water at a slow rate to saturate the filter material and sand. The base of the permeation cell was then connected to pump as shown in Figure 3.32 for the constant flow rate injection. The bentonite suspensions were prepared in the same way to that of rheological tests. The bentonite suspensions were injected into the sand column using peristaltic pump with a constant flow rate of 1.67 cm^3/sec (100 ml/min) until at least 1 pore volume of the suspensions was injected or the pressure reaches 140 kPa (not to cause any change in the sand fabric). The amount of the effluents from sand column was monitored using a balance and used to estimate the number of injected pore volumes.

3.3.3. Hydraulic conductivity

3.3.3.1. Sample preparation setup

Figure 3.33 shows a schematic of sample preparation setup. The same setup as 1-D constant flow rate tests was used except for a modified permeation cell (Figure 3.34). The permeation cell consists of 3 separate cylinders and is specifically designed and manufactured to prepare grouted specimens for hydraulic conductivity tests. The top and bottom molds are 7 cm in diameter and 5.1 cm in height. The middle section was 3.8 cm in height (and 7 cm in diameter), resulting in a total height of 15 cm. Rubber gaskets were placed between the 3 sections to form a tight seal. In order to maintain a perfect sealing between the cells, two types of aluminum plates (guide and clamping plates) were manufactured as shown in Figure 3.35. The guide plates for alignment of cells had dimensions of 9.65×9.65×1.25 cm (L×W×T) including four holes for supporting rods and the clamping plates had the same dimensions as the guide plates, but it consists of two parts of half plates with a 1mm gap between two parts for a tight clamping. After permeation, the mold was dissembled and the middle section of the mold was trimmed out with a wire saw to provide the permeated sand specimen the for hydraulic conductivity tests.

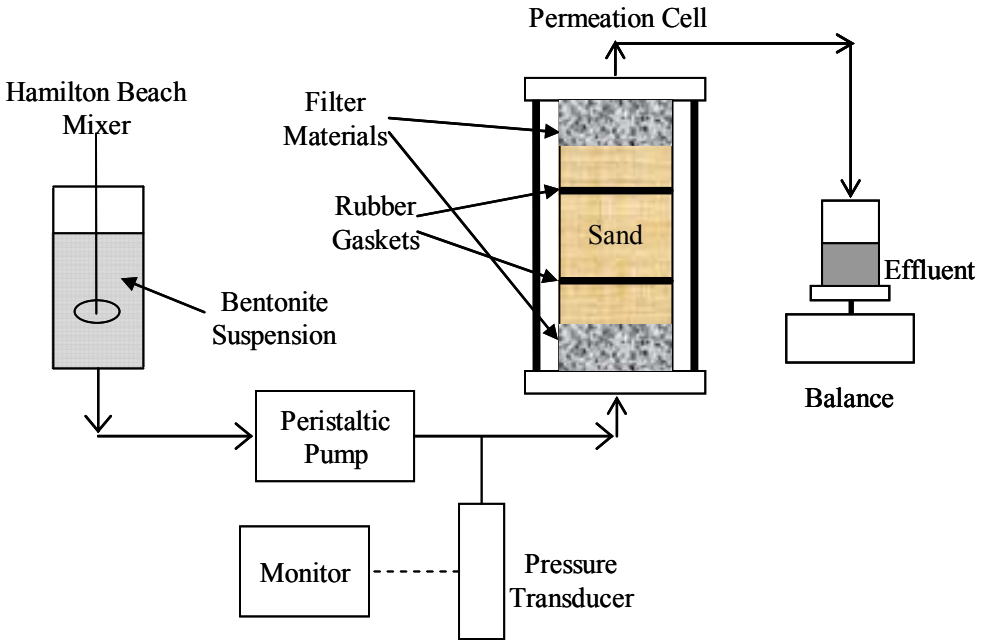

Figure 3.33 Schematic of sample preparation setup.

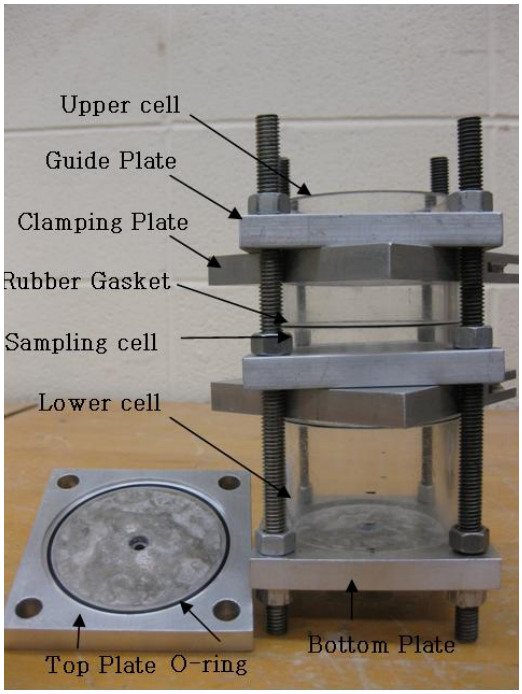

Figure 3.34 Photograph of sample preparation cell.

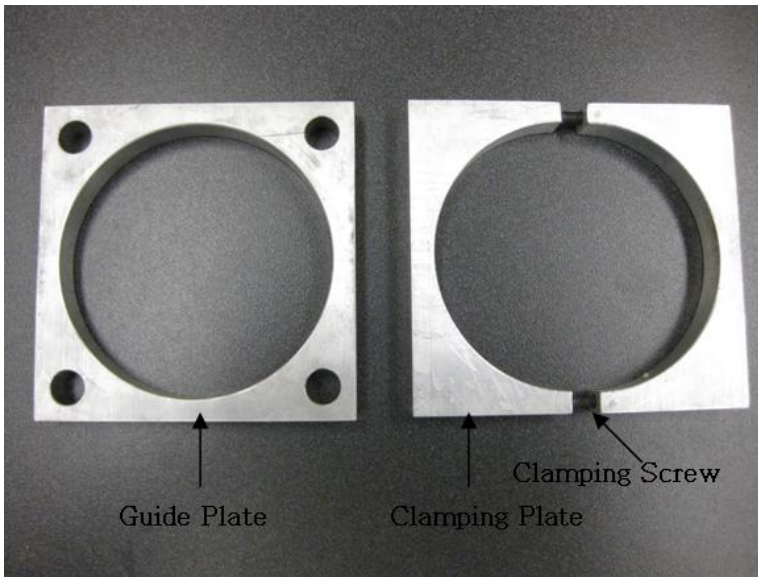

Figure 3.35 Photograph of guide and clamping plates

The specimen (both sand and filter material) was prepared in a similar procedure to that used to prepare the constant flow rate specimens. One (1) to two (2) pore volumes of grout were flushed through each specimen to investigate the effect of injected pore volumes on the hydraulic conductivity. After permeation, the specimens were seated for 24 hours, and then the middle portion of the specimens was carefully trimmed with a wire saw, resulting in a grouted sand specimen with a diameter of 7 cm and a height of 3.8 cm.

This setup allows us to obtain a uniformly grouted specimen because: 1) the presence of the filter material uniformly distribute the bentonite across the area of the specimen, and 2) the sand extended beyond the top and bottom of the middle section, and therefore, any caking formed at the base of the sand layer will be trimmed out. Removing the filter cake would lead to a conservative measurement of the hydraulic conductivity since the filter cake would have a lower hydraulic conductivity. Another main advantage of this setup is reducing the disturbance to the permeated sand by

eliminating the need to extract and trim the permeated sand to fit into a hydraulic conductivity setup.

3.3.3.2. Hydraulic conductivity setup

Figure 3.36 depicts a schematic of the hydraulic conductivity test setup. After trimming the middle section of the permeation cell (Figure 3.34), the grouted sand specimen was assembled with a top and bottom plate to measure the hydraulic conductivity, forming a rigid wall permeameter. Filter papers were placed on top and bottom of the specimens before assembly. The amount of water flow and the head difference were measured using differential transducers (Validyne Engineering, DP15) and the measurements were collected using a data acquisition system. The differential transducers used for measuring the inflow increased the accuracy of the measurements of the hydraulic conductivity especially for the grouted sands where the hydraulic conductivity was low and the amount of water drop in the burettes was small. The details on the pressure transducers will be explained later in this section. A backpressure of 300 kPa was applied to increase the degree of saturation of the specimen. The backpressure was applied gradually over 24 hours. After the backpressure saturation stage, a falling and rising head test (ASTM 5856-95) was performed with gradients ranging from 5 to 40 (depending on the estimated hydraulic conductivity of the samples). After the hydraulic conductivity tests were concluded, the bentonite content at different sections of the specimen was measured by wet sieve analysis (ASTM 117). This method was slightly modified to measure the dry weight of sand retained on a No.200 sieve instead of direct measurement of weight of bentonite. Although this method has some limitations due to multiple possible sources of error in small mass

measurements, Hwang (2010) reported that this method could estimate the bentonite contents with relatively good accuracy (standard deviation from ±0.04 to ± 0.15%).

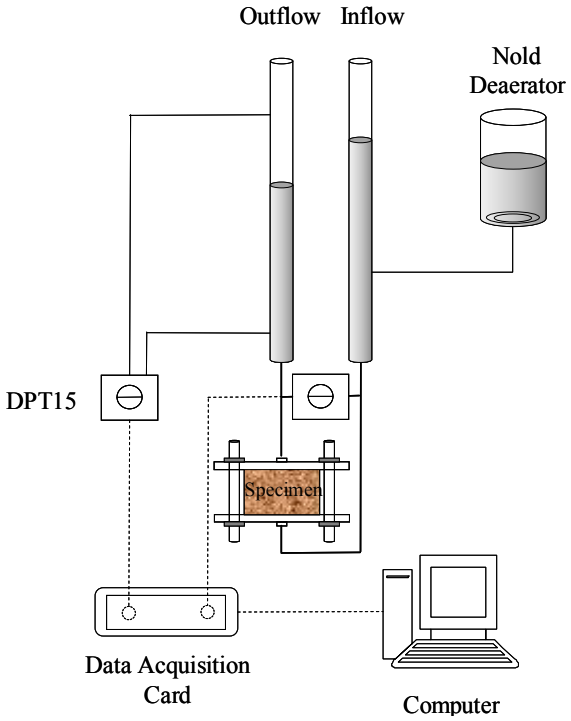

(a)

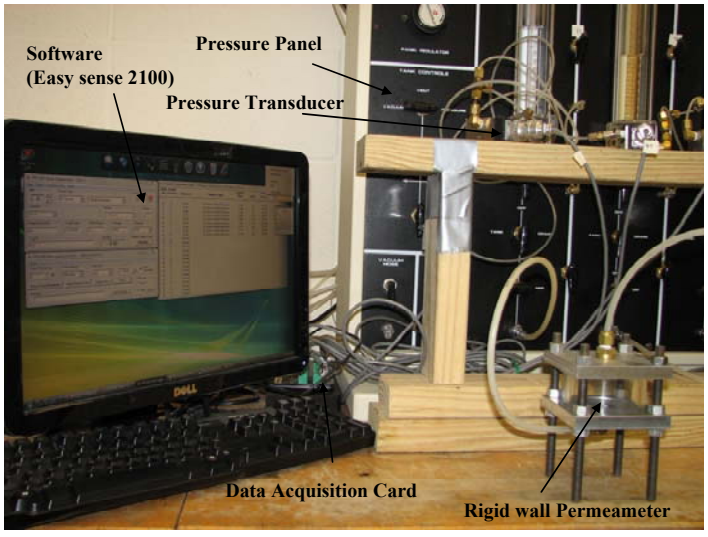

(b)

Figure 3.36 (a) Schematic of hydraulic conductivity testing setup, (b) photograph of hydraulic conductivity setup

Measurements of the hydraulic conductivity are typically performed by measuring the volume of a permeant through a soil over a given period of time under a known head difference between the top and bottom of the soil specimen. However, flow rates through the grouted sands are very low due to their low permeability; visual measurements of the volume change (reading the change in water level in a graduated cylinder or pipette) may include significant uncertainties and errors in the collected data even at relatively high hydraulic gradients. In the pipettes on the pressure panel used in study, the resolution of reading was 0.1 ml which was not enough to take an accurate reading in case of small flow rates. In order to increase the accuracy of the measurement, differential pressure transducers (DPT) were installed to digitize the volume change readings and to increase the resolution of volume measurement. The change in water level was measured by connecting the two ends of the deferential pressure lines to the top and the bottom of the pipettes. Since the DPT provided the difference between two pressures rather than the absolute value of an applied pressure, small head differences could be accurately measured even with high back pressures.

The difference in the head controlling the flow through the specimen was directly measured by connecting the two ends of the deferential pressure lines to the top and bottom of the specimen. The DPT used in this study was DP15 manufactured by Validyne Engineering. Figure 3.37 shows a DPT and the diaphragm placed inside it. The diaphragm deforms due to a pressure difference between two sides and the DPT reads the deformation of the diaphragm. This reading is transferred through an interface card (model UPC 2100 shown in Figure 3.38) as a form of electric signal to the computer system.

Figure 3.37 Photograph of pressure sensor and diaphragm

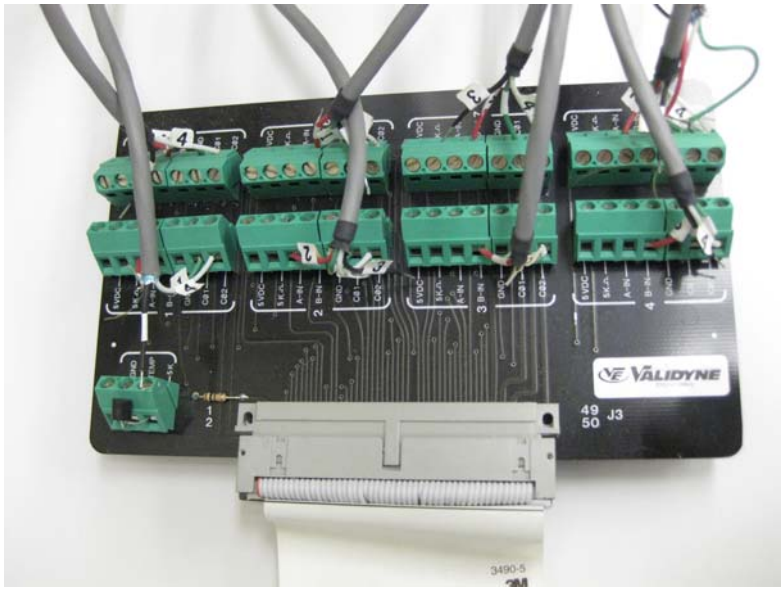

Figure 3.38 Photograph of data acquisition card (UPC 2100)

The sensor has a range of pressures or heads depending on the capacity of the diaphragm (each diaphragm has a unique number). The pressure range varies from

±0.08 psi to ±3200 psi in 24 full-scale ranges. The capacity of the diaphragm provided by the manufacturer is presented in Table 3.7. In this study, the diaphragm of No.26 was selected for the DPT for measurements of outflow to increase the precision of the measurements within the range of measurement (0 to 6 ml). For measuring head difference between top and bottom of the specimen, No. 32 and 36 diaphragms (with a capacity of 2 psi or 5 psi, respectively) were chosen considering the magnitude of hydraulic gradients being applied. As shown in Figure 3.39, the transducers were placed on a wood rack that was positioned in front of the pressure panel to provide electrical isolation from the surrounding.

Table 3.7 Pressure range chart (Modified from Validyne Engineering)

Diaphragm No.	Pressure range (psi)	Diaphragm No.	Pressure range (psi)
18	±0.08	42	±20
20	±0.125	44	±32
22	±0.2	46	±50
24	±0.32	48	±80
26	±0.5	50	±125
28	±0.8	52	±200
30	±1.25	54	±320
32	±2	56	±500
34	±3.2	58	±800
36	±5	60	±1250
38	±8	62	±2000
40	±12.5	64	±3200

Figure 3.39 Installation of pressure sensors

After installation, each sensor was calibrated with graduated pipettes on the pressure panel. The water level increased successively with an increment of 1 ml, and signals obtained from a transducer corresponding to each water level were recorded and a correlation was made between the signals and the readings from the pipettes, resulting in calibration factors for each sensor. Figure 3.40 shows a linear correlation between the signals from the sensor and the readings from the pipette. The sensors for outflow and pressure difference were calibrated with units of ml and psi, respectively. The calibration factors for each sensor are summarized in Table 3.8.

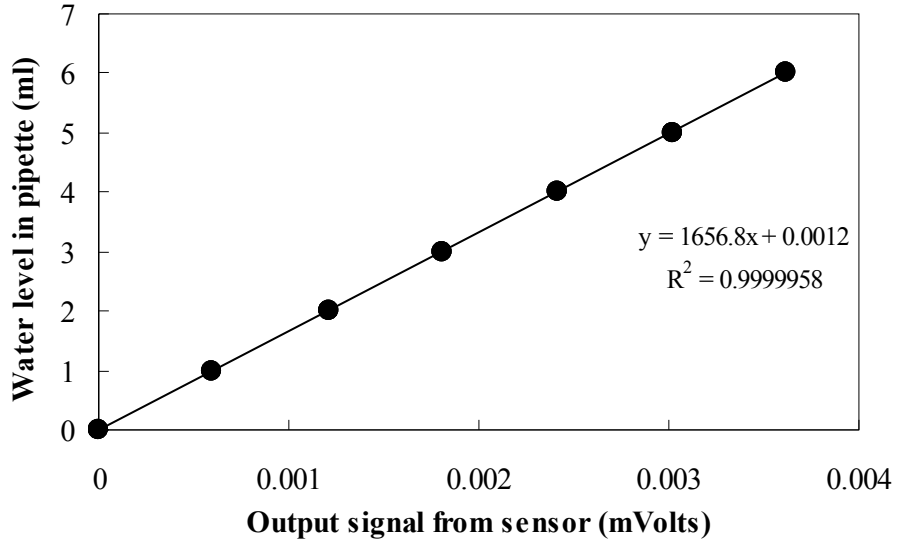

Figure 3.40 Calibration of pressure sensor number 4

Table 3.8. Summary of calibration factor

Sensor No.	Measuring variables	Diaphragm capacity (psi)	Calibration factor
1	Outflow	0.5	715.0
	Gradient	2	1727.5
	Inflow	2	2372.0
2	Outflow	0.5	248.3
	Gradient	2	1942.8
3	Outflow	0.5	288.1
	Gradient	2	1697.5
4	Outflow	0.5	294.3
	Gradient	5	1656.8

Since all hydraulic conductivity of the grouted sand has been measured for a long time scale (typically 10 days), the stability of signals from the transducers was an important issue for the accuracy in measurements. The stability of signal from each sets of transducers were checked by performing a series of tests with a permeation cell filled

with de-aired water. The water filled permeation cell was connected to the pressure panel and a back-pressure of 300 kPa was applied to cell to simulate the actual testing condition. Figure 3.41 shows a trend of signals from a transducer. The transducers exhibited a linear trend in volume and pressure measurement, indicating that the measurement was affected by the errors caused by testing environments: unstable pressure supply from pressure panel, compression of the water, noise from the sensors, and leakage from permeameter and panel connections. However, the slope of signals showed a strong linear relationship ranged from 8.7×10^{-7} to 1.57×10^{-6} ml/sec with R^2 of 0.92 to 0.99 as time elapsed. Therefore, hydraulic gradients were controlled to maintain the drift rate of signal not to exceed 25% of the flow rates through specimens in order to minimize the effect of errors from the measuring system.

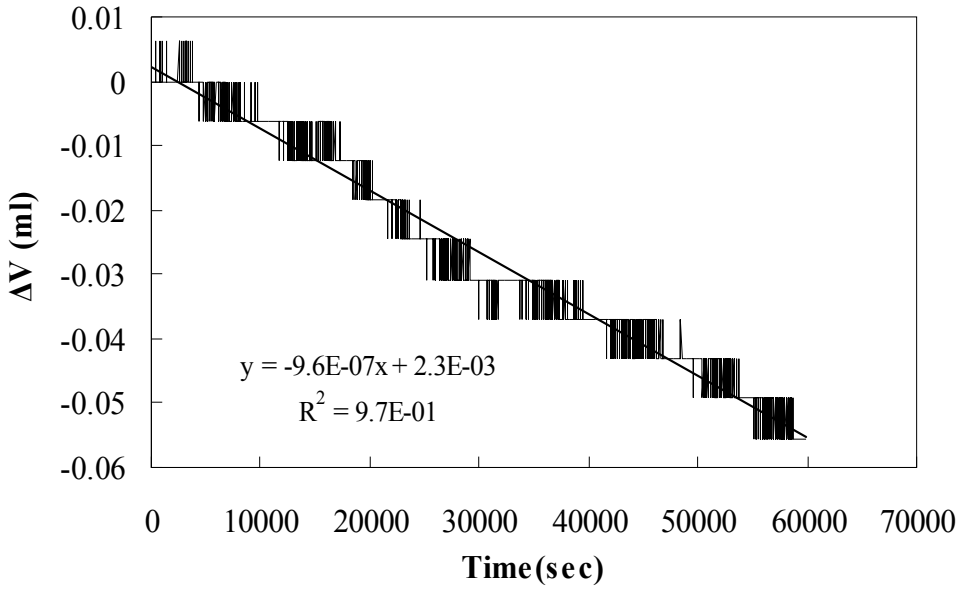

Figure 3.41 Trend of signal from DPT measuring outflow on setup

3.4. Conclusions

The index properties of the tested materials were investigated through ASTM standard testing methods. Since the chemical properties of bentonite greatly affects the rheological properties of the bentonite suspensions, detailed chemical properties of bentonite was studied by using X-ray diffraction and EDX tests along with other standard tests such as Atterberg limit, hydrometer and specific gravity. In addition, a series of water quality tests for de-ionized and tap water were performed to ensure low ionic strength in de-ionized water and quantify the concentration of cations in tap water.

The detailed procedures for rheological tests such as sample preparation, rheometry, testing setups were presented along with the experimental issues such as ramp rates, storage, frequency and pre-shearing. The experimental setups of constant pressure and constant flow rate were described along with testing procedures. Finally, hydraulic conductivity setups were presented.

CHAPTER 4: RESULT-I: RHEOLOGY

4.1. Introduction

This chapter presents the results of the rheological experiments on the unmodified and sodium pyrophosphate (SPP) modified bentonite suspensions. For the application of permeation grouting, it is required for the grout to have high enough initial mobility, followed by rapid reduction in the mobility to obtain desirable post grouting performance. For this purpose, a series of rheological experiments were conducted to investigate: 1) the effect of SPP on the initial mobility of the concentrated bentonite suspensions and 2) the time dependent changes in the mobility. The results of stress ramp and small angle oscillatory shear tests with vane geometry (unless being specified) for unmodified and SPP modified suspensions at various bentonite fractions (5, 7.5, 10 and 12%) and SPP concentrations (0 to 7%) are presented along with time dependent evolution (0 to 1 year) of the material properties. It is well known that the mobility of the bentonite suspensions is closely related to the formation of the microstructures (3-D networks) which are highly affected by both physicochemical properties of bentonite itself and experimental conditions (pH, electrolytes and resting times). Three types of material properties (yield stress, apparent viscosity and modulus) are mainly utilized to describe the flow behavior of the bentonite grouts. These properties were chosen because they include information on the strength of the flocculated 3-D network structures and the phase transition from liquid like to solid like behavior of the suspensions. The time dependent changes in rheological properties were explained through Environmental Scanning Electron Microscope (ESEM) study on the modified and unmodified 7.5% bentonite suspensions at different resting times (2, 20 and 216 hours). Other factors

affecting rheological behavior of the bentonite suspensions such as hydration, sedimentation, pH, hydrolysis of SPP and rheometry are also described.

4.2. Initial flow behavior

4.2.1. Yield stress

A series of the stress ramp tests were performed with both the unmodified and sodium pyrophosphate (SPP) modified bentonite suspensions immediately after mixing (zero resting time). At least three tests at each bentonite fraction (fresh mixed suspensions) were performed. Figure 4.1 shows yield stress growth with weight fraction of the unmodified bentonite suspensions. The average yield stresses increased exponentially with the increase of weight fraction of bentonite, indicating that the yield stress is a function of particle fraction in the suspensions (Dzuy and Boger 1983). However, yield stresses at 5% suspensions appeared to have relatively large standard deviations, indicating that the ramp rate of 1 Pa/step was not low enough to accurately capture the yield stress for the diluted suspensions.

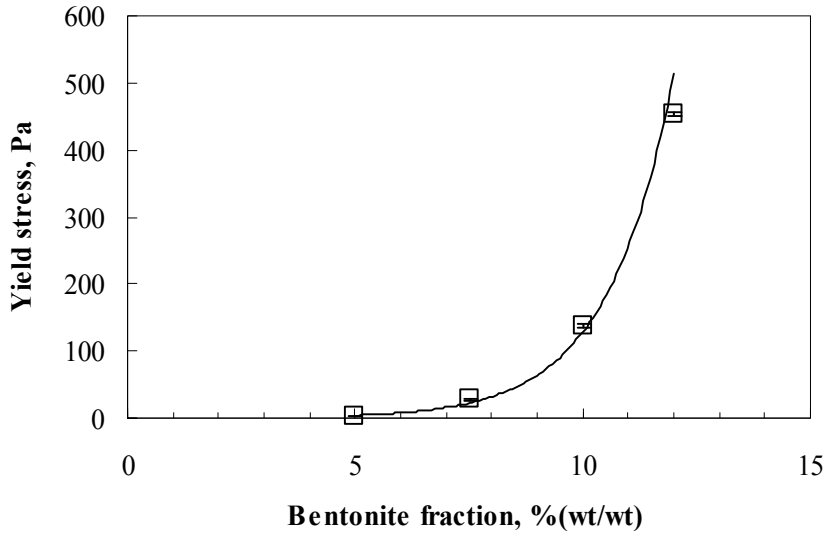

Figure 4.1 Yield stress at weight fraction of bentonite of: 5, 7.5, 10, and 12%

With the addition of SPP, yield stress of the bentonite suspensions begin to decrease and the amount of reduction is dependent on the SPP concentration and weight fraction of bentonite. Figure 4.2 shows the yield stress reduction for 7.5, 10, and 12% suspensions with the addition of 0 to 7% SPP. The yield stress decreased significantly from 27.9, 137.5 and 457.1 to approximately zero at 2, 3, and 4% SPP respectively (for yield stresses of 7.5, 10, and 12% suspensions with 2, 3, and 4% SPP, the minimum stress step of 1 was assigned since the strains were perfectly proportional to the stresses applied within a small stress range). The result implies that the SPP disrupts the formation of the condensed 3-D network of the concentrated bentonite suspensions, which produce a gel state with high yield stress, leading to a liquid state with low yield stress. In addition, the results showed that the mobility of the suspensions could be significantly improved with a very small amount of SPP (0 to 4% by dry weight of bentonite). Due to the little amount of networks at a certain amount of SPP (e.g. 2% SPP for 7.5% suspensions), the addition of more SPP beyond the amounts will have a minimal effect on yield stress. Furthermore, the 7.5% suspensions displayed approximately 90% reduction in yield stress compared to 50% reduction in 12% suspension at 1% SPP concentration. This is attributed to the fact that the higher bentonite concentrations have more 3-D networks than the diluted suspensions and thus, require more SPP to lower the yield stress.

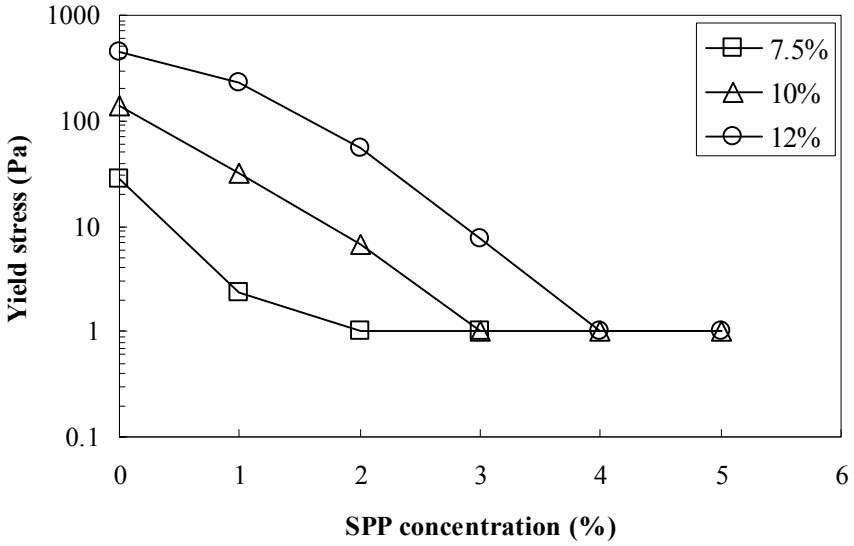

Figure 4.2 Yield stress of 7.5, 10, and 12% bentonite suspensions with various SPP concentrations (0 to 7%) measured at zero resting time

4.2.2. Apparent viscosity

The effect of electrolyte such as SPP on flow behavior of bentonite suspensions has been typically studied with apparent viscosity (Kelessidis et al., 2007). Figure 4.3 displays the changes in apparent viscosity with bentonite fraction at various shear rates. Since the stress ramp technique is a stress-controlled test, apparent viscosity of the diluted suspensions could not be measured at low shear rates. The apparent viscosity increased with the weight fraction of bentonite particles at a constant shear rate and decreased with shear rates at a given bentonite fraction. A similar phenomenon was observed in the suspensions with a high percentage of SPP. Figure 4.4 shows the apparent viscosity of 12% bentonite suspensions at SPP concentrations of 0 to 7%. While the suspensions at low SPP concentrations showed viscoelastic responses, almost pure viscous behavior was observed at the high SPP concentration, indicating that those suspensions exhibit more liquid-like behavior.

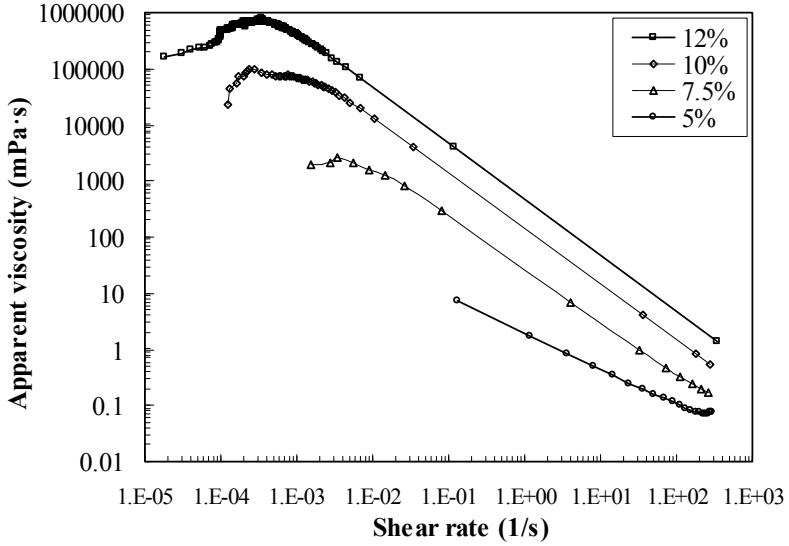

Figure 4.3 Apparent viscosities of 5, 7.5, 10, and 12% bentonite suspensions

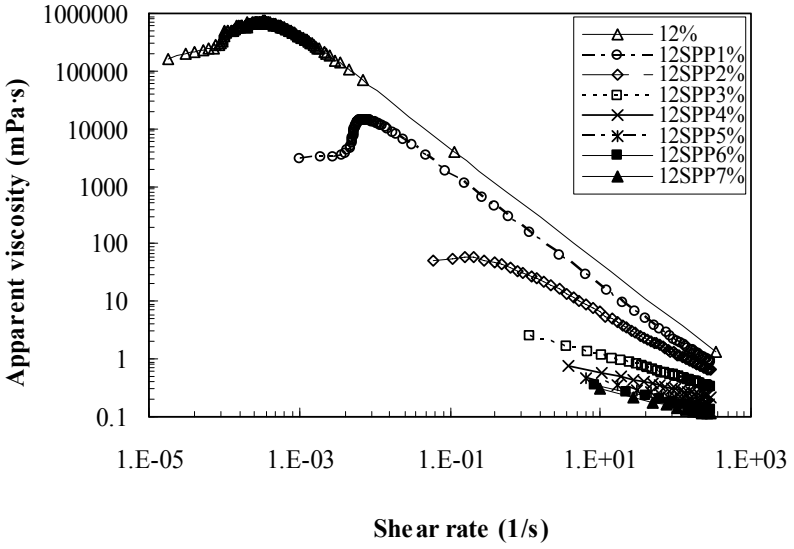

Figure 4.4 Apparent viscosity of 12% bentonite suspensions at 0 to 7% SPP concentrations

The apparent viscosity at a shear rate of 200 s^{-1}, for suspensions with various SPP concentrations, is shown in Figure 4.5. As can be seen from the figure, the apparent viscosity was reduced by approximately 66, 86 and 90% for the 7.5, 10, and 12% suspensions by adding 2, 3 and 4% SPP respectively. However, it was observed that the rate of reduction tends to converge as SPP increases, since the apparent viscosity becomes a function of the delaminated particle fractions. Due to this fact, the effect of SPP on viscosity is limited; the viscosities of the modified suspensions were still approximately 100 times greater than the viscosity of water (0.001Pa·s). Moreover, the high dosage of 3, 5 and 7% SPP to 7.5, 10 and 12% suspensions did not cause any coagulation, indicating that the amount of SPP was still less than critical coagulation concentration (the concentration of an ion where coagulation induces). Once coagulation occurs, the apparent viscosity would increase significantly (Penner and Lagaly, 2001).

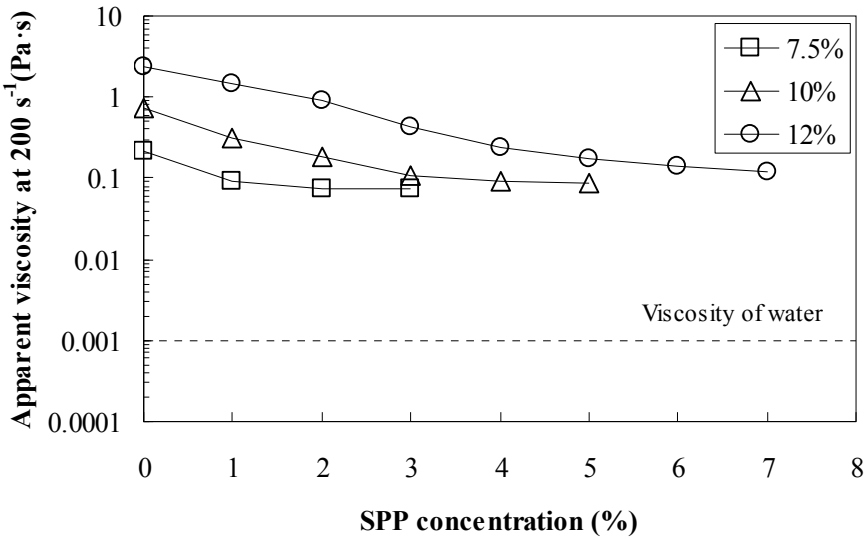

Figure 4.5 Apparent viscosity at shear rate of 200 s^{-1} for 7.5, 10 and 12% suspensions with various SPP concentrations (0 to 7%)

4.2.3. Critical modulus, critical strain and phase angle

The results of strain sweep tests also clearly illuminate the liquefying effect of SPP on bentonite suspensions. Figure 4.6 shows critical storage modulus and critical strains at bentonite fractions of 5, 7.5, 10, and 12%. The critical modulus and strains (at least three tests) were found using the method presented in Chapter 3. The average critical storage modulus increased from 3.1 to 1915 Pa in a similar way to yield stress, suggesting that critical storage modulus is also a function of particle fractions. Mahaut et al. (2008) observed similar phenomenon with the mixture of bentonite and glass beads.

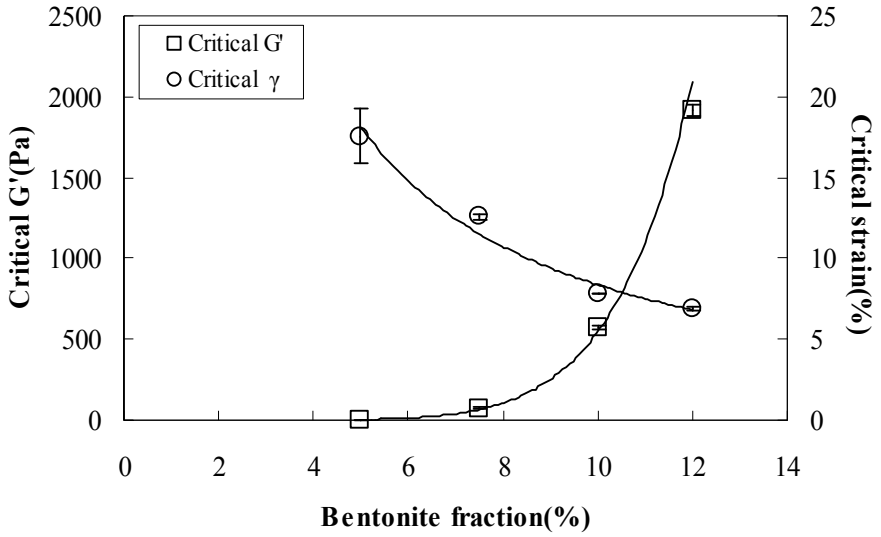

Figure 4.6 Critical storage modulus and strain at 5, 7.5, 10 and 12% bentonite suspensions

Figure 4.7 depicts phase angles with strains at different bentonite fractions. All suspensions displayed a solid-like behavior ($\delta<45^{o}$) at the small strain ranges, but the phase angle at small strain ranges decreased with bentonite fractions, indicating more solid-like behavior in the concentrated suspensions which is evidence of a gel type microstructure (Clarke, 2008). As strain level increases, the phase angle maintained a

constant value until the strains reach critical values, and then increased due to the phase transition from solid to liquid-like behavior due to the degradation of microstructure at a given bentonite fraction.

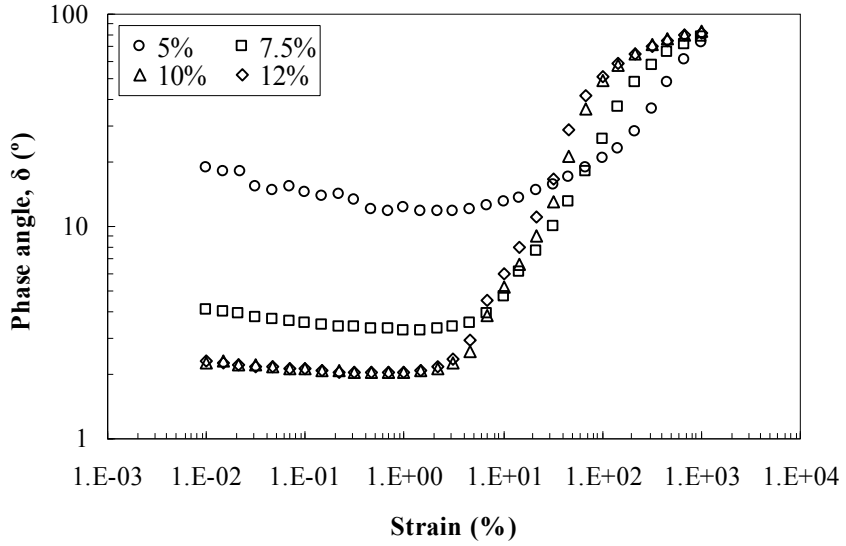

Figure 4.7 Variation of phase angle with strain at 5, 7.5, 10 and 12% bentonite suspensions

The modification of bentonite suspensions with SPP disrupts the formation of the 3-D network structure in the suspensions and reducing the stiffness of the bentonite suspensions as well. Figure 4.8 displays the variation of critical storage modulus with SPP concentrations. Similar to yield stress, critical storage modulus decreased with an increase in SPP concentration, but the rate of reduction was more significant compared to yield stress. The critical storage modulus of 7.5, 10 and 12% decreased from 73.9, 571.5 and 1915 Pa to 0.1, 0.5, and 2.3 Pa, respectively. Similar to what was observed with the apparent viscosity, the effect of SPP on critical storage modulus also tended to be limited at high percentages of SPP.

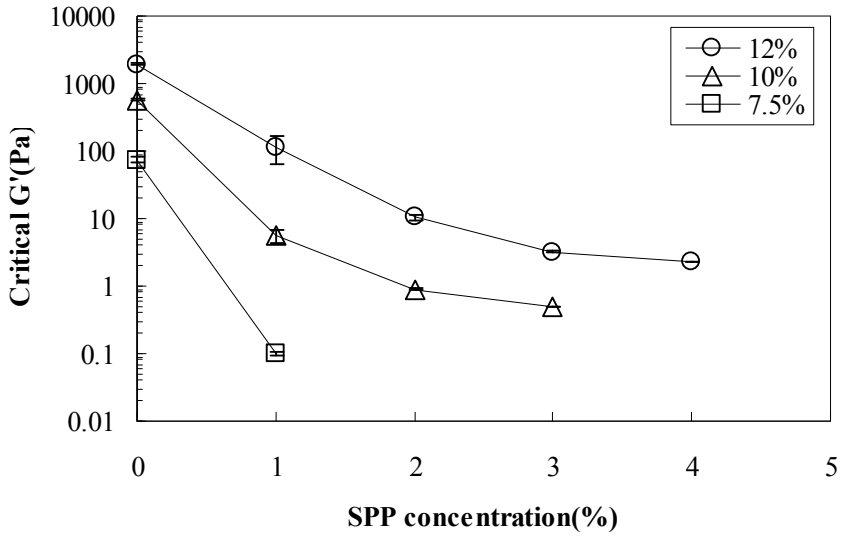

Figure 4.8 Critical storage modulus of 7.5, 10, and 12% bentonite suspensions with various SPP concentrations (0 to 4%) measured at zero resting time.

Figure 4.9 shows the variation of the phase angle in 12% bentonite suspensions with 0 to 4% SPP. At low SPP concentrations, the suspensions displayed solid-like behavior (the phase angles at small strains was below 45 º), but the suspensions became more liquid-like as the SPP concentrations increased (the phase angles at small strains was above 45 º). As shown in Figure 4.10, the critical strain increased with the SPP concentrations, but tended to converge with an excessive addition of SPP. The increasing trends with SPP addition are similar to what is observed in the diluted suspensions (5%); the critical strains tended to increase in the diluted suspensions.

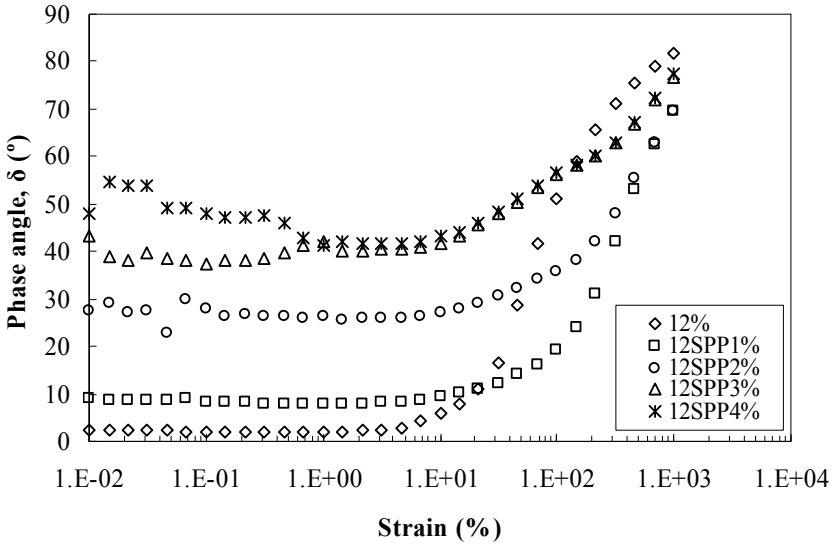

Figure 4.9 Critical storage modulus of 12% bentonite suspensions with various SPP concentrations (0 to 4%)

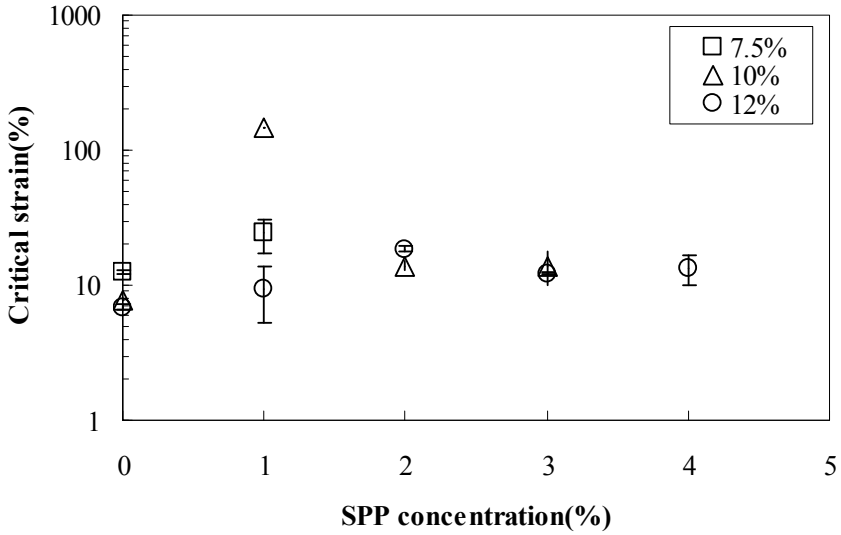

Figure 4.10 Critical strain of 7.5, 10, and 12% bentonite suspensions with various SPP concentrations (0 to 4%)

4.3. Time dependent behavior

4.3.1. Flow behavior

As previously stated, the advantage of SPP is that bentonite suspensions do not lose their thixotropic nature by the addition of SPP. The 3-D network keeps growing and is strengthened with time, changing the modified suspensions' flow behavior. Figure 4.11 and Figure 4.12 show the flow curves for the unmodified and modified 12% suspensions (3% of SPP) at different resting times. The unmodified suspensions clearly showed viscoelastic behavior even at the earlier times while the modified suspension displayed a transition from almost pure viscous to viscoelastic behavior as time elapses due to network buildup. The flow behavior of the modified suspensions was changed rapidly even at the short resting times (0.5 and 1 hour), showing viscoelastic behavior. This transition process is almost completed after 24 hours, resulting in the similar response to the unmodified suspensions. Beyond this time, the shear rates suddenly increase when the applied stress exceeds the yield stress rather than gradually increase with shear rate as shown at short resting times (0.5 and 1 hour). This implies that the flow resistance at rest condition beyond 24 hours becomes dominated by yield stress from this moment.

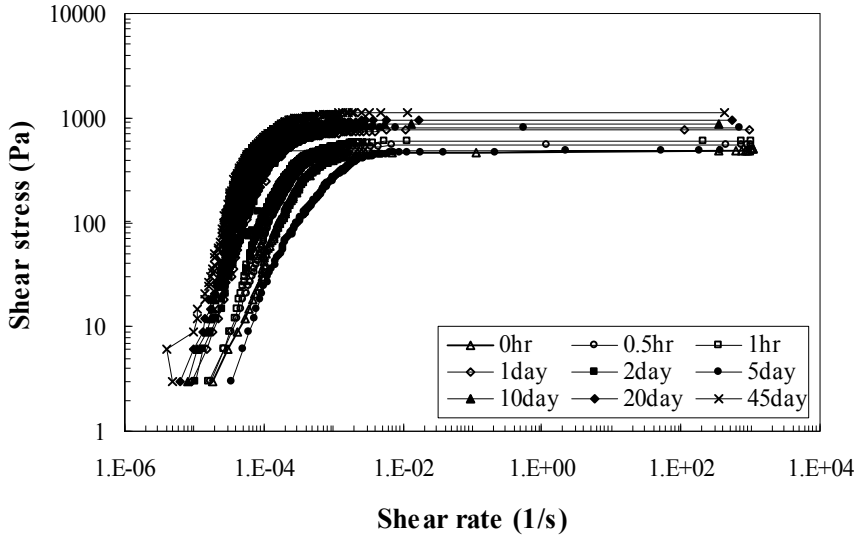

Figure 4.11 Flow curves for 12% suspensions at the resting time of 0 to 45 days

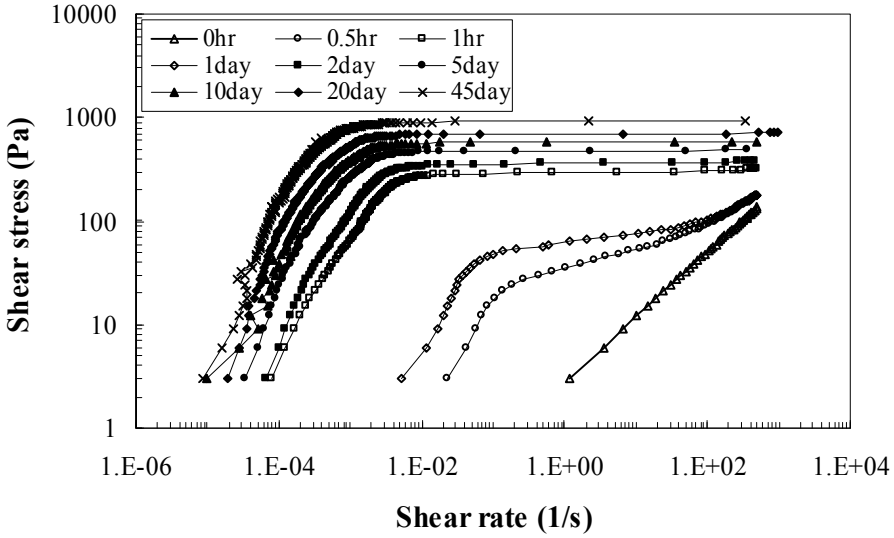

Figure 4.12 Flow curves for 12% modified with 3% SPP at the resting time of 0 to 45 days

4.3.2. Yield stress

This time dependent behavior of bentonite suspensions is more clearly shown by investigating the evolution of yield stress at different resting times; all suspensions were rested at least 3 months and some suspensions (7.5, 10, 12, 7.5 with 1% SPP, 10 with 2% SPP, and 12% with 3% SPP) were rested up to 1 year. Each of the data points shown on the plot is an average of measurements on at least three different suspensions. On average, the C.O.V. was 0.02 to 0.32, showing higher C.O.V. at short resting times. Figure 4.13 shows the increase in yield stresses of the unmodified 5, 7.5, 10, and 12% bentonite suspensions with time measured using the vane geometry. The yield stresses gradually increased from 3.4, 25.8, 135.6, and 457.1 Pa to 45.8, 175.4, 544.5, and 1292.7 Pa, respectively, after 3 months. After 3 months, it was observed that yield stresses at most of suspensions decreased, implying that sedimentation might have occurred (the details will be presented in section 4.4.4). All suspensions showed high increase in yield stress at short resting times, and then the increase in yield stress diminished as time elapses.

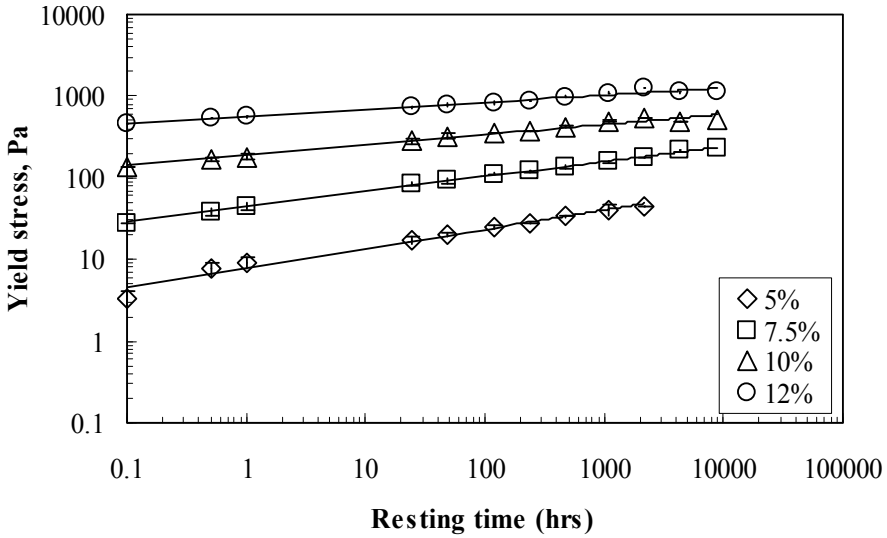

Figure 4.13 Time dependent buildup of yield stress of the bentonite fraction of 5, 7.5, 10 and 12% at the resting times from 0 to 1 year

Figure 4.14 (a), (b) and (c) depict yield stress of 7.5, 10 and 12% bentonite suspensions at various resting times and SPP concentrations. The yield stress of the modified suspensions increased with time, approaching yield stresses comparable to those of the unmodified bentonite suspensions. This implies that SPP only retards the formation of yield stresses in the unmodified bentonite suspensions by interrupting the formation of 3-D networks. The time required for the yield stress of the modified suspensions to catch up to those yield stress of the unmodified suspensions increased with an increase in SPP concentrations (i.e. 5 days for 1% SPP, 20 days for 2% SPP, and greater than 45 days for 3% SPP in 12%). However, yield stresses at low SPP concentrations exceeded those of the unmodified suspensions after a certain resting time. This phenomenon can be possibly explained with the hydrolysis of SPP (the details will be presented in section 4.4.5).

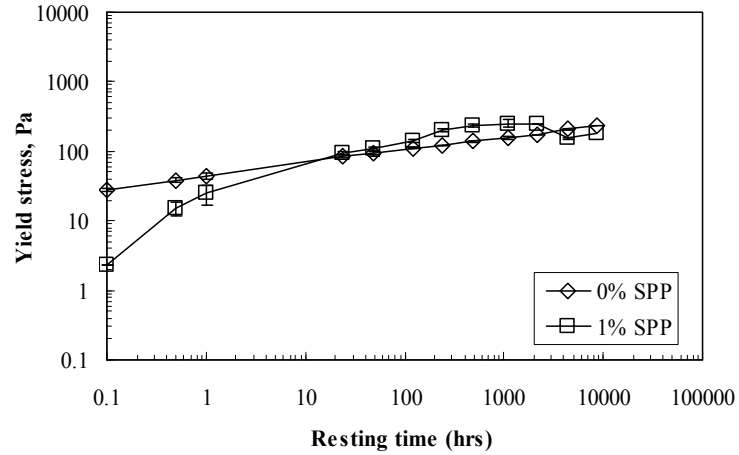

(a)

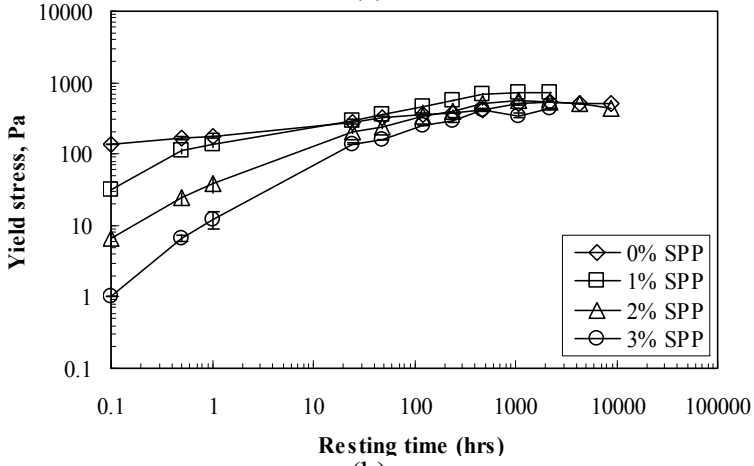

(b)

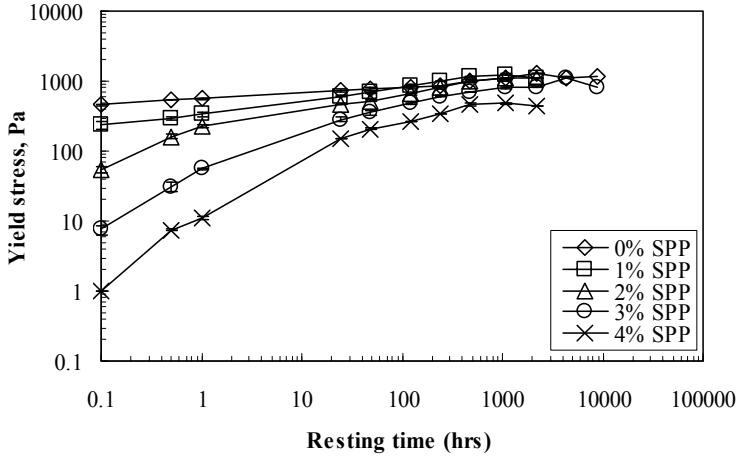

(c)

Figure 4.14 Yield stress evolution for (a) 7.5% suspensions with 0 and 1% SPP (b) 10% suspensions with 0 to 3% SPP and (c) 12% suspensions with 0 to 4% rested for 0 to 1 year

The amount of structure buildup varies with bentonite fraction and SPP concentration due to its effect on the Brownian motion of particles. Additionally, there is an effect from bentonite hydration at short resting times, but it was attempted to trace the change of microstructures from the mixing stage to a certain resting stage to simulate the field condition (permeation is performed right after mixing and not after hydrations times). The effect of hydration on yield stress measurements will be more discussed in 4.4.1.

4.3.3. Thixotropy ratio

Figure 4.15 displays the thixotropy ratio (the ratio of the yield stress at a given resting time to that at zero resting time) at each fraction. Although the yield stresses of the diluted suspensions were small, the thixotropy ratio was larger than those for the concentrated suspensions. This is because the Brownian motion of particles in the concentrated suspensions is constrained so the increase of yield stress with time is reduced compared to that of the diluted suspensions.

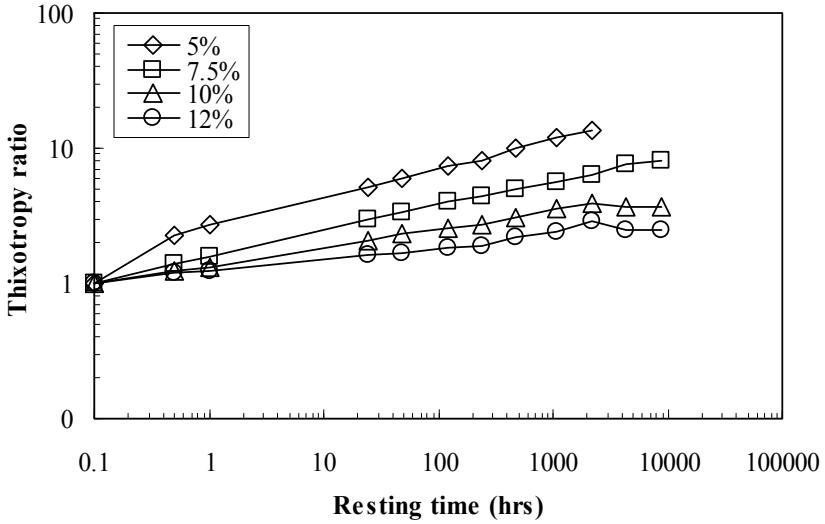

Figure 4.15 Thixotropy ratio for 5, 7.5, 10, and 12% suspensions at 0 to 1 year

Figure 4.16 (a), (b) and (c) show the variation of thixotropy ratio with time for 7.5, 10 and 12% bentonite suspensions with various SPP concentrations. While the absolute yield stresses were small in the modified suspensions, the thixotropy ratio becomes much larger with the addition of SPP due to the build-up of the inter-aggregate bonds. This behavior is similar to what was observed in the suspensions with low bentonite concentrations. Due to reduction of inter-aggregate bonds, Brownian motion in the modified suspensions increased, which then led to high thixotropy ratios.

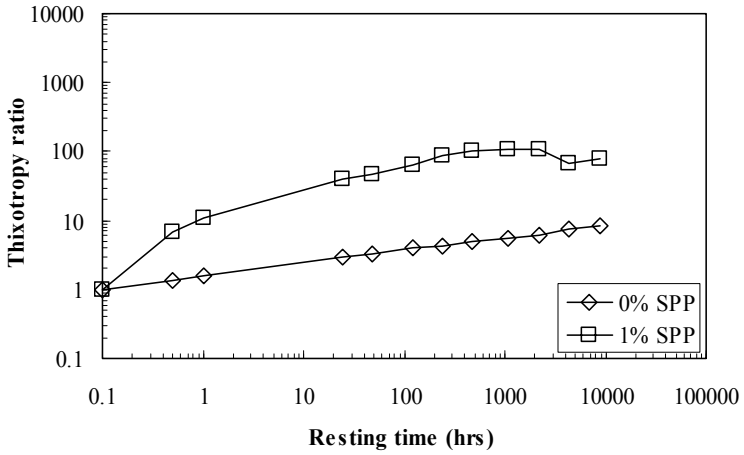

(a)

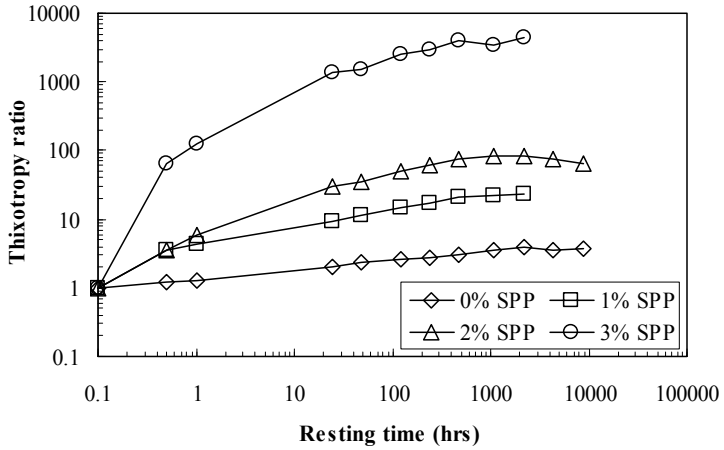

(b)

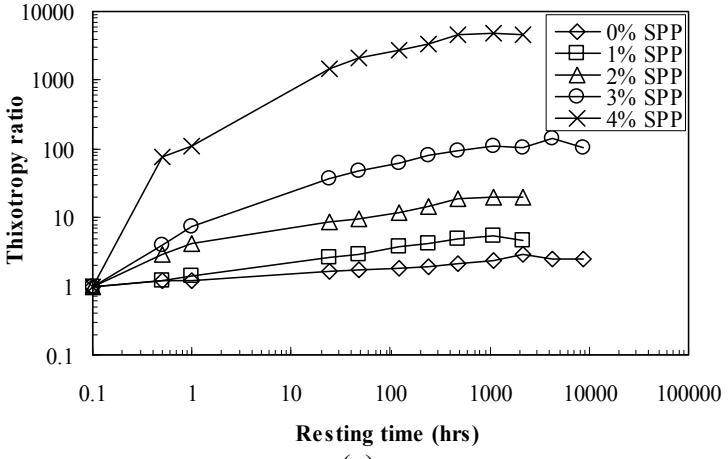

(c)

Figure 4.16 Thixotropy ratio for (a) 7.5% suspensions with 0 and 1% SPP (b) 10% suspensions with 0 to 3% SPP and (c) 12% suspensions with 0 to 4% rested for 0 to 1 year

4.3.4. Apparent viscosity

The time dependent response of the bentonite suspensions can be observed through the apparent viscosity measurements as well. The apparent viscosity of 12% bentonite suspension with 3% SPP at varying resting times is shown in Figure 4.17. The suspension displayed a pure viscous behavior immediately after mixing, followed by showing a viscoelastic behavior after resting. This suggests that the modified bentonite suspensions formed the 3-D network structures, resulting in the viscoelastic behavior similar to what was observed in the unmodified suspensions.

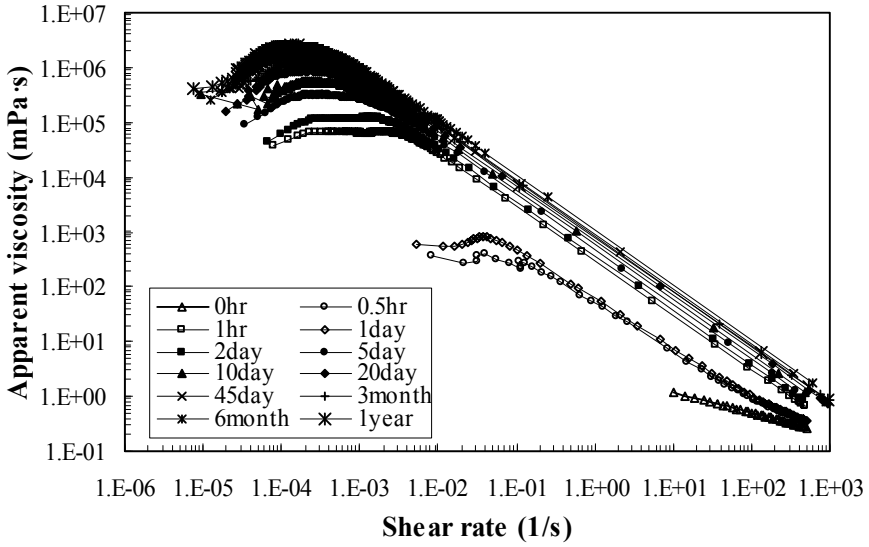

Figure 4.17 Time dependent change in apparent viscosity of 12% bentonite suspensions with 3% of SPP: 0 to 1 year

4.3.5. Characteristic recovery time

The rate of yield stress build-up is usually modeled with a constant parameter; this parameter can provide another way to investigate the time dependent response of the suspensions. Nguyen and Boger (1985) developed a structural model based on the first order chemical reaction to investigate the recovery of bauxite residue suspensions.

Heymann et al. (1996) proposed a similar model for build-up of yield stress in newsprint ink after shearing. Moreover, Leong (1988) proposed a structural recovery model (equation 4.1) for brown coal suspensions based on the Smoluchowski coagulation theory. In this study, the Leong (1988) model was selected to investigate the effect of SPP on the rate of the yield stress build-up. This model was chosen because the model (1) is based on microstructure in suspensions, (2) has been validated with Na-montmorillonite-based clay suspensions (de Krester and Boger, 2001), and (3) utilizes one simple parameter which can be useful to investigate the rate of the yield stress build-up. However, this model does not capture the increase in yield stresses at a short resting time since it utilizes the second order kinetics, and the predicted values were found to be less accurate at long resting times because $\tau_{y,\infty}$ used in the model should be obtained at a finite time (de Krester and Boger, 2001).

$$\tau_y(t) = \tau_y^{\infty}\left(1 - \frac{1 - \left(\frac{\tau_y^{\infty}}{\tau_y^{0}}\right)^{3/2}}{1 + K_r t}\right)^{2/3} \tag{4.1}$$

Where $\tau_y(t)$ is the yield stress at time t, τ_y^{∞} is the yield stress at time $t\rightarrow\infty$, τ_y^{o} is the yield stress at time t=0, and K_r is the recovery rate constant (1/time). Because the regression analyses utilized by de Krester and Boger (2001) produced significant errors in evaluation of $\tau_{y,}^{\infty}$ due to highly non-linear relationship between $1/\tau_y$ and 1/t, the yield stresses at long resting times could not be fully captured. Instead of this method, a root mean square error method was utilized to match the experimental data to the model in this study. $\tau_{y,}^{\infty}$ was also calculated as an unknown value (along with the recovery rate parameter, Kr) to investigate the discrepancy of $\tau_{y,}^{\infty}$ and yield stresses at long resting times. Figure 4.18 (a), (b), and (c) show comparison of the model with experimental

data of 7.5%, 10%, and 12% suspensions with 0 to 3% of SPP. While the model could capture the overall behavior well, there were still discrepancies at short resting times due to the limitation of the Leong (1988) model mentioned above.

Table 4.1 summarizes the recovery rate parameter (K_r), the predicted yield stresses at infinite time ($\tau_{y,\infty}$), and the ratio between the predicted yield stresses at infinite time and the measured yield stresses at 45 days obtained from this analysis. 45 days was considered an infinite time since it produced the small enough value of 1/t (approximately 6×10^{-6}/min) without showing a sedimentation effect; sedimentations result in a decrease in yield stress with time. The recovery rate increased as bentonite concentration increased since the diluted suspensions have high Brownian motion due to lower initial inter-aggregate bonds than the concentrated suspensions, resulting in lower build-up rate than the concentrated suspensions. However, the particle motion produces high thixotropy ratios. De Krester and Boger (2001) observed similar results in Na-montmorillonite based suspensions. Increasing the SPP concentration for a given suspension resulted in increasing the characteristic recovery time ($1/K_r$); this was expected due to lower initial inter-aggregate bonds that will require longer times to build up the 3-D networks. Furthermore, the measured yield stresses at 45 days were close enough (standard deviations of 0.1) to the predicted yield stress at the time (considered as yield stress at infinite time).

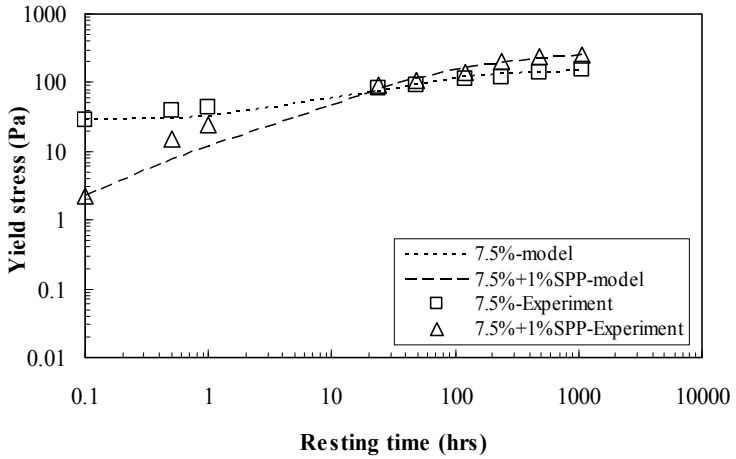

(a)

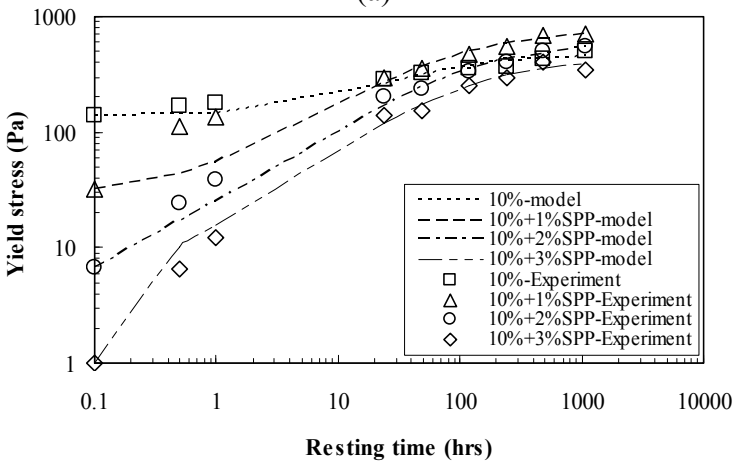

(b)

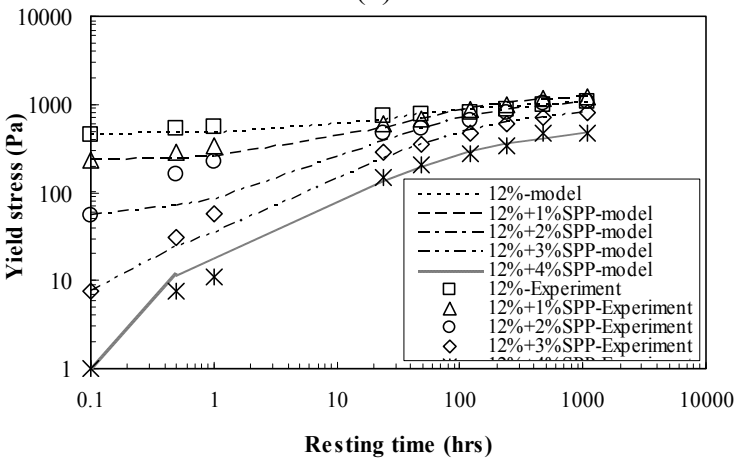

(c)

Figure 4.18 Leong model fitted with experimental data: (a) 7.5 (0 and 1%), (b) 10 (0, 1, 2 and 3%), and (c) 12 (0, 1, 2, 3 and 4%) bentonite suspensions.

Table 4.1 Recovery rate constant (Kr), predicted yield stresses at infinite time and ratios between measured (M) at 45 days and predicted (P) yield stresses

Parameters		Kr (1/hr)				Predicted $\tau_{y,\infty}$ (Pa)				P ($\tau_{y,\infty}$)/M ($\tau_{y\ at\ 45days}$)			
Suspension concentration (%)		5	7.5	10	12	5	7.5	10	12	5	7.5	10	12
SPP concentration (%)	0	0.011	0.018	0.019	0.020	38	148	459	1024	0.94	0.95	0.92	0.94
	1	N/A	0.009	0.012	0.013	N/A	257	708	1225	N/A	1.02	1.00	0.99
	2	N/A	N/A	0.009	0.011	N/A	N/A	550	1071	N/A	N/A	1.00	0.99
	3	N/A	N/A	0.007	0.008	N/A	N/A	438	876	N/A	N/A	0.97	0.97
	4	N/A	N/A	N/A	0.007	N/A	N/A	N/A	495	N/A	N/A	N/A	1.03

4.3.6. Critical modulus, critical strain and phase angle

As shown in Figure 4.6, the critical storage modulus increased with the increase of bentonite fraction similar to yield stress. This is because the stiffness of bentonite suspensions is also controlled by the 3-D network in bentonite suspensions. Figure 4.19 depicts the time dependent growth of critical storage modulus at 5, 7.5, 10 and 12% suspensions. The critical storage modulus increased from 3.1, 73.9, 571.5, and 1965 to 52.3, 423.5, 1770, and 5460 Pa, respectively, after 20 days. Similarly, critical storage modulus of the modified suspensions increased with time as shown in Figure 4.20. However, the critical storage modulus of the modified suspensions did not exceed those of the unmodified suspensions indicating that it requires much more time for the critical storage modulus to catch up to those of the unmodified suspensions. As time elapses, the modified bentonite suspensions became stiffer and stronger, showing a gel-like behavior.

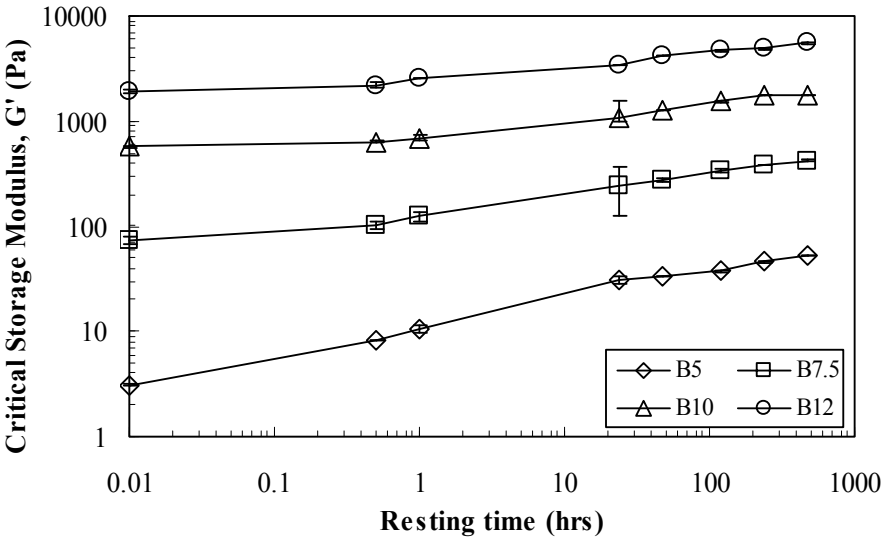

Figure 4.19 Critical storage modulus of 5, 7.5, 10, and 12% suspensions (0 to 20days)

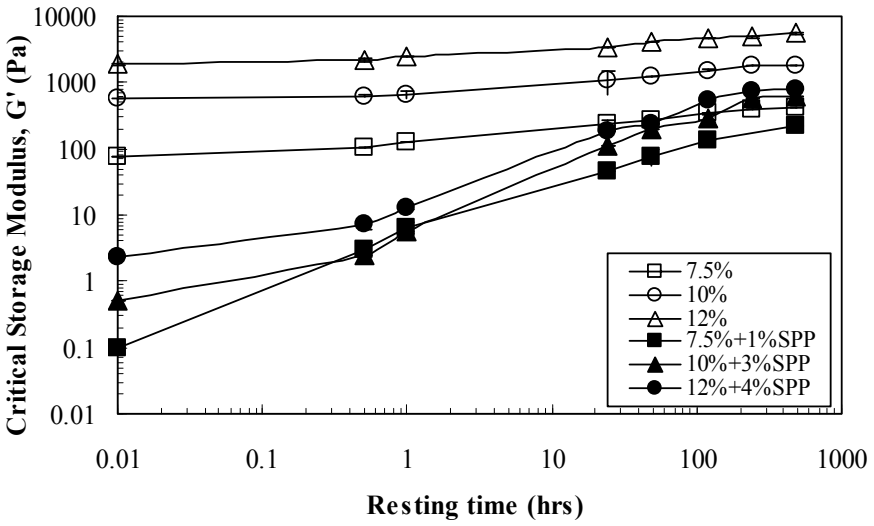

Figure 4.20 Critical storage modulus of the bentonite concentrations of 7.5, 10 and 12% modified with 1, 3 and 4% SPP (0 to 20days)

Figure 4.21 shows the phase transition of the 12% bentonite suspensions modified with 4% SPP from the initial mixing to the resting time of 20 days. The initially liquefied bentonite suspensions (δ>45 º) were gradually transformed into a gel-like material which have the phase angle less than 45 degrees. The phase transition caused a

reduction in elastic range (critical strains) of the suspensions as shown in Figure 4.22. The critical strains initially increased significantly, with the addition of SPP, followed by gradual converging with the unmodified suspensions after 24 hours. However, a large scatters were found at short resting time possibly due to hydration and random orientation of bentonite particles.

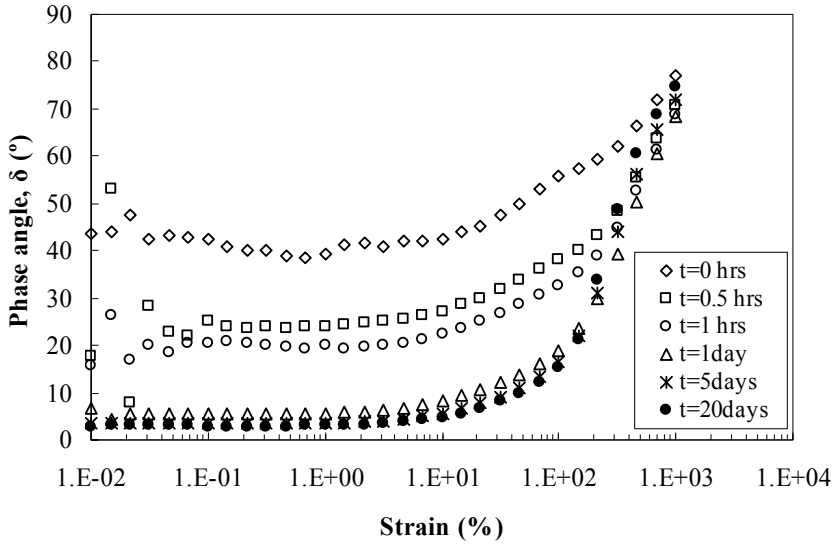

Figure 4.21 Variation in phase angle at 12% suspensions modified with 4% SPP

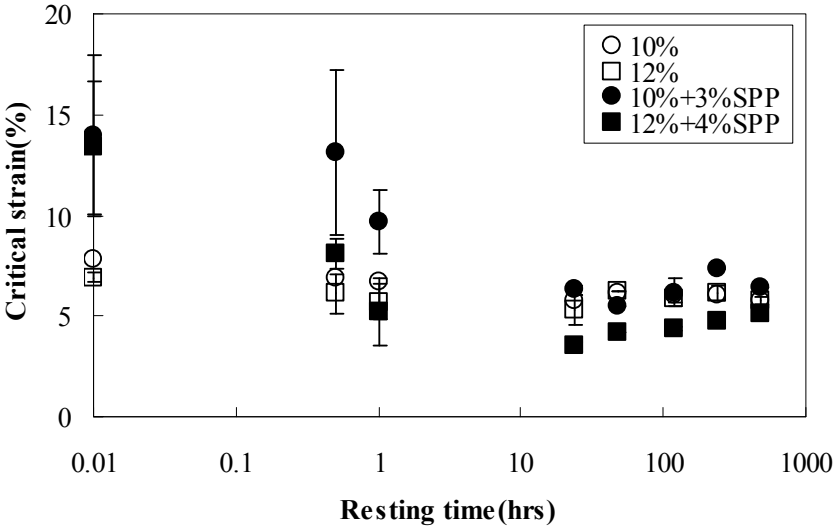

Figure 4.22 Variation in critical strain at 10 and 12% suspensions modified with 3 and 4% SPP

4.3.7. Relationship between yield stress and critical storage modulus

As shown previously, both yield stress and critical storage modulus vary with particle fractions and time in a similar way so that an attempt was made to correlate both parameters to each other. Figure 4.23 shows the relationship between yield stress and critical storage modulus of the unmodified suspensions at various resting times. As can be seen, yield stress increased with an increase in critical storage modulus without showing any time dependent variations. The increase of resting times only caused an increase of yield stress and critical storage modulus while maintaining the same correlation between the two parameters. Based on this observation, regression analysis was performed with the modified and unmodified suspensions. Figure 4.24 displays the relationship between critical storage modulus and yield stress on both the modified and unmodified suspensions. Yield stress and critical modulus in both cases showed strong relationships. Especially, the modified suspensions exhibited a unique relationship regardless of the percentage of SPP. The relationship may be beneficial in that 1) results from drag shear tests can be correlated to those from the oscillatory tests in laboratory, and 2) if permeation grouting is performed for mitigating seismic hazards such as liquefaction, the time dependent measurement of yield stress will provide information of the stiffness as well, reducing the number of tests required to obtain both parameters.

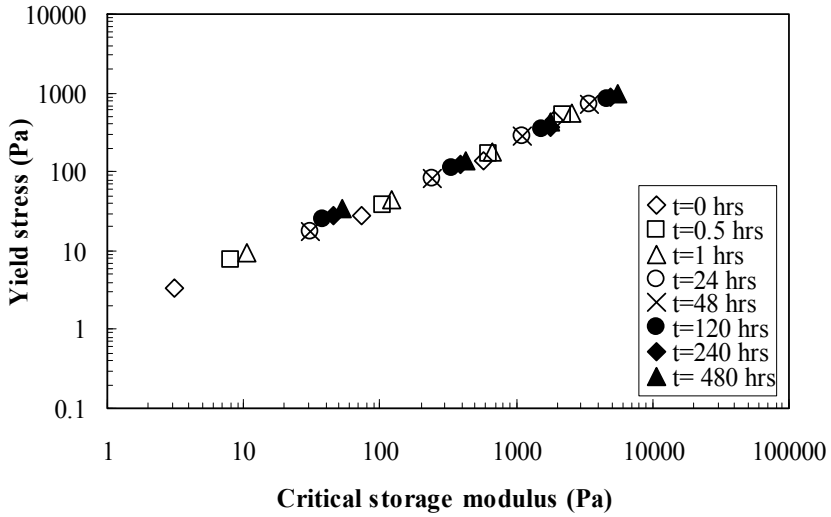

Figure 4.23 Comparison of yield stress and critical storage modulus at various resting times

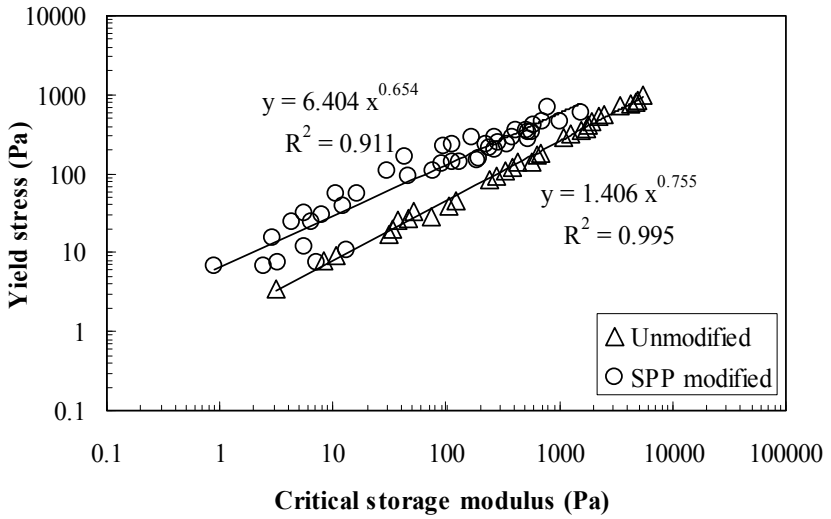

Figure 4.24 Relationship between yield stress and critical storage modulus of the unmodified and modified suspensions

4.4. Parameters affecting time dependent rheological experiments

4.4.1. Hydration

Hydration time of bentonite greatly affects flow behavior of bentonite suspensions, and it is important in the proposed application since the modified suspensions are determined based on two criteria: 1) significant reduction in the initial flow properties and 2) fast recovery of the reduced properties, especially yield stress. Although the high shear mixing somewhat enhances the hydration of bentonite particles (i.e. the fresh bentonite suspensions in this section actually means partially hydrated bentonite suspensions), it is well known that the hydration of bentonite particles is a time -dependent phenomenon which typically requires 16 to 24 hours. Due to the fact, yield stress at short resting times rapidly increases as presented in the section 4.3.2. However, Nguyen and Boger (1985) also observed similar trends with bauxite residue suspensions, for which they measured the recovery of yield stress from the equilibrium condition (>20 hours mixing). This implies that the initial rapid increase in yield stress is affected by not only the hydration of bentonite particles, but also Brownian motion; as time elapses, Brownian motion of particles become constrained due to developed network structures.

Without the addition of SPP, yield stress of bentonite suspensions increases with time (at rest condition) and decreases (at preshearing condition) until hydration stops. For at-rest condition, bentonite suspensions were rested for a given period of time (0 to 48 hours) without shearing before being tested. For preshearing condition, the bentonite suspensions were rested for 24 hours without shearing, and then a high shear rate of 500 s^{-1} was applied for 1 min prior to measurements to provide similar condition as high shear mixing. Finally, the presheared suspensions were rested in the rheometer for a designated period of time (0 to 48 hours).

Figure 4.25 shows thixotropy ratio of 7.5% bentonite suspensions at fresh (partially hydrated) and hydrated condition. The yield stresses of hydrated suspensions were slightly smaller after the hydration period of 24 hours as compared to those of fresh suspensions. Moreover, thixotropy ratios of hydrated suspensions were slightly lower than those of unhydrated suspensions, indicating that the recovery is also affected by hydration.

After mixing, particles approach each other under the influence of Brownian motion to building up the 3-D network structure with time. However, the adsorption of water molecules between the interlayer of clay pallets causes swelling of bentonite (Luckham and Rossi, 1999), producing higher repulsive forces and a weak structure is formed by delaminated pallets. This weak structure is easy to be separated under shearing, and thus, reducing the yield stress under preshearing condition. The degree of separation in bentonite particles depends highly on the amount of cations in bentonite, especially calcium ions. The more calcium the bentonite includes, the less separation occurs (Madsen and Müller-Vonmoos, 1989).

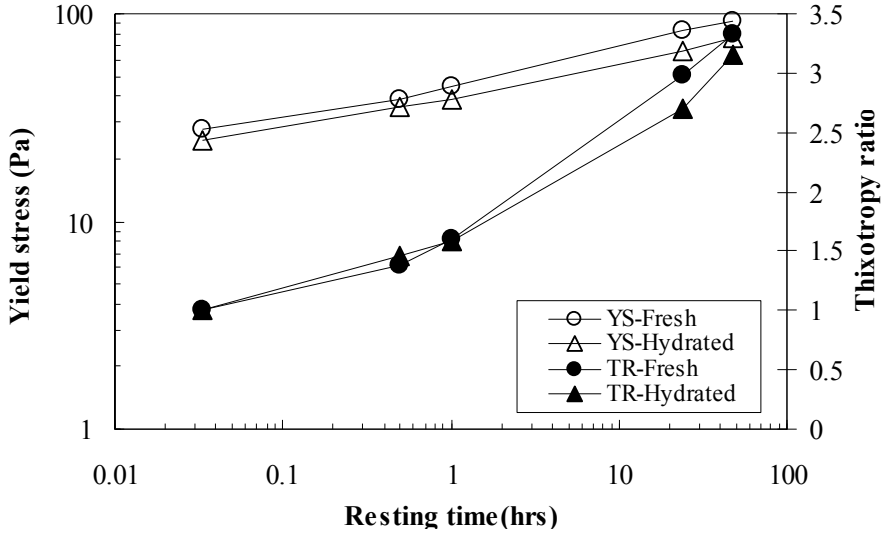

Figure 4.25 Yield stress and thixotropy ratio of hydrated and unhydrated 7.5% bentonite suspensions at various resting times (0 to 48 hours)

4.4.2. Mixing procedure

In this study, 5% SPP solution was mixed with bentonite and water without any resting periods for immediate application of bentonite grouts in field. However, the mixing procedure can greatly affect the rheological properties of the bentonite suspension. Especially, the mixing sequence of SPP significantly changes the yield stress buildup in the bentonite suspensions.

Figure 4.26 shows the yield stresses from two different mixing methods for 7.5% bentonite suspensions modified with 1% SPP: 1) mix 5% SPP solution with bentonite and water, and 2) mix 5% SPP solution with prehydrated (24 hours) bentonite suspensions. The initial yield stresses were very similar in both methods; however, the increase in yield stress was significantly less with time in the latter method, which is not desirable for the proposed application. When SPP is added during fresh mixing, bentonite particles are dispersed due to the adsorption of phosphate ions on the edge, but they still tend to be associated since the calcium ions continue exerting an electrostatic attraction. The addition of SPP after hydration strongly increases repulsive force between the separate pallets under the attractive force, which is weakened as hydration proceeds, resulting in low yield stresses.

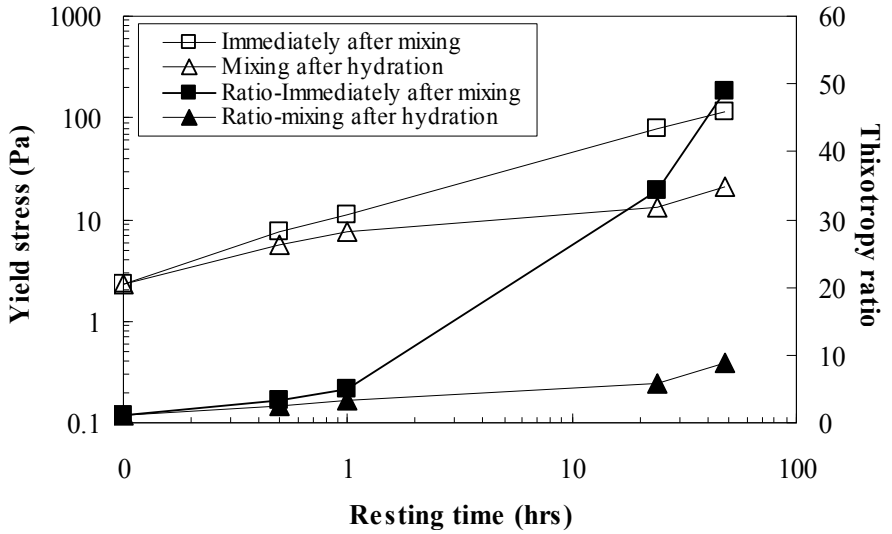

Figure 4.26 Yield stress and thixotropy ratio at various resting times (0 to 48 hours) with two different mixing methods:1) immediate mixing and 2) mixing SPP with hydrated bentonite suspensions

4.4.3. pH

Previous researches showed that the flow behavior of the bentonite suspensions is highly dependent on the pH conditions since the 3-D network could be greatly affected by them (Brandendurg and Lagaly, 1988; Abend and Lagaly, 2000; Laribi et al., 2006; Kelissidis et al., 2007). SPP changes the pH of water depending on the SPP concentrations by producing negatively charged anions. As shown in Chapter 3, the pH of deionized water increased from 6 to 9.5 when adding SPP to create a 5% solution, indicating that the addition of SPP may change pH in bentonite suspensions. In addition, it is well known that the pH evolves with time during hydration of bentonite particles. However, Kelessidis et al. (2007) reported that the pH values of the concentrated bentonite suspensions (6.42% by weight) beyond the natural pH (approximately 9.0) was rapidly adjusted (within 10-15 min) so that there was little difference of pH values between the moment of mixing and full hydration (16 hours). In addition, Clarke (2008) reported that the pH of the SPP modified suspensions did not

significantly vary with the resting times and SPP concentrations. Therefore, all pH measurements were conducted at the moment of mixing with 15 min of stabilizing time.

Figure 4.27 shows the variation of pH in the modified suspensions. Similar to the unmodified suspensions (the average of 9.33, the standard deviation of 0.21 and C.O.V. of 0.02 from the total 11 samples), the pH values of the modified suspensions showed a consistent alkalinity with the average pH value of 9.35, the standard deviation of 0.28 and C.O.V. of 0.03 (total 33 samples). Therefore, it was concluded that rheological behaviors in this study is not significantly affected by an alteration of microstructures due to pH variations.

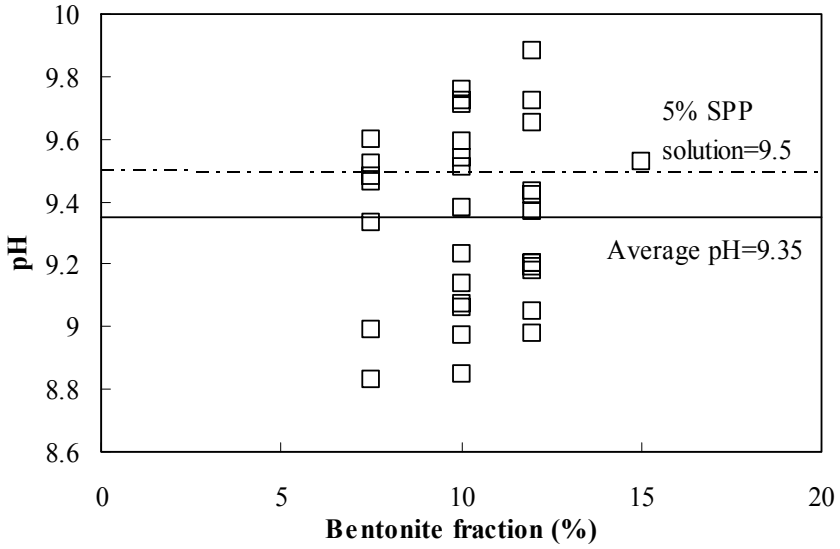

Figure 4.27 pH variation of modified suspensions at different bentonite fractions

4.4.4. Sedimentation

Since all yield stress measurements were performed over a long time period, sedimentation of bentonite particles was a concern. To investigate the sedimentation, the bentonite fraction in the suspensions at the bottom of the storage cups was measured

after 45, 90 and 180 days by taking a portion of suspensions at the bottom of the storage cup and drying it out. Before that, visual inspection was conducted, resulting in no distinct sedimentation in all suspensions. Figure 4.28 Sedimentation of bentonite suspensions at long resting timesshows the comparison of the measured bentonite fraction after different resting times versus the bentonite fraction measured immediately after mixing. The measured bentonite fraction at the bottom increased with time, and the difference between the measured and target values were within 10%. For the samples showing the extremely high bentonite fraction (Figure 4.28), it was observed that the cover mineral oil penetrated into the suspensions, allowing the sample to be dried out. The data was not used for any analysis in this study. This implies that sedimentation of bentonite particles at long resting times may contributed to the drop of yield stress and viscosity. However, the relatively small variation in both values was because large fraction of bentonite particles formed 3-D network that is enough to fill the entire volume of suspensions and prevent free settlement of individual particles. Some samples displayed an increase in yield stress and bentonite fraction due to evaporation.

Abend and Legaly (2000) reported that the montmorillonite suspensions having low fraction of particles at high ionic strength showed sedimentation (by visual inspection) and the storage modulus and reversible compliance becomes zero. In addition, apparent viscosity reduced significantly. However, montmorillonite suspensions having high fraction of particles (>3%) maintained a characteristic gel properties at high ionic strength.

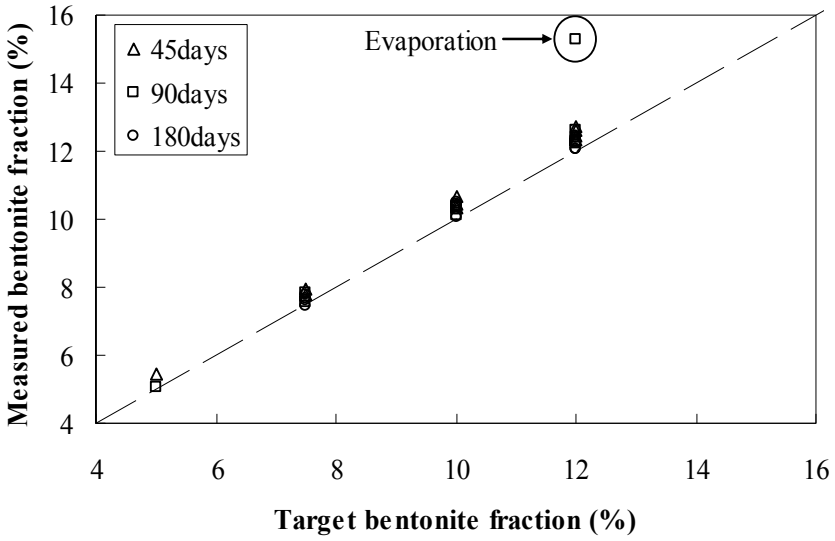

Figure 4.28 Sedimentation of bentonite suspensions at long resting times

4.4.5. Hydrolysis (mixing water effect)

The time dependant behavior of the modified suspensions is possibly affected by the hydrolysis of SPP. Due to the hydrolysis of SPP in bentonite suspensions, the cation exchange capacity increases due to partial replacement of Ca^{2+} and/or Mg^{2+} by Na^{+}, increasing cation concentration in suspensions (Michaels, 1958). Once two particles closely approach each other, the increased cations reduce the thickness of the diffuse layer, increasing the attraction at edge (-) to edge (-) and edge (-) to face (-) (Brandenburg and Lagaly, 1988). This causes a faster buildup of network compared to pure bentonite suspensions and strengthens the bonds between particles. The effect of the increased cations is more pronounced at the diluted suspensions and low percentage of SPP as shown in Figure 4.14 (a), (b) and (c).

The results imply that the time dependent rheological behavior of the bentonite suspensions significantly changed if cations are introduced from external sources such as the use of mixing water including cations. Since the utilization of deionized water for

suspensions mixing is limited in the field, the hydrolysis of SPP is affected by cations included in tap water, changing rheological properties of the bentonite suspensions.

Figure 4.29 shows comparison of yield stresses from the modified suspensions mixed with two different types of water: de-ionized and tap water. The suspensions were rested from 0 to 48 hours. As can be seen, the tap water produced similar small yield stresses at initial mixing compared to de-ionized water; however, the yield stresses of suspensions with tap water became higher yield as time elapses. The effect was not significant at the suspensions having high bentonite fractions since the particles are under strong attraction forces. This implies that the utilization of tap water in the field may not significantly affect the permeation stage, but will increase the post grouting stability especially when diluted suspensions are utilized.

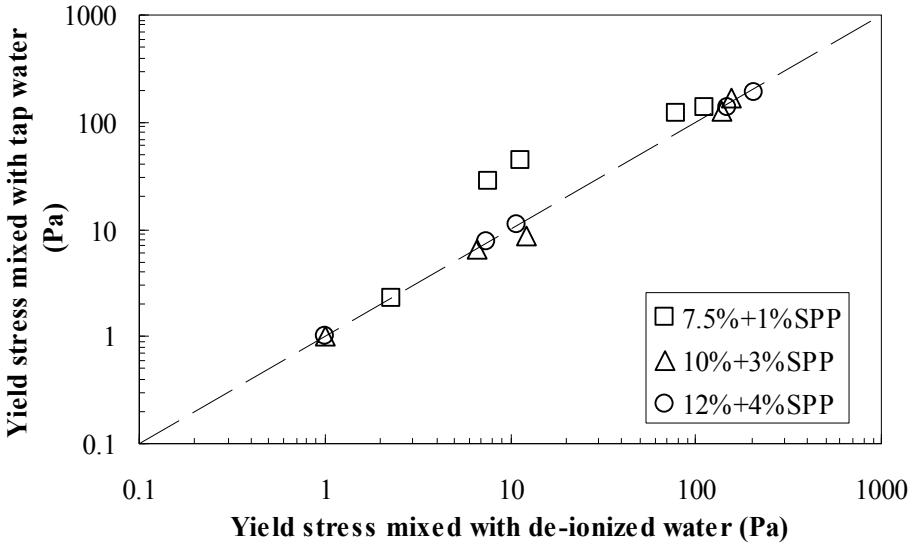

Figure 4.29 Comparison of yield stress in the modified suspensions mixed with two different types of water: deionized and tap water

4.4.6. Structural kinetics

Since parameters such as yield stress and storage modulus are a function of 3-D network structures in the suspensions, an Environmental Scanning Electron Microscope (ESEM) study was conducted with the unmodified 7.5% suspensions and 7.5% modified with 1% SPP to explain various flow behavior of bentonite grouts at different time scales.

Figure 4.30-Figure 4.32 display SEM pictures of the unmodified 7.5% suspensions at 2, 20 and 216 hours after mixing. At the very short resting time, there exists a residual 3-D network structures mainly consisted of edge to edge association, but it still has edge to face association. However, the bentonite particles swell as hydration of bentonite particles proceeds, resulting in more complex structures dominated edge to face association. Since the swelling pressure separates the clay particles, more delaminated particles are observed in the later pictures. This structure is similar to what was observed by Kelessidis et al. (2007) at similar alkaline condition (pH=9.1) and bentonite fraction (=6.42%).

This structure supports the adsorption of phosphate anions at the edge sites of bentonite particles in alkaline medium, despite of the presence of the negatively charged edges by the adsorption of OH^- and the relatively small area. This may be possibly explained with the presence of a considerable portion of the exchangeable cations formed by the spilled double layer into the edges (Abend and Lagaly 2000; Tombácz and Szekeres, 2004). Moreover, Goh et al. (2011) reported that yield stress of 7% (wt/wt) bentonite suspensions increases with an increase of the squared value of zeta potential at alkaline pH levels. This was attributed to the existence of positive-negative charge attraction between the bentonite particles, which forms edge to face associations. With a longer resting time, the bentonite particles are associated under the influence of Ca^{2+}, forming a large volume of stronger structures.

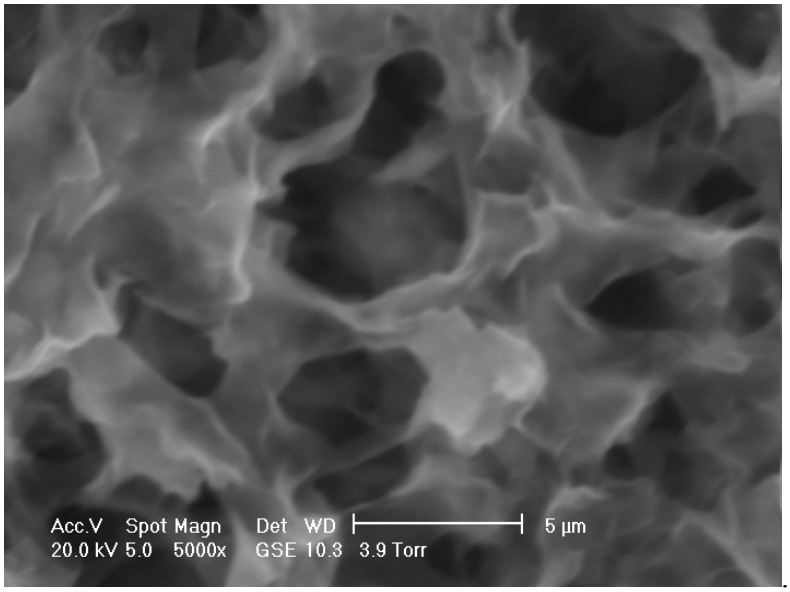

Figure 4.30 Unmodified 7.5% bentonite suspensions after 2 hours

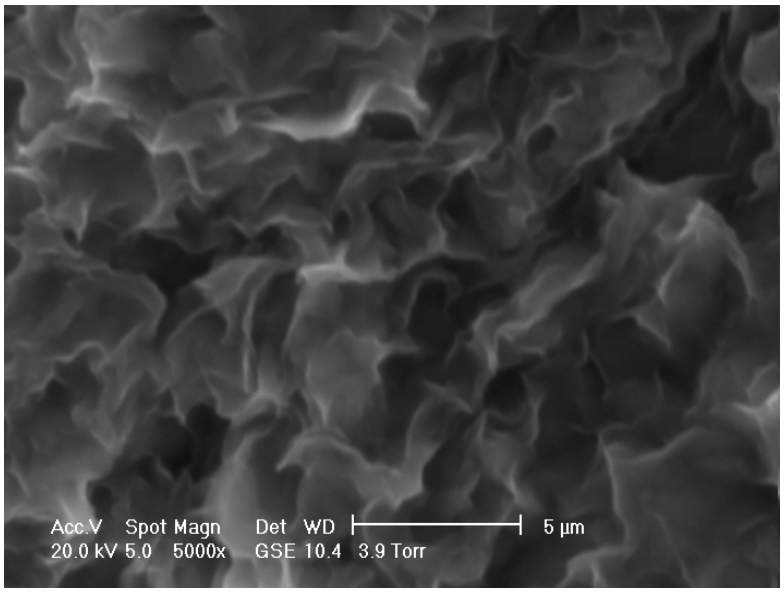

Figure 4.31 Unmodified 7.5% bentonite suspensions after 20 hours

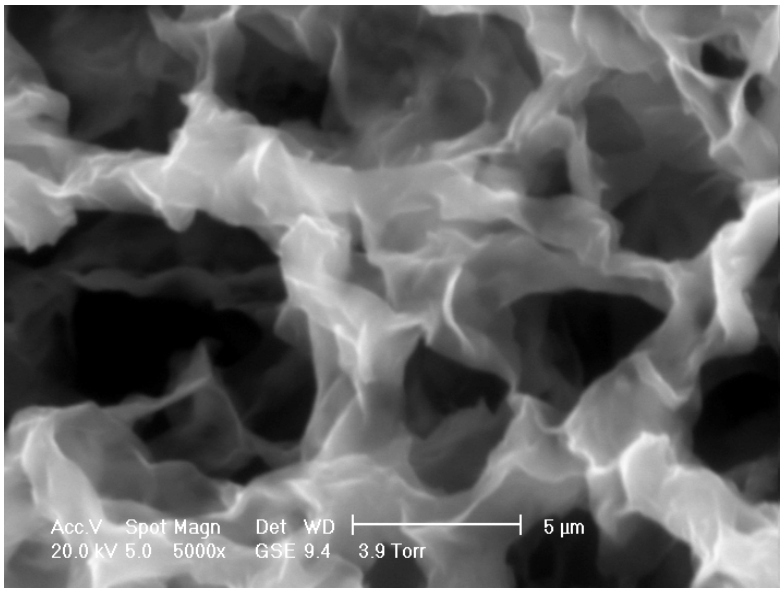

Figure 4.32 Unmodified 7.5% bentonite suspensions after 216 hours

On the other hand, the addition of SPP disrupts the formation of the inter-aggregate bonds, reducing the yield stress and viscosity of the suspensions. Figure 4.33, Figure 4.34 Modified 7.5% bentonite suspensions with 1% SPP after 20 hoursand Figure 4.35 show 7.5% bentonite suspensions modified with 1% SPP at 2, 20 and 216 hours after mixing. As shown in Figure 4.33, the adsorption of phosphates ions on the edge of bentonite particles (either by the attachment of phosphate ions to the edges or their adsorption at the edges by exchanging structural OH^- groups of bentonite particles) increases negative edge charge and repulsion between particles, resulting in decreased attractive edge (-) and face (-) (EF) contacts. The increased negative charge and repulsion between particles result in reduced yield stress and viscosity of bentonite suspensions by retarding a formation of 3-D network (Abend and Lagaly, 2000 and Penner and Lagaly, 2001). However, yield stress and viscosity increase with time due to build-up of the bonds as particles assume their positions of minimum free energy under Brownian motion, producing face (-) to face (-)association as shown in Figure 4.34 and

Figure 4.35. The modified suspension displayed a band like network consisting of FF associations, which produced large flakes and stronger gels (Norrish, 1954; Callaghan and Ottewill, 1974; Duran et al., 2000; Tombácz and Szekeres, 2004). Suspensions with a low degree of inter-aggregate bonds, such as those having low bentonite concentration or high percentages of SPP, take more time to establish their 3-D network structures due to a high degree of Brownian motion.

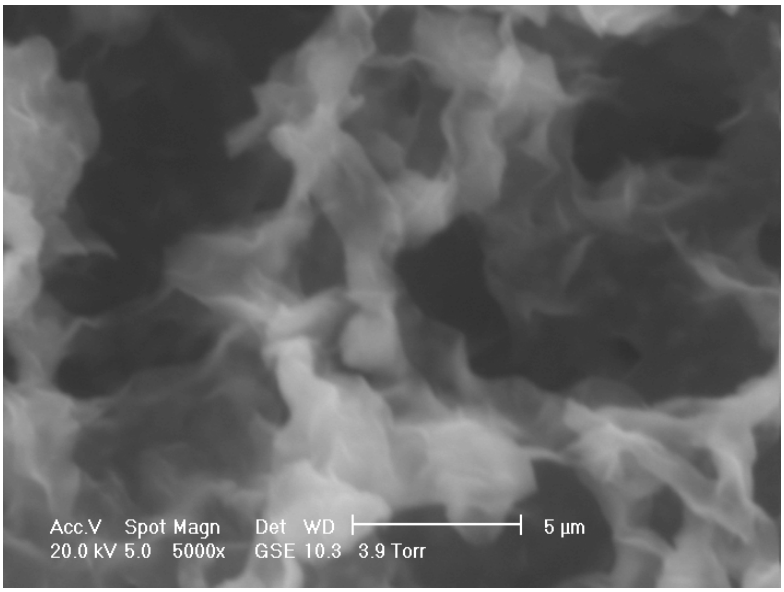

Figure 4.33 Modified 7.5% bentonite suspensions with 1% SPP after 2 hours

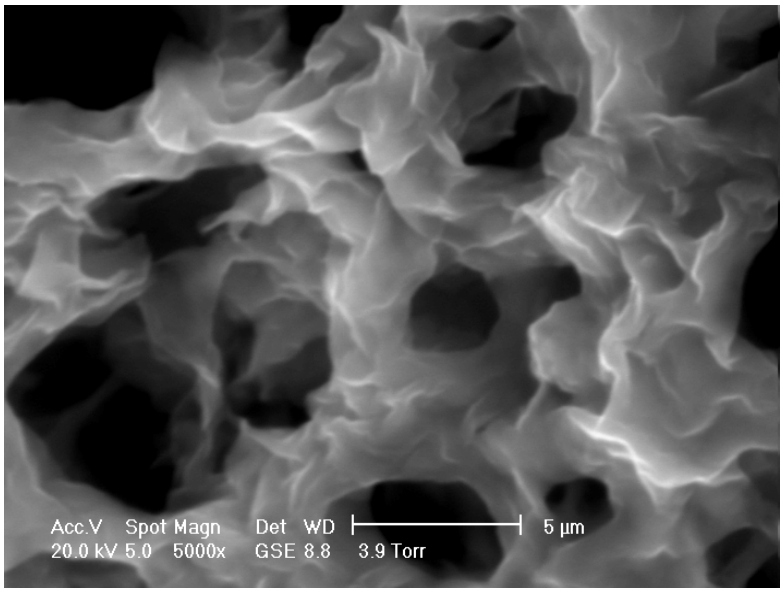

Figure 4.34 Modified 7.5% bentonite suspensions with 1% SPP after 20 hours

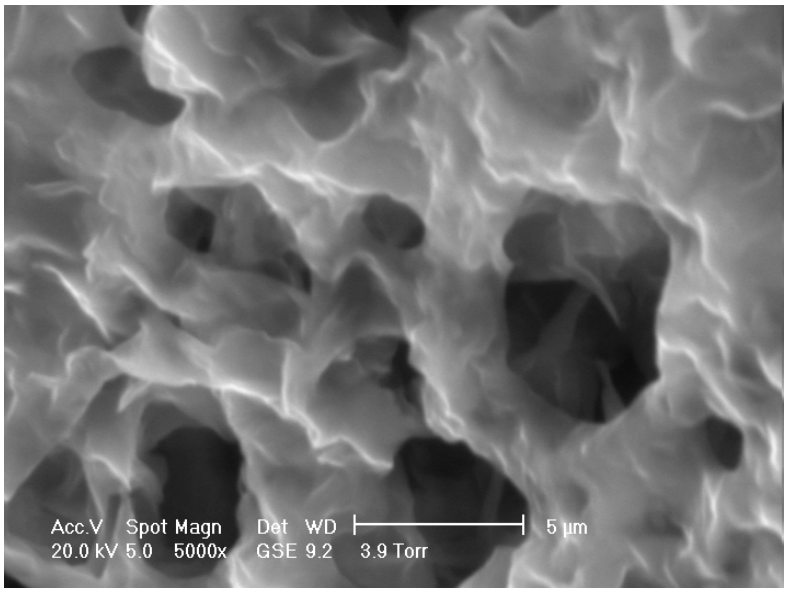

Figure 4.35 Modified 7.5% bentonite suspensions with 1% SPP after 216 hours

4.4.7. Chemical composition of bentonite

In this study, two batches of raw bentonite were obtained from the same company (CETCO, CP-200), but it was found that the rheological properties of two bentonite

suspensions are significantly different, especially the time-dependent behavior. Figure 4.36 shows yield stress evolution of 7.5, 10 and 12% modified with 1, 3 and 4% SPP at the resting time of 0 to 5 days. For the comparison, all bentonite was sieved with a No. 200 sieve and labeled as "Old" and "New". The "Old" bentonite was the material used through this study and "New" is the bentonite obtained at the end of this study. As can be seen, the "Old" bentonite showed higher time dependent increase compared to the "New" bentonite. The discrepancy was more pronounced in the diluted suspensions (7.5%) compared to the concentrated ones (10 and 12%). Moreover, little increase was observed in yield stress of modified 7.5% suspensions.

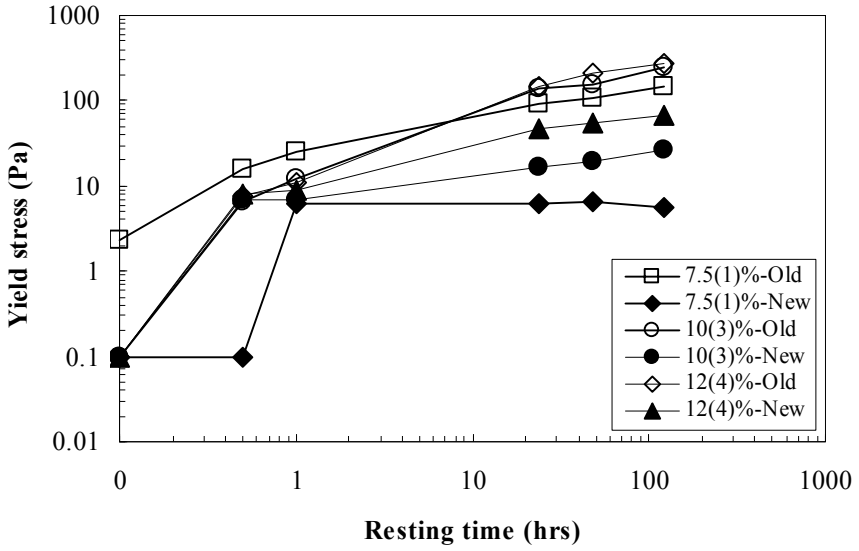

Figure 4.36 Yield stress with time at various modified suspensions (Old and New)

In order to explain the different rheological behavior, a series of index tests (XRD, Atterberg limit, CEC, and hydrometer) were performed. Table 4.2 presents a comparison of index test results between the two types of bentonite. Both of the bentonite showed similar particle sizes and the "New" bentonite produced slightly lower

plasticity. However, most of index properties did not show any significant difference. EDX tests were performed on both bentonites to identify chemical compositions. Table 4.3 summarizes a comparison of EDX results of two types of bentonite. As can be seen, most of the chemical components were similar in both bentonites, except for Ca^{2+}. The "New" bentonite included less Ca^{2+} (approximately 1/5) than the "Old" bentonite.

These results confirmed that the rheological behavior of the bentonite suspensions is highly dependent on the chemical composition of bentonite. It is well known that Na^{+} montmorillonite shows higher time dependent increase in yield stress compared to Ca^{2+} montmorillonite; this is generally attributed to the more constrained Brownian motion of particles in Ca^{2+} montmorillonite than in Na^{+} montmorillonite due to the strong attractive forces between particles (Brandenburg and Lagaly, 1988; Penner and Lagaly, 2001; Goh et al., 2011). Similarly, the rheological behavior at the same Na^{+} montmorillronite changes depending on the amount of Ca^{2+} included in the bentonite (Brandenburg and Lagaly, 1988; Penner and Lagaly, 2001; Kelissidis et al., 2007; Goh et al., 2011).

Table 4.2 Comparison of Index tests of the sieved bentonite, (Old/New)

Particle size(d_{95},μm)	25
LL (%)	442/315.4
PL (%)	38.3/40.8
PI (%)	403.7/274.6
Activity	4.8/4.0
CEC (meq/100g)	91/89
Specific surface area (m^2/g)	712.5/696.8
001 spacing (XRD glycolation, Å)	18/18

Table 4.3 Comparison of EDX results of the sieved bentonite, (Old/New)

O	53.05/67.55	K	0.52/0.25
Na	2.27/2.36	Ca	1.2/0.26
Mg	1.52/1.38	Ti	0.15/0.11
Al	9.07/6.7	Cr	0.11/0.1
Si	28.77/19.3	Mn	0.2/0.12
P	0.46/0.55	Fe	2.31/0.84
S	0.43/0.36	Total	100/100
Cl	0.09/0.13	Na/Ca	1.89/5.2

4.4.8. Rheometry

Bentonite suspensions are well known thixotropic fluids so the strength of the aged fluids decreased when large stresses or strains are applied, but it is recovered over time after the stresses/strains are removed. Figure 4.37 shows the change in yield stress with the number of tests. Preshearing of 500 s^{-1} was applied for 1 min prior to each measurement after 24 hours of resting. Initially, the rested bentonite suspensions gained high yield stress, but it significantly decreased with the preshearing process. However, the decreased yield stresses recovered with a subsequence of resting time (30 min). Despite of the increase of the number of tests, it maintained the similar thixotropic increase.

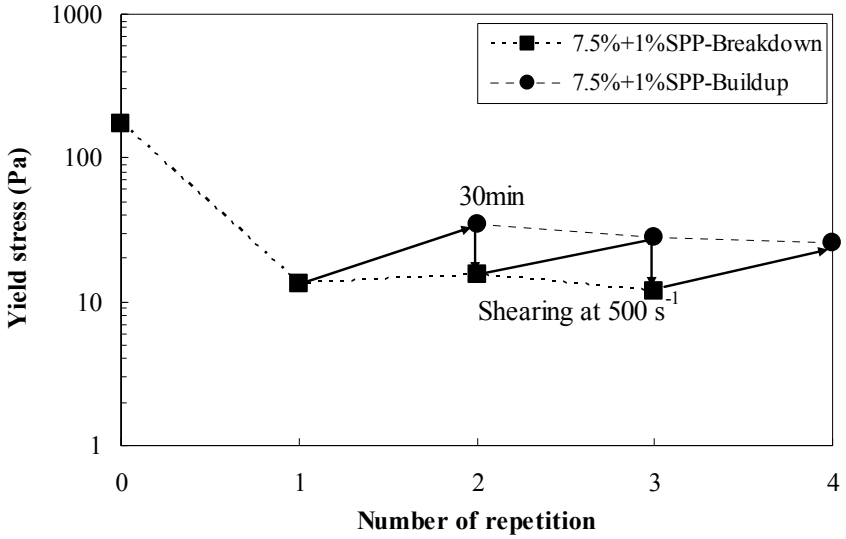

Figure 4.37 Time dependent behavior of modified 7.5% (1% SPP) bentonite suspensions based on number of repetition

Because of this phenomenon, it is challenging to maintain an intact initial structural state of fluids for time dependent measurements with the conventional geometries (cone and plate, plate and plate, and bob and cup). The microstructures are susceptible to be disturbed during the setup for testing when using these conventional geometries. In order to eliminate the disturbance and provide consistent initial condition, preshearing is typically applied prior to yield stress measurement (Ketz et al., 1988; Bekkour et al., 2005; Coussot et al., 2002, 2006; Uhlherr et al., 2005; Mahaut et al., 2008), and then the samples remains in the rheometer for a resting time after preshearing and before testing. The preshearing technique provides consistency in the initial yield stress measurements under flow conditions; this measurement is desirable for the initial grout yield stress (immediately after mixing) since the grouts will be flowing during the grouting process. However, the disadvantage of this approach is that the samples should remain in the rheometer for the entire resting time (a few days to a month) after

preshearing. More importantly, it will be practically impossible to prevent evaporation of such a small amount of sample for a long time.

The more practical approach would be to store suspensions in separate vessels (or one large vessel) under well controlled environments (humidity and temperature), and then scoop a certain amount of suspensions on the plate or into the cup with a minimal disturbance (careful sampling). Despite of this careful treatment of the sample, the placement of the measuring system on the sample will cause inevitable disturbance, leading to an underestimation of the yield stress. Squeeze flow approach can be used with normal force measurements, but it produces transient and inhomogeneous flow with difficulty in ensuring correct boundary conditions (Engmann et al., 2005). In addition, a disturbance during the loading of the samples into the measuring system (scooping) may affect the normal stress measurements, especially when the yield stress of fluids is relatively small. Therefore, the vane geometry has been utilized in this study for the measurement of "undisturbed" yield stress. With the vane geometry, disturbance can be minimized by inserting thin blades into the sample (Cheng, 1986; Barnes and Carnali, 1990; Barnes and Nguyen, 2001), and therefore, the measurements will be much closer to the truly undisturbed values. The effects of the disturbance from inserting the vane into the suspensions was assumed minimal and ignored in this study. By resting samples in separate cups for the desired resting times, disturbance during sample loading can be avoided. Separate storage cups are required to test the samples at different resting times without having disturbance induced by sample placement into cup. The samples are placed in the separate storage cups outside the rheometer and stored until testing times under controlled conditions. For more details, refer to Chapter 3.

Besides the disturbance, wall slip, which occurs due to the depletion of particles near the surface of the cone and the plate, was a concern because no treatment was

applied. When the viscosity-stress curve displays continuous drop without a low-stress Newtonian plateau, it is considered that wall slip did not occur (Buscall et al., 1993). To confirm if wall slip occurred, the viscosity-stress curves from cone and plate and vane, for 7.5% and 10% bentonite suspensions, are shown in Figue 4.38. The values measured using cone and plate geometry were scaled up (based on the relation presented later in Figure 4.40) to match those measured using vane geometry. If the viscosity curve from cone and plate showed a continuous trend similar to that obtained from vane, it was considered that no slippage occurred (dashed line). However, if a plateau (or sudden discontinuity) in apparent viscosity was observed (long dashed line), it was considered that wall slip occurred. In the latter case, yield stresses are significantly underestimated. Cone and plate tests that showed slippage were disregarded and excluded from all the results presented in this study.

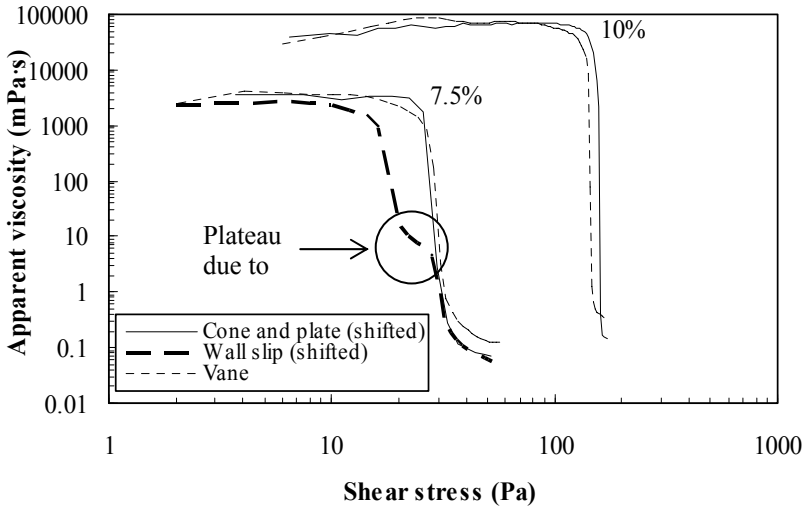

Figure 4.38 Wall slip on cone and plate for 7.5% and 10% suspensions (long dashed line shows occurrence of wall slip)

Despite these disadvantages, the cone and plate has a preference over vane, particularly: 1) cone and plate requires small amount of samples, 2) it produces

homogeneous flow and 3) it is too expensive to manufacture many storage cups for a specific project. Based on these reasons, one may prefer to use cone and plate for measuring yield stress after a long resting time even though there is obvious disturbance effect on the measurement. In this case, a quantification of disturbance may be crucial to evaluate "undisturbed" yield stress from "disturbed" yield stress, resulting in more accurate evaluation of the post grouting performance.

In this study, yield stresses of bentonite suspensions were measured using cone and plate and compared with the results from the vane geometry. At least three tests were performed at each bentonite fraction. A simple linear relationship was developed between yield stresses with the geometries to quantify the degree of disturbance induced by cone and plate geometry. Although the vane still induces some disturbance into the suspension, yield stresses with cone and plate and vane geometry are considered as "disturbed" and "undisturbed" yield stress, respectively. Based on the quantified degree of disturbance, an attempt was made to predict "undisturbed" yield stress from "disturbed" yield stress. In addition, the mechanism of disturbance is explained by structural kinetics.

For these series of tests, the stress ramp test was performed with cone and plate immediately after mixing the suspensions. At lease three tests were performed at fresh mixed suspensions (vane) and samples scooped from the stored suspensions (cone and plate). Without a rest period, it is assumed that the microstructures of bentonite suspensions reach an equilibrium state during the mixing process, and therefore, there is no effect from disturbance. Figure 4.39 shows a comparison of yield stress growth with weight fraction of bentonite for cone and plate and vane geometry immediately after mixing. The average yield stresses from both geometries increased exponentially with the increase of weight fraction of bentonite, indicating that the yield stress is a function of

particle fraction in clay suspensions (Dzuy and Boger, 1983). However, the vane geometry consistently provided higher yield stress values than the cone and plate geometry. At higher weight fraction of bentonite, a larger difference in yield stress was observed; a linear relationship between the yield stresses from the two geometries shown in Figure 4.40. The slope and R^2 were 0.326 and 0.999, respectively. However, yield stresses at 5% appeared to be a little bit offset with large standard deviations, indicating that 1 Pa/step is not low enough to accurately capture the yield stress for the diluted suspensions.

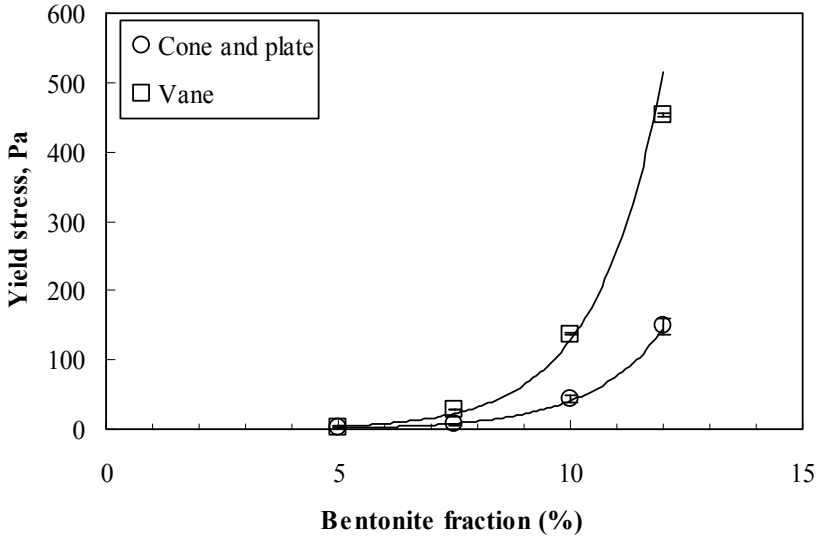

Figure 4.39 Yield stresses from cone and plate and vane based on weight fraction of bentonite: 5, 7.5, 10, and 12%

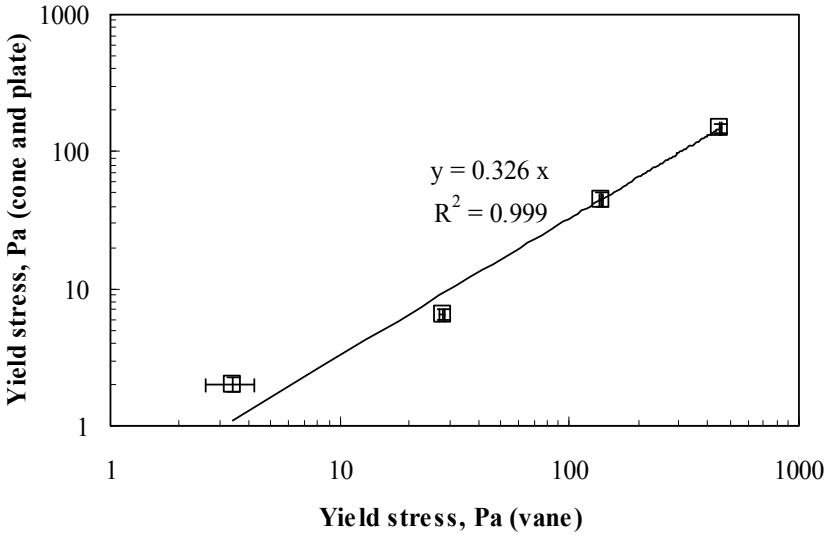

Figure 4.40 Correlation between yield stresses from cone and plate and vane at zero resting time

Yield stresses obtained from the two geometries were measured at bentonite fractions of 5, 7.5, 10, and 12% and the resting times from 0 to 3 months. Figure 4.41 shows the thixotropic increase in yield stress measured by cone and plate. The measurement of the yield stress was done without preshearing the sample to capture the disturbance due to the testing procedure. The yield stresses from the cone and plate geometry did not show a noticeable increase over time compared to the yield stresses from vane geometry, which distinctly increased with resting times (Figure 4.13). This indicates that cone and plate geometry significantly underestimated the undisturbed yield stresses at no flow condition due to the disturbance of the suspension during loading the specimen into the rheometer and moving the cone down to the measuring position.

Figure 4.42 displays the comparison of corrected yield stresses from cone and plate with those from vane for a 10% bentonite suspension. Yield stresses from cone and plate geometry was corrected using the factor of 1/0.326 obtained from the slope at zero resting time. This correction assumes that the ratio between cone and plate and

vane remains constant if there are no disturbance effects, which seems to be a reasonable assumption since the ratio was constant over a large range of yield stresses as shown in Figure 4.40 earlier. Even with the correction applied, there still exists a large difference between the yield stresses from both geometries. This discrepancy in measured yield stress values is the result of the disturbance occurring during the placement of the specimen on cone and plate and when the cone is lowered to the measuring position, resulting in high strains in the specimen before the stress ramp tests even started.

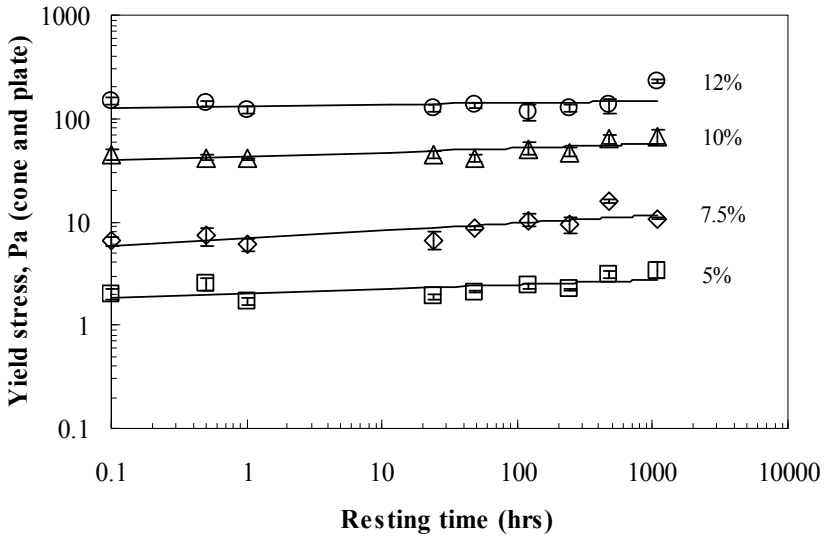

Figure 4.41 Yield stress at various weight fractions of bentonite (5, 7.5, 10, and 12%) and resting times measured by cone and plate

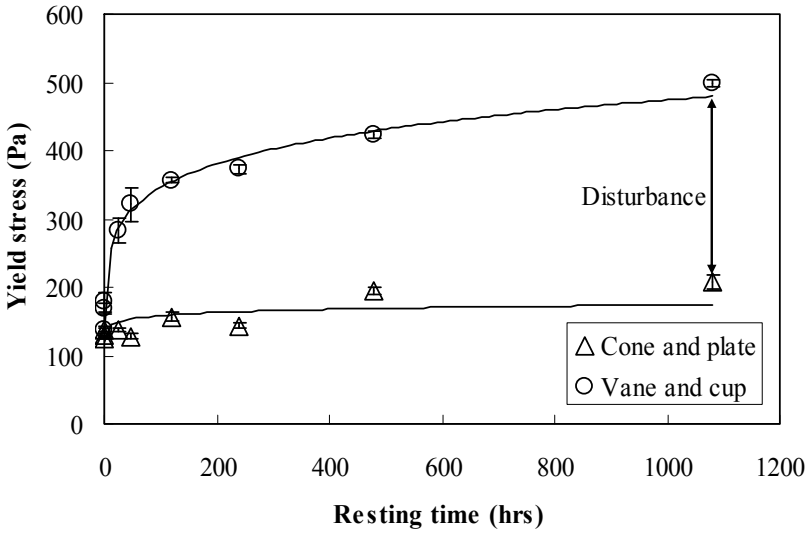

Figure 4.42 Comparison of yield stress from cone and plate and vane: 10% bentonite suspension (yield stresses from cone and plate were corrected with the factor of 1/0.326)

The correlation between the yield stresses from the two geometries, at various resting times and suspension concentrations, was investigated in this study (similar to the correlation presented in Figure 4.40). The magnitudes of the slopes are summarized in Table 4.4. Similar to zero resting time, regression analyses was performed to find a relationship between the two geometries, resulting in linear relationships with R^2 of 0.980 to 0.999. The slopes significantly increased at short resting times (0.5 and 1 hour), and gradually converged at long resting times (10 to 45 days). The magnitude of disturbance was quantified by using the change of the slopes with the resting times. The disturbance was assumed to be zero immediately after mixing, and for other resting times, it was calculated by the following expression:

$$D(\%) = \left(1 - \frac{S_t}{S_O}\right) \times 100 \tag{4.2}$$

Where D is the disturbance (%), S_o is the slope at zero resting time (immediately after mixing), and S_t is the slope at any resting time. As shown in Figure 4.43, the

disturbance significantly increased at short resting times (0.5 and 1 hour), and gradually converged at long resting times (120 and 240 hours). With increasing resting times, the cone and plate geometry significantly underestimated the yield stress up to approximately 60%. Since this correlation considers a wide range of bentonite fractions, the disturbance becomes only a function of resting time in the proposed application.

Table 4.4 Regression parameters and disturbance

Time (hours)	Slope	R^2	Disturbance (%)
0	0.326	0.999	0
0.5	0.256	0.999	22
1	0.217	0.998	33
24	0.171	0.993	48
48	0.167	0.980	48
120	0.139	0.996	57
240	0.135	0.992	59
480	0.138	0.996	58
1080	0.129	0.958	60

* The values presented here is average values of three samples at each concentration and resting time

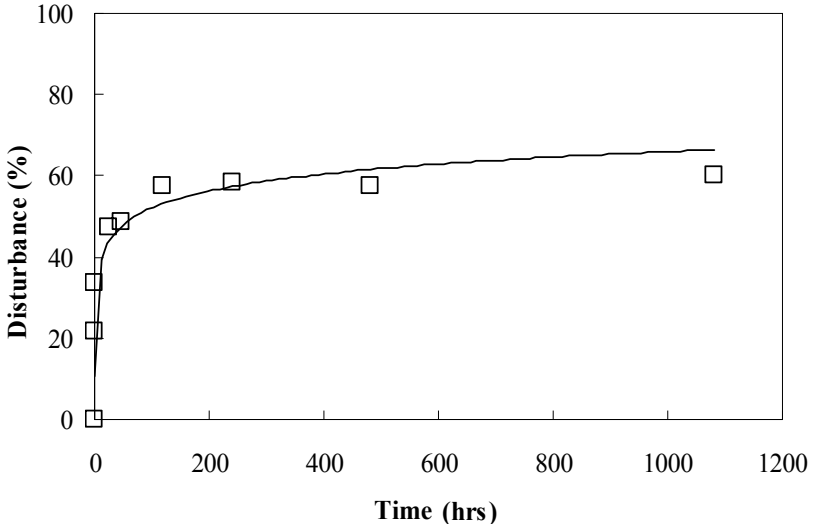

Figure 4.43 Average disturbance at various resting times

Based on the quantified degree of disturbance, an attempt was made to predict the "undisturbed" yield stress (vane) from the "disturbed" yield stress (cone and plate) by using the following relationship:

$$\left(\tau_{y\,undisturbed}\right)_{t_r} = \left(\tau_{y\,disturbed}\right)_{t_r} \cdot \left(\frac{\tau_{y\,vane}}{\tau_{y\,cone}}\right)_{t_r} \cdot \frac{1}{1 - D(t_r)} \qquad (4.3)$$

Where t_r is the resting time, $\tau_{y,\,undisturbed}$ is the predicted yield stress from vane at t_r, $\tau_{y,\,disturbed}$ is the measured yield stress from cone and plate at t_r, $(\tau_{y,\,vane}/\tau_{y,\,cone})_{tr=0}$ is the correlation between two geometries at t_r=0, (in this study, 1/0.326), and $D(t_r)$ is the disturbance as a decimal at t_r. The proposed correlation considers the yield stress ratio between the two geometries at zero resting time (also after preshearing), disturbed yield stress from cone and plate and the disturbance (which is a function of time).

To test the proposed model, the undisturbed yield stresses for 6, 8, 9, 11, 13, 14 and 15% bentonite suspensions were calculated using yield stresses measured by cone and plate at 0, 0.5, 1, and 24 hours. And then, the predicted values were compared to the yield stress measured by vane at the same weight factions and resting times. Figure 4.44 Comparison of predicted and measured yield stress: 6, 8, 9, 11, 13, 14 and 15% bentonite suspension at 0, 0.5, 1, 24 and 48 hours (the dashed lines are ± standard deviation lines) shows the predicted versus the measured values of 6, 8, 9, 11, 13, 14 and 15% bentonite suspensions with the resting time from 0 to 48 hours. All calculated values were well agreed with the measured values, but relatively large scatters were observed at low (6%) and high (15%) bentonite fractions. The scatter at the low bentonite fraction was attributed that the ramp rate of 1 Pa/step was not slow enough to capture accurate yield stress in the diluted suspensions. Moreover, the discrepancies at the high bentonite fraction might be due to un-uniform distribution of water since it was too close to the liquid limit of the bentonite. However, the results showed that the

undisturbed yield stress can be predicted with a good accuracy using the proposed correlation. This estimation of the undisturbed yield stress is possibly beneficial in that the stability of grouts after any resting times (resistance to the in situ hydraulic gradient) can be estimated from cone and plate results.

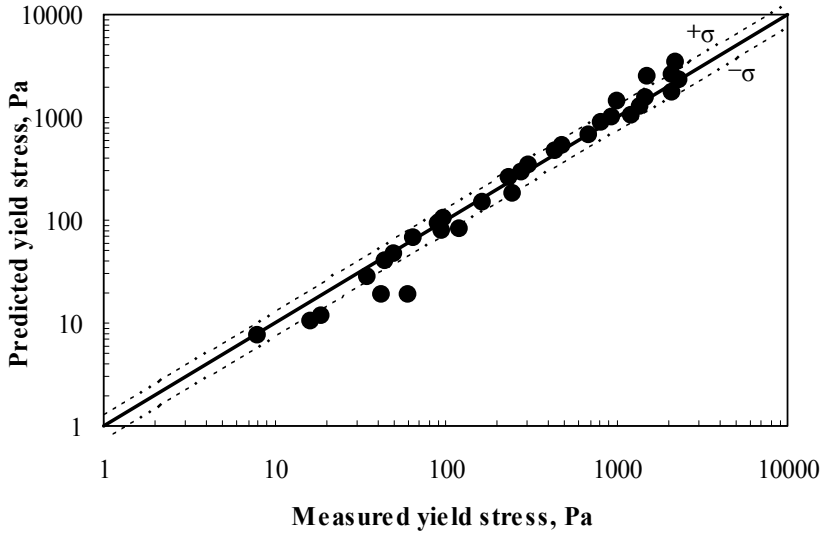

Figure 4.44 Comparison of predicted and measured yield stress: 6, 8, 9, 11, 13, 14 and 15% bentonite suspension at 0, 0.5, 1, 24 and 48 hours (the dashed lines are ± standard deviation lines)

The modified bentonite suspensions produced a different trend. Figure 4.45 shows the comparison between yield stress from vane and cone and plate geometries. As can be seen, yield stresses measured by two different geometries produced a linear trend with the variation of 5 to 10%. This indicates that the disturbance in bentonite suspensions is highly dependent on the variation of microstructure induced by the compression of the sample.

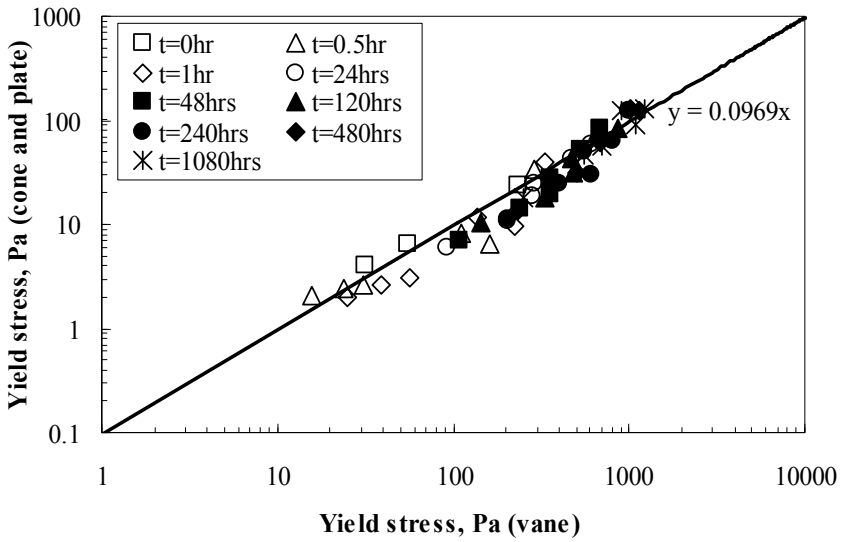

Figure 4.45 Comparison of yield stress measured by two geometries: the modified suspensions from 0 to 45 days

Structural kinetics of bentonite suspensions may allow us to qualitatively explain the disturbance in yield stress. Depending on pH conditions, bentonite suspensions have a card-house (van Olphen 1977) or band-like structure (Norrish, 1954 and Weiss and Frank, 1961) in 3-D space. This structure is continuous and integrated in the suspensions, affecting their mobility: yield stress and viscosity. Nguyen and Boger (1985) postulated that two types of bonds (inter-aggregate and inter-particle bonds) are present in mud suspensions. Inter-aggregate bonds contribute to form a 3-D network, relating to the strength of the suspensions. These type of bonds can be broken if the applied stress exceeds the yield stress; however, this breakage is reversible with time and the bonds are recovered slowly. Nguyen and Boger (1985) observed that red mud suspensions have a finite yield stress even after long term mixing, and Jones and Brodkey (1970) observed similar behavior in colloidal alumina suspensions. This indicates that

the inter-aggregate type bonds cannot be completely destroyed even with an excessive external shearing (residual inter-aggregate bonds).

Inter-particle bonds are dependent on the shear rate. As the shear rate increases, the aggregates are broken into smaller particles, and suspensions become more dispersed. Recovery of this bond occurs practically instantaneously due to inter-particle interaction or bond formation by sudden stoppage of flow (Amorós et al. 2002). Amorós et al. (2002) observed that storage modulus of clay suspensions increased with two different recovery rates: almost instantaneous and slow time-dependent, which correspond to the recovery of inter-particle and inter-aggregate bonds, respectively. The amount of recovery increases with an increase in particle fractions.

The underestimated yield stresses from cone and plate are attributed to the damage of inter-aggregate bonds during scooping, loading the specimen in the rheometer, and positioning the measuring system, and trimming the specimen before running the test. Figure 4.46 shows the change in normal force at the trimming position (initial compression from lowering the cone on the sample) and yield stresses for 7.5 and 12% bentonite suspensions with resting times. The yield stress from vane and the normal force from cone and plate increased with the similar rates due to the increase of the amount of network during resting. The rate of recovery or thixotropy is affected by particle movement. In the concentrated suspensions (12%), Brownian motion of particles is constrained so the thixotropic increase in inter-aggregate bonds is reduced compared to that of the diluted suspensions (7.5%). Because of this confinement of particle movement, the rate of increase in normal force is reduced in the concentrated suspensions. However, lowering the cone to the trimming position squeezed the sample and initiated a radial flow (the applied stress by compression is always high enough to induce the flow), leading to structural damage in both types of bonds. As the radial flow

stops, the inter-particle bonds are recovered rapidly but the inter-aggregate bonds need more time to be recovered, resulting in an underestimation of the yield stress measured by cone and plate at a given resting time. Pignon et al. (1997) observed this change in microstructure of clay suspensions with cone and plate using static light scattering technique; once an applied stress is beyond the yield stress, the microstructure breaks into smaller scales which are different from the at-rest condition.

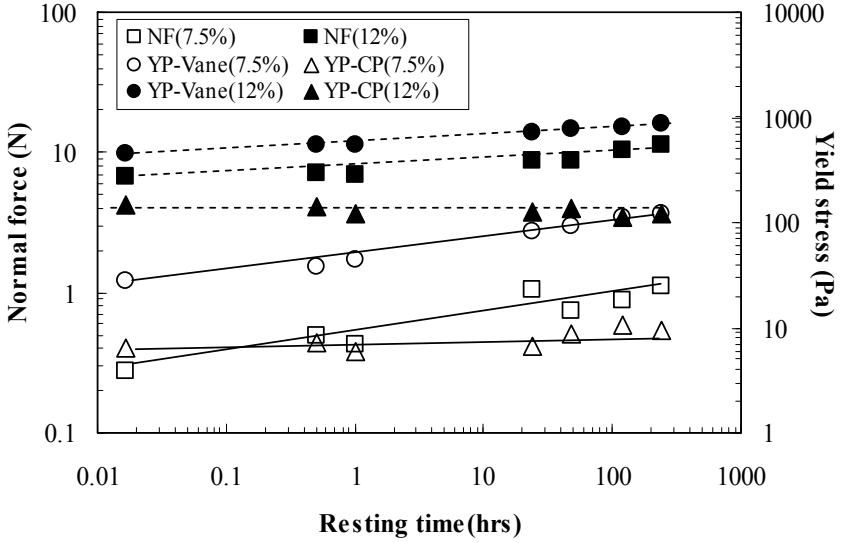

Figure 4.46 Normal force and yield stress for 7.5 and 12% bentonite suspensions (NF, *normal force*, YP, *yield stress*, CP, *cone and plate*, and the solid and the dashed lines are drawn for the visual aids of 7.5% and 12% respectively)

The addition of SPP caused the formation of band-like structures which have mainly parallel alignment as shown in section 4.4.6. Because the alignment of the bonds, the compression causes less significant breakdown in microstructures than the unmodified suspensions, resulting in less reduction in yield stress. Figure 4.47 shows the thixotropy ratio of the unmodified 12% suspensions and the modified 12% (1% SPP) suspensions from the two different geometries. Due to the structural damage from cone

and plate, the yield stress of the unmodified suspensions measured from cone and plate was significantly underestimated compared to the yield stress measured by vane. However, the modified suspensions showed similar thixotropy ratio between each other due to less damage in microstructures.

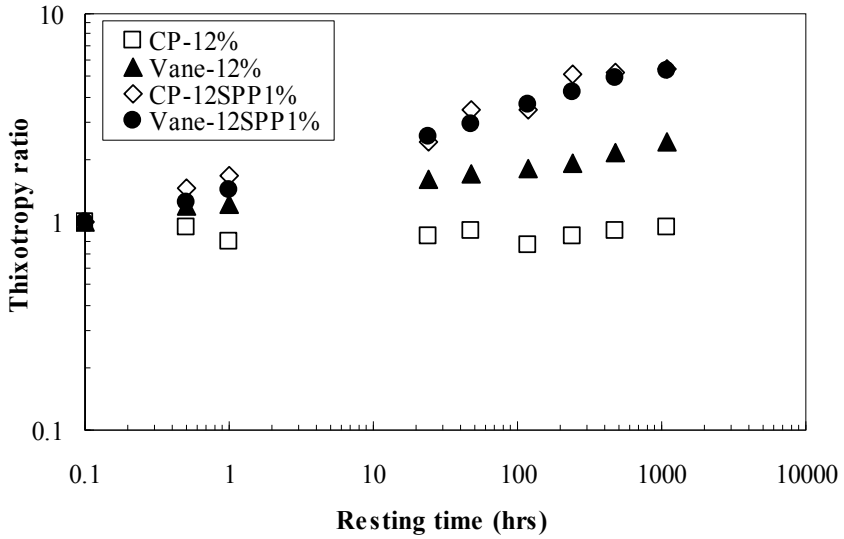

Figure 4.47 Thixotropy ratio for 12 and 12(1)% bentonite suspensions from two different geometries (cone and plate and vane) at 0 to 45 days

4.5. Determination of optimum mix

Figure 4.48 displays the ratio of the yield stresses at 24 hours and immediately after mixing for 7.5, 10 and 12% suspensions with various SPP concentrations. The 24 hours of resting is chosen because the rate of change in yield stress starts to decrease at this time, implying that yield stress increases at a slower rate after 24 hours. The thixotropy ratio at 24 hours increases up to a certain SPP concentration and then starts decreasing afterwards. This fact is consistent with the previous observations in yield stress and apparent viscosity, indicating the limited effectiveness of SPP. Based on the limited effect of SPP on yield stress and apparent viscosity of bentonite suspensions, an

optimum mix for field application was found. Figure 4.49 shows the comparisons of yield stress, apparent viscosity, and thxiotropy ratio of each bentonite suspension. By comparing those properties, the optimum mixing formulas for the bentonite suspensions is determined as 2, 3, and 4% of SPP for the 7.5, 10, and 12% bentonite suspensions, respectively. These suspensions have the lowest yield stress, low apparent viscosity, and the highest thixotropy. An excessive amount of SPP may disrupt one or all of these three criteria, resulting in being impractical.

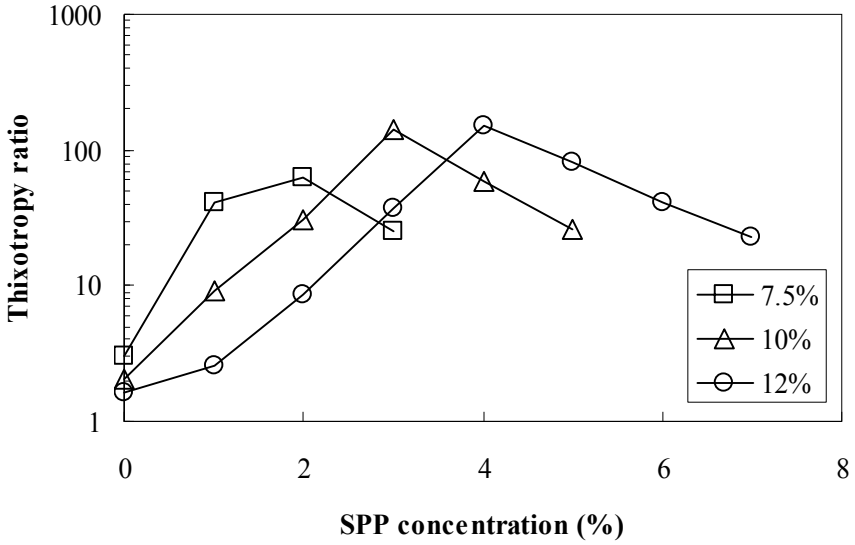

Figure 4.48 Thixotropy ratio at 24 hours for 7.5, 10, and 12% suspensions with 0 to 7% of SPP

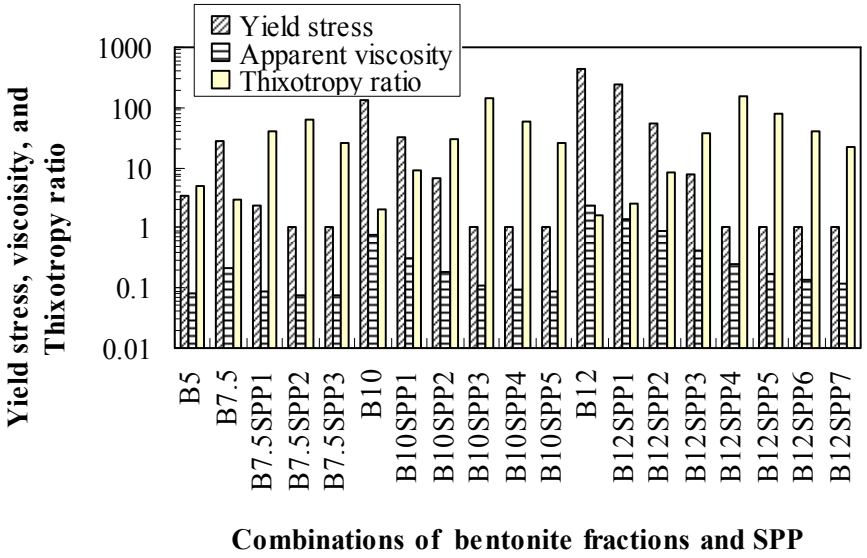

Figure 4.49 Optimum combinations of SPP and bentonite fraction

4.6. Conclusions

The yield stress and apparent viscosity of the modified bentonite suspensions were investigated using the vane geometry. The addition of a small amount of sodium pyrophosphate was found to significantly reduce the yield stress and apparent viscosity in bentonite suspensions. However, this reduction tended to converge after a threshold percentage of SPP (2, 3, and 4% for 7.5, 10, and 12% bentonite suspensions, respectively). It was concluded that a small amount of SPP (1 to 4%) was enough to improve the mobility of the concentrated bentonite suspensions effectively, and an excessive amount of SPP may not be effective in further reducing the yield stress and apparent viscosity.

The reduced yield stress and apparent viscosity was recovered gradually with time. The results showed that the concentrated suspensions produced a lower degree of increase in yield stress with time (lower thixotropy ratio) than the diluted suspensions; similarly, larger percentages of SPP induced higher degrees of build-up at a given resting

time (higher thixotropy ratio). This observation can be explained through looking into the structural kinetics of the different suspensions. The constrained Brownian motions in the concentrated suspensions produced low thixotropy ratios. On the other hand, the SPP modified suspensions, which showed a high degree of Brownian motion due to the reduction of inter-aggregate bonds (3-D network), produced higher thixotropy ratios than those in the unmodified suspensions. In addition to the Brownian motion of particles, the thixotropy ratios are also affected by the degree of hydration.

The recovery rate of bentonite suspensions was determined based on the Leong model (1988). The results showed that the recovery rate increased with bentonite concentrations and decreased with SPP concentrations, indicating that the suspensions having high Brownian motion (low-bentonite-concentration and/or high-percentage-of-SPP) have slower yield stress build up over time than the suspensions having low Brownian motion (high-bentonite-concentration or low-percentage-of-SPP). The model could capture the overall time dependent build-up of yield stress in the bentonite suspensions by estimating yield stresses at infinite time from measured data. This may be useful to estimate long-term performance of grouts after being injected into the soil pores or rock fractures.

Disturbance effect on yield stress measurement of bentonite suspensions was investigated using the cone and plate and vane geometries. Yield stresses at increasing resting times measured by the cone and plate geometry were found to be significantly underestimated due to disturbance. When using the cone and plate configuration, the tested bentonite suspensions showed little to no increase in yield stress with time. On the other hand, relatively undisturbed yield stresses measured using the vane geometry displayed a more distinct increase with time.

Regression analyses of yield stresses measured using both geometries produced a linear relationship at zero rest time when it was assumed that there was no disturbance (since no thixotropy occurred to start with). Similar linear regression relations were developed for different bentonite suspensions tested at increasing resting times. Based on these relationships, it was found that cone and plate underestimated yield stress up to approximately 60% after long resting times. The disturbance tends to increase with increasing time and converge at long resting times. Using the quantified degree of disturbance, "undisturbed" yield stress from "disturbed" yield stress could be reasonably predicted. The degree of disturbance was found to be unique for the range of bentonite concentrations studied. Although the proposed model was developed for bentonite suspensions, the same model can be used for different thixotropic suspensions; however, a new disturbance function, $D(t_r)$ should be developed for the different suspensions. This method is attractive in terms of an optimal usage of equipment and cost-effectiveness (no need to manufacture many storage cups for vane). More importantly, this work provides a method to measure the aged "undisturbed" yield stress of bentonite suspensions which is critical for accurate evaluation of the grout stability inside porous media.

CHAPTER 5: RESULT-II: PERMEATION

5.1. Introduction

This chapter covers the results from two types of injection techniques (constant pressure and constant flow rate) to investigate the permeation of bentonite suspensions through sand. Although the term the "groutability" typically includes both the "penetrability" and "injectability" of a grout through a soil, this study uses the separate definitions of the two terms since they are assessed by different flow quantities. The term "penetrability" refers to the permeation distance the suspensions can travel during injection and is evaluated by monitoring the penetration distance of a grout at a predetermined maximum pressure (Markou and Atmatzidis, 2002; Santagata and Santagata, 2003). The groutability refers to the ease with which the suspensions permeate through a soil and is estimated by the injected pore volume of a grout at a given length of soil column (Markou and Atmatzidis, 2002; Mittag and Savidis, 2003; Schwarz and Chirumalla, 2003; Ozgurel and Vipulanandan, 2005).

One dimensional (1-D) injection test in laboratory has been adopted as the conventional technique conducted in laboratory to evaluate the groutability and penetrability for the grout in granular soils. Although these tests tend to underestimate filtration occurring in the field (Mittag and Savidis, 1999) and do not reflect the in-situ multistage injection (Santagata and Santagata, 2003), the constant pressure technique is useful to study the effect of the soil, grout and experimental parameters on the grout flow as well as the effectiveness of the treatment (Dupla et al., 2004). A series of experimental results presented herein evaluate the effect of 1) the SPP modification and 2) other experimental parameters such as effective grain size (d_{10}), relative density (Dr), fines content (FC), and injection pressure (P) on the penetration distance and injected pore volume of bentonite suspensions.

The constant pressure technique tends to produce bentonite cakes at the bottom of the sand column, which may interrupt the flow of grouts, resulting in low penetration distance. As an alternative, a constant flow rate technique was utilized to inject the suspensions. The advantage of this technique is that the formation of the filter cake is retarded, leading to a lower injection pressure and higher penetration distances/injected pore volumes than those by the constant pressure technique. The pressure variation during the constant flow rate tests is monitored throughout the test.

5.2. Constant pressure injection

In this technique, the volume of injected suspensions was determined by measuring the effluent weight of water and the number of injected pore volumes was estimated based on the pore volumes of the sand and the filter layers. Since the volume of 5 to12% bentonite suspensions are very close to that of water, the effluent weight of water was considered as the volume of grout intakes. Moreover, the final penetration distances were measured visually by taking an average of three measurements on different sides of the column.

5.2.1. Grout intake

The time dependent response of the suspension flow was monitored by the variation of grout intake based on injection time since it is an indicator of the morphological changes in pore channels as particles are deposited (Schwarz and Chirumalla 2003). Figure 5.1 shows grout intake with time for unmodified 5, 7.5 and 10% bentonite suspensions under 35 kPa constant pressure injected through a clean sand at a relative density of 30%. Initially, the suspensions penetrated through the filter

material and a portion of the sand column with very high flow rate, and then the effluent flow rates started to decrease as the penetration proceeds through the sand column. This is due to the initial replacement of pore water, followed by an additional deposition of particles and gradual pore filling until the grout is completely stopped (Schwaz and Chirumalla, 2003 and Axelsson et al., 2009). As the particle fraction increased, a faster retardation of the suspension flow was observed. Zebovitz et al. (1989) and Dupla et al. (2004) observed similar behavior; they performed a series of injection tests with microfine cement and observed that the cement grouts with high W/C ratio produced better injectability (larger injected volume). The time dependent response of the 12% suspensions could not be measured since it showed very small amount of grout intake with almost instantaneous stoppage of flow (less than 10 sec), which was not measurable on the time scale.

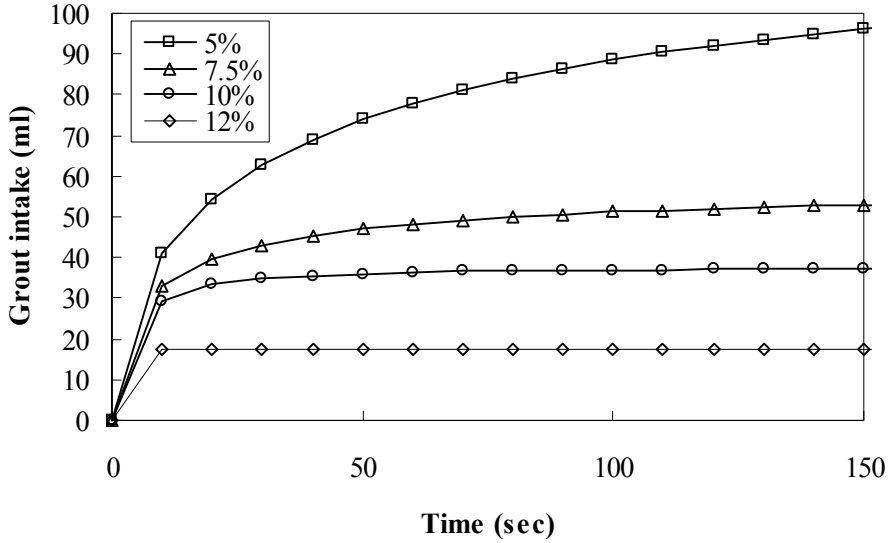

Figure 5.1 Grout intake of 5, 7.5 and 10% suspensions: d_{10}=0.20 mm, Dr=30%, FC=0%, and P=35 kPa

The addition of SPP changes the permeation of bentonite suspensions. Figure 5.2 shows the grout intake of 7.5, 10 and 12% suspensions modified with 1, 3 and 4% SPP, respectively, under the same experimental conditions as the previous test. The grout intake of all modified suspensions increased compared to the unmodified suspensions (see Figure 5.1) while maintaining a similar trend. Less effluent was observed for suspensions with higher bentonite fractions. In addition, the suspensions with low fractions of bentonite showed higher flow rates in the initial profile of the curve than those with high fractions. The 12% suspension showed measurable grout intakes with time after the modification with 4% SPP, indicating that the concentrated suspensions become more injectable after the addition of SPP.

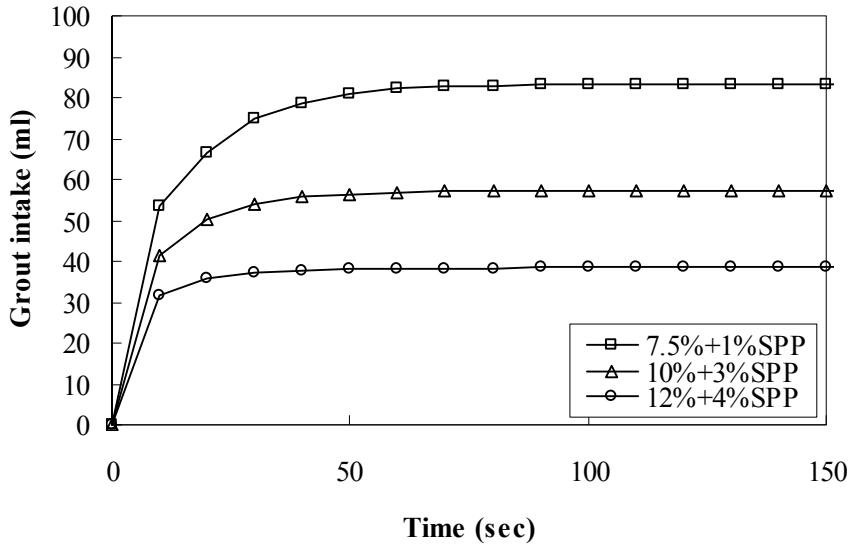

Figure 5.2 Grout intake of 7.5, 10 and 12% suspensions with 1, 3, and 4% SPP: d_{10}=0.20 mm, Dr=30%, FC=0%, and P=35 kPa

The extent of the increase in grout intake depends on the amount of SPP. Figure 5.3 displays the grout intakes of 10% suspensions with 0, 1, 2 and 3% SPP at the same experimental conditions as those of the unmodified suspensions (d_{10}=0.20 mm, Dr=30%,

FC=0%, and P=35 kPa). As the amount of SPP increases, more suspensions could be injected at a given time. The flow rate of the modified suspensions decreased at a slower rate than the unmodified suspensions. Moreover, the 10% suspensions with 3% SPP produced similar grout intakes to the unmodified 7.5% suspensions. This indicates that the groutability of a suspension through a given soil should be evaluated with the combination of SPP and bentonite fraction in the grout, which is reflected in rheological properties of the grout as shown in Chapter 4.

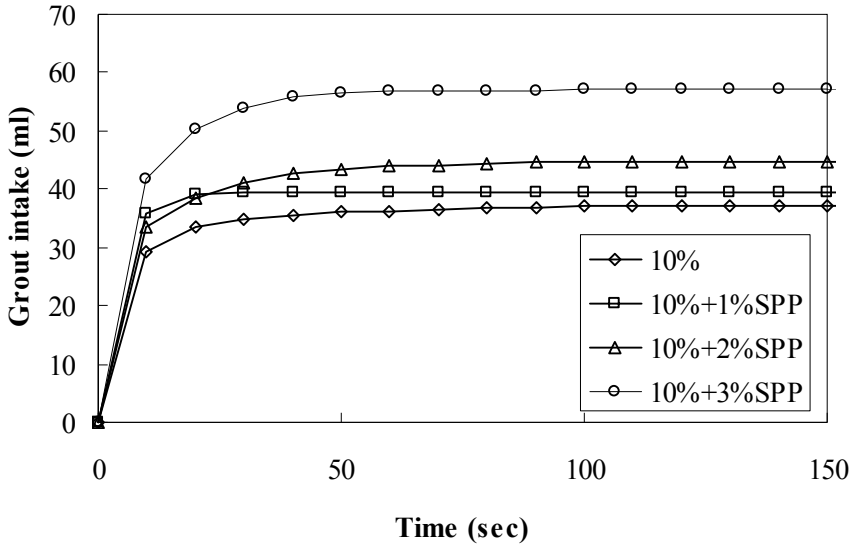

Figure 5.3 Grout intake of 10% suspensions with 0, 1, 2 and 3% SPP at d_{10}=0.20 mm, Dr=30%, FC=0%, and P=35 kPa

In order to investigate the effect of various soil parameters and testing conditions, the modified suspensions were permeated through sand columns prepared with different effective grain size, relative density and fines content. In addition, the effect of injection pressure was estimated by running tests under two different constant pressure levels of 35 kPa and 140 kPa. Figure 5.4 displays the effect of effective grain size on the penetration of 12% suspensions modified with 4% SPP at 140 kPa. The flow

rate in the initial portion of the curve increased as the effective grain sizes increased, and the soil with larger effective grain size showed much slower retardation in suspension flow than the soil with smaller effective grain size. The significant increase in the grout intake is possibly due to the presence of large pore space where suspensions can flow through with limited filtration. Aggregate sand tested at the higher relative density (80%) produced a larger amount of grouted suspension than Ottawa sand at the low relative density (30%). Nevada sand (the effective grain size of 0.12 mm) produced very low grout intake even with the modified 7.5% suspensions with almost instantaneous stoppage of flow (less than 10 sec), which was not measurable.

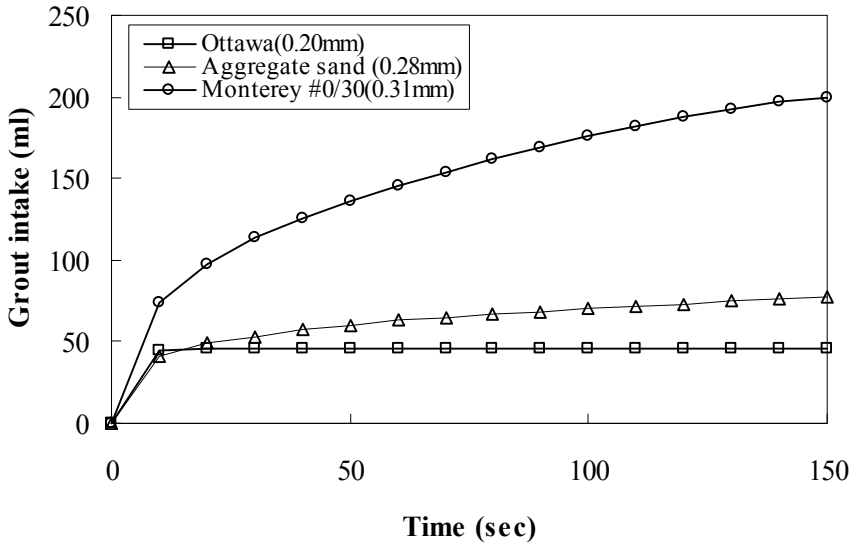

Figure 5.4 Grout intake of 12% with 4% SPP bentonite suspensions based on the injection time: d_{10}=0.20, 0.28 and 0.31 mm, Dr=30% (for aggregate sand, Dr=80%), FC=0% and P=140 kPa

The relative density of sand affects the penetration of bentonite suspensions. As can be seen in Figure 5.5, the loose specimens (relative density of 30%) initially produced higher flow rates than the dense specimens (relative density of 80%), but the

amount of grout intake varies with the fractions of bentonite. While 7.5% suspensions showed larger grout intake in the dense soil, the difference between the grout intake measured at the two relative densities decreased as the bentonite fractions increased. This may be attributed to the fact that the creep flow (additional filling of voids which occurs after the initial penetration of the suspensions) was increased due to the decreased filtration (Axelsson et al., 2009). Overall, the relative density affected the initial flow rate but no significant effect on the final grout intake.

In addition, the flow of all suspensions was retarded more gradually in the dense specimens than the loose specimens. This is possibly due to the facts that 1) the increase of flow velocity in dense soil decreased filtration of bentonite particles and 2) smaller surface area in dense packing might decrease the possibility of capturing bentonite particles, reducing filtration. The relatively concentrated suspensions (10 and 12%) exhibited faster stoppage of flow compared to the relatively diluted suspensions (7.5%) due to a higher degree of filtration. However, the concentrated suspensions could not be injected sufficiently through the soil, meaning that the treatment of the soil with the concentrated suspensions (either low or high relative density) will require higher injection pressure to achieve a sufficient amount of grout intake.

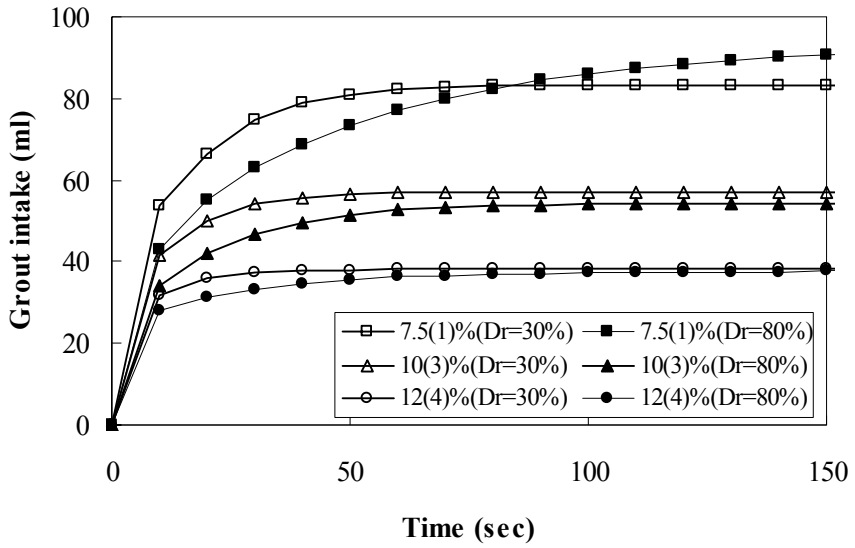

Figure 5.5 Grout intake of 7.5, 10 and 12% suspensions with 1, 3 and 4% SPP: d_{10}=0.20 mm, Dr=30 and 80%, FC=0% and P=35 kPa

The effect of injection pressure was investigated by applying two constant pressures of 35 and 140 kPa. Even though a higher injection pressure would increase the grout intakes, there was a concern that applying too high of a pressure may induce the movement of soil grains, resulting in fracturing of the soil which may change properties of the treated soils. In the field, the high pressure may disrupt the uniform distribution of the grouts by gathering the grouts in artificial voids near the drilling well (Akbulut and Saglamer, 2002).

As shown in Figure 5.6, the grout intakes of 7.5, 10 and 12% suspensions with 1, 3 and 4% SPP increased with an increase of injection pressures. The increase in grout intake was more pronounced in the modified 7.5% suspension as compared to the 10 and 12% ones. The stoppage of flow was retarded by increasing the injection pressure except for the 12% modified suspensions. The results indicate that the high injection

pressure increases the penetration, but the effect is limited depending on the fraction of bentonite.

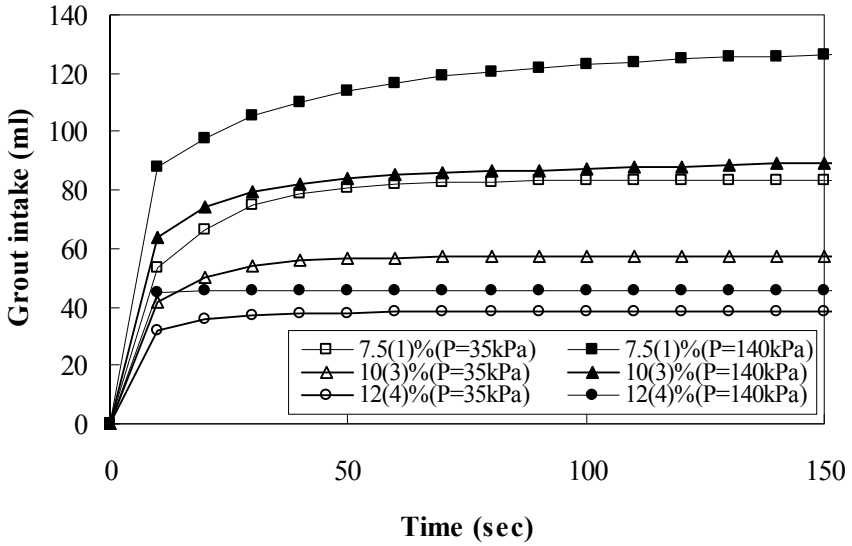

Figure 5.6 Grout intake of 7.5, 10 and 12% suspensions with 1, 3 and 4% SPP: d_{10}=0.20 mm, Dr =30%, FC=0%, and P=35 and 140 kPa

For the field application, the effect of fines on permeation of the suspensions should be evaluated since the sand in the field typically includes a portion of fines. Sand columns were prepared with sand mixed with non-plastic fines forming specimens at a skeletal relative density of approximately 30% to investigate the effect of fine contents. Figure 5.7 depicts the effect of low plasticity fines content on grout intake. The flow rates at the initial portion of the curves were reduced with an increase in fines content, but the sand including 5% fines produced a similar flow rate to that of the clean sand, indicating that low fines content less than 5% will not significantly affect the permeation of bentonite suspensions. However, the high fines content of 10 and 15% greatly reduced the initial flow rates, producing low grout intakes. This is because the fines in sand limit the penetration of the bentonite suspensions. The soils which have

greater than 20% fines were not tested since such soils are typically considered ungroutable with particulate grouting: either cement based or bentonite grouts (Karol, 2003).

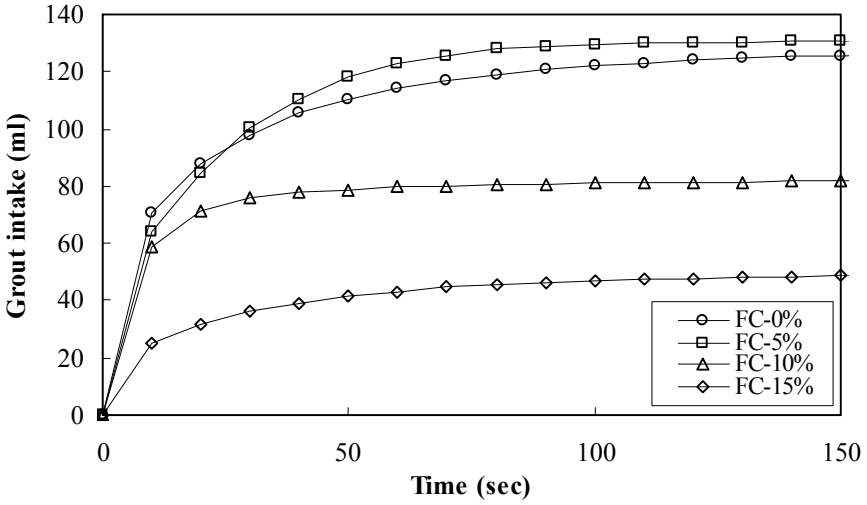

Figure 5.7 Grout intake of 7.5% suspensions with 1% SPP: d_{10}=0.20 mm, $Dr_{,skeletal}$=30%, FC=0, 5, 10 and 15%, and P=140 kPa

5.2.2. Injected pore volume

Since the grout intake includes the amount of intake through the filter layer, the grout intake was corrected by considering the pore volumes of the filter layers, and the corrected grout intake was normalized with the pore volume of the sand column for consistent comparison between different experimental parameters without having any effects from different porosities. Figure 5.8 displays the injected pore volume based on the weight fraction of bentonite for various suspensions. As bentonite fraction increased, the number of injected pore volumes of the unmodified suspensions decreased from 1.4 to 0.1, following a power function. Moreover, the number of injected pore

volumes increased with the modified suspensions (e.g. 0.6 to 0.9 for 7.5% and 7.5% modified with 1% SPP respectively).

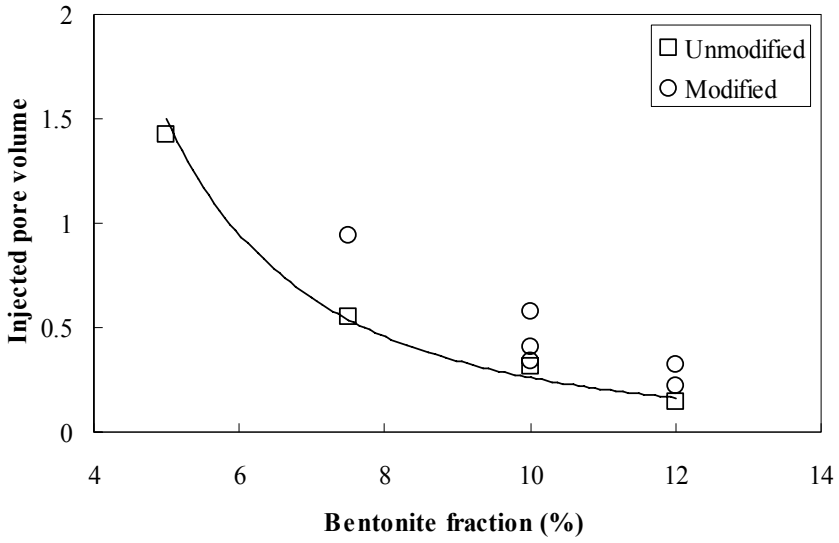

Figure 5.8 Injected pore volume with bentonite fractions at various suspensions: 7.5, 10 and 12% suspensions with 0, 1, 2, 3 and 4% SPP, d_{10}=0.20 mm, Dr=30%, FC=0%, and P=35 kPa

Figure 5.9 displays the variation of the number of injected pore volumes with SPP concentration. The number of injected pore volume of all the suspensions increased with the increased dosage of SPP. However, the extent of the increase was dependent on particle fraction and SPP concentration. As bentonite fraction in the suspensions increased, the increase in the number of injected pore volumes of the suspension was less.

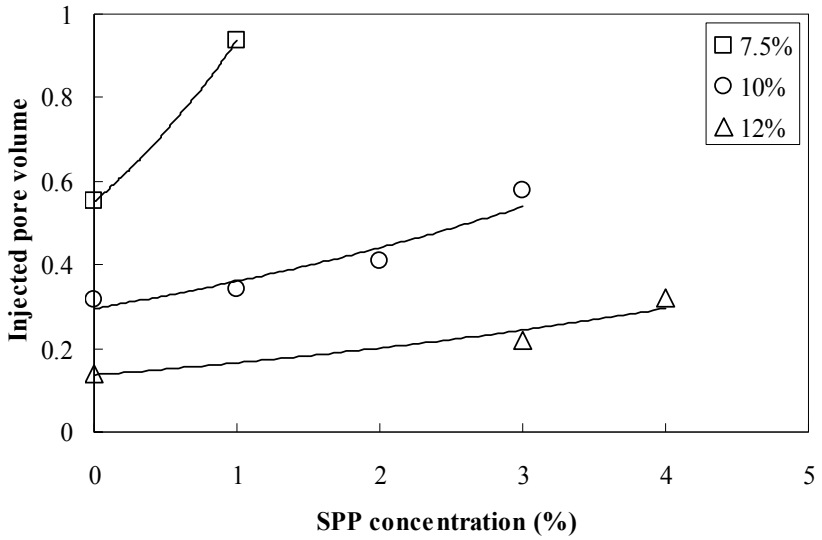

Figure 5.9 Injected pore volume with SPP concentrations at 7.5, 10 and 12 % suspensions with 0, 1, 2, 3 and 4% SPP, d_{10}=0.20 mm, Dr=30%, FC=0%, and P=35 kPa

Figure 5.10 shows injected pore volumes of 12% bentonite suspension with 4% SPP depending on the effective grain sizes of sands. The injected pore volume of the suspensions increased exponentially with the increase in the effective grain size of soils, indicating the possibility of injection increased with effective grain size of soils. The similar effect has been reported in the literatures (Akabulut and Saglamer 2002 and Santagata and Santagata 2003). In addition, Ozgurel and Vipulanandan (2005) found that the injection pressure in chemical (acrylamide) grout exponentially increased with the increase in effective grain size.

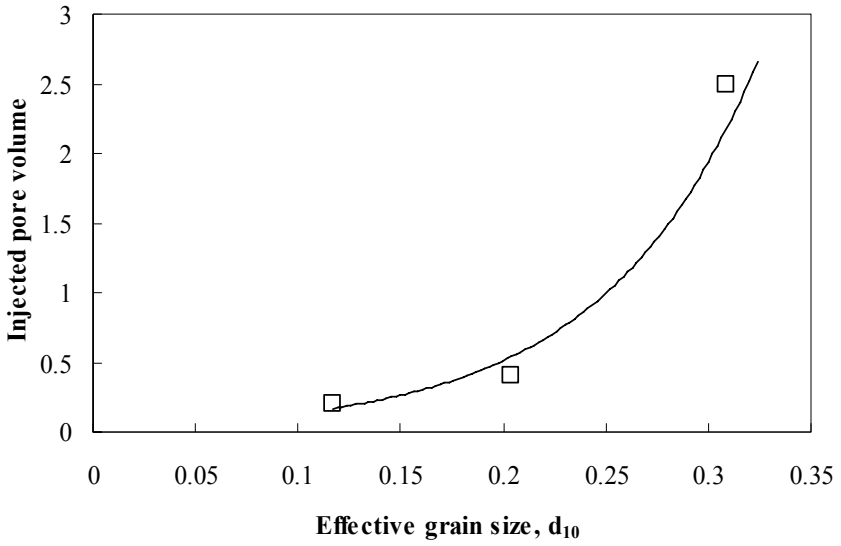

Figure 5.10 Injected pore volume based on effective grain sizes of sands: 12% suspension with 4% SPP, FC=0%, Dr=30% and P=140 kPa

Figure 5.11 displays a comparison of injected pore volumes at relative density of 30 and 80%. As the relative density increased, the injected pore volumes of suspensions remained relatively unchanged in the concentrated suspensions (10 and 12%) and slightly increased in the diluted suspensions (7.5%). This may be attributed to the fact that the reduced filtration increased the creep flow, leading to less difference in the final grout intakes despite of the reduction in initial penetration. In addition, the reduction in the porosity of the sand column compensated the increase in grout intakes by approximately 10% in the volume calculation.

Since the injection pressure of 35 kPa was not enough to differentiate the effect of relative density in the concentrated suspensions, the 10% suspensions with 3% SPP was injected with the higher pressure of 140 kPa. However, the difference was still small (approximately 10%) even at the higher injection pressure. Based on these observations, it was concluded that the overall effect of relative density on the injected

pore volume was small compared to other parameters such as the effective grain size and the addition of SPP.

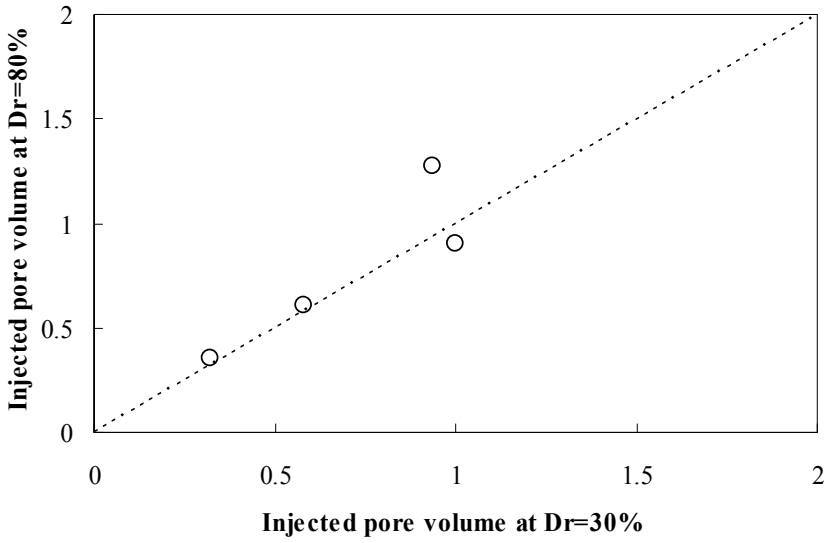

Figure 5.11 Comparison of injected pore volume from different relative density of sands: 7.5, 10, and 12% suspensions with 1, 3, and 4% SPP, FC=0%, d_{10}=0.20 mm, and P=35 kPa or 140 kPa.

Figure 5.12 depicts the effect of fine contents on the injected pore volumes. As can be seen, the injected pore volume of suspensions remains unchanged at the fines content of 5%, indicating that the soils which have less than 5% non plastic fines will have a similar injectability to clean sand. However, the soils with the fines content greater than 5% showed exponential decrease in the injected pore volumes. The results imply that the presence of non-plastic fine negatively affects the groutability of the soil by impeding the grout propagation.

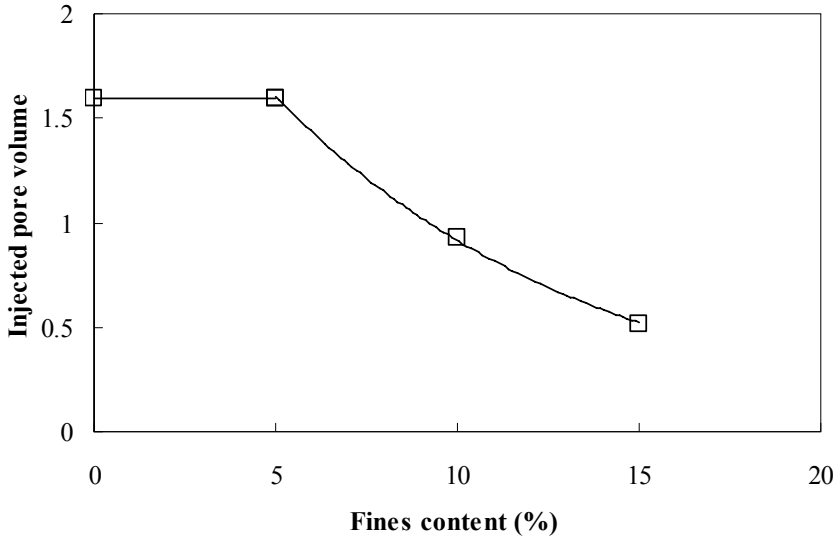

Figure 5.12 Injected pore volume based on fines content of 0, 5, 10, and 15% (by weight of sand) in sands: 7.5% suspension with 1% SPP, d_{10}=0.20 mm, Dr=30% and P=140 kPa

Figure 5.13 shows the comparison of the injected pore volumes at 140 kPa and those at 35 kPa. As the injection pressure increased, the injected pore volume increased approximately 1.4 to 1.8 times. However, the increase in the injected pore volumes was not proportional to the applied pressure at all grouts due to filtration which is a function of particle fraction. The filtration process may be promoted by separation of particles and water and accelerated by high pressures (Akabulut, 1999), causing reduced effect of high pressure on the injected pore volumes. Due to the phenomenon, "filter cake" was formed at the bottom of the sand columns.

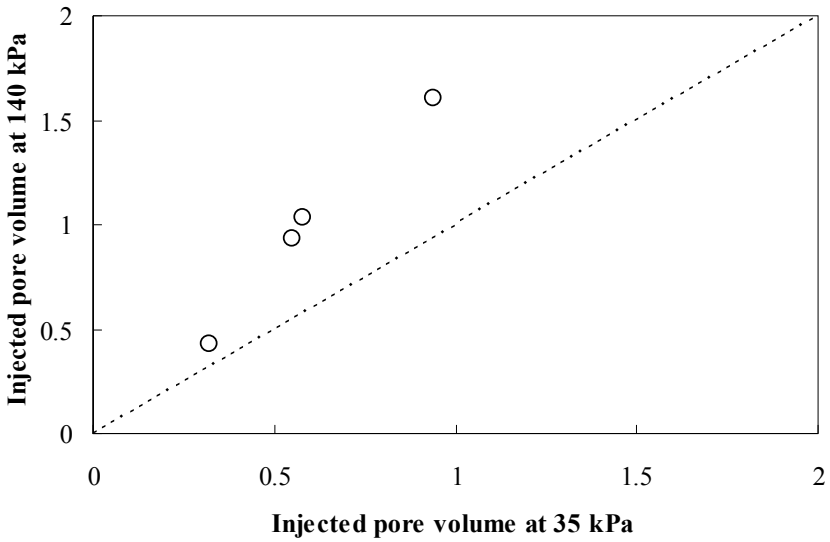

Figure 5.13 Comparison of injected pore volume from different injection pressures of 35 and 140 kPa: 7.5, 10, and 12% suspensions with 1, 3, and 4% SPP, and 7.5% unmodified suspension, FC=0%, d_{10}=0.20 mm, and Dr=30%

5.2.3. Penetration distance

Figure 5.14 shows the penetration distance based on bentonite fraction. Similar to the injected pore volumes, the modified suspensions produced an increased penetration distance through sands. Especially, 7.5% suspension with 1% SPP could penetrate the whole length of specimen (15.5 cm) at the low pressure of 35 kPa.

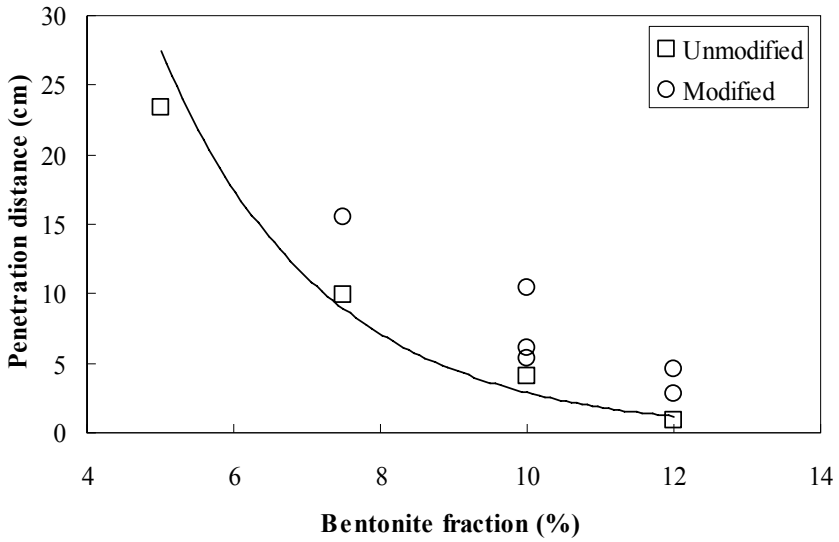

Figure 5.14 Penetration distance with bentonite fractions at various types of grouts: 7.5, 10 and 12% suspensions with 0 to 4% SPP, d_{10}=0.20mm, Dr=30%, FC=0%, and P=35 kPa

When the grout was injected through sand with a large effective grain size, the penetration of grouts significantly increased as shown in Figure 5.15. The 12% suspension with 4% SPP could be injected up to 45 cm through Monterey #0/30 sand (d_{10} of 0.3 mm) at the injection pressure of 140 kPa compared to 0.2 and 6.4 cm through Nevada and Ottawa sand (d_{10} of 0.12 and 0.2 mm respectively). However, the penetration distance did not very significantly with the relative density of soil. Figure 5.16 depicts a comparison of the penetration distance at two different relative densities. As can be seen, both the relative densities produced similar penetration distances.

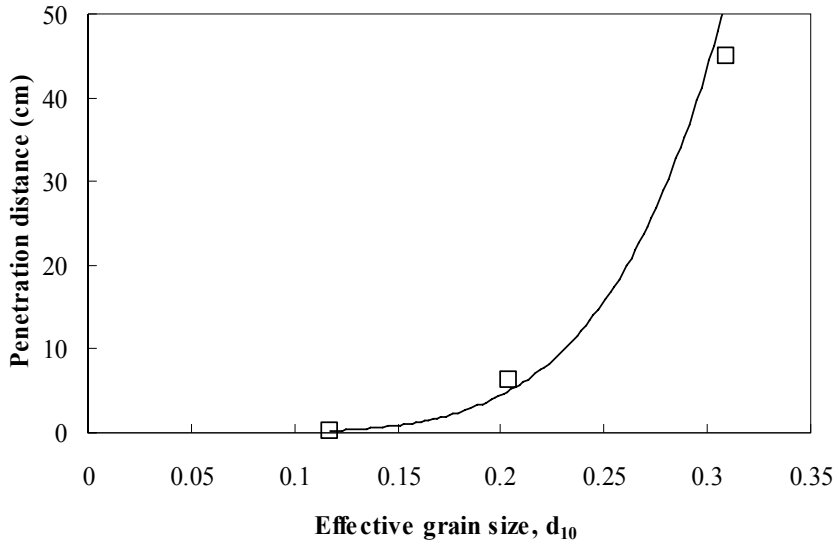

Figure 5.15 Penetration distance based on effective grain sizes of sands: 12% suspension with 4% SPP, FC=0%, Dr=30% and P=140 kPa

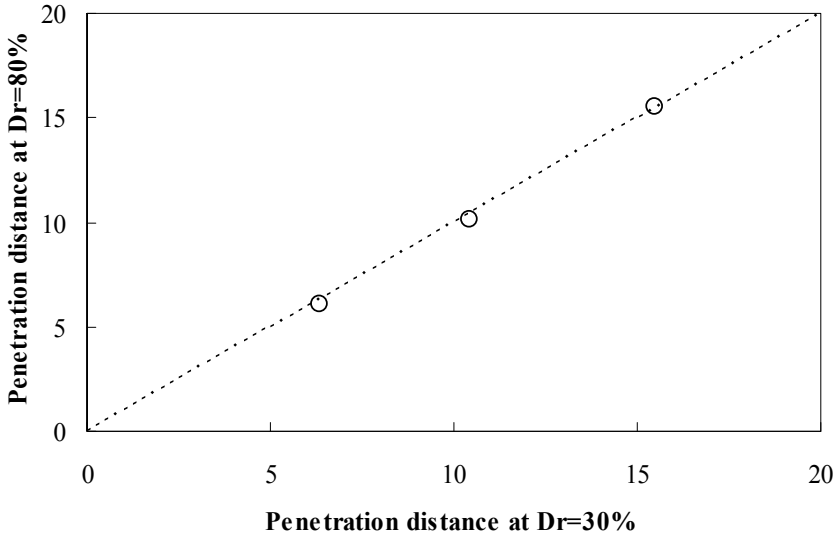

Figure 5.16 Comparison of penetration distance from different relative density of sands: 7.5, 10, and 12% suspensions with 1, 3, and 4% SPP, FC=0%, d_{10}=0.20 mm, and P=35 kPa

The presence of fines in sand reduced the penetration distance of the grouts as shown in Figure 5.17. The sand including 5% fines did not produce a significantly different penetration distance. However, the penetration distance greatly decreased with fine contents beyond 5% with a high non-linearity. Ozgurel and Vipulanandan (2005) observed the similar high non-linearity of injection pressure depending on fine contents with a chemical (acrylamide) grout. Figure 5.18 shows the comparison of the penetration distance at 140 kPa and those at 35 kPa. As the injection pressure increased, the penetration distance increased significantly. The pressure effect was pronounced at the suspensions with low bentonite fraction compared to those having high bentonite fraction.

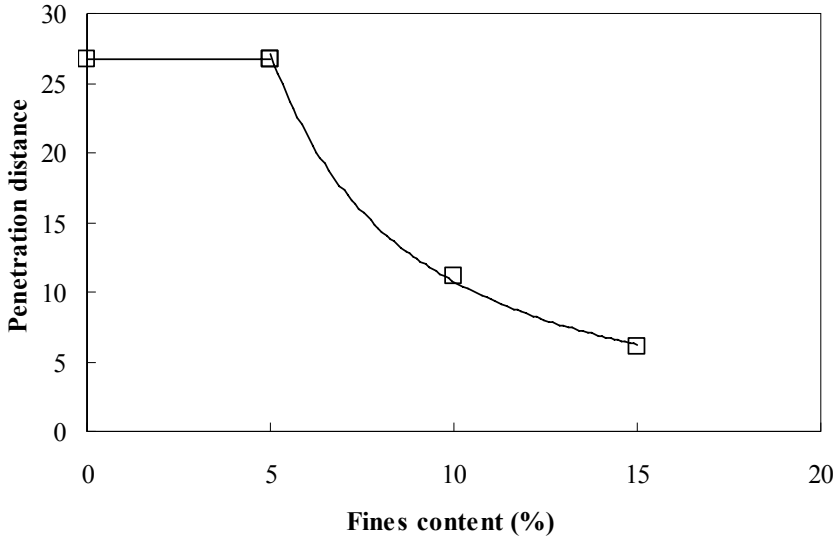

Figure 5.17 Penetration distance based on fines content of 0, 5, 10, and 15% (by weight of sand) in sands: 7.5% suspensions with 1% SPP, d_{10}=0.20mm, Dr=30% and P=140 kPa

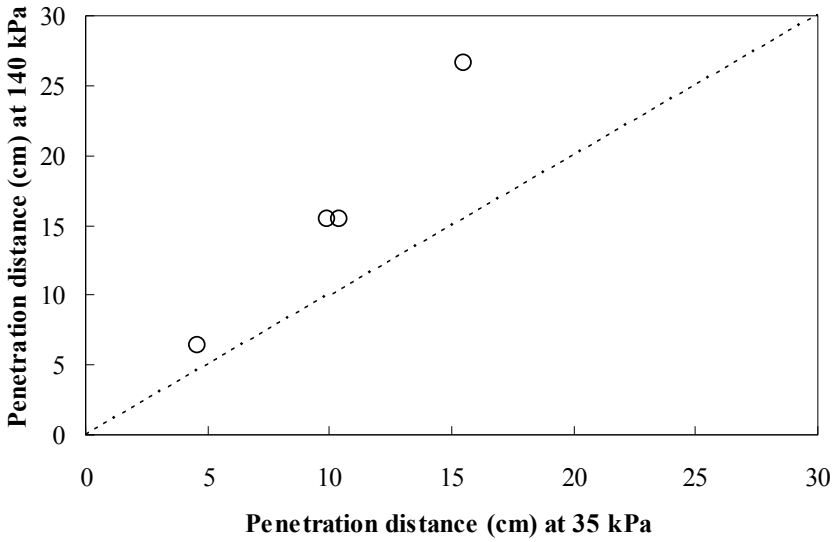

Figure 5.18 Comparison of penetration distance from different injection pressures of 35 and 140 kPa: 7.5, 10, and 12% suspensions with 1, 3, and 4% SPP, and 7.5% unmodified suspension, FC=0%, d_{10}=0.20 mm, and Dr=30%

5.3. Constant flow rate injection

During the constant pressure injection technique, the suspension flow stopped at relatively short time, producing low penetration distance and injected pore volume. Alternatively, a constant flow rate technique has been widely adopted for the permeation of particulate grouts since it retards the formation of filter cakes, increasing the penetration distance. In this study, a series of tests were conducted to characterize the effect of soil and suspension parameters in injection pressure at different pore volumes.

The 7.5, 10, and 12% bentonite suspensions modified with 1, 3 and 4 % SPP were utilized for injection tests based on the optimum combination of bentonite and SPP obtained from the rheological tests. However, it was a concern that the bentonite suspensions produced different flow rates due to the different apparent viscosities. In order to confirm constant flow rate of pump, the actual pump rate was monitored with

various bentonite suspensions permeated through Ottawa sand with the relative density of 30%. As shown in Figure 5.19, the peristaltic pump used for this study produced relatively constant flow rate which was similar to the designated pump rate of 1.67 cm^3/sec regardless of concentrations of suspensions.

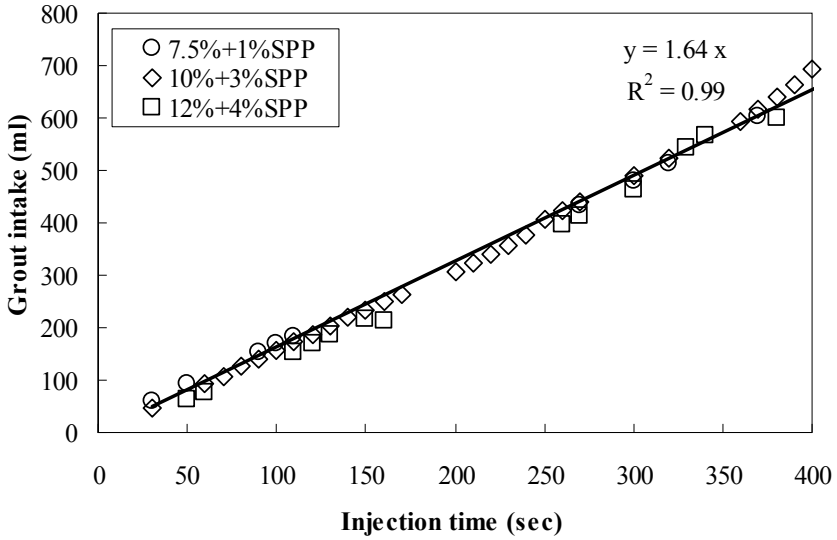

Figure 5.19 Grout intake based on injection time for various suspensions: Ottawa sand (d_{10}=0.20 mm), Dr=30% FC=0%, q=1.67 cm^3/sec, L=25.4 cm and 2 pV

Figure 5.20 shows injection pressure variation at different sand (Ottawa and Monterey #0/30 sand) and bentonite suspensions. As can be seen, all suspensions could be injected up to 2 pV in both sands below the pressure limit of 140 kPa. The injection pressures increased linearly as time elapses. This was expected since the pressure gradient is proportional to the flow rate when Darcy's law is valid. No observable filer cakes are formed. This implies that the constant flow rate technique retards the formation of bentonite filter cakes, and therefore, more suspension could be injected by using this method than the constant pressure technique.

The suspensions with high bentonite fraction showed a larger buildup in injection pressures. However, the injection pressures for all suspensions were much lower in Monterey #0/30 sand than those in Ottawa sand. Even the thickest suspensions (12% suspension with 4% SPP) exhibited a low final injection pressure (less than 35 kPa) compared to those in Ottawa sand. This was expected since Monterey #0/30 sand has a larger effective grain size (0.3 mm) compared to Ottawa sand (0.2 mm). Due to the lager pore space, the suspensions could flow easily without developing a significant pressure.

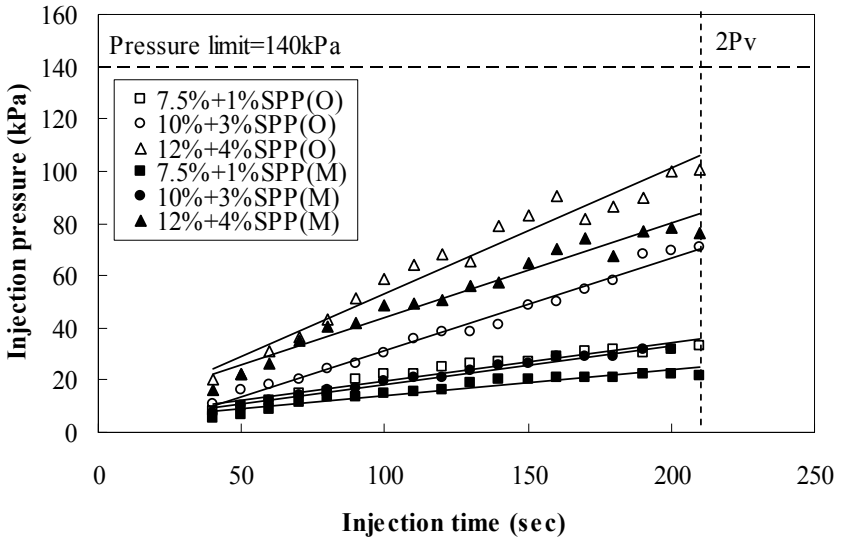

Figure 5.20 Injection pressure build-up with time for various suspensions: Ottawa (O) and Monterey #0/30 (M) sand (d_{10}=0.20 and 0.31 mm), Dr=30% FC=0%, q=1.67 cm^3/sec, L=14 cm and 2 pV

The injection pressure increased with an increase in relative density. Figure 5.21 depicts the comparison of injection pressure buildup with time at the relative density of 30 and 80% at Ottawa sand. At the relative density of 30%, all three suspensions could be injected up to 2 pore volumes (pV) below the pressure limit of 140 kPa. In dense

specimens (Dr=80%), the overall injection pressure increased compared to the loose specimens (Dr=30%). This is because the dense specimens require applying a higher pressure to maintain the constant flow rate due to smaller pore size (Akbulut and Saglamer, 2002). While two types of suspensions (7.5 and 10% suspensions with 1 and 3% SPP) could be injected at the relative density of 80% below the pressure limit, the 12% suspensions modified with 4% SPP could be injected only up to 1 Pv under the pressure limit; injecting additional suspensions resulted in high pressures exceeding the pressure limit. In addition, the time to reach 2 pV slightly decreased due to the small porosity of the dense specimen.

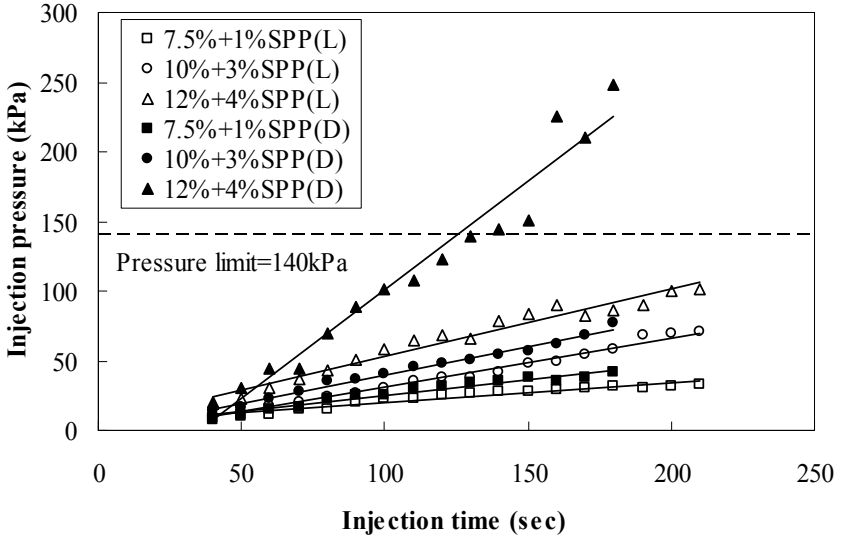

Figure 5.21 Injection pressure with time for various modified suspensions: Ottawa sand (d_{10}=0.20 mm), Dr=30 (L) and 80% (D) FC=0%, q=1.67 cm^3/sec, L=14 cm and 2 pV

The pressure buildup is also influenced by the applied flow rates. Figure 5.22 displays variation in injection pressure with time at two different flow rates of 0.33 and 1.67 cm^3/sec. Although the pressure buildup was still affected by the type of suspensions, the injection pressures were significantly reduced when the lower flow rate

(0.33 cm^3/sec) was applied. However, the time to reach a certain pore volume (1 pV) was also greatly increased (approximately 5 times). The results imply that the flow rate in the field should be determined considering both time for treatment and the injection pressure. While the use of the lower flow rate may reduce the pressure buildup, the rheological properties of suspensions will be changed with time (apparent viscosity and yield stress increases with time).

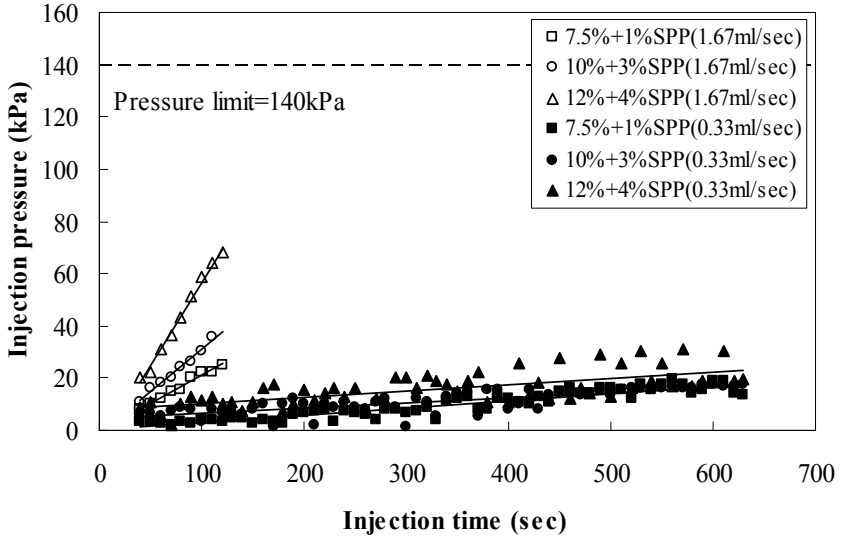

Figure 5.22 Injection pressure with time for various modified suspensions: Ottawa sand (d_{10}=0.20 mm), Dr=30%, FC=0%, q=0.33 and 1.67 cm^3/sec, L=14 cm and 1 pV

The effect of fines content on the injection pressure was studied by mixing non plastic fines with Monterey #0/30 sand. Figure 5.23 shows the pressure variation in the mixed specimens having different fines content. Due to the presence of fines, the measured pressures showed high variability, but it was clearly shown that the presence of fines impeded the flow of suspensions through the specimens, increasing the injection pressures. Even with 5% fines content, the injection pressure greatly increased and more significantly increased as the fines content increases.

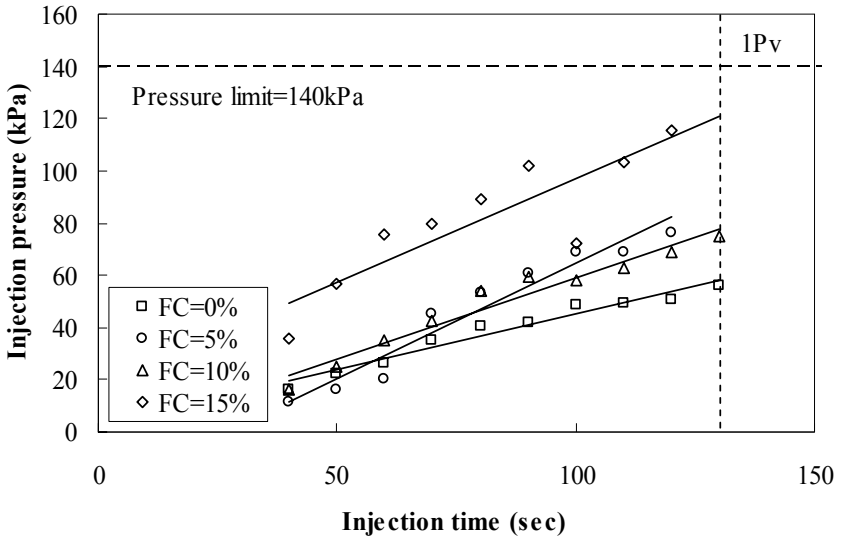

Figure 5.23 Injection pressure with time for 12% suspensions modified with 4% SPP: Monterey #0/30 sand (d_{10}=0.30 mm), Dr=30%, FC=0, 5, 10 and 15%, q=1.67 cm^3/sec, L=14 cm and 1 pV

In order to apply the modified suspensions in larger scale, the bentonite suspensions were injected into a longer permeameter. Figure 5.24 shows the pressure variation with time at various modified suspensions at 1 foot permeameter. As can be seen, two types of suspensions (7.5 and 10% suspensions modified with 1 and 3% SPP) could be injected below the pressure limit, but the unmodified 7.5% and 12% suspensions modified with 4% SPP could not be injected under the pressure limit. This result was different from what was observed in the short permeameters. This effect may be attributed to the fact that the long permeameter may have a localized variation in density than short permeameter which affects the permeation of the concentrated suspensions more than the diluted suspensions (see Figure 5.21 and Figure 5.22). In addition, the injection pressure from the middle size permeameter implies that the effect of filtration will be minimal up to 2 Pv since the pressure buildup was not significant.

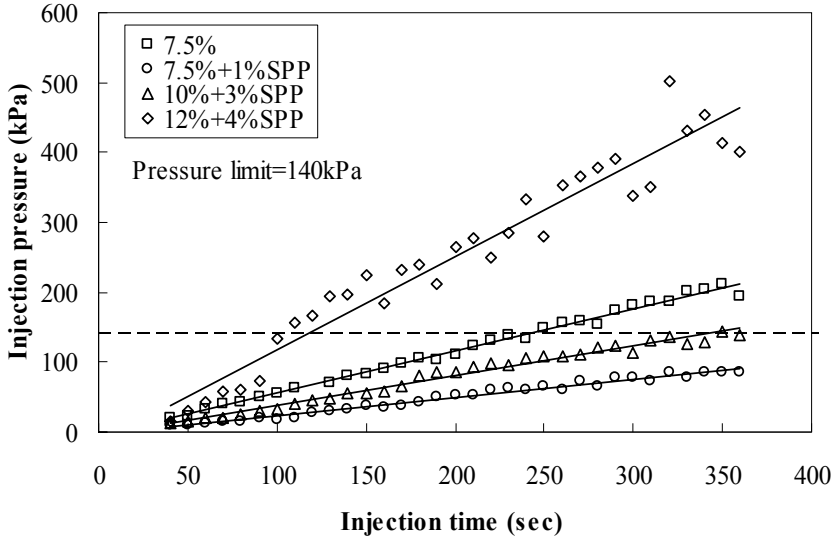

Figure 5.24 Injection pressure variation with time: 7.5, 10 and 12% suspensions with 0 and 1, 3, and 4% SPP at Ottawa sand (d_{10}=0.20 mm), Dr=30%, FC=0%, q=1.67 cm^3/sec and 1 pV

Figure 5.25-5.27 show the pressure variations in different permeameters having different lengths. The 7.5% with 1% SPP displayed compatible results between different permeameters even the injection pressures slightly increased with the increase in the length of permeameter. However, the effect becomes more significant as the bentonite concentration increased.

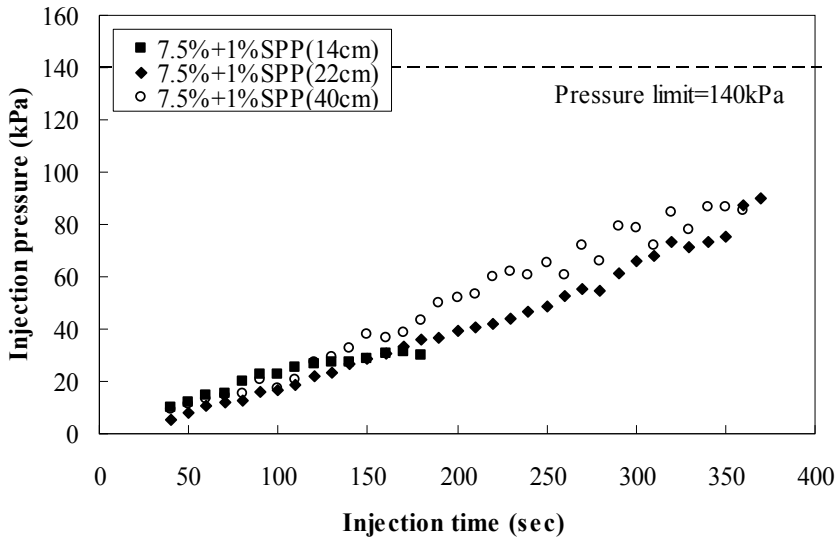

Figure 5.25 Injection pressure variation with time: 7.5% suspensions with 1% SPP at Ottawa sand (d_{10}=0.20 mm), Dr=30%, FC=0%, q=1.67 cm^3/sec and 1 and 2 pV at different length of permeameters

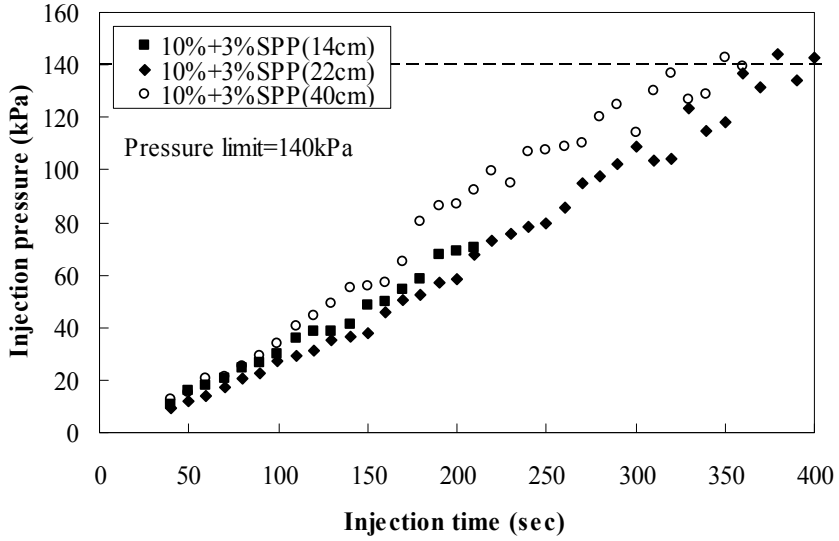

Figure 5.26 Injection pressure variation with time: 10% suspensions with 3% SPP at Ottawa sand (d_{10}=0.20 mm), Dr=30%, FC=0%, q=1.67 cm^3/sec and 1 and 2 pV at different length of permeameters

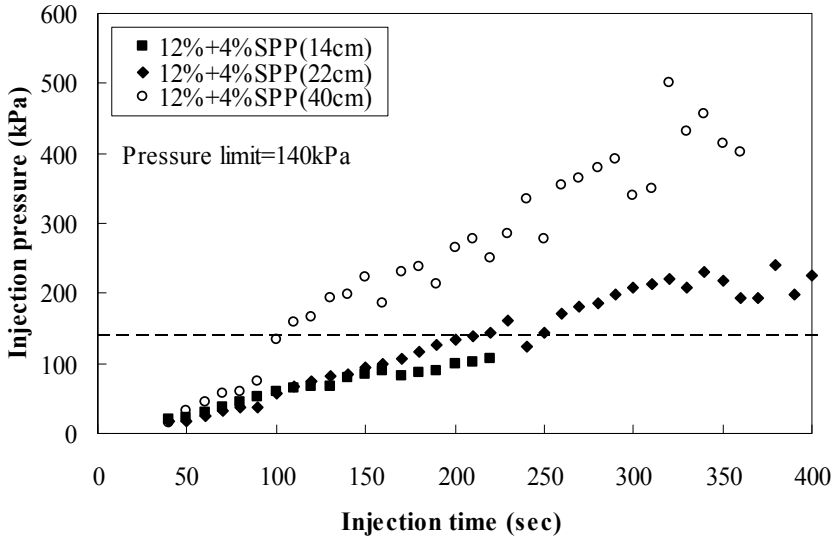

Figure 5.27 Injection pressure variation with time: 12 suspensions with 4% SPP at Ottawa sand (d_{10}=0.20 mm), Dr=30%, FC=0%, q=1.67 cm^3/sec and 1 and 2 pV at different length of permeameters

5.4. Conclusions

Two types of injection techniques were used to investigate the permeation of the modified and unmodified bentonite suspensions through various sands. The results showed that the permeation of the modified suspensions was affected by not only the sand properties, but also grout properties. In addition, the experimental condition such as injection pressure greatly changes the permeation of the suspensions. As the bentonite fraction increased, the grout intake, injected pore volume and penetration distance were significantly reduced. Moreover, concentrated suspensions stopped much faster than the diluted suspensions. With the addition of SPP, the grout intake, injected pore volume and penetration distance were increased, but the extent of the increase was dependent on the amount of SPP added. The larger effective grain size and higher injection pressure increased the grout intake, injected pore volume and penetration distance. The effect of relative density was dependent on the particle fraction; the grout

intake and injected pore volume increased with the diluted suspensions as the relative density increased, but relatively unchanged with the concentrated suspensions for the different relative densities. The penetration distance was little influenced by the relative density. Overall, the effect of relative density was thought to be relatively small in the grout intake, the pore volume and penetration distance. However, the high relative density produced more gradual retardation of the suspension flow due to the reduced filtration.

The pressure variation from the constant flow rate tests showed a linear increase in the injection pressure with time. The injection pressures increased more steeply in the concentrated suspensions and soil with smaller effective grain size (Ottawa sand) than the diluted suspensions and soil with larger effective grain size (Monterey #0/30 sand). The dense specimens showed higher injection pressures than the loose specimens and the 12% suspensions with 4% SPP could not be injected up to 2 pV through the dense specimens. The application of slower flow rate significantly reduced the pressure buildup during permeation, but increased the time to permeate the whole specimen. Since the increased time may affect the rheological properties of the bentonite suspensions, it was suggested that the determination of an appropriate flow rate should be based on both the injection time and pressures.

The presence of non-plastic fines impeded the suspension flow through soils, developing high injection pressures. The pressure buildup was most significant at the fines content of 15%. The long permeameter revealed that the unmodified 7.5% suspensions and 12% with 4% SPP could not be injected without exceeding the pressure limit, which was contradictory to the results from the short permeameters. Scale effect was investigated by comparing the pressure buildup in different length of permeameters (14, 22, and 40 cm). All types of suspensions showed compatible results between two

permeameters (14 and 22 cm), but the long permeameter showed higher injection pressures, especially when the concentrated suspensions were flushed. This may be attributed to the local variation of relative density in long permeameter.

CHAPTER 6: RESULT-III: HYDRAULIC PERFORMANCE OF GROUTED SAND

6.1. Introduction

This chapter covers the hydraulic performance of grouted sand. The proposed application of bentonite grouts is to form a hydraulic barrier (referred as grout curtain), and therefore, the grouted soils are required to have a low enough (saturated) hydraulic conductivity to significantly reduce the underseepage. However, the hydraulic performance of the grouted sand depends on many variables such as grout mix, bentonite contents, and properties of pore space where water passes. The next sections describe the variation of hydraulic conductivity depending on soil, grout and flow rate.

6.2. Hydraulic conductivity of clean sand

Since the relative reduction in hydraulic conductivity (the ratio of hydraulic conductivity of grouted sand to hydraulic conductivity of clean sand) is more efficient way to evaluate the performance of the grouted sands, hydraulic conductivity of clean sands were initially measured at different relative densities to provide a base line hydraulic conductivity. Figure 6.1 displays hydraulic conductivity of Ottawa and Monterey #0/30 sand at various relative densities. Hydraulic conductivity of both sands decreased with the increase in relative density, and Monterey #0/30 sand produced higher hydraulic conductivity values as compared to Ottawa sand at the same relative density due to its large effective grain size.

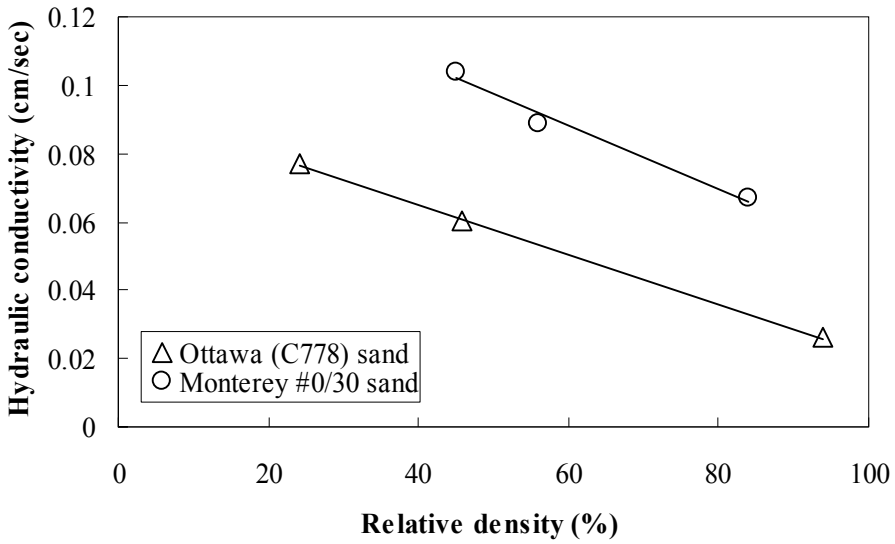

Figure 6.1 Hydraulic conductivity of clean sands at various relative densities

6.3. Hydraulic conductivity of clean sand with non plastic fines

The presence of non plastic fines in soil may not only impede the grout flow, but also affect hydraulic conductivity of the grouted soils. In addition, sand including fines better simulate the field condition since clean sands are not very common. Therefore, the effect of non plastic fines on the hydraulic conductivity of clean sands were investigated and also used for the base line value to estimate the relative hydraulic conductivity of the grouted sands with fines.

Figure 6.2 shows the effect of non plastic fines on the hydraulic conductivity of clean sands. The results are summarized in Table 6.1. Since the soil with the fines content greater than 20% (by the weight of dry sand) may not be possible to be grouted using particulate grouts (Karol 2003), the maximum fines content was limited to 15%. As the fines content increases, the hydraulic conductivity in both sands was reduced and Ottawa sand showed more significant drop in hydraulic conductivity (approximately 2 orders of magnitudes) than Monterey #0/30 sand (approximately one order of

magnitude). This is because Monterey #0/30 sand has larger pore space (due to the larger effective grain size) which is less filled with the given fine contents. Even with 15% fines content, the hydraulic conductivity of Monterey #0/30 sand was greater than that of Ottawa sand without fines. Moreover, the results confirmed that the introduction of plastic fines such as bentonite to clean sand is more effective way to control hydraulic conductivity of clean sand than the use of non plastic fines.

Table 6.1 Summary of hydraulic conductivity of Monterey #0/30 sand

Non-plastic Fines content (%)	Skeletal relative density (%)	Hydraulic gradient	Hydraulic conductivity (cm/sec)
0	30.2	0.2	1.0×10^{-1}
5	29.2	0.6	5.4×10^{-2}
10	31.4	0.6	3.6×10^{-2}
15	30.4	0.6	1.0×10^{-2}

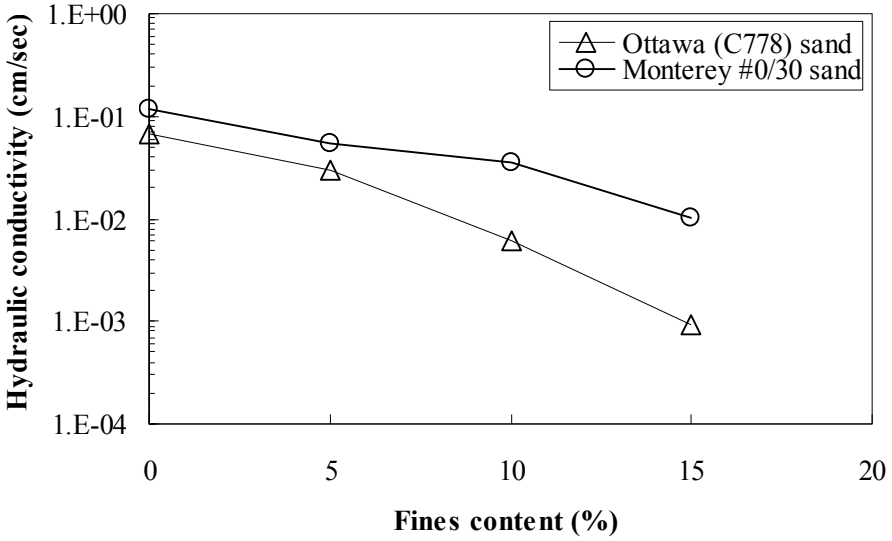

Figure 6.2 Hydraulic conductivity of sands based on non plastic fines content (0, 5, 10 and 15%)

Figure 6.3 shows the comparison of hydraulic conductivity of sand bentonite mixtures (SBMs) and sands mixed with non plastic fines at the similar relative density

(skeletal relative density of 25 to 30%). The sand bentonite mixtures (SBMs) were prepared by mixing of the designated amount of Monterey #0/30 sand with the sieved bentonite powder followed by hand compaction with spraying water to obtain the relative density of 25 to 30% and target bentonite content of 3 to 8%. As can be seen, the hydraulic conductivity of SBMs was more significantly reduced than the sand mixed with non plastic fines even at the low fines content. For instance, the hydraulic conductivity of sand mixed with non plastic fines were reduced approximately factor of 2, but the hydraulic conductivity of the SBMs decreased up to approximately 7 orders of magnitudes at 5% fines content.

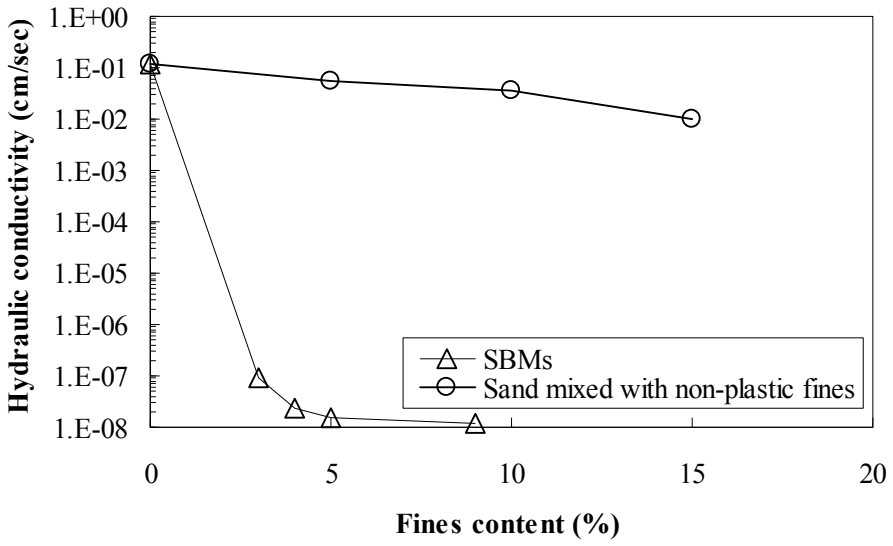

Figure 6.3 Comparison of hydraulic conductivity of SBMs and sand mixed with non plastic fines, Monterey #0/30 sand

6.4. Effect of SPP on hydraulic conductivity

As a preliminary test, the hydraulic conductivity of SBMs prepared by mixing dry sand with SPP modified suspensions were measured to investigate the effect of SPP on hydraulic conductivity. Figure 6.4 shows the hydraulic conductivity change of SBMs

with time. The sand bentonite mixtures are prepared in the same way mentioned in 6.3 with the designated amount of Ottawa sand and the bentonite suspensions. The skeletal relative density of 25 to 30% was controlled by hand compaction at a target bentonite content of 3%. It was observed that the specimens mixed with the modified suspensions consistently produced a slightly higher hydraulic conductivities than those of the specimen mixed with unmodified suspensions. It may be attributed to the fact that the modified suspensions formed bend-like microstructures which consisted of larger pores compared to the unmodified suspensions as shown in Chapter 4. However, the difference was relatively small (within the range of ±25% which is typically acceptable in hydraulic conductivity tests), producing a similar value (approximately 10^{-8} cm/sec) of hydraulic conductivities, concluding that the effect of SPP on hydraulic conductivity is minimal.

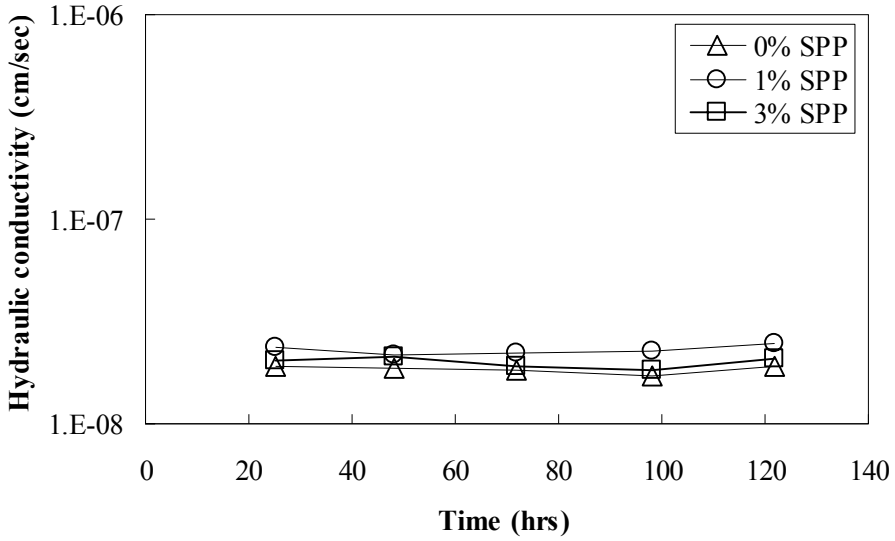

Figure 6.4 Effect of SPP on hydraulic conductivity of SBMs: 12% suspensions modified with 0, 1 and 3% SPP, BC=3%, and Dr =25 to 30%

6.5. Particle fraction in bentonite suspension

Figure 6.5 shows the normalized hydraulic conductivity of the permeated specimens using various particle fractions in bentonite suspensions. As can be seen, hydraulic conductivity of clean sand is reduced 3 to 7 orders of magnitude depending on bentonite fractions in suspensions (lower hydraulic conductivity is produced using suspensions with higher bentonite fractions), indicating that hydraulic conductivity of a clean sand can be effectively controlled by permeation. The lower bentonite fractions could not be tested since they did not produce strong enough specimens which can be self-standing during specimen preparing. However, large variations of hydraulic conductivity were observed even at the same bentonite fraction, because the different suspensions were produced various bentonite contents depending on soil and flow conditions.

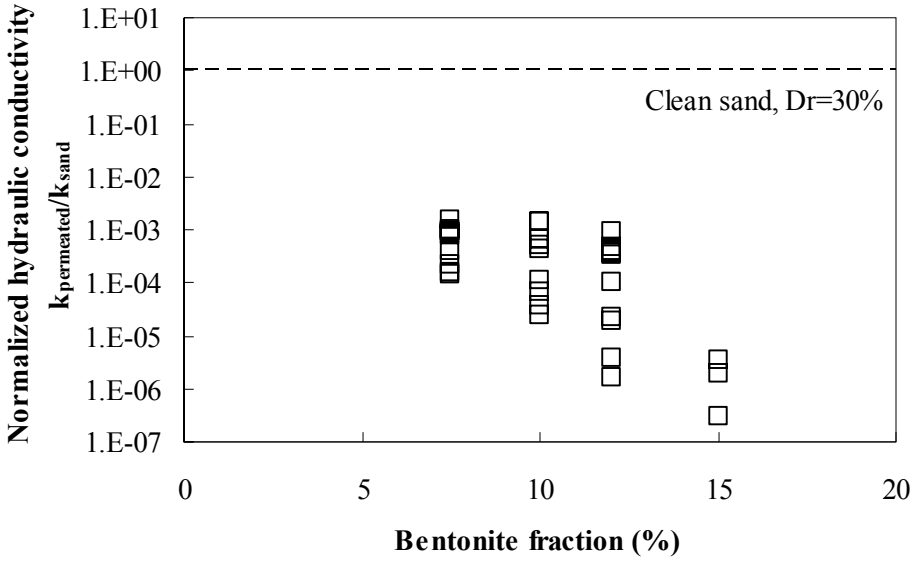

Figure 6.5 Normalized hydraulic conductivity of permeated specimens: 7.5, 10, 12 and 15% bentonite suspensions modified with 1, 3, 4 and 10% SPP, respectively (Normalized hydraulic conductivity of Ottawa sand, Dr=30%, is included for reference)

6.6. Bentonite content

After measuring the hydraulic conductivity, the bentonite content at different sections of the specimen was measured, in accordance with the method presented in Chapter 3, to investigate: 1) the retained bentonite content produced in the specimen and 2) particle migration. It was hypothesized that higher bentonite contents would be observed at the upper portion of samples if a particle migration occurs; however, the lower portion of most of the sample retained higher bentonite contents than the upper portion. Based on this hypothesis, it was assumed that no particle migrations occurred at the hydraulic gradients of 20 to 40 which were used throughout this study.

The bentonite contents varied with various testing conditions such as relative density, flow rate, amount of permeated suspension, particle fractions in suspensions injected, and distance from injection points. Figure 6.6 shows the bentonite content at various particle fractions in suspensions. Bentonite content tended to increase with the increase of bentonite fractions in suspensions. However, bentonite contents varied significantly even at the same particle fraction depending on testing conditions such as the amount of suspensions permeated into the sand, relative density, and the injection flow rate.

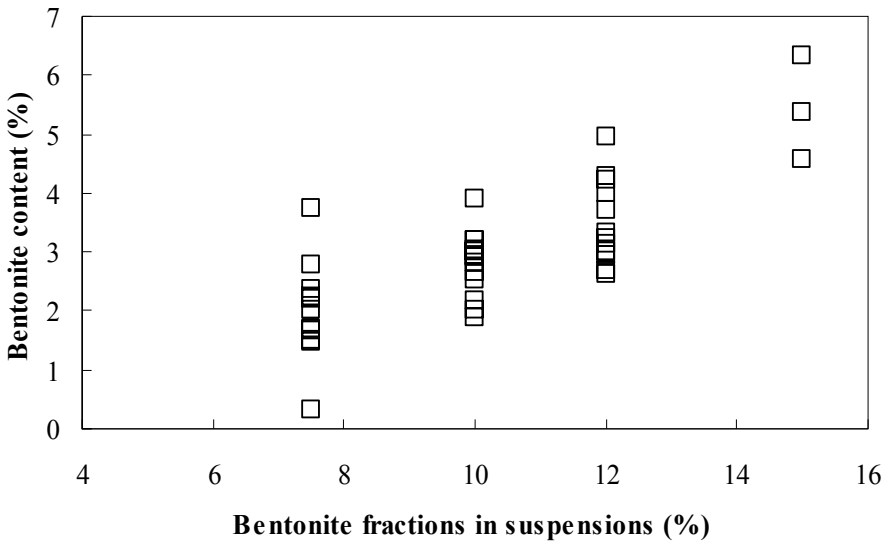

Figure 6.6 Bentonite content at various bentonite fractions in suspensions

As shown in Chapter 5, the properties of the grout and porous media change the characteristic of particle deposition (referred as to filtration) during the permeation process, producing various bentonite contents in the sand. Figure 6.7 shows bentonite contents versus bentonite fraction for specimens that were injected with 1 and 2 pore volumes (Pv). The flow rate was maintained at 1.67 cm^3/sec. The injection of 2 pore volume consistently produced 10 to 20% higher bentonite contents than the 1 pore volume. However, the increase in bentonite content was greater at higher bentonite fractions than at lower ones.

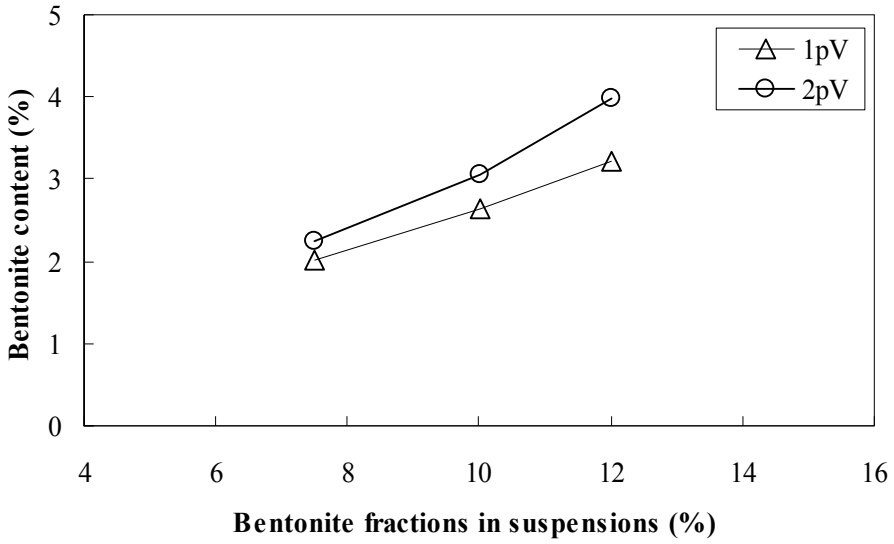

Figure 6.7 Bentonite content of various bentonite fractions in suspensions at the injected pore volume of 1 and 2 pV

The relative density of sand also affects the bentonite contents as shown in Figure 6.8. At the same flow rate, 2 pV of suspensions were injected into sands having two different relative densities of 30 and 80%. The bentonite content decreased approximately 17 to 24% with the increase in relative density. The decrease of bentonite contents in dense sands at the same pore volume attributes to the decrease in pore size that bentonite particles can occupy.

The reduction in flow rate is beneficial to decrease injection pressure, although it significantly increases the injection time. However, the decreased flow velocity retards filtration of particles, leading to smaller bentonite contents. Due to the significant increase in injection time, all suspensions for the tests were permeated up to 1 pV. Figure 6.9 depicts the effect of the flow rate on the bentonite contents. Two flow rates were used in these tests: 0.33 cm^3/sec and 1.67 cm^3/sec. The flow rate of 0.33 cm^3/sec produced the bentonite contents of 10 to 20% less than those from the flow rate of 1.67 cm^3/sec.

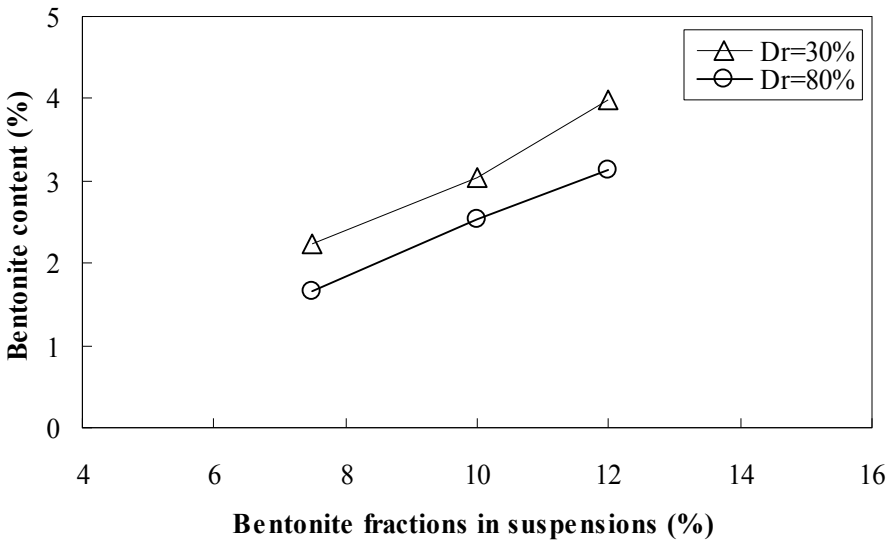

Figure 6.8 Bentonite content of various bentonite fractions in suspensions at the relative density of 30 and 80%

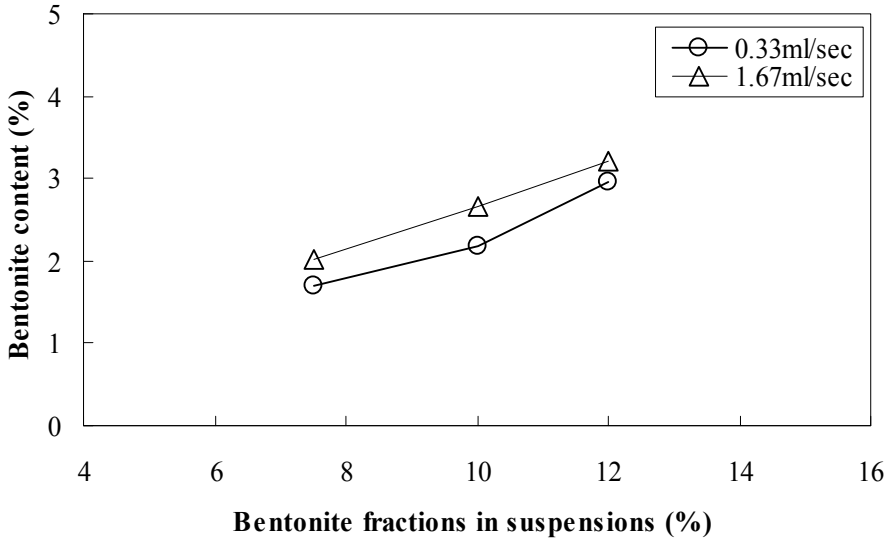

Figure 6.9 Bentonite content of various bentonite fractions in suspensions at the flow rate of 0.33 and 1.67 cm^3/sec and 1pV

A series of tests were conducted with a larger permeation cell (which consists of three split cylinders) to investigate the bentonite contents variation at different distances from the injection point. The permeation cell was utilized to facilitate the handling of

the long specimen, resulting in more accurate measurements of bentonite contents at each distance. As shown in Figure 6.10, the measured bentonite contents consistently decreased in all suspensions as the distance from injection point becomes further. All suspensions exhibited similar reduction of 30 to 35% in bentonite contents from the bottom to the top. However, 7.5% suspension showed larger differences of approximately 50% than other suspensions. This may be attributed to the fact that slightly more suspensions was injected at the bottom of the sand column by the residual flow after termination of testing, collecting more particles. The bentonite contents at the top were similar to those from 1 pV injection.

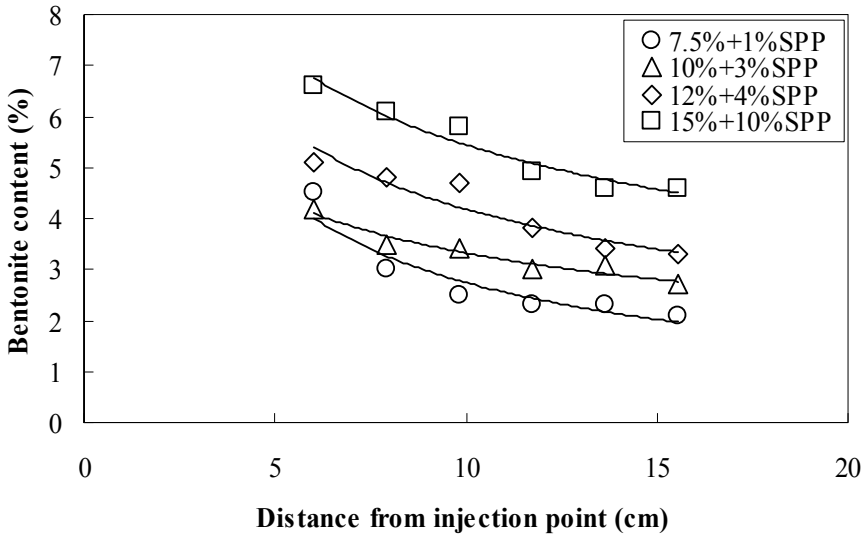

Figure 6.10 Bentonite contents with distance from injection point: 7.5(1), 10(3), 12(4)% and 15(10)% bentonite suspensions at Ottawa sand (d_{10}=0.20 mm), Dr=30%, FC=0%, q=1.67 cm^3/sec and 1pV

Figure 6.11 depicts normalized hydraulic conductivity of the permeated specimens with bentonite contents. The normalized hydraulic conductivity tended to decrease with increasing bentonite content, but it was observed that the normalized

hydraulic conductivity at low bentonite contents was independent of the bentonite content, implying that other factors such as pore properties should be considered to explain water flow through the permeated soils.

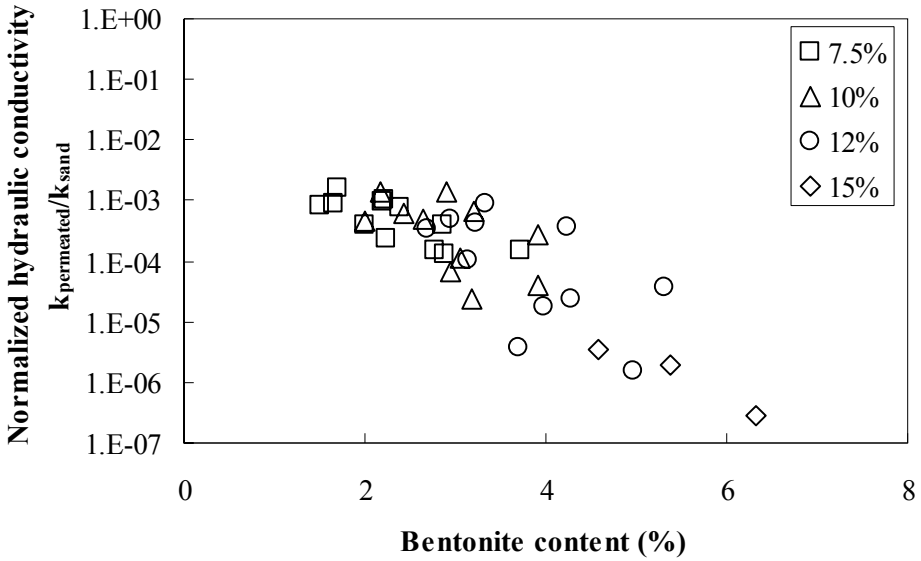

Figure 6.11 Normalized hydraulic conductivity based on bentonite content

6.7. Characterization of pore space

In order to consider the variation of hydraulic conductivity depending on the bentonite content, the physical properties of the pore spaces were investigated because water flow through a mixture is affected by physical pore space formed by sand grains. Depending on degree of clogging of the pore space, the hydraulic conductivity changes significantly. Figure 6.12 shows proportionality of pore space formed by sand grains based on bentonite contents. The changes in pore space with bentonite volume were calculated by assuming bulk saturation of 100% (all pores are occupied by water and bentonite particles without air). The volume occupied by the bentonite was calculated based on the maximum swelling of the bentonite as provided by the manufacturer (8

mL/g). The void space occupied by the bentonite suspensions increased proportionally with bentonite content, showing the different maximum value depending on relative density of the sand. This is reasonable in that the pore space which bentonite can occupy decreases with an increase in relative density.

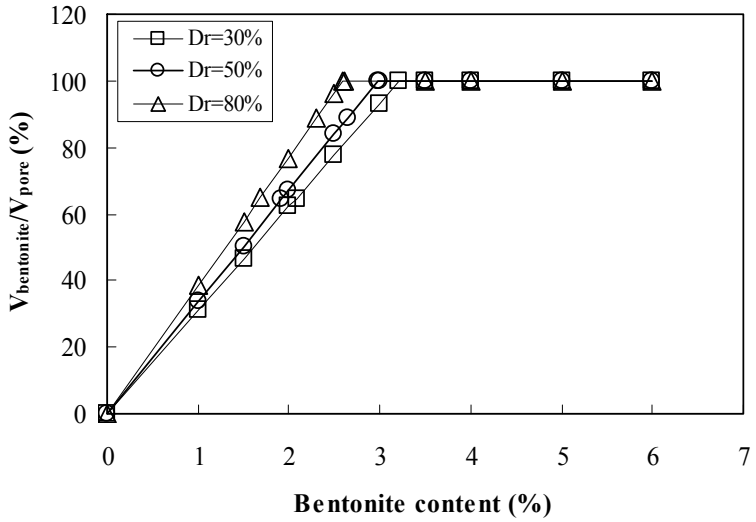

Figure 6.12 Proportionality of pore space with bentonite content: Dr=30, 50, and 80%

To overcome the proportionality of pore space occupant on the relative density, the bentonite content was normalized by BCmax; where BCmax is the bentonite content needed to fill the pore space at a given relative density. Figure 6.13 displays physical pore volume changes due to volume of fully hydrated and swollen bentonite particles with BC/BCmax. This relationship may be useful to explain changes in pore spaces since it does not depend on relative density of given sand, but provide a direct relationship between changes in pore space and bentonite content. Moreover, the normalized bentonite contents are independent of the type of soils and their different grain sizes.

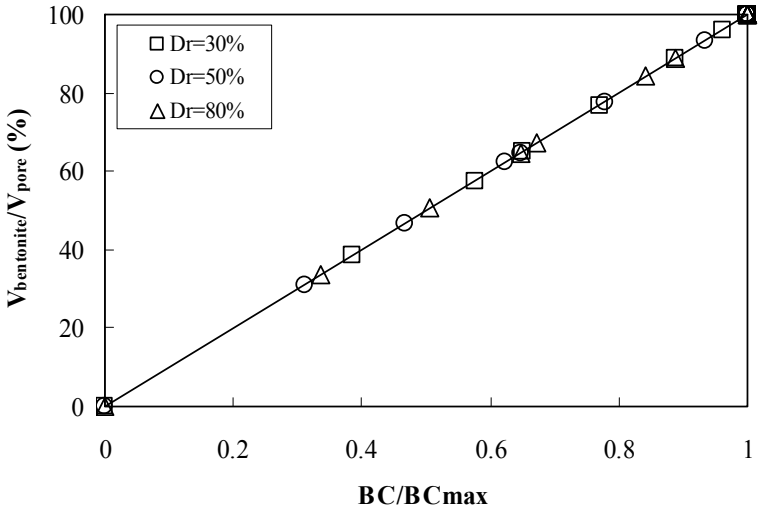

Figure 6.13 Changes in pore space with BC/BCmax: Dr=30, 50, and 80%

Figure 6.14 shows the hydraulic conductivity of the permeated sands based on BC/BCmax. When BC/BCmax is less than 1, it was considered that the pore space formed by sand grains was not fully blocked with the bentonite suspension; therefore, water could flows through the unblocked portion of pore space and is controlled by the hydraulic conductivity of the un-grouted sand (a reduced percentage of that hydraulic conductivity). The hydraulic conductivity tended to decrease as BC/BCmax increased due to reduction in pore space. However, hydraulic conductivity at BC/BCmax greater than or equal to 1 showed large variations, implying that water flows through clay voids rather than pores formed by sand grains.

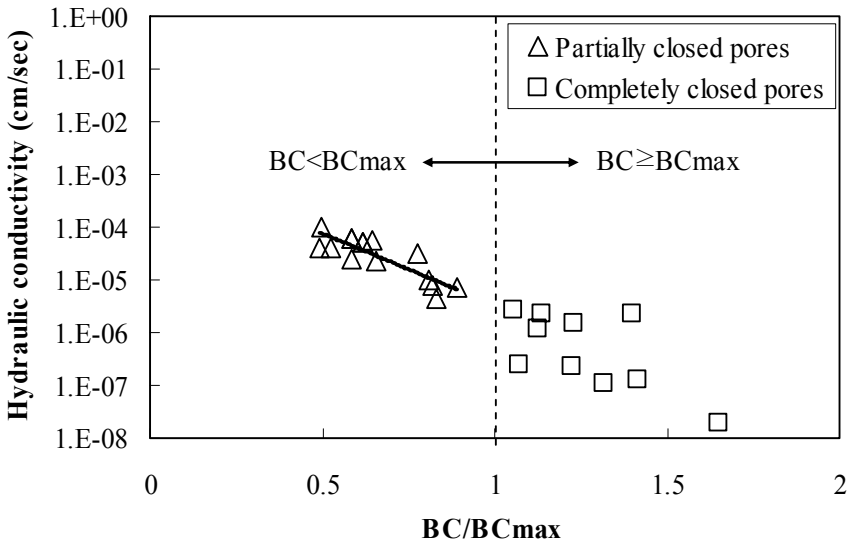

Figure 6.14 Hydraulic conductivity based on BC/BCmax

6.8. Clay void ratio

Once the sand pore is fully blocked with bentonite suspensions, water starts to flow through pores formed by clay particles. This phenomenon can be explained with the concepts of clay void ratio. The clay void ratio was estimated by the ratio between volumes of water and clay. This ratio can be directly related to clay content since it uses the volume of clay. Figure 6.15 shows the relationship between clay void ratio and bentonite content. As bentonite content increased, clay void ratio decreased. It is that the hydraulic conductivity of mixtures of granular material and clay varies linearly with void ratio of clay (Olson and Daniel, 1981; Pandian et al., 1995; Yang and Barbour, 1992; Mollins et al., 1996; Sivapullaiah et al., 2000; Hwang, 2010).

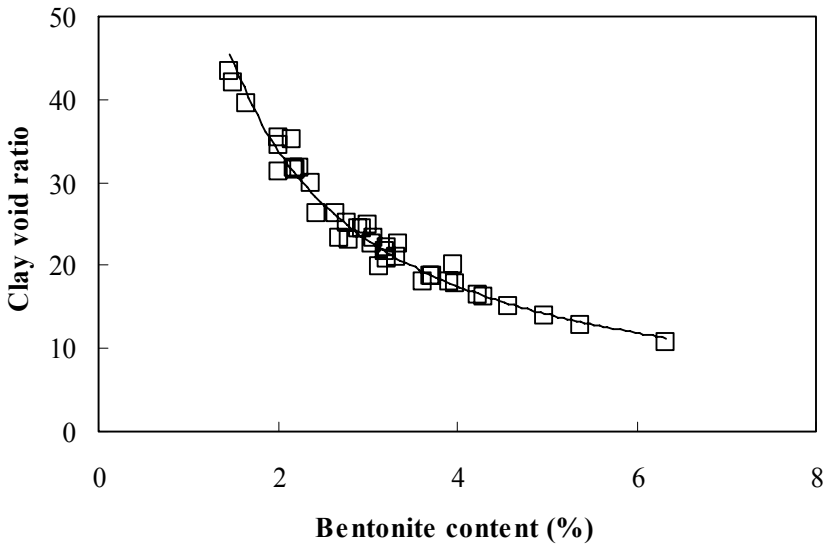

Figure 6.15 Relationship between clay void ratio and bentonite contents

Figure 6.16 displays linear relationship between clay void ratio and hydraulic conductivity for different mixtures. Although sand properties and sample preparation are different in each study, a linearity of hydraulic conductivity was commonly shown. Hwang (2010) used the same sand and bentonite used in this study to prepare SBM specimens. By comparing the results from this study and Hwang (2010) results, the hydraulic conductivity of permeated soils is higher than that of the compacted soils at the same clay void ratio. This is because the permeation process produces less uniform distribution of bentonite particles. Even though all pore spaces are thought to be occupied by bentonite suspensions, a local variation in properties of pore spaces could result if not all the water was replaced by bentonite suspensions, resulting in water channels.

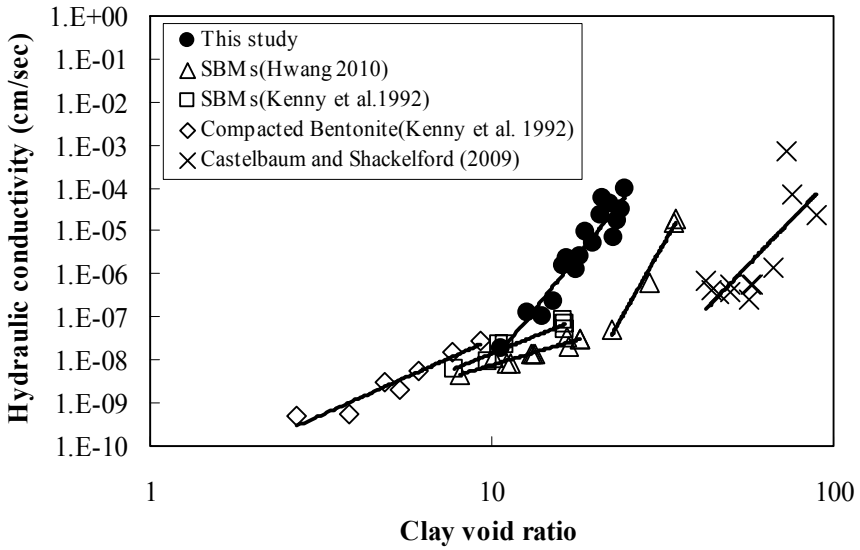

Figure 6.16 Hydraulic conductivity based on clay void ratio

Hwang (2010) reported that the effect of particle distribution on hydraulic conductivity of the dry mixture could produce different hydraulic conductivities by a factor of 2 to 5. Figure 6.17 shows a comprehensive picture of hydraulic conductivity based on characteristics of pore space such as clay void ratio and BC/BCmax. As clay void ratio increase, hydraulic conductivity increases linearly up to approximately 23 (BC≈3%), but hydraulic conductivity does not increase significantly even with very high clay void ratio, indicating most of water flows through the unblocked sand pores.

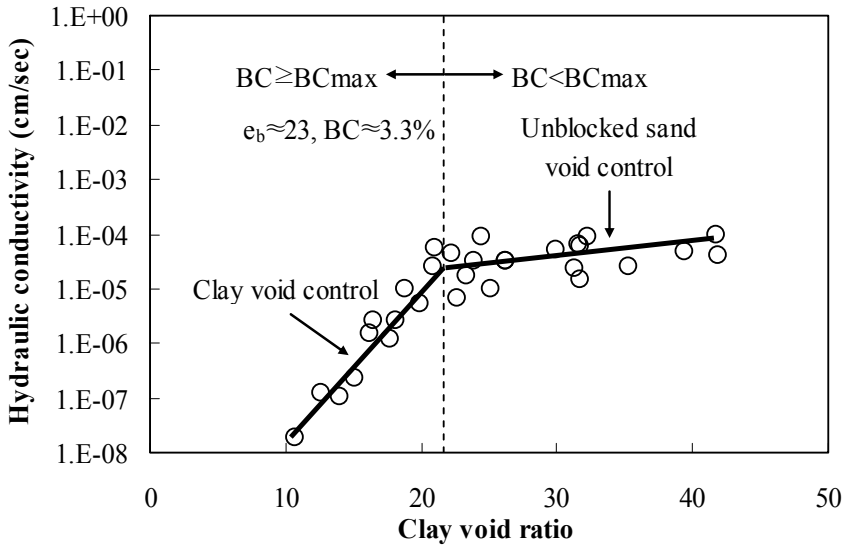

Figure 6.17 Hydraulic conductivity with clay void ratio and BC/BCmax

6.9. Spatial variation of hydraulic conductivity

Since the bentonite content varies with the distance from injection point, hydraulic conductivity changes with the distance from injection point, resulting in variation in hydraulic conductivity with distance. Figure 6.18 shows the variation of hydraulic conductivity at various distances from the injection point. Due to the decrease in bentonite content as the distance increases, the hydraulic conductivity tended to increase with the distance from injection point, followed by converging to a certain value of hydraulic conductivity. The result indicates that the pores at the top were not fully blocked with all bentonite, producing an upper bound hydraulic conductivity (approximately 10^{-5} cm/sec) which is independent of particle fraction in the suspensions (BC/BCmax<1). Moreover, this implies that the increase in the injected pore volume from the same injection point may not be an effective way to control hydraulic conductivity at a certain distance. The difference in the hydraulic conductivity between the top and bottom increased as the bentonite fraction increased reaching up to three

orders of magnitude difference at 12% suspensions. However, less difference was observed in 15% bentonite suspensions due to the high solid contents, implying that highly concentrated suspensions may decrease the spatial variation of hydraulic conductivity by producing high bentonite content through further distances. Moreover, it was observed that the hydraulic conductivities of the specimens from the top tended to converge since the unblocked sand pores controlled the water flow rather than the clay voids.

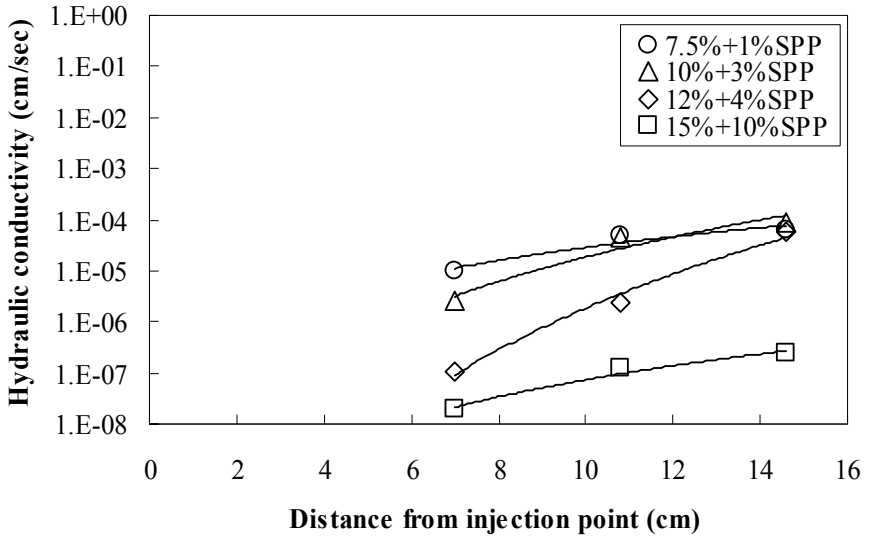

Figure 6.18 Hydraulic conductivity with distance from injection point

6.10. Effect of non-plastic fines on hydraulic conductivity

For field application, the fines included in the in-situ soils may affect the overall fine content after grouting, and therefore, the hydraulic conductivity of the grouted soils. In order to simulate these conditions, non-plastic fines were mixed with Monterey #0/30 sand to produce sands with different fine contents (by weight of clean sand), while forming a skeletal relative density of 25 to 30% as described in section 6.3. 12%

suspensions modified with 4% SPP were injected through the specimens at 1.67 cm^3/sec. Figure 6.19 displays the fines content after permeation tests compared to the fines content before the permeation. At the low fine contents, the overall fine contents increased from 5 to 7.6% due to the presence of the bentonite particles from the suspensions. This can be interpreted that the filling of voids from the injected suspensions was larger than the washing of non plastic fines during injection, although some portion of the fines was still washed during the permeation (the effluents carrying fines were clearly observed during permeation). The 12% bentonite suspensions produced about 3.6% of bentonite contents in clean sand which is greater than the increased amount of fines (about 2.6%). However, the overall fines content more decreased in for sands with higher fines content to start with (approximately 20%) than those with low fines content. This is possibly explained that a large portion of non plastic fines were washed out during injection tests and the amount of washed out fines was greater than that of bentonite particles filling voids.

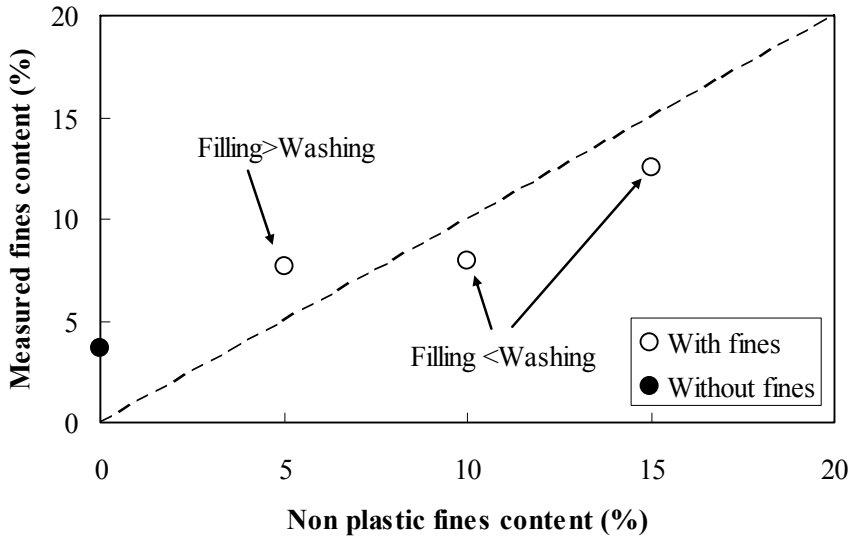

Figure 6.19 Effect of the initial non plastic fines content on overall fines content

Figure 6.20 depicts the comparisons of the relative hydraulic conductivity of the permeated sands with and without fines. The relative hydraulic conductivity was calculated as the ratio of the hydraulic conductivity of the permeated specimen to that of a non-permeated specimen at the same initial non-plastic fines content and relative density. The hydraulic conductivities of the permeated specimens which include fines were lower than those of permeated specimens without fines by a factor of 6 (15% fines), but the relative hydraulic conductivity was similar in both cases, indicating that the effect of non plastic fines on the hydraulic performance of permeated specimens is minimal.

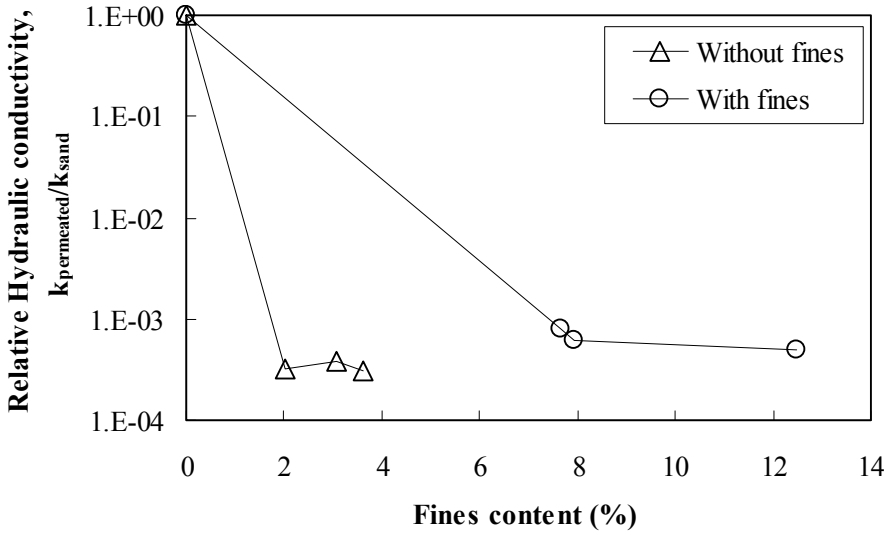

Figure 6.20 Effect of non plastic fines on relative hydraulic conductivity of permeated sand: Monterey #0/30 sand and FC=0, 5, 10 and 15%

6.11. Conclusions

The saturated hydraulic conductivity of the bentonite grouted sand was measured to investigate the hydraulic performance of the grouted sands. The hydraulic conductivity of the permeated sand decreased approximately 4 to 5 orders of magnitude, showing the effectiveness of the bentonite grout to improve the hydraulic performance of

the permeable sand deposits. The hydraulic conductivity decreased with bentonite content but varied with the experimental conditions such as relative density, distances from injection point and the injected pore volumes. However, the hydraulic conductivity at low bentonite content was less affected by the changes in bentonite content because of the physical configuration of the pore spaces. The physical pore changes with bentonite content were calculated based on the volume of fully swollen bentonite and a normalized parameter, BC/BCmax, was proposed to explain the variations in pore space. When BC/BCmax was less than 1, hydraulic conductivity of the permeated sand was controlled by the unblocked pore spaces. However, the hydraulic conductivity linearly increased with logarithmic increase in clay void ratio at BC/BCmax>1, indicating that the water flow occured through the clay voids.

CHAPTER 7: ANALYSIS

7.1. Introduction

This chapter provides a link between the rheological parameters and the flow characteristics of the bentonite suspensions through granular soils. The effect of rheological parameters on the penetration distance and groutability was investigated by constant pressure tests. Moreover, the limited penetration of the suspension was explained based on rheological properties and physical changes in porous medium. Empirical correlations for the groutability was proposed considering rheological and soil parameters to evaluate the possible treatment of a soil with modified bentonite suspensions for field application. An advanced flow model for groutability was adopted and the results were compared to the proposed groutability in this study.

From the constant flow rate technique, the apparent viscosity was back-calculated using the pressure variation at a given penetration distance and flow rate, and compared to the measured apparent viscosity. Different modes of grout propagation (1-D and 3-D) were compared by using numerical and experimental approaches to simulate the field injection of the proposed modified suspensions. Post grouting stability was also studied based on the time dependent evolution of yield stress with a proposed levee configuration.

7.2. Constant pressure injection

7.2.1. Stop mechanisms

The penetration of a grout into soil deposits is limited by the properties of the grout (rheological blocking) and the porous medium (filtration). The rheological blocking occurs when the grout flow is retarded because the reduced pressure gradient

becomes too small to maintain the grout flow through pore channels. In addition, the suspension flow can be limited by the physical changes in the pore space: the reduction in pore channels (deep bed filtration) and blockage of pore entrance with separated particles (pressure filtration).

In the deep bed filtration, grout particles are filtered from the liquid grout by soil grains, retarding grout flow. Due to this phenomenon, the size of the pores gradually decreases, increasing hydrodynamic resistance and gradually causing clogging of the flow channels (Herzig et al., 1970 and Kim and Whittle, 2005). This type of filtration is dominant when the relatively diluted suspensions flow through porous medium. The use of the diluted suspensions to increase penetration depth may promote this type of filtration and could result in a negative effect on the penetration of grouts. The extrusion of the placed suspensions is possible by reversing the flow direction (Herzig et al., 1970 and Guin, 1972) and high injection pressures may help to increase the penetration distance. Since the specific surface area of the bentonite particles is larger than that of the cement particles, the possibility of clogging by this type of filtration may become pronounced in bentonite grouts (Eklund, 2003). The change in flow conditions (i.e. velocity) and chemical properties of the grouts can affect the filtration process. Especially, the increase in ionic strength provides a favorable condition to particle deposition, retarding the grout flow (Rege and Folger, 1988). Rege and Folger (1988) showed that the filtration of bentonite suspensions treated with KCl increased as the concentrations of KCl increased.

On the other hand, water can be separated from a liquid grout when a pressure grouting is used, accumulating particles in front of a filter medium (referred as to pressure filtration). The suspensions will then behave as thick slurry with a rapid increase in viscosity, reducing the penetration of grout through small pores (Landry et al.

2000 referred in Kim and Whittle, 2005). This type of filtration causes the formation of filter cakes close to the injection point. The use of dispersant (improvement of rheological properties in grouts) reduces the formation of filter cakes, resulting in an increase in the penetration distance.

7.2.2. Rheological blocking

Previous researches (Raffle and Greenwood, 1961; Jefferis, 1992; Jancsecz and Steiner, 1994; Gustafson and Stille 1996) proposed that the yield stress of a grout controls its 1-D penetration through porous media and related the yield stress to soil parameters as well as the injection pressure to estimate the maximum penetration distance of the grout. Raffle and Greenwood (1961) suggested the following expression:

$$s = \frac{\Delta P \cdot \alpha}{2.0 \cdot \tau_y} \tag{7.1}$$

Where s is the penetration distance, ΔP (=p-u) is the pressure difference between grout pressure (p) and water pressure (u), τ_y is the yield stress of the grout, and α is the average minimum pore size (1/10 of the average minimum particle size). The German Standard DIN 4126 1986 substitutes α by d_{l0} for tunneling, where d_{l0} is the particle size that 10% by mass of soil is of smaller size (GSL, 2006). Jancsecz and Steiner (1994) proposed a similar formula but with the number 2.0 replaced by 3.5. However, these types of formulas do not take into account the variation of porosity, soil density and grading as well as particle shape. Jefferis (1992) produced an expression considering those factors as follows:

$$s = \frac{\Delta P \cdot d_{10}}{\tau_y} \frac{n}{1-n} \cdot f \tag{7.2}$$

Where s is the penetration distance, ΔP (=p-u) is the pressure difference between grout pressure (p) and water pressure (u), τ_y is the yield stress of grouts, n is the porosity of soil, f is the factor considering the geometry and tortuosity of the flow paths within the soil (typically 0.3) and d_{10} is the effective grain size of the soil.

Gustafson and Stille (1996) produced a theoretical expression of the maximum penetration distance for Bingham fluids considering the specific surface area of soil.

$$I_{\max} = \frac{\Delta P}{\tau_O} \cdot \frac{4}{S \cdot (1-n) \cdot \pi} \tag{7.3}$$

Where, I_{max} is the maximum penetration distance of grout (m), τ_o is the yield stress of grout (Pa), ΔP is the pressure difference (Pa), L is the length of grouted zone (m), n is the porosity of the soil, d_{10} is the effective grain size (m), and S is the specific surface (m^2/m^3). They proposed the estimation of specific surface area based on grain size distribution

$$S = 6 \cdot e^{\left(-\ln d_{10} + 0.84 \ln(U) + 0.21 \ln(U^2)\right)} \tag{7.4}$$

Where, U is the coefficient of uniformity (d_{60}/d_{10}) of the soil.

Figure 7.1 shows the comparison of the calculated penetration distance using the empirical and theoretical expressions with the experimental data (from constant pressure injection) based on the yield stress and soil parameters (effective grain size, specific surface and porosity) measured in this study. At the moment of the maximum penetration, the effluent flow velocity approaches zero, indicating that the apparent (wall) shear rate becomes zero (equation 7.6). As a result, the flow can not be mobilized due to yield stress. The calculated penetration distances at high yield stresses (greater than 20 Pa) tended to produce relatively good agreement with the observed penetration distances, indicating that the yield stress controls the stoppage of the suspension flow. All of the expressions predicted a higher penetration distances at the range of low yield

stress (less than 20 Pa) than the measured penetration distances. This implies that the flow stoppage of the modified bentonite suspensions with yield stresses lower than 20 Pa may be controlled by filtration rather than rheological blocking.

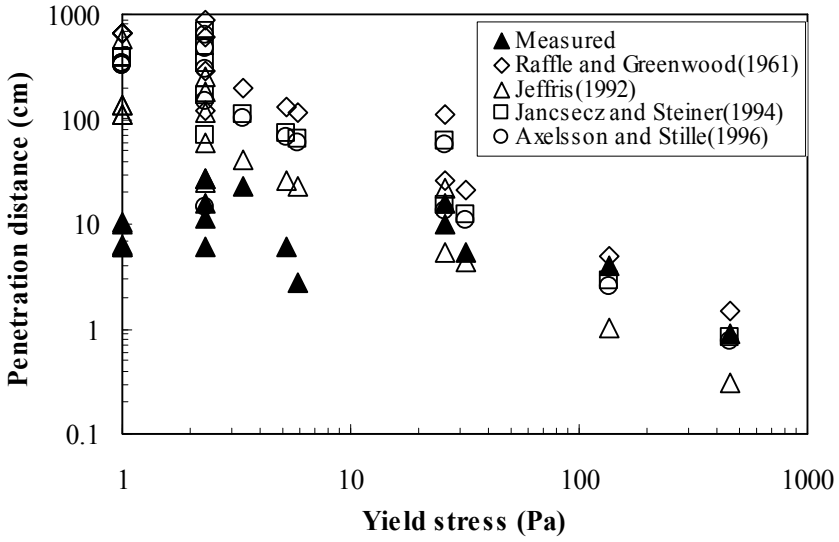

Figure 7.1 Measured and calculated penetration distance based on yield stress

However, the filtration is still influenced by the rheological properties of the suspensions. The modified suspensions produced consistently higher penetration distances than the unmodified suspensions as shown in Figure 7.1. The increase in the penetration distance with the modification at the same bentonite fractions may be attributed to the fact that the flocculated network structures (contributing to yield stress) formed by bentonite particles impeded the penetration of the suspensions though the porous medium. Since the SPP disrupts the formation of the network structures, the modified suspensions includes more delaminated particles than the unmodified suspensions, reducing the possibility of blocking the flow channels.

The penetration distance of the modified suspensions also showed a dependency on particle fractions, leading to different penetration distances even at the very low yield

stresses. For example, by comparing 10 and 12% suspensions with 3 and 4% SPP, respectively, both suspensions had comparable yield stresses but produced different penetration distances (Figure 7.2). This difference is because the presence of the different amount of particles produces different rate of particle deposition (Coussot, 2005 and Dupla et al., 2005). In addition, the suspensions with high bentonite fractions increase the pressure filtration compared to the suspensions with low bentonite fractions, resulting in faster stoppage of flow.

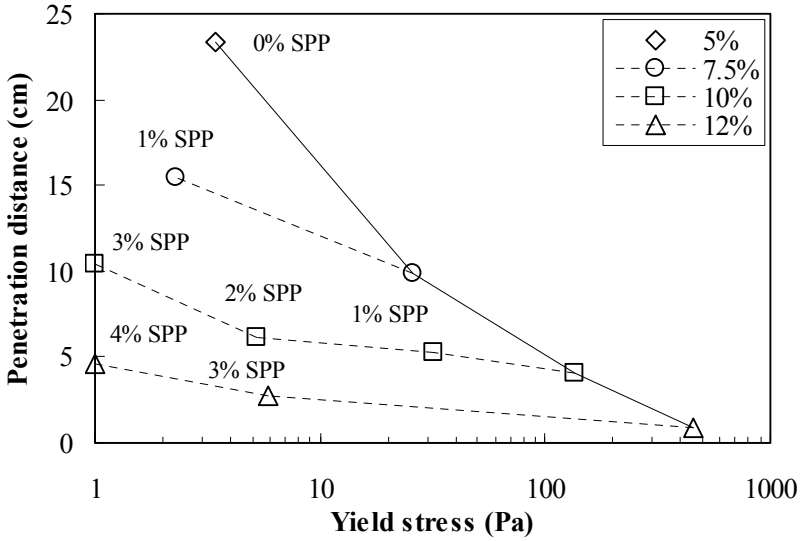

Figure 7.2 Penetration distance based on yield stress (the solid line is for the unmodified grouts (0% SPP) and the dashed line is for the modified grouts)

Rheological blocking can also be explained with rheological models (e.g. Herschel-Bulkley and Bingham). Based on the models, the apparent viscosity of Non-Newtonian fluids consists of two components such as yielding and viscous component (De Paoli et al., 1992a). By using the Herchel-Bulkley model, the yielding and viscous component can conceptually be expressed as follows:

$$\underbrace{\frac{\tau}{\dot{\gamma}}}_{\text{Apparent viscosity}} = \underbrace{\frac{\tau_y}{\dot{\gamma}}}_{\text{Yielding component}} + \underbrace{\frac{K\dot{\gamma}^n}{\dot{\gamma}}}_{\text{Viscous component}} \qquad (7.5)$$

Where τ_y is the yield stress, K is the flow consistency index and n is the flow behavior index. The yielding component decreases with an addition of SPP, followed by increasing the viscous component as shown in Figure 7.3. At a high dosage of SPP, the apparent viscosity becomes totally dependent on the viscous component, which is highly dependent on particle fractions (Coussot, 2006). Due to the different degree of the viscous component, the penetration of suspensions varies at the similar yield stresses.

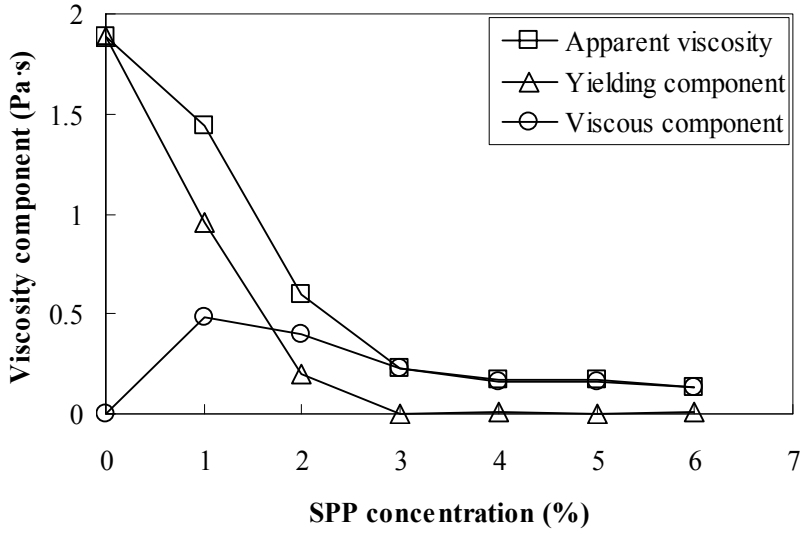

Figure 7.3 Contribution of yielding and viscous component in apparent viscosity (12% suspensions with 0 to 6% SPP) at the shear rate of 250 s^{-1} (fitted to the data from stress ramp tests)

The Herschel-Bulkley parameters and R^2 values are presented in Table 7.1. The yield stresses consistently decreased with the increase in the dosage of SPP, but the flow consistency and flow behavior indices did not show any consistent trends. This result is similar to what Kelessidis et al. (2007) found in bentonite suspensions with a wide range of pH values. In addition, they reported that the effect of electrolytes on the suspension flow could not be fully captured by the rheological behavior of bentonite suspensions (n).

Table 7.1 Herschel-Bulkley parameters for 12% suspensions

Grout mix	τ_y	K	n	R^2
12	471.1	0.001	1	0.993
12(1)	238.9	0.48	1	0.998
12(2)	49.5	8.70	0.52	0.999
12(3)	1.0	3.87	0.59	0.999
12(4)	1.3	0.86	0.76	0.999
12(5)	1.0	0.53	0.78	0.999
12(6)	1.1	0.39	0.81	0.999

* Numbers in the parenthesis are SPP concentrations (by weight of dry bentonite)
** The experimental data was fitted to the model within the shear rate range of 10^{-5} to 500 s^{-1}
*** The yield stresses presented herein are slightly different from the numbers presented in Chapter 4 since they are calculated based on model fitting and not the graphical method proposed in Chapter 4.

A single parameter, either yield stress or particle fractions (or viscous component), is not able to fully capture the stoppage of the various suspensions having both the yield and viscous components, since there is still a contribution of yield stress to the flow resistance by providing an additional drag forces even when the viscous component is dominant. The additional resistance may contribute to retard the suspension flow, increasing the filtration. In order to consider both effects, the apparent viscosity, which includes both parameters, was correlated to the penetration distance.

The apparent viscosity of Non-Newtonian fluids is strongly affected by the shear rate applied (as compared to the apparent viscosity of Newtonian fluids which is independent on the shear rate). However, the apparent viscosity of bentonite

suspensions tends to approach a steady state at high shear rates (Figure 7.4). In order to take into account the shear rate effect on the apparent viscosity, apparent shear rates through porous media was approximated by shear rates at the wall of the round tube (Metzer and Reed, 1955):

$$\dot{\gamma}_a = \left(\frac{3n+1}{4n}\right)\left(\frac{8V}{D}\right) \tag{7.6}$$

Where n is flow behavior index from power law equation, V is the velocity of pore fluids, and D is the diameter of capillary tube. Since the modification of bentonite suspensions changed the flow behavior to close to power law fluid (the yield stresses approached very small values (less than 1 Pa)), the n values can be obtained by matching the experimental data to the power law model. This approximation produced a range of the average shear rates of 250 to 450 s^{-1} for 7.5, 10 and 12% suspensions with 1, 3 and 4% SPP, respectively, where the apparent viscosity approximately approaches equilibrium values as observed in the experiments. Although the shear rates decrease as flow stops, the equilibrium values were adopted as representative apparent viscosities of bentonite suspensions during permeation because the initial penetration of bentonite suspensions with a high velocity mainly controls the penetration of the suspensions.

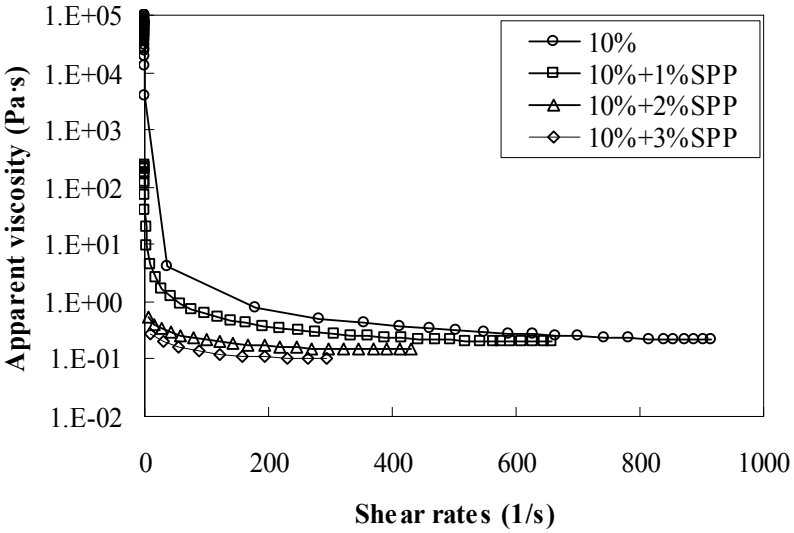

Figure 7.4 Apparent viscosity based on shear rates

Figure 7.5 presents the relationship between the equilibrium apparent viscosity and penetration distance for Ottawa sand ($d_{10} \approx 0.2$ mm) at the injection pressure of 35 kPa. As the apparent viscosity increased, the penetration distance consistently decreased regardless of the particle fraction. This was expected since the apparent viscosity includes both the yielding and viscous components which cause the variation in filtration. In the unmodified suspensions, the yielding component is dominant component in the apparent viscosity, and their penetration distances are consistently low similar to what was observed in Figure 7.2.

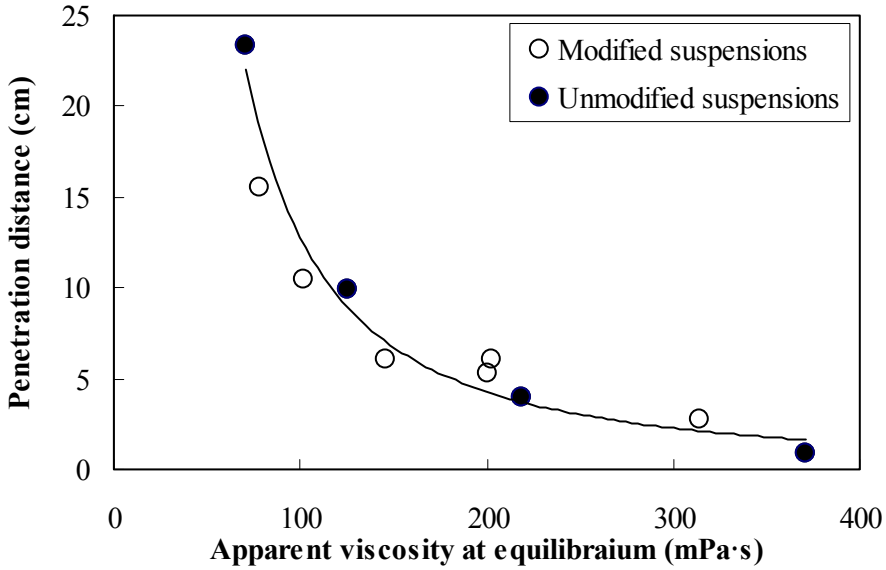

Figure 7.5 Penetration distance based on apparent viscosity at equilibrium

The penetration distance is affected by not only rheological properties of grouts, but also the physical properties of grout particles and porous medium. The penetration distance increases with an increase in the effective grain size (d_{10}), but a grout may not be able to penetrate into a soil when its grain size is too large. Therefore, both physical configurations of soil and grout should be considered to evaluate the penetrability of bentonite suspensions. In order to consider the particle sizes of both, porous media and grout, the effective grain size (d_{10}) was normalized by the larger grain sizes of the grout (d_{95}), which is similar to the groutability ratio (N) proposed by Burwell (1958). However, it should note that the effective grain size used in this study is independent of fines content since the fines content is considered as an independent soil parameter and the suspension flow is dominated through skeletal pores (fines tended to be washed out) as shown in Chapter 6. As the normalized effective grain size increases, the possibility of blocking pore spaces reduces, leading to the increased penetration distance. The

penetration distance of 12% bentonite suspensions with 4% SPP depending on the normalized effective grain size (d_{10}/d_{95}) is presented in Figure 7.6. The penetration distance of grouts increased as a power function with an increase in the normalized effective grain size.

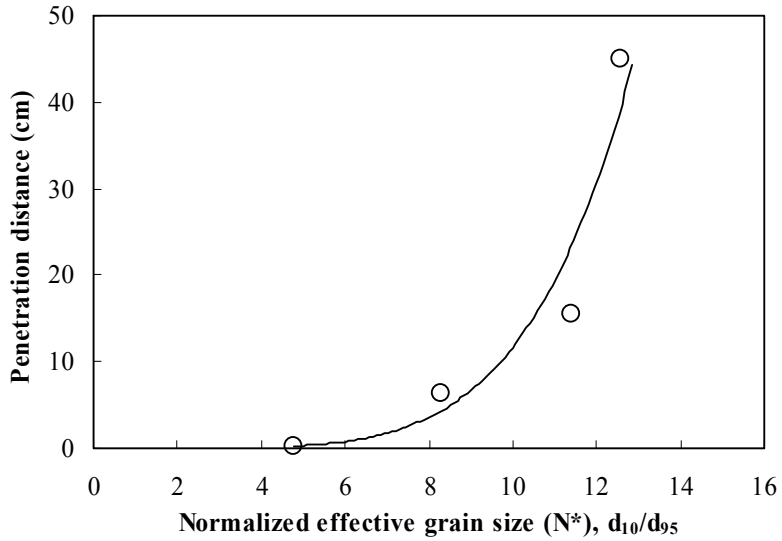

Figure 7.6 Penetration distance based on normalized effective grain size of sand; 12% grout with 4% SPP

7.2.3. Empirical correlation

Since the previous theoretical and empirical expressions do not consider the filtration due to properties of grout such as particle size and rheological properties, and tended to be an overestimate when the filtration is a dominant stop mechanism, an empirical correlation to predict the penetration distance is proposed. The empirical correlation may capture the stoppage of grout flow when the filtration is dominant considering the apparent viscosity, grain sizes of grout and soil. In the proposed correlation, the effect of filtration was included by considering the particle sizes in soil/grout, fines contents and injection pressure as well as the apparent viscosity of grout.

Although the filtration is a transient phenomenon, the time dependent propagation of grout was not considered because the purpose of the correlation is to predict the final distance which is practically more important than a penetration distance with a time interval. Based on the observations of the individual parameters (Table 7.2), the following correlation is proposed to predict the penetration distance of bentonite grout.

Table 7.2 Observed correlations of penetration distance and individual parameters

Parameter	Effect	Parameter	Effect
Yield stress	Depending on particle fractions	Relative density	No effect
Apparent viscosity	Decrease in power	Fines content	Decrease in exponential
$N_c = \frac{d_{10,sand}(mm)}{d_{95,bentonite}(mm)}$	Increase in power	Injection pressure	Increase in power

$$h(cm) = \phi_1' \left[\frac{\left(P/1\ atm\right)^{\phi_2'}}{\left(\mu_{r,equilibrium}\right)^{\phi_3'}} \left(N_c{}^{\phi_4'}\right) \right] \left[e^{\left(\phi_5 \frac{FC}{100}\right)} \right] \quad (7.7)$$

Where h is the penetration distance (cm), Φ_1 is the scaling constant (cm), Φ_2 is the empirical constant for normalized pressure (dimensionless), Φ_3 is the empirical constant for normalized viscosity (dimensionless), Φ_4 is the empirical constant for normalized effective grain size (dimensionless), Φ_5 is the empirical constant for fine contents (dimensionless), P is the injection pressure (kPa), $\mu_{r,\ equilibrium}$ is the relative viscosity at the equilibrium shear rate ($\mu_{suspensions}$ (Pa·s)/ μ_{water} (Pa·s)), FC is the non-plastic fines content in granular soils (%), and Nc is the normalized effective grain size of sand ($d_{10,sand}$ (mm) / $d_{95,bentonite}$ (mm)), where the effective grain size is considered as a property of sand without considering its change due to the presence of fines. Figure 7.7 displays the calibration of the proposed empirical correlation with the experimental data. The

empirical constants are determined by using the root mean square error method, and are determined to be Φ_1, Φ_2, Φ_3, Φ_4 and Φ_5 of 0.79, 1.40, 4.51, 0.31 and -9.33 respectively.

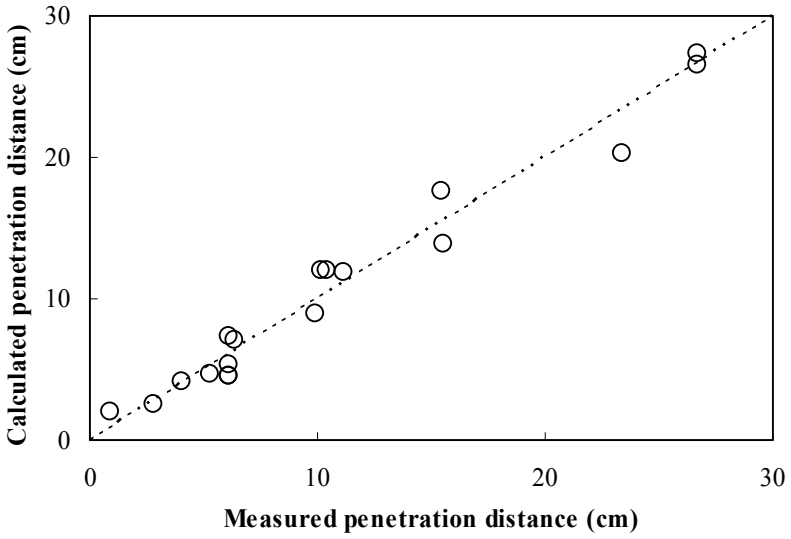

Figure 7.7 Penetration distance based on suspension concentration: SPP modified and unmodified grouts, FC=0-15%, P=35 and 140 kPa, Dr=30 and 80%, and d_{10}=0.12, 0.20, 0.28, and 0.31 mm

However, it should be noted that the proposed correlation based on the laboratory experiments is reasonable between the following intervals: 5≤bentonite fraction≤12%, 0≤SPP≤4%, 4.8<Nc<12.6, 30≤Dr≤80%, 0≤FC≤15%, k≥0.01 cm/sec and P≤140 kPa. If the Nc<4.8 and FC>20%, the bentonite grout did not penetrate into the soil and pressure filtration caused almost instantaneous stoppage even with very diluted grouts. In addition, the proposed empirical correlation should be carefully utilized for the prediction of the penetration distance in the field due to the 1-D nature of the test (Santagata and Santagata, 2003). It may provide a good prediction only when the injection mode is similar to 1-D flow or may be possible to use it with a correlation based on the field injection (3-D radial flow) as being proposed in section 7.5.3.

Although it is convenient to evaluate the apparent viscosity from vane geometry since the geometry allows us to obtain yield stress and equilibrium viscosity from a single run, the measurement of apparent viscosity from vane geometry may not reflect the actual apparent viscosity because the vane only provides relative value of apparent viscosity (Anton Paar, 2006). To evaluate the measured equilibrium apparent viscosities using the vane, the apparent viscosity (equilibrium) from the vane geometry was correlated with the apparent viscosity from cone and plate (at the similar apparent shear rates). Stress ramp tests were performed with fresh mixed bentonite suspensions of 7.5, 10 and 12% modified with 0 to 4% SPP. Similar to the yield stress relationship shown in Chapter 4, the two geometries produced a constant ratio of 0.41 (Figure 7.8). Based on this observation, it is suggested that the equilibrium value of apparent viscosity should be corrected for equation 7.7 when the cone and plate geometry is used to evaluate the apparent viscosity.

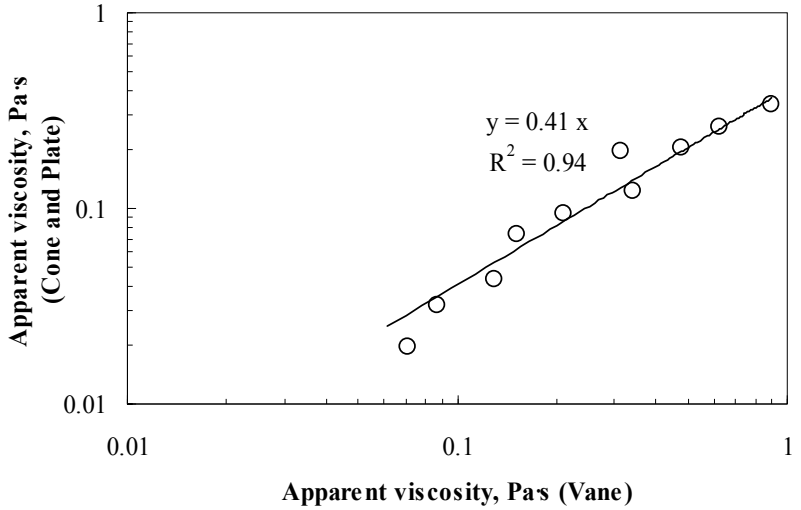

Figure 7.8. Viscosity relationship between cone and plate and vane geometry

7.3. Groutability

7.3.1. Empirical correlation

The groutability of sand is often determined by using grain size distribution and hydraulic conductivity. As shown in Figure 7.9, all the tested sands were assessed as groutable based on the particle size distribution. In addition, the saturated hydraulic conductivity of the tested sands ranged from 10^{-2} to 10^{-1} cm/sec as shown in Chapter 6, indicating that all sands used in this study will be groutable based on Table 2.1 (see Chapter 2).

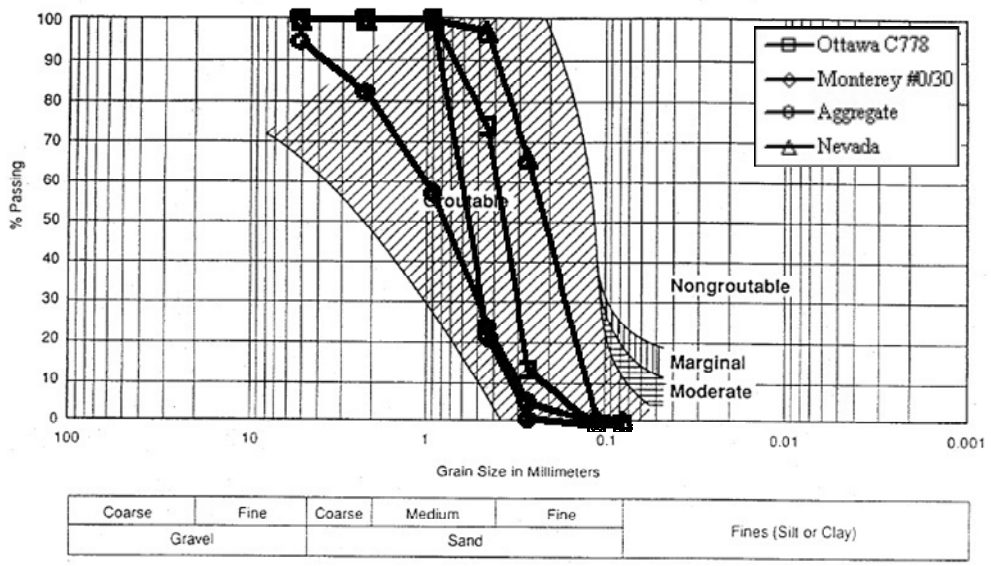

Figure 7.9 Groutability of the tested sands based on the grain size distribution curve (Modified from Karol, 2003)

However, the permeation of grouts also depends on the grout properties as well as other experimental parameters such as injection pressure. Akbulut and Saglamer (2002) proposed a groutability criterion of granular soils considering factors that the Burwell's (1958) groutability did not include such as injection pressure, relative density, fine contents, and water cement ratio. However, both criteria do not provide either the

penetration distance or the quantity of the injected grout pore volumes; therefore, the definition of a successful grouting was vague or should be determined based on performance criteria after trial grouting.

In addition, there is no consensus to determine a successful grouting since it varies with types of grouts, field conditions and performance of the grouted soil. Ozgurel and Vipulanandan (2005) considered a successful grouting in chemical grouts (acrylamide) if the injected volume of grouts was 1 pore volume at 140 kPa after 8 min. Markou and Atmatzidis (2002) utilized the criterion of 2 pore volumes at less than 200 kPa. Moreover, Mittag and Savidis (2003) introduced the German criterion of 3 pore volumes at 600 kPa with constant flow rate tests for micro-fine cement grouts, and the sample height should be 4 times greater than the sample diameter. In this study, a grouting was considered successful if at least 1 pore volume could be injected at the pressure of 140 kPa within 10 min (this criterion was adapted from what was recommended for chemical grouting by Ozgurel and Vipulanandan, 2005). This criterion was selected based on similarity of injection technique (constant pressure) and use of low injection pressures.

A groutability criterion for bentonite suspensions was developed using the relationships observed for each parameter. The proposed groutability is similar to what Akbulut and Saglamer (2002) suggested in that the similar parameters (grain size of sand and grouts, injection pressure, fine contents, and relative density) are utilized to evaluate groutability, but it includes the apparent viscosity rather than weight ratios.

The summarized step by step procedures include: 1) selection of the global model, 2) determination of model parameters, 3) development of a groutability equation, 4) calculation of equation constants, and 5) determining a successful grouting based on the injected pore volumes. For the global model to correlate the injected pore volume to

groutability, a power function was selected since the apparent viscosity showed a dominant effect on injected pore volume (equation 7.8). Using the measured pore volumes, the model coefficients were found by regression analyses controlling the target range of groutability which has a perfect correlation (R^2=1) to the injected pore volumes within the range. The target range (0 to 15) was determined by trial and error basis to produce a similar range of groutability to the existing criteria for comparison purposes.

$$IPv = C \times N^{*n} \tag{7.8}$$

Where IPv is the injected pore volume of grouts, N* is the groutability of bentonite grout, C and n are the empirical constants, estimated to be 2.2×10^{-4} and 3.5 respectively. The calculated groutability (N*) was plotted with each parameters (effective grain size, relative density, fine contents, apparent viscosities, and injection pressures), producing a form of N*=f(Nc)+f(P/μ)+f(Dr)+f(FC). Based on these functions, an empirical equation to estimate groutability considering the effects of each component on groutability was proposed as follows:

$$N^* = Nc + \phi_1 \frac{(P/1\ atm)^{\phi_2}}{(\mu_r)^{\phi_3}} + \left(\frac{Dr}{100}\right)^{\phi_4} - EXP\left(\phi_5 \frac{FC}{100}\right) \tag{7.9}$$

Where N* is the groutability of bentonite grout, ϕ_1, ϕ_2, ϕ_3, ϕ_4 and ϕ_5 are the empirical constants, P is the injection pressure (kPa), μ_r is the relative viscosity (μ_{grout} (mPa·s)/ μ_{water} (mPa·s)), FC is the non-plastic fines content in granular soils (%), Nc is the Burwell's (1958) groutability ($d_{10,sand}$ (mm) / $d_{95,bentonite}$ (mm)). All factors affecting groutability were normalized to obtain a dimensionless number. The empirical constants were determined by correlating the calculated groutability to the proposed equation using a root mean square error method. Based on this procedure, the empirical parameters of Φ_1, Φ_2, Φ_3, Φ_4, and Φ_5 were determined as 1900, 0.2, 1.4, 8.5, and 9.3 respectively. It should be noted that the correlation should be interpreted with the

interactive effect between the different parameters since the groutability of a suspension through a soil does not rely on one single parameter. For instance, soils having high relative density tended to slightly increase the injected pore volumes at the pressure of 35 kPa as compared to lower relative density soils, but it still required using higher injection pressures and lower viscous grouts than a soil with low relative density to achieve a successful grouting. In addition, the apparent viscosity should be corrected when a different geometry is used for the viscosity measurements similar to the penetration distance (Figure 7.8).

Figure 7.10 shows the proposed correlation between groutability and injected pore volumes. Since the proposed groutability is correlated to the injected pore volumes, a quantitative evaluation of successful grouting is possible based on the injected pore volumes. Based on this criteria, it was found that a soil is "Groutable" if N* was greater than 11, and "Ungroutable" if N* is less than 9. When the groutability presents within the range of 9 to 11, a trial grouting is recommended in the laboratory.

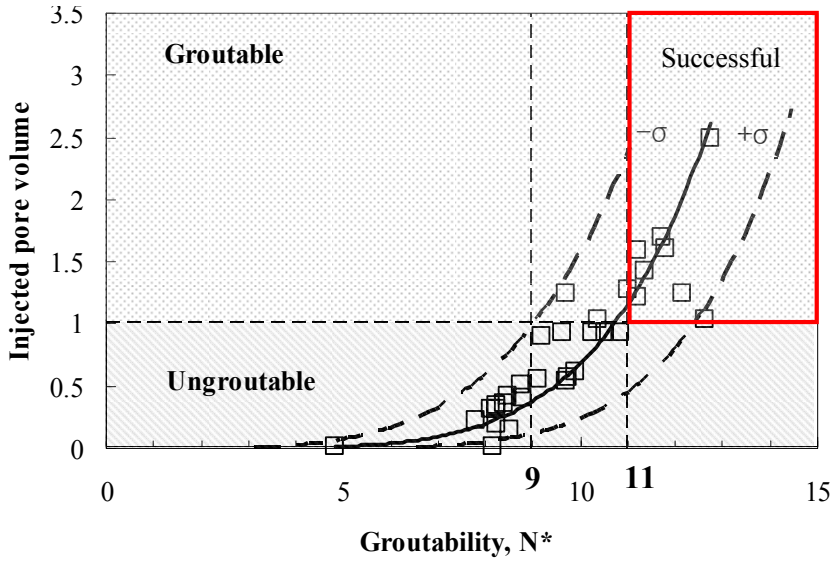

Figure 7.10 Proposed groutability criterion using the modified bentonite grouts

7.3.2. Comparison with the existing criteria

The proposed groutability criterion was evaluated by comparing it with the existing criteria. The particle size of the grout and soil has been widely used for the initial prediction of groutability in granular soils with cement grouts prior to grouting (see Chapter 2). The initial estimation based on Burwell (1958) criterion produced N ($N=d_{85,grout}/d_{15,sand}$) of 36, 50.9, 46.4 and 17.9 for Ottawa, Monterey #0/30, Aggregate and Nevada sand respectively regardless of the type of the grout mix, indicating that all sands except of Nevada sand are groutable (N>25). However, based on the second grouting criterion, 7 data points are groutable (N>11) as shown in Figure 7.11. Although the 7 data points were evaluated to be groutable, 2 data points could not reach 1 pore volume. In addition, 5 data points could be injected over 1 pore volume between 5 and 11. On the other hand, Incecik and Ceren (1995) criterion estimated most of data (except 2 data points) as groutable (N>10), but approximately 75% of data points could not be injected over 1 pore volume as shown in Figure 7.12. In Figure 7.13, the new groutability was compared to the groutability proposed by Akbulut and Saglamer (2002). The groutability by Akbulut and Saglamer (2002) evaluated 8 data points as groutable, but 3 data points could not be injected by 1 pV and 4 data points that were successfully grouted fall in the ungroutable zone. The comparisons with the existing criteria indicate that the prediction of groutability using the existing groutability may cause inaccurate prediction of groutability in granular soils when the SPP modified bentonite suspensions are used in permeation grouting.

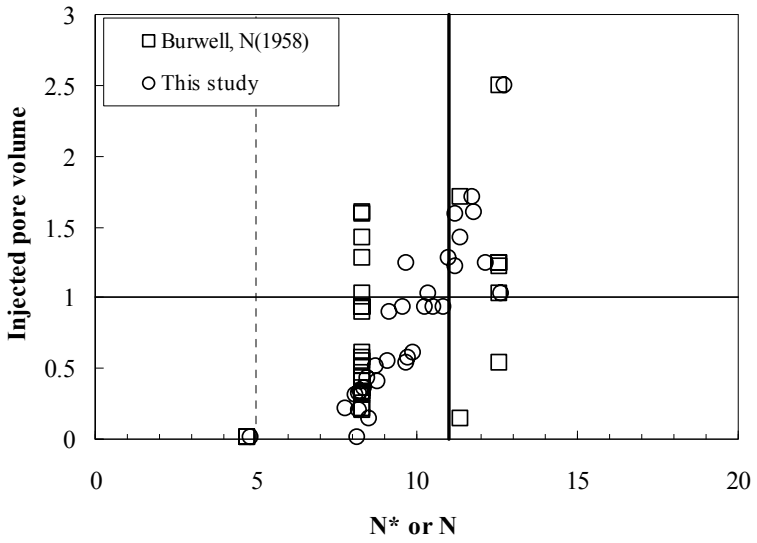

Figure 7.11 Comparison of groutability between Burwell (1958) and this study: groutable (N>11), and trial grouting (5<N<11); the thick solid line is the proposed criterion in this study (N=11)

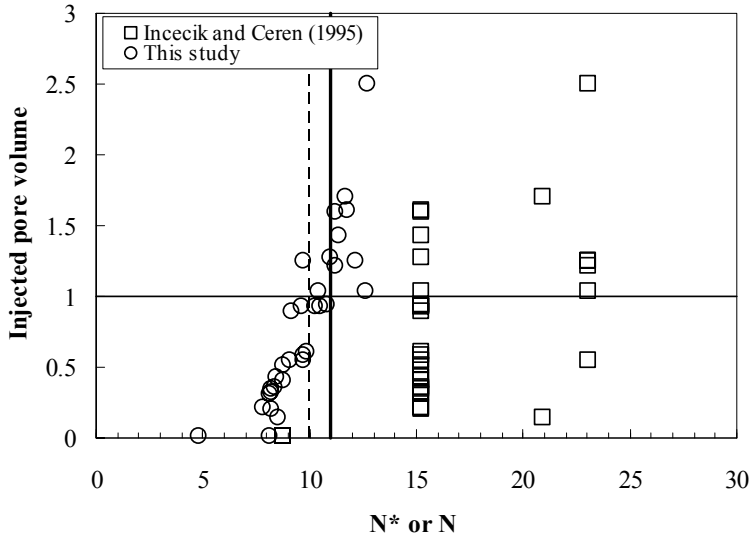

Figure 7.12 Comparison of groutability between Incecik and Ceren (1995) and this study: groutable (N>10); the thick solid line is the proposed criterion in this study (N=11)

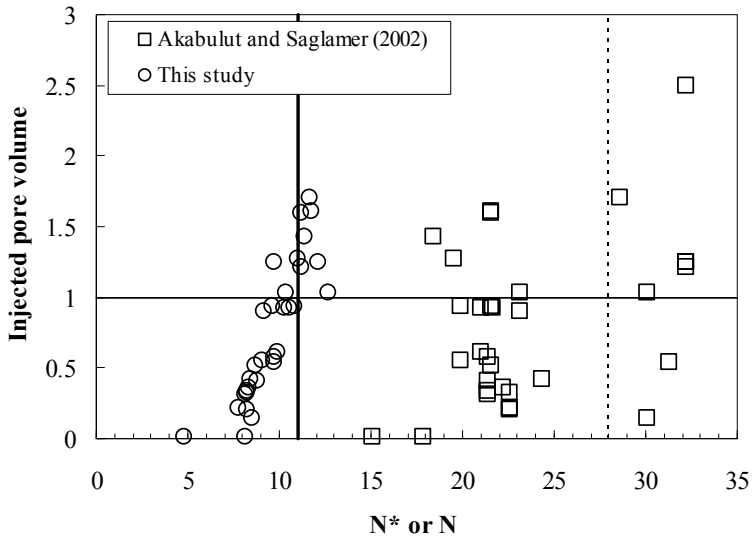

Figure 7.13 Comparison of groutability between Akbulut and Saglamer (2002) and this study: groutable (N>28)); the thick solid line is the proposed criterion in this study (N=11)

As shown in Chapter 4, the "New" bentonite produced different rheological properties from the "Old" bentonite. In order to confirm the applicability of the proposed groutability to the different type of bentonite, the groutability was calculated based on the proposed groutability criterion and the injected pore volume was monitored by the injection tests using the "New" bentonite. Note that the groutability criterion was developed based on tests performed using the "Old" bentonite only. Figure 7.14 shows the groutability of Ottawa sand using the various "New" bentonite suspensions at different experimental conditions (7.5% suspensions with 1% SPP at 35 and 140 kPa, 7.5% suspension at 140 kPa and 10% suspension with 3% SPP at 140 kPa). As can be seen, all results were placed within the $\pm 1\sigma$ of the proposed correlation. The suspensions with the groutability less than 11 produced the injected pore volume less than 1 pV. On the other hand, the suspensions with the groutability greater than 11, the suspensions could be injected greater than 1pV. Since the "New" bentonite included

low amount of Ca^{2+} ions, the apparent viscosities were lower than the "Old" bentonite. As a result, the "New" bentonite produced higher injected pore volumes than the "Old" bentonite at the same experimental conditions. The results imply that the proposed groutability would be applicable to other type of bentonite if their rheological properties are appropriately measured.

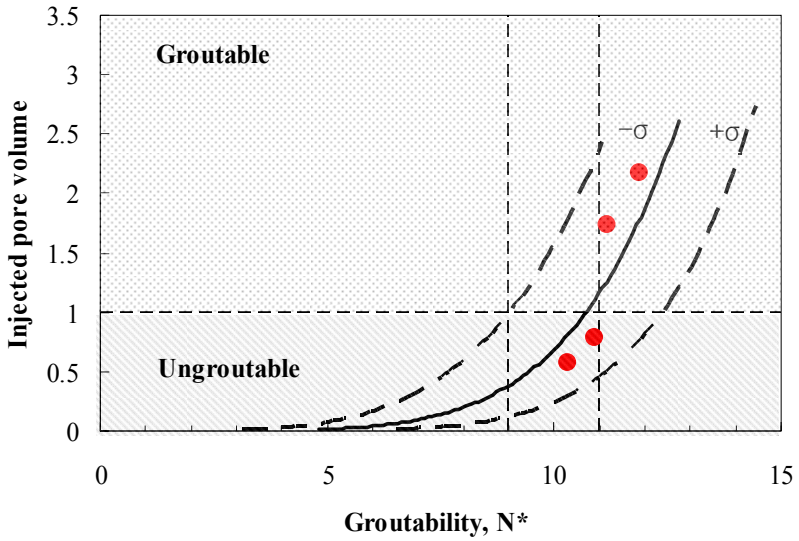

Figure 7.14 Groutability of "New" bentonite (Ottawa sand, Dr=30% and FC=0%)

7.4. Groutability using numerical approach

As shown in the previous section 7.2, the stoppage of bentonite grout flow is controlled by the filtration phenomenon rather than rheological blocking. Previous researches (Bouchelaghem and Vulliet, 2001; Saada et al. 2005; Kim and Whittle, 2009) proposed macroscopic models to simulate grout propagation based on the filtration phenomenon. However, the models did not account for the change in filtration due to the chemical properties of grouts such as ionic strength and pH, which greatly affect their viscosity. The change in chemical properties may lead to the change in the penetration

of grouts through porous medium. Moreover, the models did not account for the variation in the deposition rate which changes during the filtration process by assuming a constant deposition rate (Bouchelaghem and Vulliet, 2001; Kim and Whittle, 2009). Furthermore, the models can not directly predict groutability of a soil, and therefore, requiring additional experimental and theoretical studies.

Recently, an advanced groutability criterion for granular soils was developed using microfine cement grout (treated with quick-setting agent) in compaction grouting (Kim et al. 2009). A step-wise numerical simulation of spherical grout flow through porous media was introduced by considering the filtration phenomenon. A closed form solution using mass balance equations and a phenomenological filtration law were used to evaluate the deposition of particles in sand beds. The deposition rate was updated by taking into account the change in pore space and velocity. A lump parameter, which considers ionic strength and critical velocity of grout, and the pore properties (radius and length of pore throat) were correlated to evaluate groutability. In this study, the step-wise approach was adopted and modified to estimate groutability for bentonite grout by considering 1-D flow since the groutability typically determined from the 1-D flow in laboratory. Moreover, other properties of bentonite suspensions, which are different from cement grouts (the change in density of suspensions due to partially swelled bentonite particles and apparent viscosity due to the particle deposition in pores), were considered in the modeling.

7.4.1. Mathematical formulation

The analysis of the suspended particles through a porous medium is represented by a macroscopic problem of solute transport through a homogeneous medium. The governing equation for this type of problem is given by the advection-diffusion equation.

$$\frac{\partial}{\partial t}(nC) + \bar{v}\cdot\nabla(C) + \nabla\cdot(nD\nabla C) = 0 \qquad (7.10)$$

Where n is the porosity (n=Vv/V, when Vv is the volume of voids and V is the volume of porous medium), C is the concentration of a solute, $\bar{v}$ is the fluid velocity, D is the hydrodynamic dispersion tensor (dimension of L^2/T).

When a mass transfer occurs between the solute and the porous medium, the rate term is added.

$$\frac{\partial}{\partial t}(nC) + \bar{v}\cdot\nabla(C) + \nabla\cdot(nD\nabla C) = -\frac{\partial\sigma}{\partial t} \qquad (7.11)$$

Where σ is the specific deposit, which is defined as the mass per initial unit porous medium volume (i.e. $\sigma=M_D/V$ when M_D is the mass of deposit and V is the volume of the medium).

Although the deposition rate changes as the deposition covers the wide area of the porous medium (Herzig et al. 1970; Tien 1989), the most commonly applied kinetics for filtration rate through clean sand is the first-order law

$$\frac{\partial\sigma}{\partial t} = \lambda C \qquad (7.12)$$

Where λ is the filtration coefficient has a dimension of 1/T.

Frequently, the first order is written as a function of the fluid velocity (Darcy's),v, as below:

$$\frac{\partial\sigma}{\partial t} = v\lambda^* C \qquad (7.13)$$

In this case, the filtration rate λ* has the dimension of 1/L. This constant rate represents the filtration per unit length which is separated from the dependence on the injection rate by the pore velocity.

If the variation of the deposition rate due to the change in porous media is considered (Herzig et al. 1970), the second order kinetics can be expressed as

$$\frac{\partial \sigma}{\partial t} = \lambda_o F(\sigma) C \tag{7.14}$$

Where λo represents the deposition rate through clean beds and F(σ) is the deposition rate function. Depending on different sources in the literature, F(σ) can have various forms:

Soo and Redke (1986), $F(\sigma) = 1 - a\frac{\sigma}{n_o}$

Bai and Tien (2000), $F(\sigma) = 1 + \mathrm{k}_1\sigma + \mathrm{k}_2\sigma^2 + \mathrm{k}_3\sigma^3 + \cdots$

Where a is the flow redistribution parameter which ranges from zero to one.

In order to implement the governing equation, several assumptions were established. The sedimentation of particles is neglected due to the colloidal characteristic of bentonite in aqueous medium. The dilution of grout by hydrodynamic dispersion can affect grout propagation, but previous researches showed that the effect was small enough to ignore and the filtration was a dominant phenomenon in grout flow (Zevobits et al., 1989; Kim and Whittle, 2004; Saada et al, 2005). In addition, Herzig et al. (1970) reported that particle diffusion is negligible when the particle's size is larger than 1 μm, leading to exclude the effect in the modeling.

The detachment of the deposited particles can occur due to: 1) the collision of the moving particles with the deposited particles by a localized pressure or flow rate variation, and 2) the global change of the flow rate in the whole bed such as reversing the flow direction. Since the model in this study is based on macroscopic phenomenon which do not capture the microscale variations, the detachment of particles was not considered. The soil matrix was regarded as rigid (Bouchelaghem and Vulliet, 2001 and Saada et al., 2005). Bouchelaghem and Vulliet (2001) obtained strains in the soil structure on the order of 10^{-6} which justifies ignoring the geometry changes in pore space.

Based on the filtration term and the assumptions, equation (7.11) becomes:

$$\frac{\partial(C)}{\partial t} + V \cdot \nabla(C) = -\frac{\partial \sigma}{\partial t} \tag{7.15}$$

Where V is the pore velocity, V=v/n (when n is the Darcian velocity, n is the porosity).

By substituting the first order law of filtration, equation (7.15) becomes:

$$\frac{\partial(C)}{\partial t} + V\frac{\partial(C)}{\partial x} + \lambda C = 0 \tag{7.16}$$

If the bed is sufficiently deep, the suspension needs a substantial time to pass through it; accordingly, the instant when the suspension reaches a bed element is not the same all along the porous medium. Thus, the bed elements should be compared at the same time scale (retention age). The retention age can be expressed as:

$$\xi(x,t) = t - \frac{x}{V} \tag{7.17}$$

The term x/V is the required time for the suspension arrives at the bed depth x.

By adopting the concept of retention age, the partial differential equation is reduced to ordinary differential equation. Reddi and Bonala (1997) provided the solution in the following form:

$$C(x,t) = f_1(\xi)\exp\left(-\lambda\frac{x}{V}\right)U(\xi) + f_2(-\xi V)\exp(-\lambda t)U(-\xi) \tag{7.18}$$

Where f_1 is the function of boundary conditions and f_2 is the function of initial conditions and U is the Heaviside unit step function which has a property of

$$\text{If } \xi \geq 0,\ U(\xi)=0 \tag{7.19a}$$

$$\text{If } \xi < 0,\ U(\xi)=1 \tag{7.19b}$$

The porous media has initially no particles since grout is not introduced into the injection hole. In addition, the concentration of grout at the initial injection point is always the initial concentration of grout. Therefore, the equation can be solved by adopting the following initial and boundary conditions

$$C(x,0)=0=f_2(x)=0,\ f_1(t)=c(0,t)=Co \tag{7.20}$$

The concentration of grout suspensions are obtained by:

$$C(x,t) = C_o \exp\left(-\frac{\lambda}{V}x\right)U\left(t-\frac{x}{V}\right) \tag{7.21}$$

The amount of grout particles deposited in the soil matrix per initial unit pore volume can be expressed as:

$$\sigma(x,t) = 0,\ \left(t-\frac{x}{V}<0\right) \tag{7.22a}$$

$$\sigma(x,t) = \int_{x/V}^{t}\lambda C_o \exp\left(-\frac{\lambda}{V}x\right)U\left(t-\frac{x}{v}\right)dt \quad \left(t-\frac{x}{V}>0\right) \tag{7.22b}$$

By integrating equation (7.22b), the amount of grout particles retained in the soil matrix per initial unit pore volume is obtained by:

$$\sigma(x,t) = \lambda C_o\left(t-\frac{x}{V}\right)\exp\left(-\frac{\lambda}{V}x\right) \tag{7.23}$$

7.4.2. Coupling of porosity changes with solid density

The porosity of the porous medium keeps changing due to the mass of particles filtered. The widely adopted assumption to consider this phenomenon is that the porosity is reduced in proportion to the mass of deposited particles. The porosity changes are expressed as:

$$n = n_o - \frac{\sigma}{\rho_s} \tag{7.24}$$

Where n is the new porosity due to filtration, n_o is the initial porosity of porous medium, σ is the mass of the filtered particles per unit volume of porous medium, and ρ_s is the density of solid particles. The suspension density can be related to the concentration of the suspensions expressed as:

$$\rho = \rho_w + \mathrm{C} \cdot \left(1 - \frac{\rho_w}{\rho_s} \right) \tag{7.25}$$

Where C is the concentration of suspensions, ρ_w is the density of water, and ρ_s is the density of solid.

7.4.3. Specific gravity of partially swelled bentonite

The adsorption of water molecules between the interlayer of the clay platelets causes swelling of the bentonite (Luckham and Rossi, 1999). This swelling produces higher repulsive forces and therefore, weak structures are formed by the delaminated platelets. The degree of separation in bentonite particles depends highly on the amount of cations in bentonite, especially calcium ions; bentonite with more calcium experience less separation (Madsen and Müller-Vonmoos, 1989). Due to the swelling of the bentonite particles, the number of bentonite particles residing in a given pore space may change so that the application of a continuum approach suggested by Bouchelaghem and Vulliet (2001) can become questionable. Saada et al. (2005) proposed the three phase model to consider this effect, but ignored the different densities between sand and cement. However, it may be important in this case since the volume changes in the pore space are used to estimate the mass of the deposited particles. The swelling of bentonite changes with the degree of separation in the bentonite platelets due to the hydration of cations located between two bentonite platelets as shown in Figure 7.15. Due to this swelling, the volume of suspension increases, and the number of particles that can reside in a give pore space decreases. Although the osmotic swelling due to the gradual increase in repulsive forces is a time dependent behavior, only the effect of hydration on the swelling is considered since the injection of suspensions is performed within a relatively short time

after the mixing process. Based on that, the volume of hydrated and non-hydrated bentonite can be expressed as:

$$V_{b,hydrated} \times N = N \times (2t + 2R_{hydrated}) \times a \tag{7.26a}$$

$$V_{b,nonhydrated} \times N = N \times (2t + 2R_{nonhydrated}) \times a \tag{7.26b}$$

$$W_b = N \times W_{particle} \tag{7.27}$$

Where N is the numbers of bentonite particles in suspensions, t is the thickness of bentonite platelet (9.6Å), R is the radius of ions, a is the area of a bentonite platelet, W_b is the total weight of bentonite in suspensions, and $W_{particle}$ is the weight of the individual bentonite particle. Then, the hydrated and nonhydrated unit weights of bentonite were evaluated, followed by calculating the ratio between the specific gravity of the hydrated and non hydrated bentonite. The radius of the hydrated and non-hydrated ions is summarized in Table 7.3.

$$\gamma_{b,hydrated} = \frac{N \times W_p}{N \times (2t + 2R_{hydrated}) \times a} \tag{7.28a}$$

$$\gamma_{b,nonhydrated} = \frac{N \times W_p}{N \times (2t + 2R_{nonhydrated}) \times a} \tag{7.28b}$$

$$\frac{\gamma_{b,hydrated}}{\gamma_{b,nonhydrated}} = \frac{\dfrac{N \times W_p}{N \times (2t + 2R_{hydrated}) \times a}}{\dfrac{N \times W_p}{N \times (2t + 2R_{nonhydrated}) \times a}} = \frac{G_{s,hydrated}}{G_{s,nonhydrated}} = \frac{t + R_{nonhydrated}}{t + R_{hydrated}} \tag{7.29}$$

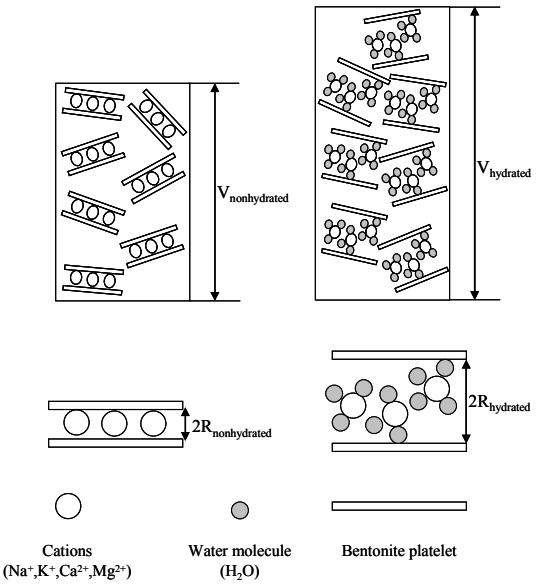

Figure 7.15 Schematic of swelling of nonhydrated and hydrated bentonite (Modified from Komine, 2003)

Table 7.3 Radius of nonhydrated and hydrated cations (Modified from Mitchell, 1993)

Ion	Nonhydrated (Å)	Hydrated (Å)
Li^+	0.68-0.78	7.3-10.3
Na^+	0.98	5.6-7.9
K^+	1.33	3.8-5.32
NH_4^+	1.43	5.37
Rb^+	1.49	3.6-5.09
Cs^+	1.65	3.6-5.05
Mg^{2+}	0.78-0.89	10.8
Ca^{2+}	1.06-1.17	9.6
Sr^{2+}	1.27-1.34	9.6
Ba^{2+}	1.43-1.49	8.8

7.4.4. Intrinsic permeability

The flow problem in porous media typically assumes the porous bed consisting of spherical particles as a bundle of capillary tubes where flow occurs according to Darcy's law. With the hydraulic radius concept, the Blake-Kozeny equation relates the intrinsic permeability with the particle diameter and porosity.

$$K = \frac{d^2 \cdot n^3}{72 \cdot C \cdot (1-n)^2} \tag{7.30}$$

Where K is the intrinsic permeability (L^2), d is the particle size, n is the porosity, and C is the empirical constant (typically 2.1) accounting for the inherent heterogeneity, interconnectivity, and geometric changes in porous medium (converging/diverging) as well as the totuosity (Balhoff, 2008). In addition, Lambe and Whitman (1969) showed that the intrinsic permeability can be approximately related to the saturated hydraulic conductivity of the porous medium (i.e. k of 1 cm/sec is equivalent to K of 1.022×10^{-5} cm^2 at 20 ºC).

Within the grouted zone, it was assumed that the intrinsic permeability of the sand is a function of the porosity and can be modeled using Kozeny-Carman equation:

$$\frac{K}{K_o} = \left(\frac{d_g}{d_{go}}\right)^2 \left(\frac{n}{n_o}\right)^3 \left(\frac{1-n_o}{1-n}\right)^2 \tag{7.31}$$

However, there is still no consensus on the particle size variation due to filtration, although there has been a general agreement on using Kozeny-Carman equation to simulate the clogged beds. Previous researches (Ling, 1955; Gosh, 1958; Sakthivadivel, 1966) introduced the "hydraulic radius" model which does not consider the change in particle size due to filtration,

$$\left(\frac{d_g}{d_{go}}\right) = 1 \tag{7.32}$$

Maroudas (1961) suggested the decrease in d_g due to filtration based on the assumption of a smooth-coating morphology and spherical grains

$$\left(\frac{d_g}{d_{go}}\right) = \left(\frac{1-n}{1-n_o}\right)^{1/3} \tag{7.33}$$

When the shape becomes cylindrical rods (Herzig et al., 1970), the change in grain size becomes

$$\left(\frac{d_g}{d_{go}}\right)=\left(\frac{1-n}{1-n_o}\right)^{1/2} \tag{7.34}$$

Since the bentonite particles are very small so that the change in grain size may be negligible, thus, the equation (7.30) was adopted in this study to simulate the change in intrinsic permeability.

$$\frac{K}{K_o}=\left(\frac{n}{n_o}\right)^3\left(\frac{1-n_o}{1-n}\right)^2 \tag{7.35}$$

7.4.5. Apparent viscosity

Under the constant flow pressure, the filtration retards the pore velocity, causing an increase in the apparent viscosity. In addition, the particle loss from the suspension will decrease its concentration leading to a decrease in the apparent viscosity. The change in apparent viscosity can be calculated using the following equation,

$$\mu=\mu_f\cdot\left(1-0.25\cdot\phi_p\right) \tag{7.36}$$

Where μ_f is the fluid phase viscosity and Φ_p is the volume fraction of particles in fluids. With the water-solid contents, Φ_p can be estimated by:

$$\phi_p=\frac{1}{1+\frac{\rho_s}{\rho_w}\cdot\left(W/S\right)} \tag{7.37}$$

$$\frac{W}{S}=\frac{1-C}{C} \tag{7.38}$$

When the fluid is a power law fluid, the viscosity can be calculated as (Bouchelaghem and Vulliet, 2001):

$$\mu = \mu_w \cdot \left(1 + \left(\frac{\mu_o}{\mu_w} - 1\right)\right) \cdot \left(\frac{\phi_p}{\phi_{p_o}}\right) \tag{7.39}$$

7.4.6. Particle deposition coefficient

The important parameter in the filtration model is the filtration rate (deposition coefficient, λ). The coefficient is difficult to estimate due to the dynamic nature of the filtration process. Therefore, it should be obtained through back analysis based on experimental results (Kim and Whittle, 2009). Bouchelaghem and Vulliet (2001) calibrated the coefficient by the effluent concentrations and pore pressure difference from sand column tests. The values varied over an order of magnitude during injection and they selected $\lambda=1.5\times10^{-4}$/s for their analysis through a statistical study.

The coefficient is also influenced by the chemical reaction and velocity of the suspensions and geometrical characteristics of the porous medium. Reddi and Bonala (1997) derived a closed form expression of the deposition coefficient based on particle capture probability approach originally proposed by Stein (1940) and modified later by Rege and Fogler (1988) to incorporate in network model simulation. The concept is that the probability of a particle capture in a pore tube is equivalent to a fraction of the total flow in the annulus between r and r-θa, as presented in Figure 7.16. They selected this approach because it determines the probability of capturing particles through a pore larger than the particle size, which is a similar condition to the particle deposition during filtration. The relation determines the fraction of flow in annulus size of a·θ under laminar flow conditions:

$$p(r) = 4 \cdot (a \cdot \theta / r)^2 - 4 \cdot (a \cdot \theta / r)^3 + (a \cdot \theta / r)^4 \tag{7.40}$$

Where p(r) is the probability of particle capture in pore tube, a is the particle radius, r is the pore radius, and θ is the parameter. The parameter, θ, accounts for the

effect of ionic strength, pH, fluid velocity and properties, particle density, and concentrations and was postulated as an exponential function:

$$\theta = \theta_o \cdot \exp\left(-\frac{V}{V^*}\right) \tag{7.41}$$

Where θ_o is a constant depending on ionic conditions, V is the fluid velocity, and V* is a critical velocity. The critical velocity can be approximated either by experiments or by theoretical approaches (Spielman and Fiztpatrick 1973; Spielman and Cukor, 1973; Mackie et al. 1987). Mackie et al. (1987) suggested the following equation by equating the tangential shear forces and London forces

$$V^* = \frac{H}{1.7005 \times 36 \times \pi \cdot \mu \cdot z_o} \tag{7.42}$$

Where H is the Hamaker constant, z_o is the distance of minimum separation, and μ is the viscosity. θ_o is a lumped parameter primarily affected by ionic strength and pH. The θ_o parameter can be obtained by running a single experimental run at a very slow velocity ($v << v^*$), and adjusting θ_o such that the model predictions match the experimental data from the run (Rege and Folger, 1988). Rege and Folger reported that the value of θ_o varies from 0 to 10 for KCl (0 to 0.01M) treated bentonite suspensions. However, it increased up to 15 based on the fluid velocity and concentration. When V/V* is relatively low, θ approaches θ_o, indicating that the change in velocity may not significantly affect the particle deposition. However, the increased velocity at relatively larger V/V* may decrease the probability of particle capturing by reducing θ. Thus, the physical effect of the pore size distribution, the size of particles migrating, and the chemical compositions of the pore fluid on particle deposition can be accounted for by the equations (7.40) to (7.42).

By considering the probability of particle capturing, discharge from each pore tube of radius a, and a pore size density function (lognormal distribution), the closed form expression of the filtration rate is as follow (Reddi and Bonala, 1997):

$$\lambda = \frac{V}{\alpha^* \cdot e^{2(b^2+m)}} \cdot \left[4 \cdot (a \cdot \theta)^2 - 4 \cdot (a \cdot \theta)^3 \cdot e^{(b^2-2m)/2} + (a \cdot \theta)^4 \cdot e^{2(b^2-m)}\right] \qquad (7.43)$$

Where V is the pore velocity, b and m are the mean and standard deviation of ln a, respectively, a is the migrating particle radius, and α* is the parameter representing the effective pore length associated with each particle. Arya and Dierolf (1989) found that α* varies from 3 to 15mm for coarse sand to silts (the particle radii is from 10^{-3} mm to 1 mm). Moreover, the predicted pore radii showed a good agreement with the measured ones using the value of 9.11 mm.

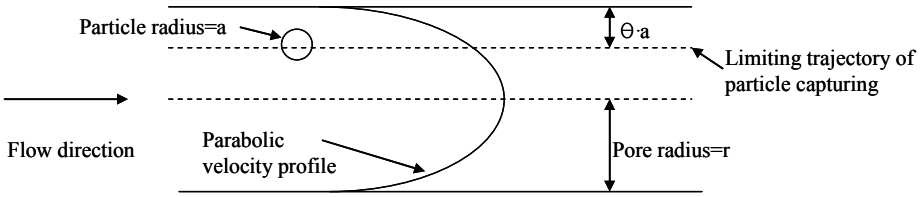

Figure 7.16 Probability of particle capture in pore tube is equivalent to fraction of total flow in annulus between r and r-θa (after Rege and Fogler, 1988)

7.4.7. Estimation of pore size distribution

In order to implement filtration or network type modeling, the geometric properties of the soil (pore size distribution, location, orientation and connectivity) should be investigated. It may be possible to obtain a spatial configuration of pore space by using stochastic simulation techniques from experimental data (Tsakiroglou and Pyatakes, 2000) or nondestructive techniques such as x-ray or magnetic resonance microtomography (Vogel and Roth, 2001). Moreover, geometric parameters, corresponding to characterize pore space, can be derived by fitting the experimentally

measured pressure-saturation relations using either mercury intrusion porosimetry (Tsakiroglou and Pyatakes, 1990) or soil water retention curves (Wilkinson and Willemsen, 1983). The derivation of the deposition rate by Reddi and Bonala (1997) estimated pore sizes from the known particle sizes distribution, which is originally proposed by Arya and Paris (1981) and updated by Arya and Dierolf (1989) for predicting moisture characteristic curves of partially saturated soils. The particle size distribution curve is subdivided into i size ranges with average diameter $2r_i$, weight fraction, w_i. Within each size range, the pore volume is represented by a single pore of radius R_i at the known macroscopic void ratio, e. Arya and Dierolf (1989) provided the updated model which relates pore radii (r) to particle radii (R) as

$$r_i = \left[\frac{4 \cdot e \cdot R_i^3}{3 \cdot \alpha^*} \right]^{1/2} \tag{7.44}$$

Where e is the void ratio, R_i is the particle radii (mm), α* is the parameter representing the effective pore length associated with each particle (3-15mm for soils ranging from coarse sand and silts), and r_i is the radii of pore (mm). The pore size distribution was estimated by using the equation (7.44) and the mean and standard deviation were found from log-normal distribution of pore radii as shown in Figure 7.17 and Figure 7.18. The mean pore diameter (D_{p50}=0.044 mm) was approximately 40 times larger than the mean particle size (D_{50}=0.001 mm) of the bentonite, but approximately 10% of pore sizes were less than D_{95} of bentonite particles (D_{95}=0.025 mm), indicating that some filtration may occur during permeation of bentonite suspensions. This may explain the reason why the Ottawa sand was classified as non-groutable ($d_{10,sand}/d_{95,grout}$<11) based on Burwell's (1958) groutability.

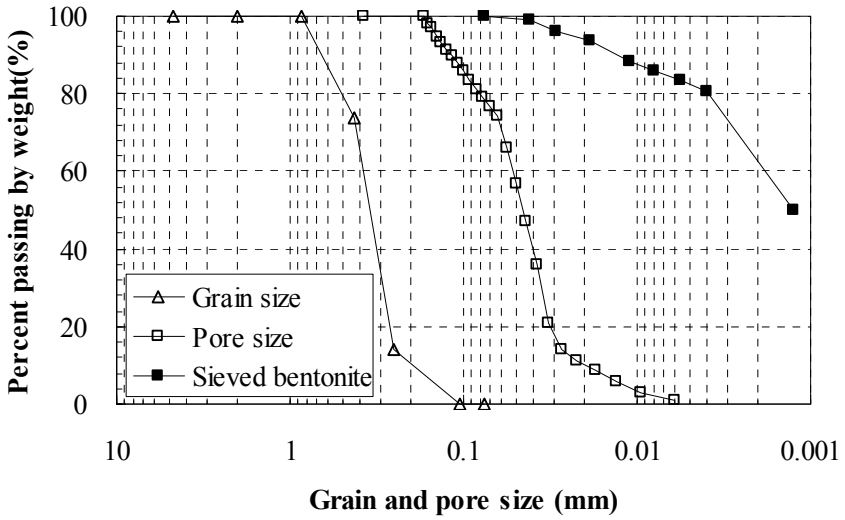

Figure 7.17 Particle and pore size (diameter) distribution of Ottawa sand (particle size distribution of the sieved bentonite is provided for comparison purposes)

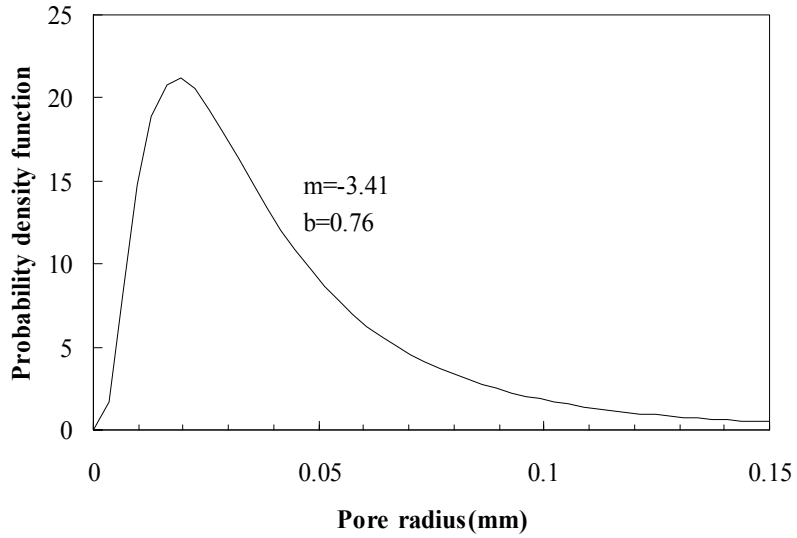

Figure 7.18 Pore size (lognormal) distribution of Ottawa sand

7.4.8. Simplified propagation model (fully decoupled volume block approach)

In order to approximate the grout propagation through sand, a grout volume block approach was introduced. Because of the filtration, the pore space reduced and the flow

rate is retarded so the penetration distance gradually decreased at a given time interval. The pressure gradient was assumed as a constant through the whole process. Since the reduced flow rate reflects the blockage of pore space, it may be possible to simulate the grout flow with the reduced volume flow through clean sand. Therefore, it was assumed that the injected volume of grouts at a given time interval occupied uniformly all pore space and propagates successively as a block without causing any coupling between blocks (fully decoupled blocks). In addition, there is no change in the pore space during each of the block propagation, using the constant initial porosity of the sand. This may be a reasonable assumption in that the change in pore space has already been taken into account in changes to the grout block. Figure 7.19 displays a schematic of the block propagation of the suspensions through a sand column. Due to the filtration, the pore space is reduced so that the injected pore volume decreased at a given time interval. The propagation of the grout block is maintained until the flow is stopped. Thus, the final distance (or the location of grout front) can be calculated by the summation of the individual height of the grout blocks. The comparison of the observed and calculated penetration distances are shown in Figure 7.20 and Figure 7.21. The calculated penetration distances were slightly overestimated, but produced overall good agreements between the measure and calculated values. The results imply that the grout propagated relatively uniformly through the sand column and the filtration property was reflected in the reduced flow rate.

$$\Delta h = \frac{\Delta Q}{\Delta t \cdot A \cdot n_o} \tag{7.45a}$$

$$\sum_{t=0}^{t} \Delta h = h_{penetration} \tag{7.45b}$$

Where Δh is the height of the grout block per unit time, ΔQ is the volume of the block, Δt is the time interval, A is the area of the sand column, and no is the initial porosity of the sand column.

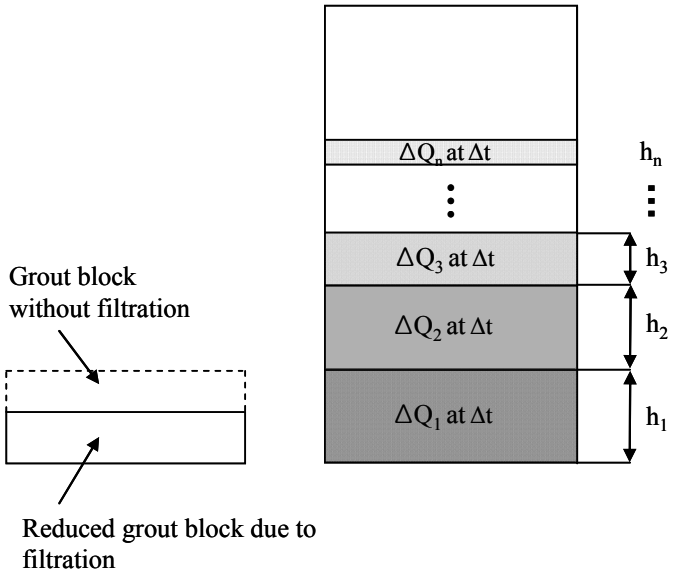

Figure 7.19 Schematic of 1-D block propagation of suspension flow considering filtration

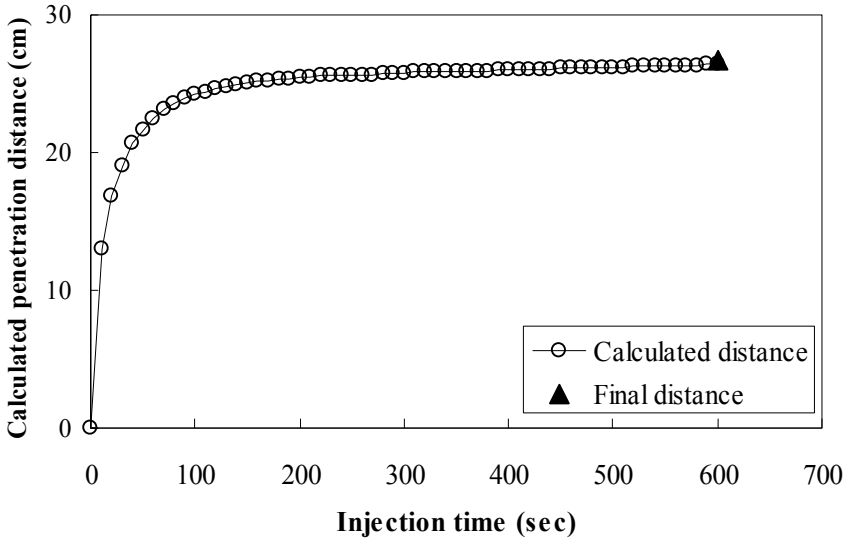

Figure 7.20 Calculated penetration distance with time (7.5% suspension with 1% SPP, P=140 kPa, Dr=30%, and FC=0%)

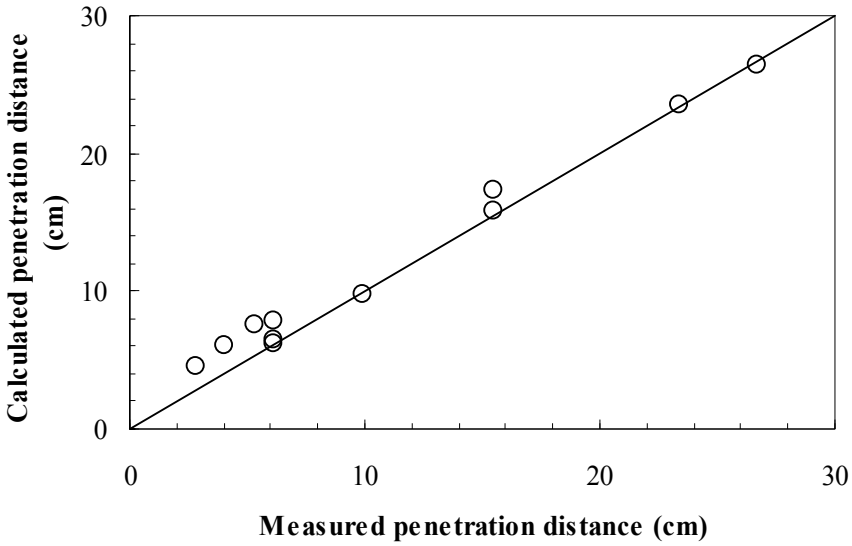

Figure 7.21 Comparison of measured and calculated penetration distance

7.4.9. Step-wise numerical approach

The sand column was discretized as infinitesimal square elements having the height of Δd and the volume of each element is calculated in a similar way to the simplified approach

$$\Delta Q = \; n \cdot A \cdot (\Delta d) \tag{7.46}$$

Where ΔQ is the pore volume of each element, n is the porosity, A is the area, and Δd is the height of the bock. With Darcy's law and the bundle-of-tube assumption, the flow rate of grout and travel time can be calculated as

$$q = \frac{\mathrm{K}\gamma_{\mathrm{g}}}{\mu_g} \cdot \mathrm{i} \cdot \mathrm{A} \tag{7.47}$$

$$\Delta \mathrm{t} = \frac{\mu_g \cdot \mathrm{n} \cdot (\Delta \mathrm{d})}{K \cdot i} \tag{7.48}$$

$$i = \frac{\Delta H}{L} \quad \text{and} \quad \Delta H = \frac{\Delta P}{\gamma_g} \tag{7.49}$$

Where, q is the flow rate, K is the intrinsic permeability (L^2), i is the hydraulic gradient, ΔH is the head loss (L), ΔP is the pressure difference from grout head (water pressure) and injection pressure, L is the length of the grouted zone, and γ_g is the unit weight of the grout, μ_g is the viscosity of the grout, and Δt is grout travel time to cover a distance of Δd.

The correct evaluation of the hydraulic gradient is crucial in this model since the travel time of the grout is mainly determined by the hydraulic gradient (the time dependent variation of apparent viscosity was not considered in this study due to relatively short injection time). Although the grout flow is modeled based on Darcy's law, it becomes invalid as filtration proceeds since the head drop will no longer be linear through the sand column. Therefore, it is difficult to estimate the correct hydraulic gradient from sand column test (Bouchelaghem and Vulliet, 2001). Kim et al. (2009) used an arbitrary constant gradient for their modeling. However, it was observed that the flow rate was relatively constant at the initial penetration ($t \approx 10$ sec) through all tests, followed by being retarded as the flow proceeds. Based on this observation, it was assumed that the hydraulic gradient is constant during the whole injection process and the variation of the flow rate was mainly due to the change in pore configurations caused by filtration.

Calculation algorithm

Although the factors affecting the grout penetrability (e.g. pore fluid velocity, porosity, and filtration coefficient) varies with time, it can be considered as a constant within the discretized infinitesimal volume block. Thus, the injection time can be expressed as:

$$\Delta t_{i,j} = \frac{(\mu_g)_{i,j} \cdot n_{i,j} \cdot (\Delta d)}{K_{i,j} \cdot (\gamma_g)_{i,j} \cdot i} \tag{7.50}$$

Where the subscripts i and j are the spatial node and time step, respectively (when i is smaller or equal to j), $K_{i,j}$ is the intrinsic permeability in the zone between d_{i-1} to d_i, and $(\mu_g)_{i,j}$ is the apparent viscosity of suspension in the zone between d_{i-1} to d_i.

Then, the pore fluid velocity can be calculated by:

$$V_{i,j} = \frac{Q_{j,j} \cdot n_{j,j}}{\Delta t_{i,j} \cdot A_{i,j} \cdot n_{i,j}} \tag{7.51}$$

Since the deposition coefficient depends on the velocity of the pore fluids, the deposition coefficient is expressed as:

$$\lambda_{i,j} = \frac{V_{i,j}}{\alpha^* \cdot e^{2(b^2+m)}} \quad \left[4 \cdot (a \cdot \theta)^2 - 4(a \cdot \theta)^3 \cdot e^{(b^2-2m)/2} + (a \cdot \theta)^4 \cdot e^{2(b^2-m)}\right] \tag{7.52}$$

With the deposition coefficient, the deposition of particles in the element can be calculated at the center of the element and the total deposition of particles is calculated as the summation of the depositions in each element.

$$\Delta\sigma_{i,j} = \lambda_{i,j} \cdot C_{i,j} \cdot \left(\Delta t_{i,j} - \frac{d_i + \Delta d/2}{V_{i,j}}\right) \cdot \exp\left(-\lambda_{i,j} \cdot \frac{d_i + \Delta d/2}{V_{i,j}}\right) \tag{7.53}$$

$$\sigma_{i,j} = \sum_{i=n}^{j} \Delta\sigma_{i,j} \tag{7.54}$$

By using the density relationship, the change in porosity of porous medium becomes

$$n_{i,j} = n_o - \frac{\sigma_{i,j}}{G_s \gamma_w} \tag{7.55}$$

Based on the permeability relationship, the variation of the intrinsic permeability is estimated by:

$$\frac{K_{i,j+1}}{K_{i,j}} = \left(\frac{n_{i,j+1}}{n_{i,j}}\right)^3 \cdot \left(\frac{1 - n_{i,j}}{1 - n_{i,j+1}}\right)^2 \tag{7.56}$$

However, the concentration of the suspensions may be reduced as filtration proceeds due to the particle loss in the previous block, affecting both the unit weight and apparent viscosity. The change in the particle concentration, unit weight and apparent viscosity was calculated by:

$$C_{i+1,j} = \mathrm{C_{i,j}} - \Delta\sigma_{i,j} \tag{7.57}$$

$$(\gamma_g)_{i+1,j} = 1 + \mathrm{C_{i+1,j}} \cdot \left(1 - \frac{1}{G_s}\right) \tag{7.58}$$

$$\mu_{i+1,j} = \mu_w \cdot \left(1 + \left(\frac{\mu_o}{\mu_w} - 1\right)\right) \cdot \left(\frac{\phi_{p\,i+1,j}}{\phi_{p_o}}\right) \tag{7.59}$$

Since the grouting process occurs at each element simultaneously, the coupling between the volume blocks should be taken into account. This effect is considered by calculating the maximum time at each block, which governs the whole grouting process at the time step j.

$$\Delta t_j = \max\left(\Delta t_{1,j}, \Delta t_{2,j}, \Delta t_{3,j} \ldots \Delta t_{j,j}\right) \tag{7.60}$$

With the determined time, the amount of filtration, change of intrinsic permeability and corresponding volume response were calculated at the middle of the elements using the equations (7.52) through (7.56). The numerical calculation was coded by the Visual basic embedded in Microsoft excel in accordance with the mathematical formulation and the calculation algorithm.

7.4.10. Simulation results

With the parameters presented in Table 7.4, the numerical simulation was performed. Since the purpose of this simulation was to find the lump parameters (θ) which are used

for estimating groutability later in this Chapter, the suspension flow was controlled to stop at the similar volume intakes (the ranges of ± 5%) to the experimental data. Figure 7.22 shows the comparisons of the calculated and measured volume evolution with the injection time. As can be seen, the model could relatively well capture the overall volume response with the range of the lump parameters (θ) of 4.7 to 13.8, which are agreed with the values reported in the literature (Rege and Fogler, 1988). As shown in Figure 7.23, the values tended to increase with the increase in particle fraction and decreased as the injection pressure increased. In addition, the soil with the larger effective grain size produced smaller value of the lump parameters, indicating the reduced filtration. The simulation results were consistent with the empirical observations in Chapter 5. Figure 7.24 shows the comparison of the calculated and measured penetration distance. The results imply that the stoppage of the suspension flow was controlled by the filtration.

Table 7.4 Parameters used in calculation (Ottawa sand)

Injection pressure (P)	140 kPa
Length of permeameter (L)	15.5/50cm
Height of elements	0.5 cm
Initial porosity (n_o)	0.406
Initial intrinsic permeability (K_o)	5.18×10^{-7} cm^2
Mean pore radius lognormal distribution (m)	-3.41
Standard deviation of pore radius lognormal distribution (b)	0.76
Effective length of pore tube (a*)	9.11 mm
*Average size of bentonite grout (a)	4.8 μm
Hydrated specific gravity (Gs)	1.39
Grout concentration (C_o)	0.077 g/cm^3
Unit weight (γ_g)	1.021 g/cm^3
Apparent viscosity at equilibrium (μ)**	0.076/0.102 Pa·s

* Weight averaged particle size

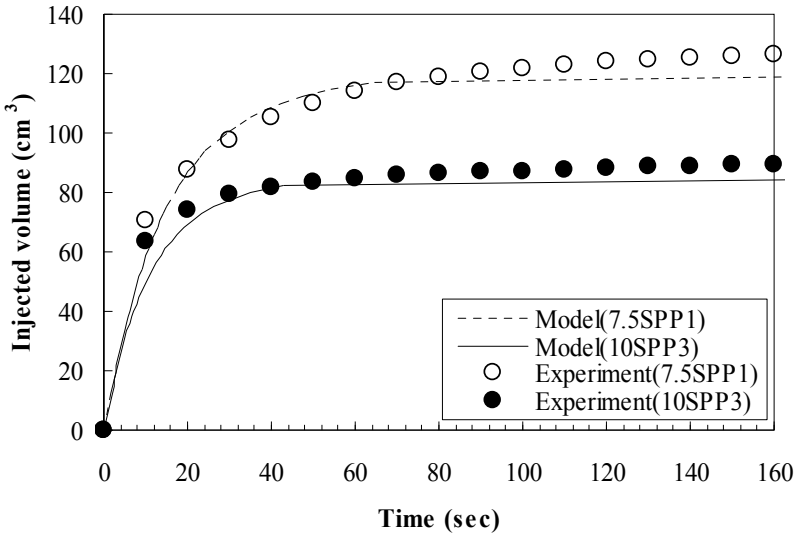

Figure 7.22 Model simulated and measured injected volume (grout intakes) with time

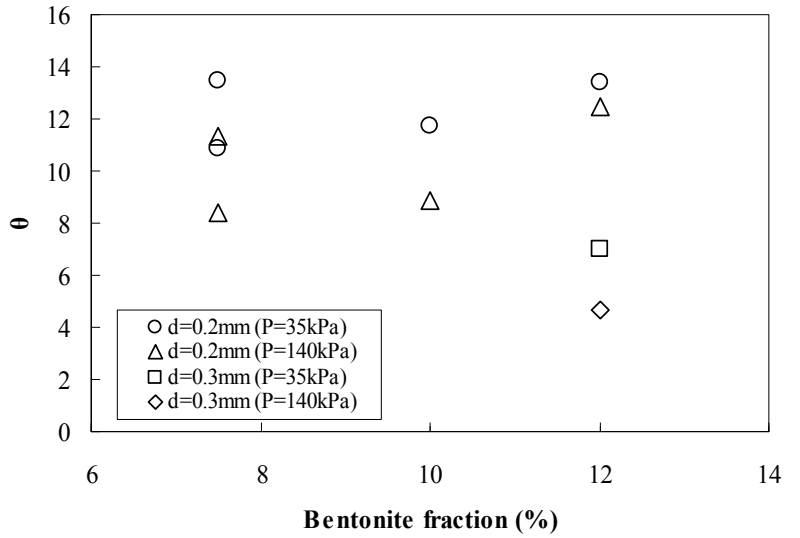

Figure 7.23 Lump parameter based on bentonite fraction: 7.5, 10 and 12% suspensions with 0 to 4% SPP

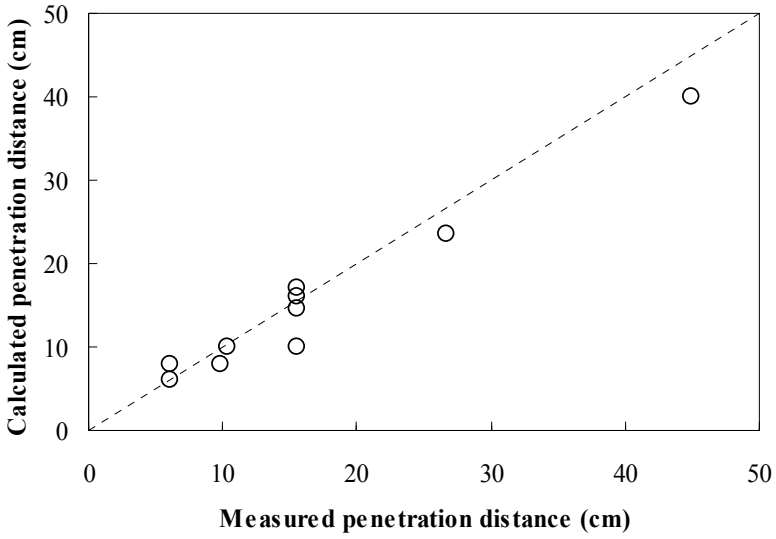

Figure 7.24 Measured and calculated penetration distance

Kim et al. (2009) proposed a new groutability criterion based on the lump parameter, particle size of grout, and pore property of porous media for microfine cement grout in compaction grouting. They classified the groutability as 4 groups depending on the degree of filtration.

$$GC = \frac{1}{9.11 \cdot e^{2(b^2+m)}} \left[4 \cdot (a \cdot \theta)^2 - 4(a \cdot \theta)^3 \cdot e^{(b^2-2m)/2} + (a \cdot \theta)^4 \cdot e^{2(b^2-m)}\right] \quad (7.61)$$

Where b and m are the mean and standard deviation of lognormal distribution of pore size, respectively, a is the migrating particle radius. Table 7.5 presents the groutability criterion and qualitative description of the groutability. With the estimated b, m, and a, the groutability of GC was calculated and presented in Table 7.6. The criterion estimated by the equation (7.61) and Table 7.5 classified the tested sands (Ottawa and Monterey #0/30 sand, Dr≈ 30%) as Group II and III which are under the effect of filtration. The GC values were compared with the new groutability (N^*) in Figure 7.25. The GC values were consistently decreased with the increase in groutability as a linear

function. This implies that the groutability increases with the decrease of the filtration and the proposed groutability criterion well reflected the filtration.

Table 7.5 Criterion and description of groutability (Kim et al. 2009)

Range of GC (1/cm)	Group	Description
GC<0.001	I	Grout can be injected successfully into soil formation. Effect of filtration is little. The other factors such as injection pressure and viscosity govern the grout penetration
0.001≤GC<0.01	II	Grout can be injected sufficiently into soil formation. Effect of filtration is a little.
0.01≤GC<0.1	III	Grout may be injected insufficiently. Effect of filtration on grout penetration is large
0.1≤GC	IV	Permeation grouting may be impossible. Filtration phenomenon governs grout penetration

Table 7.6 GC values for bentonite grouts

Grout mix (pressure)	Sand	GC	Injected pore volume	Group
B7.5(35)	Ottawa	0.060	0.6	III
B7.5SPP1(35)	Ottawa	0.038	0.9	III
B10SPP3(35)	Ottawa	0.044	0.6	III
B12SPP4(35)	Ottawa	0.059	0.3	III
B7.5(140)	Ottawa	0.041	0.9	III
B7.5SPP1(140)	Ottawa	0.025	1.6	III
B10SPP3(140)	Ottawa	0.027	1.0	III
B12SPP4(140)	Ottawa	0.050	0.4	III
B12SPP4(140)	Monterey #0/30	0.009	2.5	II

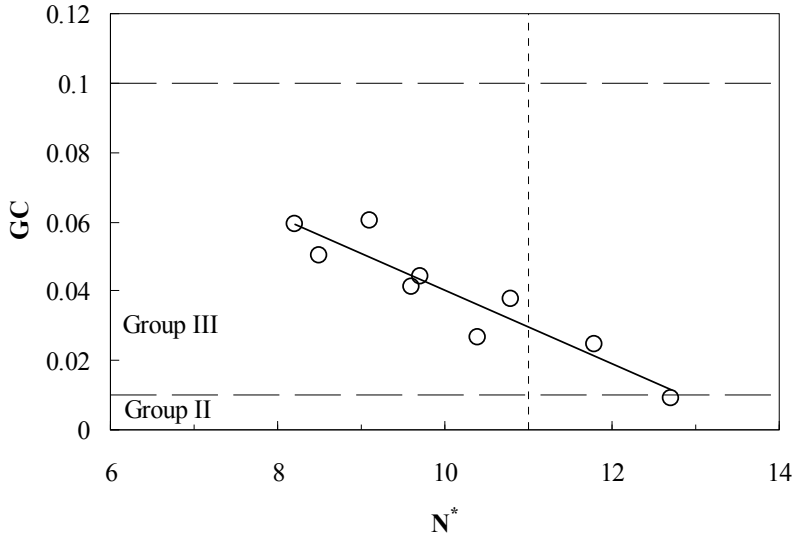

Figure 7.25 Comparison between GC and N*

7.3. Constant flow rate

The formation of filter cake retards the grout flow at constant pressure condition, accumulating particles near the injection point. Constant flow rate technique has been widely adopted for particulate grouts with high flow rate, which can retard the formation of filter cakes by reducing the filtration of particles through sand beds.

7.5.1. Grout propagation mechanism

Similar to the constant pressure technique, a simplified volume block approach was used to approximate the variation of penetration distance under a constant flow rate. Since the flow rate was maintained as a constant, a constant volume of grout block was used for the calculation. The comparison of the measured and calculated distance (Figure 7.26) showed good agreement, indicating that the effect of filtration in the constant flow rate tests are little and negligible. However, it should be noted that the

filtration at a multistage injection condition may increase due to the reduced conductivity of the sand bed.

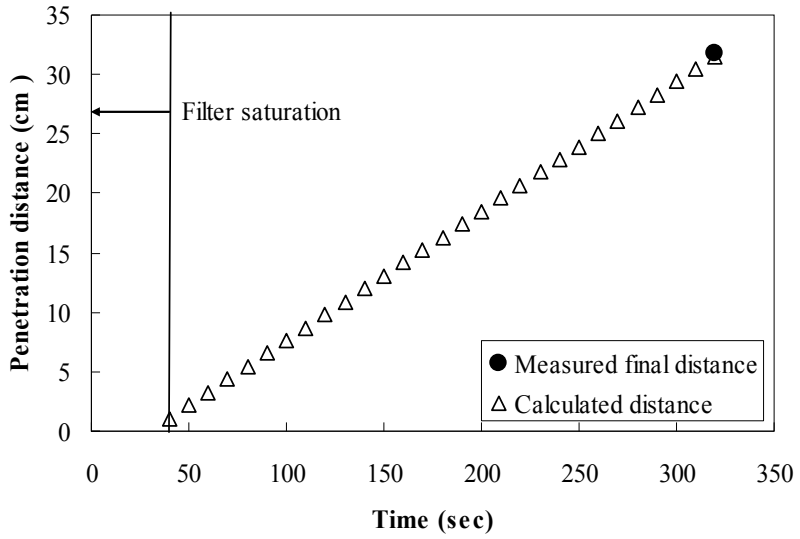

Figure 7.26 Comparison of measured and calculated distance

7.5.2. Apparent viscosity

Due to the transient nature of the rheological properties in bentonite suspensions (the rheological properties vary with time, particle loss due to filtration, and chemical reaction between bentonite and ions), it is challenging to determine a constant design value. However, the comparison of the measured values to the theory may provide a useful insight of the apparent viscosities that should be applied in design process.

Based on Darcy's law and bundle-of-tube assumption, the apparent viscosity at each element can be expressed as:

$$\mu = \frac{\Delta P}{\Delta h} \cdot \frac{K \cdot A \cdot \Delta t}{\Delta Q} \tag{7.62}$$

Where μ is the apparent viscosity, ΔP is the pressure difference, K is the intrinsic permeability, A is the area, and Δh and ΔQ are the height and volume of each element respectively. Since the flow rate was constant and the filtration was considered to be minimal in the infinitesimal elements, all variables except for the pressure difference will remain constant. With the measured pressure differences, the apparent viscosity can be estimated. Since equation (7.6) produced the approximate shear rates over 250 s^{-1}, the calculated apparent viscosity was compared to those at equilibrium state. Table 7.7 summarizes the properties used for the calculation.

Table 7.7 Parameters used in back-calculation (Ottawa sand)

Length of permeameter (L)	15 to 31.75 cm
Area of permeameter (A)	37.85 cm^2
*Initial porosity (n_o)	0.406
**Initial intrinsic permeability (K_o)	5.18×10^{-7} cm^2
Flow rate (q)	1.67 cm^3/sec
Time interval (Δt)	10 sec

* Estimated at the relative density of 30%
** Calculated based on the equation. (7.30)

The comparison of the measured (at equilibrium) and calculated apparent viscosity is presented in Figure 7.27. The apparent viscosity (equilibrium) was corrected with the relationship shown in Figure 7.8 to convert the vane values (which are relative values) to absolute viscosity measurements (as measured by the cone and plate). As can be seen, the back-calculated apparent viscosities were slightly lower than the measured values, but showed overall good agreement. This indicates that the application of the apparent viscosity measured by vane geometry as a design parameter may provide a conservative evaluation of the suspension flow.

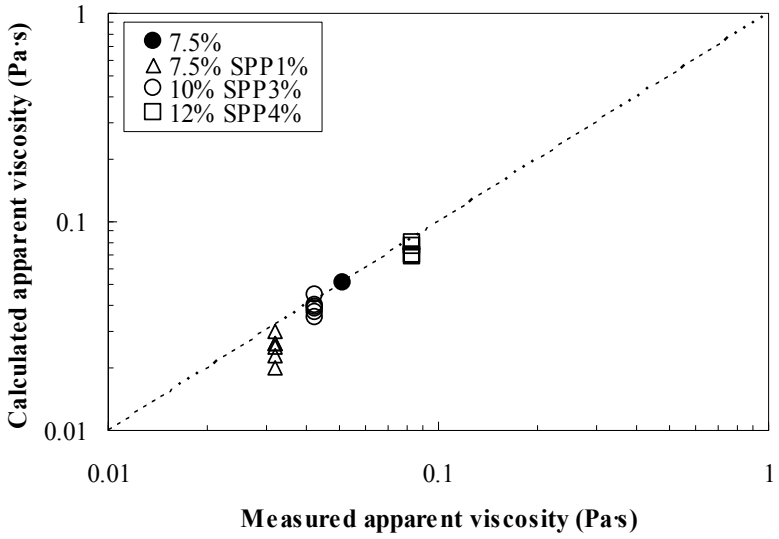

Figure 7.27 Comparison of measured and calculated apparent viscosities

7.5.3. 3-D propagation

If the effect of filtration in constant flow rate test is minimal as shown in Figure 7.26, the propagation of the one dimensional flow can be correlated to the 3-dimensional flow which is assimilated to the field injection process. Although the propagation mode depends on the types of injection methods (point injection or Tube-A'-Manchette) and geological conditions, the grout propagation through a point is typically modeled as a spherical or ellipsoidal propagation from a point source as shown in Figure 7.28 (a) and (b). In addition, previous researches reported that the cement based grout propagated with approximately spherical shape in uniform sand (Bouchelaghem et al., 2001; Saiyori et al., 2008; Kim et al., 2009):

$$\text{Sphere: } \frac{4}{3}\pi\left(R^3\right)=\frac{V_{injected}}{n} \tag{7.63}$$

$$\text{Ellipsoid: } \frac{4}{3}\pi\left(a^2 b\right)=\frac{V_{injected}}{n} \quad \text{with} \quad \frac{a}{b}=\sqrt{\frac{k_h}{k_v}} \tag{7.64}$$

Where R is the radius of the grout sphere, $V_{injected}$ is the injected volume, n is the porosity, k_h is the horizontal hydraulic conductivity, and k_v is the vertical hydraulic conductivity.

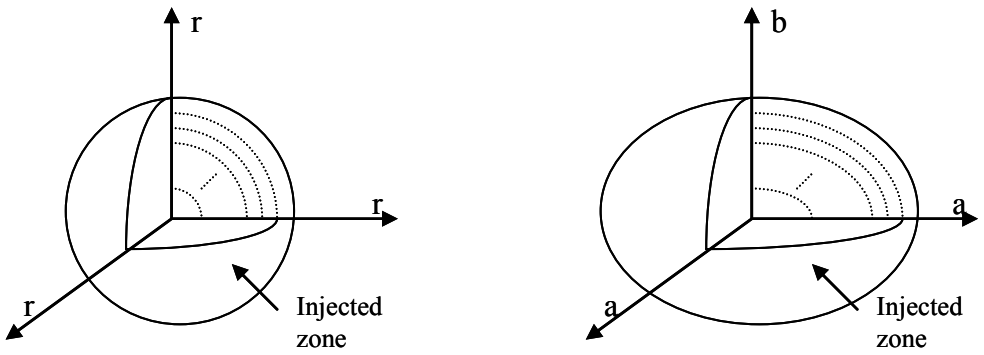

(a) (b)

Figure 7.28 (a) 3-D spherical and (b) ellipsoidal propagation of grout

Similar to the one-dimensional volume block propagation shown in Figure 7.19, the 3-D propagation with the two different modes was estimated. For spherical propagation, the increased pore volume changes with the radius, r and expressed as

$$\frac{4}{3}\pi(r_i^{\,3} - r_{i-1}^{\,3}) = \frac{V_i}{n_o} \tag{7.65}$$

Where r_i and r_{i-1} is the radius at i and i-1th segment, V_i is the injected volume per unit time. If the flow rate in 3-D case is the same as that in 1-D case, the grout front r_i can be estimated and correlated with the grout front in 1-D propagation. Similarly, the ellipsoidal propagation can be calculated as follows:

$$\frac{4}{3}\pi(a_i^{\,2}b_i - a_{i-1}^{\,2}b_{i-1}) = \frac{V_i}{n_o} \tag{7.66}$$

Where a_i and a_{i-1} is the grout front long a-axis, b_i and b_{i-1} is the grout front long b-axis at i and i-1th segment, V_i is the injected volume per unit time.

Figure 7.29 displays the comparison of penetration distance between different modes of propagation. A constant flow rate of 1.67 cm^3/sec was used in the calculations. Due to the difference in propagation mode the penetration distance (the location of the grout front) changes significantly. The 3-D sphere produced the smallest treatment range with the same volume of grouts among the three propagation modes and the difference with 1-D propagation becomes larger as the injection time elapses. This is reasonable in that the increase in radius of the volume segment becomes smaller due to the increase in the area. In the case that the heterogeneity of soil varied, that will greatly affect the penetration of the suspensions, the ellipsoidal propagation may be appropriate to simulate the suspension flows, increasing the treatment range compared to the spherical propagation. The 1-D penetration distances are linked with the 3-D propagation (Figure 7.30), and regression analyses were conducted. The regression equations and R^2 values are presented in Table 7.8. The results indicate that the penetration distance obtained from laboratory tests should carefully be extrapolated into field injection; otherwise it may overestimate the grout propagation in field application. For example, the penetration distance of 30 cm will theoretically be reduced to 6 cm in the radial direction (3-D sphere), and 20 cm in the horizontal direction (3-D ellipsoid, $a/b=\sqrt{2}$). Therefore, more grout and time would be needed to treat a similar area in the 3-D case than 1-D under the same flow rate.

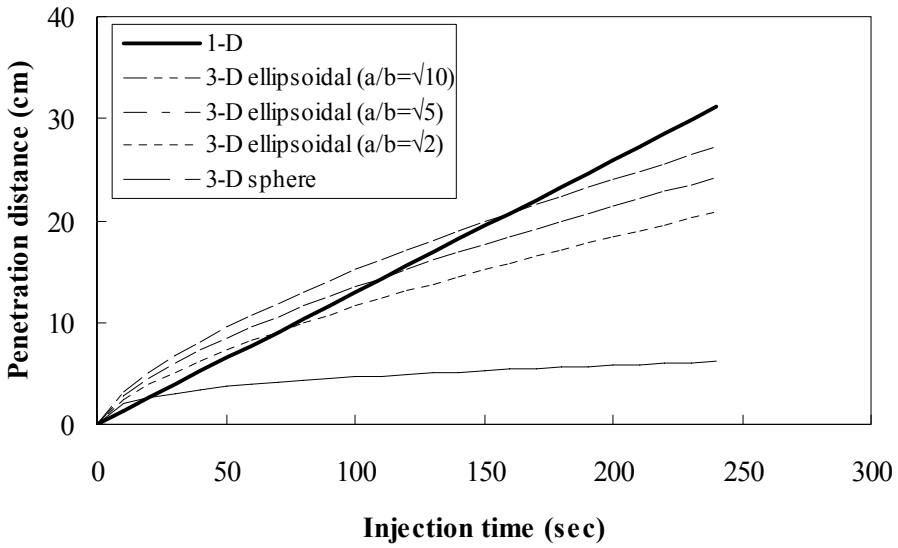

Figure 7.29 Comparison of penetration distance between different modes of propagation: the penetration distance of ellipsoidal mode is in the direction of a-axis

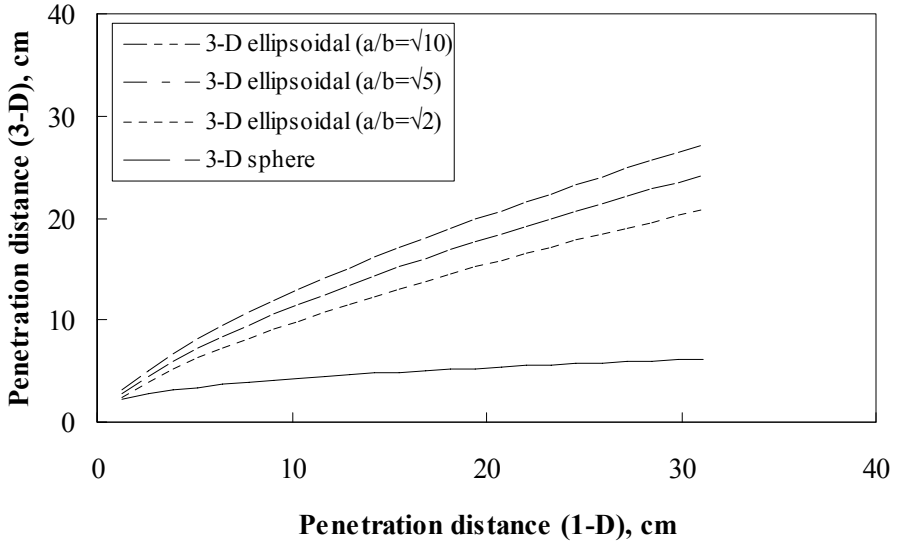

Figure 7.30 Comparison of penetration distance between 1-D and 3-D propagation: the penetration distance of ellipsoidal mode is in the direction of a-axis

Table 7.8 Correlation between 1-D and 3-D propagation (regression equations and R^2)

Propagation mode	Regression	R^2
3-D Sphere	$H_{3\text{-}D}=1.965\times H_{1\text{-}D}^{0.333}$	1
3-D Ellipsoid (a/b=√2)	$H_{3\text{-}D}=2.044\times H_{1\text{-}D}^{0.676}$	1
3-D Ellipsoid (a/b=√5)	$H_{3\text{-}D}=2.381\times H_{1\text{-}D}^{0.676}$	1
3-D Ellipsoid (a/b=√10)	$H_{3\text{-}D}=2.672\times H_{1\text{-}D}^{0.676}$	1

The change in the propagation distance may change the injection gradient, causing different injection pressures depending on the different modes of propagation (in horizontal direction). If Darcy's law is valid and the filtration is minimal in the infinitesimal segments of the sphere, the flow rate can be expressed as:

$$q = \frac{K}{\mu}\cdot\frac{\Delta P}{\Delta r}\cdot\Delta A \tag{7.67}$$

Where q is the flow rate, ΔP is the pressure difference ($P_{injection}$-u_{water}), K is the intrinsic permeability, Δr (when r is sufficiently small) is the difference in radius of grout sphere and ΔA is the area which calculated by:

$$\Delta A_{sphere} = \frac{4}{3\Delta r}\pi(r_i^{\,3} - r_{i-1}^{\,3}) \tag{7.68}$$

$$\Delta A_{ellipsoid} = \frac{2\times V}{a+b} = \frac{8}{3\times(\Delta a+\Delta b)}\pi(a_i^{\,2}b_i - a_{i-1}^{\,2}b_{i-1}) \tag{7.69}$$

If there is no change in pore properties of sand and apparent viscosity, the pressure variation in 3-D sphere can be correlated to the pressure buildup in 1-D case. For the ellipsoidal propagation, the average hydraulic gradient in the infinitesimal element was considered.

$$\Delta P_{3-D\ Sphere} = \frac{\Delta r}{\Delta d}\cdot\frac{A_{1\text{-}D}}{\Delta A_{3-D}}\cdot\Delta P_{1\text{-}D} \tag{7.70}$$

$$\Delta P_{3\text{-}D\ ellipsoid} = \frac{(\Delta a + \Delta b)}{2 \times \Delta d} \cdot \frac{A_{1-D}}{\Delta A_{3-D}} \cdot \Delta P_{1-D} \tag{7.71}$$

Figure 7.31 shows the comparison between the calculated pressure variations in the 1-D and 3-D cases. While the ellipsoidal flow produced higher injection pressures than the 1-D case, significantly lower injection pressures were developed at the spherical propagation at longer injection times. In addition, the rate of the increase in injection pressure was very low, producing essentially constant injection pressure after a steep initial increase in pressure. This is reasonable in that the area the flow path through increases significantly as the sphere evolves with time.

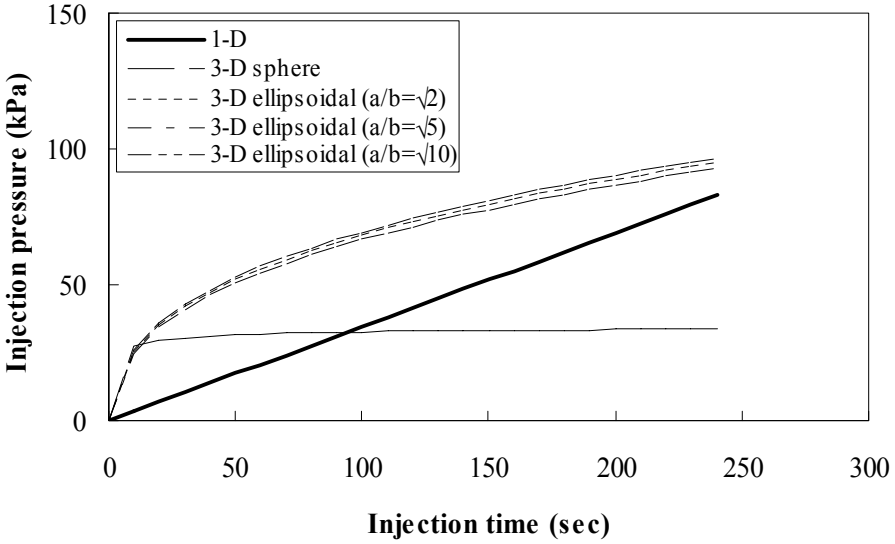

Figure 7.31 Comparison of injection pressure based on different mode of propagation; 7.5% suspensions with 1% SPP, q=1.67 cm^3/sec

In order to confirm the theoretical estimation of pressure evolution in 3-D cases, a radial flow test was conducted similar to the 1-D test at the same constant flow rate of 1.67 cm^3/sec. Figure 7.32 depicts a schematic of radial flow test setup. The permeameter had an internal diameter of 14 cm and the height of 37 cm. This setup had

an outer drainage layer of 1.5 cm and inside filter layer of 3 cm in diameter for the uniform distribution of bentonite suspension. At the top and bottom of the permeameter, drainage layers (3 cm) were placed respectively. Moreover, the two injection holes, having the diameter of 0.16 cm, were placed at the middle of the permeameter (approximately 17.8 cm from the top plate). The other setups were the same as what used for the 1-D constant flow rate test.

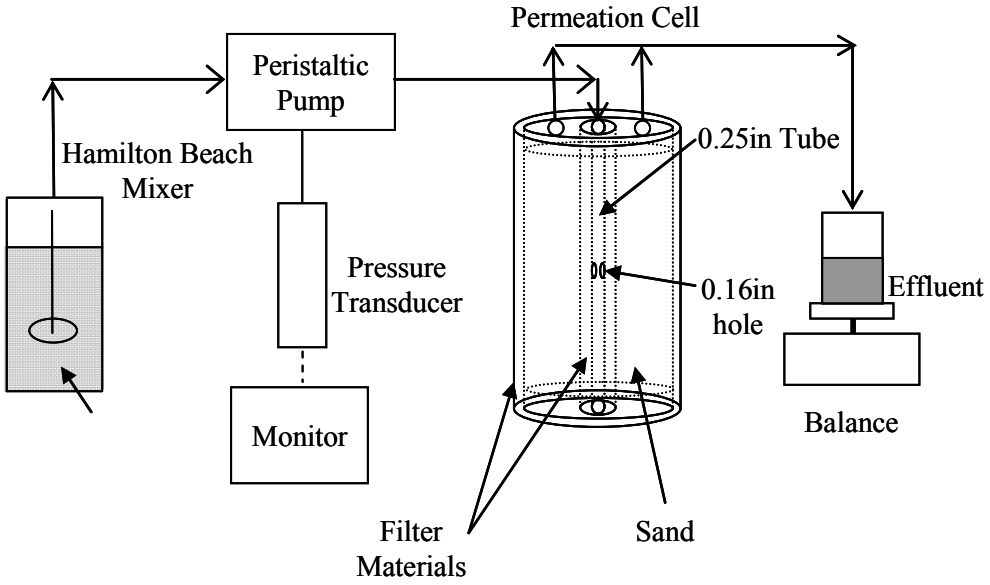

Figure 7.32 Schematic of radial flow setup

The injection pressure of 7.5% suspension with 1% SPP was monitored with the injection time and compared with the theoretical calculations as shown in Figure 7.33. The similar amount of grout (approximately 500 ml) to what used in 1-D test was injected for the comparison purposes. As can be seen, the injection pressures in radial flow were developed more slowly than the 1-D case and produced essentially constant injection pressures. The result showed that the pressure evolution was similar to what was calculated based on the 3-D sphere propagation. The slightly high injection pressure is

possibly due to the higher relative density than 1-D case. In addition, the shape of grout propagation was examined by trimming the grouted specimen after a week of resting time (Figure 7.34). The specimen was carefully trimmed until a distinct grout layer was observed. As can be seen, the radial injection produced approximately spherical bulb with the diameter of approximately 10 cm, which was similar to the calculated value. The results suggest that the treatment range (Center to Center distance between bore holes; $2R_{design}$) in field application can be approximated by using the design injection time and flow rate.

$$R_{design} = \sqrt[3]{\frac{3}{4\pi} \cdot \frac{q_{design} \cdot t_{design}}{n_o}} \tag{7.72}$$

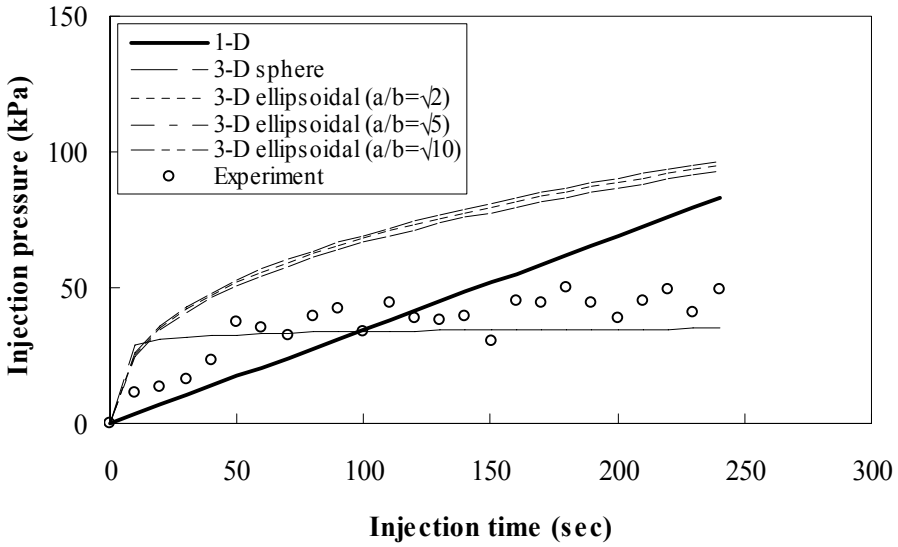

Figure 7.33 Comparison of the measured and calculated injection pressures with time : Ottawa sand, Dr≈35% , q=1.67 cm^3/sec and FC=0%

Figure 7.34 Grout bulb excavated from radial injection test

7.4. Post grouting stability

Once the suspensions are permeated into the sand pores, the yield stress increases gradually with time forming a gel-like pore fluid. However, the suspensions still may be subject to wash-out when an external water pressure is applied beyond the yield stress. Since the modification of bentonite suspensions significantly reduces their yield stress and retards its time dependent buildup, the possibility of wash-out should be evaluated in terms of time and the applied hydraulic gradients. To evaluate the modified grout stability, a model levee with a grout cut-off curtain is assumed. The sand properties and hypothetical installation of grout curtain (3 rows with the center-to-center distance of 30 cm) are presented in Table 7.9. In accordance with the equation (7.73), the time dependent stability of the placed bentonite grout was estimated for 7.5, 10 and 12% bentonite suspensions with 1, 3 and 4% SPP, respectively (Figure 7.35-Figure 7.37).

$$\frac{P}{L} = \tau_O \cdot S \cdot (1 - n) \tag{7.73}$$

Table 7.9 Parameters used in back-calculation

Height of the model levee (H)	4.6 m
Length of the grouted zone (L)	1.8 m
*Porosity (n)-Ottawa sand	0.406
*Porosity (n)-Monterey #0/30 sand	0.434
*Porosity (n)-Aggregate sand	0.366
**Specific surface (S)-Ottawa sand	15371.5 (1/m)
**Specific surface (S)-Monterey #0/30 sand	10266.2 (1/m)
**Specific surface (S)-Aggregate sand	5687.4 (1/m)

* Estimated at the relative density of 30%
** Calculated based on Axelsson and Gustafson (2007)

All of the modified suspensions were evaluated to be stable after the resting time of 24 hours at a hydraulic gradient of 5. As the hydraulic gradient increases, the stability of the placed suspensions decreases and the suspensions required more time to be stabilized under higher hydraulic gradients. For instance, the 7.5% suspensions with 1% SPP will be stable after 0.5 hour at a hydraulic gradient of 1. However, it requires approximately 5 days at a gradient of 20.

The stability of the placed grout also varied with the types of sands because the grout flow will be readily initiated in the sand having large specific area. The 7.5% suspensions with 1% SPP will be stable in Ottawa sand at the hydraulic gradient of 40 after 5 days, but it was estimated to be unstable in Monterey #0/30 and aggregate sand which have larger effective grain size at the same gradient and resting time. The modified 7.5% suspensions could not reach a stable state in the aggregate sand. This indicates that the selection of the type of grouts should be incorporated with not only groutability, but also post grouting stability.

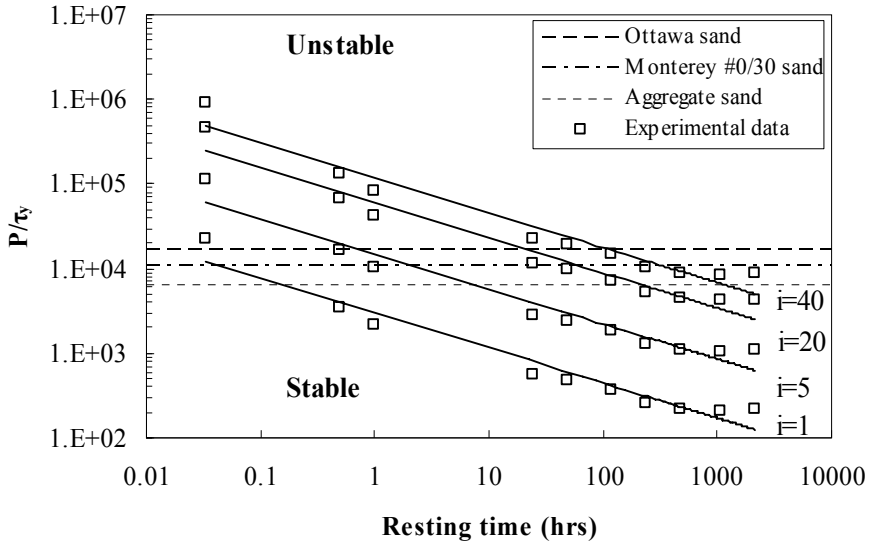

Figure 7.35 Stability chart of the placed grout at various hydraulic gradients for 7.5% suspensions with 1% SPP

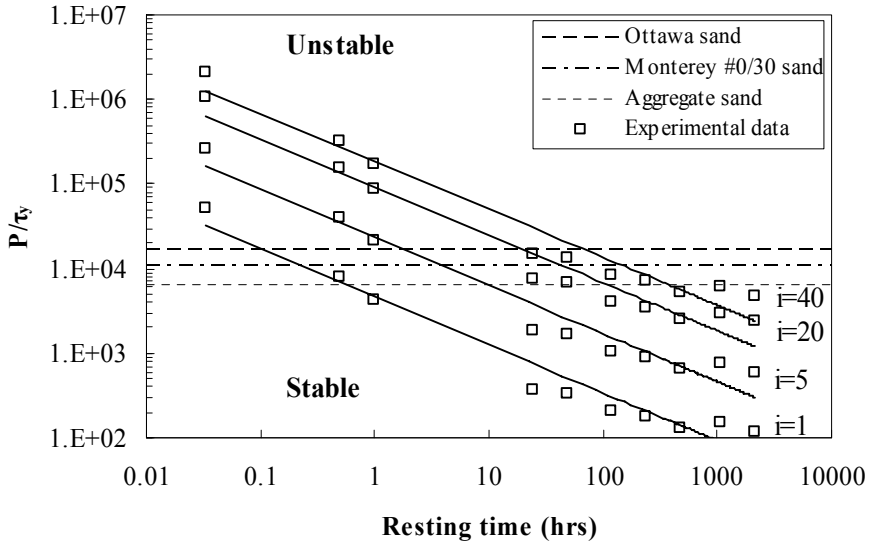

Figure 7.36 Stability chart of the placed grout at various hydraulic gradients for 10% suspensions with 3% SPP

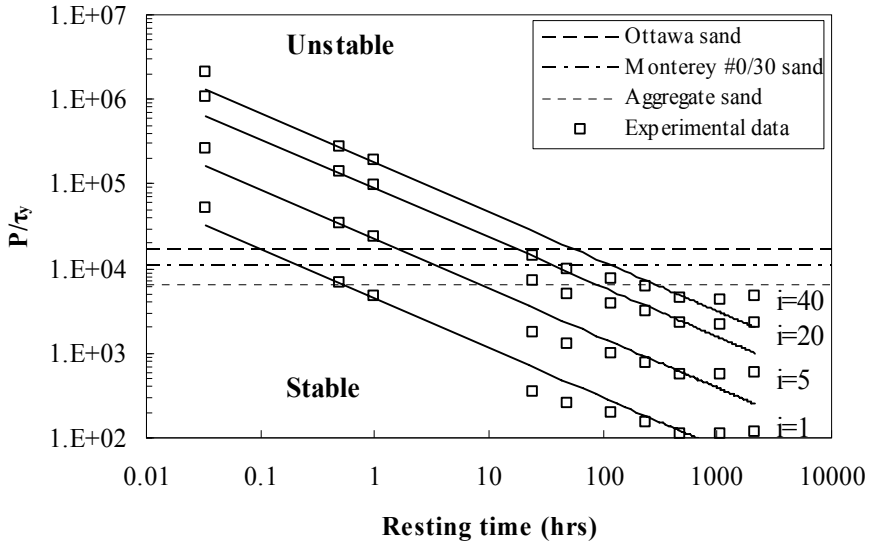

Figure 7.37 Stability chart of the placed grout at various hydraulic gradients for 12% suspensions with 4% SPP

7.5. Conclusions

The stoppage mechanism of the suspension flow was studied and revealed that the stoppage of the modified suspensions through sand can be controlled by rheological blocking or filtration. The comparison of the theoretical models and the experimental data showed that the stoppage of the modified suspensions in this study is mainly controlled by filtration rather than rheological blocking. An empirical correlation to predict the penetrability of the suspensions was proposed with constant pressure technique. Moreover, a new groutability criterion for the modified bentonite suspensions was proposed considering soil/grout and experimental parameters. An advanced groutability using macroscopic flow model was compared to the proposed groutability. It was found that the GC values decreased as N* increased, indicating that the reduced filtration increases the groutability of soil.

With constant flow rate tests, it was concluded that the measured apparent viscosities were somewhat lower than the calculated ones, indicating the use of the apparent viscosity from vane geometry will provide a conservative evaluation. However, the apparent viscosities corrected using the relationship between the two geometries (cone and plate and vane and cup) were comparable to the calculated ones. Different propagation models were compared to project the 1-D laboratory results into the field injection. The spherical propagation produced the least treatment range, but the lowest injection pressure, meaning that a longer injection time may be required in the field to achieve the typical center distance of bore holes.

The post grouting stability of the placed bentonite suspensions was evaluated based on the relationship proposed by Cambefort (1964). A stability chart based on time dependent yield stress evolution and hydraulic gradient (from imaginary levee configuration) was developed. The chart showed that the placed suspensions will become stable as the resting time increases and unstable as the external hydraulic gradient increases. However, the stability of the suspensions increases with the decrease in specific area of treated soil.

CHAPTER 8: CONCLUSIONS AND FUTURE WORK

8.1. Introduction

This chapter summarizes the major findings through this study. The main objective of this study was to investigate a possible application of the concentrated bentonite suspensions to improve hydraulic performance of granular soils. The rheological properties of the modified bentonite suspensions, their permeation through various sands and hydraulic conductivity of the treated sands were investigated based on the extensive experimental and numerical studies.

Based on that, this research will make an important contribution to understand 1) the rheological properties of modified bentonite suspensions, 2) the flow behavior of clay suspensions through granular soils and 3) the hydraulic performance of the grouted soils. In details, the current research will help understand the theory behind 1) the mechanism of interaction between bentonite and sodium pyrophosphate ions, 2) the time dependent behavior of the bentonite suspensions, 3) the parameters affecting the suspension flow through granular soils, and 4) the physical changes in the pore spaces due to bentonite grouting, and their effect on hydraulic conductivity.

In addition, the following practical contributions will be drawn from this research: 1) by permeating the problematic sub-layer only (as compared to a slurry-wall fix), the amount of grout can be reduced by using engineered bentonite grouts, 2) developing a site-specific optimum engineered grout to maximize the effective grouting radius, 3) developing an empirical correlation for predicting the penetration depth of grouts based on the properties of both, the grout and the targeted soil, and 4) modifying the current criteria for groutability of granular soils to increase the chances of a successful grouting.

8.2. Conclusions

The research focused on 1) measuring the rheological properties of the various engineered bentonite suspensions over time, 2) investigating the parameters affecting the flow of the bentonite suspensions through granular soils, and 3) determining the hydraulic performance of the grouted granular soils. Based on the extensive laboratory and numerical studies, the following conclusions were drawn:

1. The addition of a small amount of sodium pyrophosphate was found to significantly reduce the yield stress and apparent viscosity in bentonite suspensions. However, this reduction tended to converge after a threshold percentage of SPP (2, 3, and 4% for 7.5, 10, and 12% bentonite suspensions, respectively). It was concluded that a small amount of SPP (1 to 4%) was enough to improve the mobility of the concentrated bentonite suspensions effectively, and an excessive amount of SPP may not be effective in further reducing the yield stress and apparent viscosity. The critical storage modulus showed similar trends with the flow properties and revealed that yield stress has a unique relationship with the critical storage modulus. This may be beneficial to reduce the number of tests required to estimate both the penetrability and resistance to dynamic loading.

2. The reduced yield stress and apparent viscosity was recovered gradually with time. The results showed that the concentrated suspensions produced a lower degree of increase in yield stress (lower thixotropy ratio) than the diluted suspensions with time; similarly, larger percentages of SPP induced higher degrees of build-up at a given resting time (higher thixotropy ratio). The constrained Brownian motions in the concentrated suspensions produced low thixotropy ratios. On the other hand, the SPP modified suspensions, which showed a high degree of Brownian motion due to the reduction of

inter-aggregate bonds (3-D network), produced higher thixotropy ratios than those in the unmodified suspensions.

3. The rheological properties of the modified bentonite suspensions were found to be strongly influenced by the amount of cations (Na^{+}/Ca^{++}), pH, hydrolysis of SPP and hydration of bentonite. Especially, the amount of cations in the suspensions controlled time dependent behavior of the bentonite suspensions. However, the measurement of the rheological properties was affected by sedimentation of particles, especially when a long resting time was applied (longer than 3 months).

4. Yield stresses at increasing resting times measured by cone and plate geometry was found to be significantly underestimated due to disturbance. When using the cone and plate configuration, the tested bentonite suspensions showed little to no increase in yield stress with time. On the other hand, relatively undisturbed yield stresses measured using vane geometry displayed a more distinct increase with time. The proposed methodology to predict "undisturbed" yield stress from "disturbed" yield stress will be convenient and relatively accurate way to predict time dependent evolution of yield stress. Although the proposed model was developed for bentonite suspensions, the same model can be used for different thixotropic suspensions; however, a new disturbance function, $D(t_r)$ should be developed for the different suspensions. This method is attractive in terms of an optimal usage of equipment and cost-effectiveness (no need to manufacture many storage cups for vane). More importantly, this work provides a method to measure the aged "undisturbed" yield stress of bentonite suspensions which is critical for accurate evaluation of the grout stability inside porous media.

5. Two types of injection techniques were used to investigate the permeation of the modified bentonite suspensions through various sands and link the rheological properties with the flow characteristics of the bentonite suspensions. The results from

constant pressure tests showed that the permeation of the modified suspensions greatly increased the penetration of concentrated bentonite suspensions. However, it was affected by not only the sand properties, but also grout properties as well as the experimental condition such as injection pressure. The pressure variation from the constant flow rate tests showed a linear increase in the injection pressures, showing the minimal effect of filtration.

6. The saturated hydraulic conductivity of the bentonite grouted sand was measured to investigate the hydraulic performance of the grouted sands. The hydraulic conductivity of the permeated sand decreased approximately 4 to 5 orders of magnitude, showing the effectiveness of bentonite grout to improve the hydraulic performance of the permeable sand deposit. The hydraulic conductivity was reduced with bentonite contents which vary with the experimental conditions such as relative density, distance from injection point and the injected pore volumes. However, the hydraulic conductivities at low bentonite contents were less affected by the bentonite content because of physical configuration of pore spaces (hydraulic conductivity was still controlled by the unblocked pore space). The physical pore changes with bentonite contents were calculated based on the volume of fully swollen bentonite. However, the hydraulic conductivities linearly increased with increased logarithmic clay void ratios, indicating that water flows through the clay voids.

7. The stoppage mechanism of the suspension flow was studied and revealed that the stoppage of the modified suspensions through sand can be controlled by the rheological blocking or filtration. The comparison of the theoretical models and the experimental data showed that the stoppage of the modified suspensions is more probably controlled by filtration rather than rheological blocking. An empirical correlation to predict the penetrability of the suspensions was proposed with constant pressure

technique to predict the penetration distance of the bentonite suspensions. The proposed relationship may be helpful to approximate the treatment range, when 1) the filtration is the dominant stoppage mechanism and 2) the grouting is performed under 1-D flow condition such as relatively thin constrained layers. Moreover, a new groutability criterion for the modified bentonite suspensions was proposed considering soil/grout and experimental parameters. In addition, an advanced groutability using macroscopic flow model was compared to the proposed groutability. It was found that the GC values decreased with an increase in N*, indicating that the reduced filtration increases the groutability of soil.

8. Different propagation models were compared to project the 1-D laboratory results into the field injection. The spherical propagation produced the least treatment range, but the lowest injection pressure, meaning that a higher flow rate could be utilized in the field to achieve the increased treatment ranges. However, the injection time should be adequately controlled considering the evolution of grout bulb.

9. The post grouting stability of the placed bentonite suspensions was evaluated based on the relationship proposed by Cambefort (1964). A stability chart based on time dependent yield stress evolution and hydraulic gradient (from a proposed levee configuration) was developed. The chart showed that the placed suspensions will become stable as the resting time increases and less stable as the external hydraulic gradient increases. However, the stability of the suspensions is also dependent on the types of soil treated.

8.3. Future work

This dissertation showed a possibility of using the modified bentonite suspensions in permeation grouting to improve hydraulic performance of the permeable granular soils. However, previous researches showed that the SBMs with low percentage of bentonite were subjected to erosion when a high hydraulic gradient is applied (Kaoser et al. 1999; Chapuis 2000). Since the stability of the placed bentonite grout has been studied based on numerical calculation during this work, the extensive study of the erosion characteristic of the grouted sand may be required to ensure the sustainability of the grouted sand.

Since the application of the proposed bentonite suspensions is to minimize underseepage of water under levee foundation, chemical compatibility tests for the modified suspensions were not performed in this study. However, the proposed material may be useful to isolate the contaminated ground by forming less permeable barrier around the area. In the case, the chemical compatibility may be an important issue, requiring an extensive knowledge of chemical reaction between chemicals and bentonite gel which has already included SPP.

This work was focused on laboratory tests (small scale), the full scale grout propagation could not be captured in this study. Hence, large scale tests would be recommended to the actual field application for 1) the determination of the center-to-center distance of bore holes and 2) investigate of the actual pressure variation in field application, and 3) investigate the effects of heterogeneity in the field on preferential grout propagation.

REFERENCES

Abend, S., and Lagaly, G. (2000). "Sol-gel transitions of sodium montmorillonite dispersions," Applied Clay Science, Vol. 16, No. 3-4, pp. 201-227.

Abichou, T., Benson, C. H., and Edil, T. B. (2000). "Foundry Green Sands as Hydraulic Barriers: Laboratory Study," Journal of Geotechnical and Geoenvironmental Engineering, Vol. 126, No. 12, pp. 1174-1183.

Ahmad, F., and Kelso, W.I. (2001). "Pyrophosphate as a source of phosphorus: Hydrolysis under different conditions," Journal of Research Science, Vol. 12, pp. 130-139.

Akbulut, S., and Saglamer, A. (2002). "Estimating the groutability of granular soils: a new approach," Tunneling and Underground Spaces Technonlogy, Vol. 17, No.4, pp. 371-380.

Akbulut, S. (1999). "The improvement of geotechnical properties in granular soils by grouting." Ph. D. dissertation, The institute of Istanbul Technical University, Istanbul, Turkey.

American Petroleum Institute (2008). "ANSI/API recommended practice 13B-1. Recommended practice for field testing water-based drilling fluids," 4th ed.

Amorós, J.L., Sanz, V., Mestre, S., and Beltrán, V. (2002). "Kinetic study of concentrated clay suspension gelling by dynamic viscoelasticity measurements: effect of solids and deflocculant content," British Ceramic Transaction, Vol. 101, pp. 194-199.

Anderson, S.J., and Sposito, G., (1991). "Cesium adsorption method for measuring accessible structural surface charge," Soil Science Society of America Journal, Vol. 55, pp. 1569-1576.

Anton Paar Germany (2006). "Physica MCR series instruction manual," <www.anton-paar.com>

Arya, L.M., and Dierolf, T.S (1989). " Predicting soil moisture characteristics from particle size distributions: An improved method to calculate pore radii from particle radii," In:Indirect method for estimating the hydraulic properties of unsaturated soils, Vagenuchten M.T. and Leij, F.J. (eds.) U.S Sanitary laboratory, Riverside, California, pp. 115-124.

Arya, L.M., and Paris, J.F. (1981). "A physicoempirical model to predict soil moisture characteristics from particle size distribution and bulk density data," Soil Science of Society America Journal. Vol. 63, No. 5, pp. 1063-1070.

ASTM D 422-63 (2002). “standard test method for particle-size analysis of soils,” American society for testing and materials, Philadelphia, PA.

ASTM D854-02 (2002). “Standard test methods for specific gravity of soil solids by water pycnometer,” American society for testing and materials, Philadelphia, PA.

ASTM D4253-00 (2006). “Standard test methods for maximum index density and unit weight of soils using a vibratory table,” American society for testing and materials, Philadelphia, PA.

ASTM D4254-00 (2006). “Standard test methods minimum index density and unit weight of soils and calculation of relative density,” American society for testing and materials, Philadelphia, PA.

ASTM D 4318-00 (2000). “Standard test methods for liquid limit, plastic limit, and plasticity index of soils,” American society for testing and materials, Philadelphia, PA.

ASTM D5084-00 (2007). “Standard Test Methods for Measurement of Hydraulic Conductivity of Saturated Porous Materials Using a Flexible Wall Permeameter,” American Society for Testing and Materials, Philadelphia, PA.

ASTM D5856-95 (2007). “Standard Test Method for Measurement of Hydraulic Conductivity of Porous Material Using a Rigid-Wall, Compaction mold Permeameter,” American society for testing and materials, Philadelphia, PA.

ASTM C837-09 (2009). “Standard Test Method for Methylene Blue Index of Clay,” American society for testing and materials, Philadelphia, PA.

ASTM D1126-02 (2007). “Standard Test Method for Hardness in water”. American society for testing and materials, Philadelphia, PA.

Axelsson, M., (2006). “Strength criteria on grouting agents for hard rock,” Thesis, Chalmers University of Technology, Sweden.

Axelsson, M., and Gustafson, G. (2007). “Grouting with high water-cement ratios-literature and laboratory study,” Report no. 2007:5, Chalmers University of Technology, Sweden.

Axelsson, M., Gustafson, G., Fransson, Å., and Funehag, J. (2008). “Design criteria for permeation grouting in hard rock at great depths,” World tunnel congress-underground facilities for better environment and safety, India.

Axelsson M., Gustafson, G., and Fransson, Å. (2009). “Stop mechanism for cementitious grouts at different water-to-cement ratios,” Tunneling and Underground Space Technology, Vol. 24, pp. 390-397.

Bai, R.B., and Tien, C. (1997). “Particle detachment in deep bed filtration,” Journal of Interface and Colloids Science, Vol. 186, No. 2, pp. 307-317.

Balhoff, M. (2005). “Modeling the flow of Non-Newtonian fluids in packed beds at the pore scale,” Ph.D. dissertation, Louisiana State University. LO.

Barnes, H.A, Hutton, J.F., and Walters, K. (1989). “An introduction to rheology,” Amsterdam, New York.

Barnes, H.A., and Carnali, J.O. (1990). “The vane-in-cup as a novel rheometer geometry for shear thinning and thixotropic materials,” Journal of. Rheology, Vol. 34, pp. 841-867.

Barnes, H.A. (1999). “The yield stress-a review or ‘παυτα ρ^{ε}ι’-everything flows?” Journal of Non-Newtonian Fluid Mechanics, Vol. 81, pp.133-178.

Barnes, H.A., and Nguyen, Q.D. (2001). “Rotating vane rheometry a review,” Journal of Non-Newtonian Fluid Mechanics, Vol. 98, No. 1, pp. 1-14.

Barr, M., and Guth, E.P. (1950). “Observations on the pH of suspensions of Volclay bentonite in distilled water and clark-lubs buffer solutions,” Scientific Edition, pp. 646-647.

Bell, F.G. (1993). “Engineering treatment of soils,” E&FN Spon, London.

Benna, M., Kbir-Ariguib, N., Magnin, A., and Bergaya, F. (1999). “Effect of pH on rheological properties of purified sodium bentonite suspensions,” Journal of Colloid and Interface Science, Vol. 218, pp. 442-455

Besq, A., Malfoy, C., Pantet, A., Monnet, P., and Righi, D. (2003). “Physicochemical characterization and flow properties of some bentonite muds,” Applied Clay Science, Vol. 23, pp. 275-286.

Bekkour, K., Leyama, M., Benchabane, A., and Scrivener, O. (2005). “Time-dependent rheological behavior of bentonite suspensions: An experimental study,” Journal of Rheology, Vol. 49, pp. 1329-1345.

Beven, K., and Germann, P. (1982). "Macropores and water flow in soils," Water Resources Research, Vol. 18, No. 5, pp. 1311-1325.

Borgesson, L., Johannesson, L., and Gunnarsson, D. (2003). “Influence of soil structure heterogeneities on the behaviour of backfill materials based on mixtures of bentonite and crushed rock,” Applied Clay Science, Vol. 23, pp. 121-131.

Bouchelaghem, F., and Vulliet, L. (2001) “Mathematical and numerical filtration-advection-dispersion model of miscible grout propagation in saturated porous

media," International Journal for Numerical and Analytical Methods in Geomechanics, Vol. 25, pp. 1195-1227.

Brandenburg, U., and Lagaly, G. (1988). "Rheological properties of sodium montmorillonite dispersions," Applied Clay Science Vol.3, pp. 263-279.

Burwell E.B. (1958). "Cement, clay grouting of foundations: Practice of the corps of engineering," Journal of the Soil Mechanics and Foundations Division, ASCE, Vol. 84, No. 1551, pp. 1-22.

Buscall, R., McGowan, J.I., and Morton-Jones, A. (1993). "The rheology of concentrated dispersions of weakly attracting colloidal particles with and without wall slip," Journal of Rheology, Vol. 37, pp. 621-641.

Cambefort, H. (1964). "Injection des Sols," Eyrolles, Paris.

Cambefort, H. (1977). "The principles and applications of grouting," Q.Jl. Engineering Geology, Vol. 10, pp. 57-95.

Callaghan, I.C., and Ottewill, R.H. (1974). "Interparticle forces in montmorillonite gels," Discussion of Faraday Society, Vol. 57, pp. 110-118.

Casagrande, A. (1948). "Classification and identification of soils," Transactions, ASCE, Vol. 113, pp. 901-991.

Castelbaum, D., and Shackelford, C. (2009). "Hydraulic conductivity of bentonite slurry mixed sands," Journal of Geotechnical and Geoenvironmental Engineering. Vol. 135, No. 12, pp. 1941-1956.

Chapuis, R. (1990b). "Sand-bentonite liners: predicting permeability from laboratory tests," Canadian Geotechnical Journal, Vol. 27, No.1, pp. 47-57.

Chapuis, R. (2002). "The 2000 RM Hardy Lecture: Full-scale hydraulic performance of soil-bentonite and compacted clay liners," Canadian Geotechnical Journal. Vol. 39, No. 2, pp. 417-439.

Chapuis, R. (2004b). "Predicting the saturated hydraulic conductivity of sand and gravel using effective diameter and void ratio," Canadian Geotechnical Journal, Vol. 41, No. 5, pp. 787-795.

Chegbeleh, L., Nishigaki, M., Akudago, J., and Katayama, T. (2009). "Experimental study on ethanol/bentonite slurry injection into synthetic rock fractures: Application to seepage control," Applied Clay Science, Vol. 45, No. 4, pp. 232-238.

Cheng, D.C.H. (1986). "Yield stress: a time-dependent property and how to measure it," Rheologica Acta, Vol. 25, pp. 542-554.

Chrzastowski, M. (1994). "The great flood of 1993: geologic perspectives on flooding along the Missisippi River and its tributaries in Illinois," Special report/Illinois State geological survey.

Clarke, J. P. (2008). "Investigation of time-dependent rheological behavior of sodium pyrophosphate-bentonite suspensions,". M.S. Thesis, Purdue University, West Lafayette, IN.

Coussot, P., Huynh, H.T., Nguyen, Q.D., and Bonn, D. (2002) "Viscosity bifurcation in thixotropic, yielding fluids," Journal of Rheology, Vol. 46, pp. 573-590.

Coussot, P. (2005). "Rheometry of Pastes, Suspensions and Granular Materials: Applications in Industry and Environment," New York, Wiley.

Coussot, P., Tabuteau, H., Chateau, X., Tocquer, L., and Ovarlez, G. (2006) "Aging and solid or liquid behavior in pastes," Journal of Rheology, Vol. 50, pp. 975-995.

California Department of Water Resources. (2007). "Delta Risk Management Strategy Phase 1." Draft report, California.

de Krester, R.G., Scales, P.J., and Boger, D.V. (1998). "Surface chemistry-rheology inter-relationships in clay suspensions," Colloid Surface. A. Physicochem. Eng. Asp. Vol. 137, pp. 307-318.

de Krester, R.G., Boger, D.V. (2001). "A structural model for the time dependent for the mineral suspensions," Rheologica Acta, Vol. 40, pp. 582-590.

Dergaguin, B.V., and Landau, L.D. (1941). "Theory of stability of highly charged lyophobic sols and adhesion of highly charged particles in solutions of electrolytes." Acta Physicochemistry. USSR, Vol. 14, pp. 633-662.

Dixon, D., Graham, J., and Gray, M. (1999). "Hydraulic conductivity of clays in confined tests under low hydraulic gradients," Canadian Geotechnical Journal, Vol. 36, No. 5, pp. 815-825.

Dupla, J.C., Canou, J., Gouvenot, D. (2004). "An advanced experimental set-up for studying a monodirectional grout injection process," Ground improvement, Vol.8, No.3, pp. 91-99.

Duran, J.D.G., Ramos-Tejada, M.M., Arroyo, F.J., Gonzalez-Caballero, F. (2000). "Rheology and electrokinetic properties of sodium montmorillonite suspensions," Journal of Colloid and Interface Science, pp. 107-117.

Dzuy, N., and Boger, D. (1983). “Yield stress measurement for concentrated suspensions,” Journal of Rheology, Vol. 27, pp. 321-350.

El Mohtar, C.S., Clarke J.P., Bobet, A., Santagata, M., Drnevich, V., and Johnston, C., (2008). “Cyclic response of a sand with thixotropic pore fluid,” Proceedings of Geotechnical Earthquake Soil Dynamics Congress, Sacramento, CA, 1-10.

Eklund, D. (2003). “Penetrability for cementitious injection grouts,” Thesis, Royal Institute of Technology, Sweden.

Eriksson, M., Firedrich, M., and Voschulze, C. (2004). “Variations in the rheology and penetrability of cement-based grout-an experimental study,” Cement and Concrete research, Vol. 34, pp. 1111-1119.

Fisher Scientific (2001). “Material safety data sheet: Sodium pyrophosphate decahydrate.” NJ.

Fernuik, N., and Haug, M. (1990). "Evaluation of in situ permeability testing methods," Journal of Geotechnical Engineering, Vol.116, pp. 297.

Ford, T., Loomis, A., and Fidiam, J. (1940). “The colloidal behavior of clays as related to their crystal structure.” Journal of Physics and Chemistry-us. Vol. 44, No. 1, pp. 1-12.

Fukushima, Y. (1984). “X-ray diffraction study of aqueous montmorillonite emulsions,” Clay and Clay Minerals, Vol. 32, No.4, pp. 320-326.

Gajan, S. (2006). “Physical and numerical modeling of nonlinear cyclic load-deformation behavior of shallow foundations supporting rocking shear walls,” Ph.D. dissertation, University of California, Davis, CA.

Geier, D.L. (2004). “Rheological investigation of bentonite based suspensions for geotechnical applications,” Thesis, Purdue University, West Lafayette, IN.

Ghidaglia, C. (1994). “Filtration en profondeur de particules,” University of Paris VI, Paris, France.

Goh, R., Leong, Y. K., and Lehane, B. (2011). “Bentonite slurries-zeta potential, yield stress, adsorbed additive and time-dependent behaviour,” Rheologica Acta, Vol. 50, pp. 29-38.

Gonzalez, J., and Martfn-Vivaldi, J. (1963). “Rheology of bentonite suspensions as drilling muds,” Stockholm, Sweden.

Gonzalez P. E., Villafranca, S. M., and Gallego C. A. (1992). “Effects of experimental variables on phosphate adsorption on bentonite,” Journal of Chemistry Technology and Biotech. Vol. 54, No. 3, pp. 291-295.

Gosh, G., (1958). “Media characteristics in water filtration,” Journal of Sanitary Engineering Division, ASCE, Vol. 1533, pp. 1-25.

Guin, J.A. (1972). “Clogging of nonuniform filter media,” Industrial Engineering Chemistry and Fundamentals. Vol. 11, No. 3, pp. 345-349.

Gustafson, G., and Stille, H. (1996). “Prediction of groutability from grout properties and hydrogeological data,” Tunneling and Underground Space Technology, Vol. 11, pp. 325-332.

Haug, M. D., and Wong, L. C. (1992). "Impact of molding water-content on hydraulic conductivity of compacted sand bentonite." Canadian Geotechnical Journal, Vol. 29, No. 2, pp. 253-262.

Hauser, E.A., and Reed, C.E. (1937). “The thixotropic behavior and structure of bentonite,” Journal of Physic and Chemistry, Vol. 41, No. 7, pp. 911-934.

Hazirbaba, K. (2005). “Pore Pressure Generation Characteristics of Sands and Silty Sands: A Strain Approach,” Ph.D. dissertation, The University of Texas at Austin, Austin, TX.

Haltz, R.D., and Kovacs, W.D. (1981). “An introduction to geotechnical engineering,” Prentice-Hall, New Jersey.

Herzig, J.P., Leclerc, D.M., Le Goff, P. (1970). “ Flow of suspensions through porous media. Application to deep filtration.,.” Industrial and engineering chemistry Vol. 62, No. 5, pp. 8-35.

Heiser, J.H., and B. Dwyer. (1997). “Summary report on close-coupled subsurface barrier technology initial field trials to full-scale demonstration.” Brookhaven National Laboratory, BNL-52531.

Heymann, L., Noack, E., Kämpfe, L., and Beckmann, B. (1996). “Rheology of printing inks-some new experimental results,” Proceedings of International 12th Congrress in Rheology, Laval University, Quebec City, Canada, pp. 451.

Hoeks, J., Glas, H., Hofkamp, J., and Ryhiner, A. (1987). "Bentonite liners for isolation of waste disposal sites," Waste Management & Research, Vol. 5, No. 1, pp. 93.

Hwang, H. (2010). “The effects of prehydration on hydraulic conductivity of SBMs,” M.S. Thesis, The University of Texas at Austin, Austin, TX.

Incecik, M., and Ceran, I. (1995). “Cement grouting model tests.” Bulteni-Istanbul Teknik Universitesi, Vol. 48, pp. 305-318.

Ioannou, A., and Dimirkou, A., (1997). “Phosphate adsorption on hematite, kaolinite, and kaolinite-hematite (kh) systems as described by a constant capacitance model* 1.” Journal of Colloid and Interface Science, Vol. 192, No. 1, pp. 119-128.

Janczesz, S., and Steiner, W. (1994). “Face support for a large mix-shield in heterogeneous ground conditions,” Tunneling ’94 of Mining and Metallurgy and British Tunneling society, Chapman and Hall, London, pp. 531-549.

Jones, L.G., and Brodkey, R.S. (1970). “Thixotropic behavior of a colloidal suspension,” Proceedings of International 5th Congress of Rheology Vol. 2, pp. 267.

Jeffris, S.A. (1992). “Slurries and Grouts.” In: Doran,K.(ed) construction materials reference book. Butterworth-Heinemann, Oxford, Ch.48.

Jessen, F., and Turan, F. (1961). “Deflocculation of fractionated montmorillonite by sodium polyphosphates,” Society of Petroleum Engineering Journal, Vol. 1, No. 4, pp. 229-234.

Johnston, C.T., and Tombácz, E. (2002). “Surface chemistry of soil minerals.” In: Dixon, J.B. and Shulze. D.G. (Eds.), Soil mineralogy with environmental applications. Soil Science Society of America, Madison, WI, pp. 37-67.

Karim, L., and Salem, A. (2011). “Analysis of bentonite specific area by kinetic model during activation process in presence of sodium carbonate,” Microporous and Mesoporous materials, Vol. 141, pp. 81-87.

Kasperski, K.L., Helper, ch. T. and Helper, L.G., (1986). “Viscosities of dilute aqueous suspensions of montmorillonite and kaolinite clays,” Canadian Journal of Chemistry, Vol. 64, pp. 1919-1924.

Karol, R.H. (2003). “Chemical grouting and soil stabilization,” 3rd ed. Marcel Dekker, New York.

Kaoser, S., Barrington, S., Elektorowicz, M., and Ayadat, T. (2006). "The influence of hydraulic gradient and rate of erosion on hydraulic conductivity of sand-bentonite mixtures," Soil and Sediment Contamination, Vol. 15, No. 5, pp. 481-496.

Kenney, T.C., van Veen, W.A., Swallow, M.A., and Sungaila, M.A. (1992). “Hydraulic conductivity of compacted bentonite-sand mixtures” Canadian Geotechnical Journal, Vol. 29, No. 3, pp. 364-374.

Kim, J.S., Lee, I.M., Jang, J.H., Choi, H.S. (2009) “Groutability of cement-based grout with consideration of viscosity and filtration phenomenon.” International Journal

for Numerical and Analytical Methods in Geomechanics, Vol. 33, No. 16, pp. 1771-1797.

Kim, Y.S., and Whittle, A.J. (2009). "Particle network model for simulating the filtration of a microfine cement grout in sand," Journal of Geotechnical and Geoenvironmental Engineering, Vol. 135, No. 2, pp. 224-236.

Keentok, M. (1982). "The measurement of the yield stress of liquids," Rheologica Acta, Vol. 21, pp. 325-332.

Kelessidis, V. C., Tsamantaki, C., and Dalamarinis, P. (2007). "Effect of pH and electrolyte on the rheology of aqueous wyoming bentonite dispersions," Applied Clay Science, Vol. 38, No. 1-2, pp. 86-96.

Ketz, R.J., Prud'homme, R.K., Graessley, W.W. (1988) "Rheology of concentrated microgel solutions," Rheologica Acta, Vol. 27, pp.531-539.

Kolb C.R. (1976). "Geologic Control of Sand Boils Along Mississippi River Levees," Geomorphology and Engineering, Geomorphology Symposium, Binghamton, NY.

Komine, H., and Ogata, N. (2003), "New equations for swelling characteristics of bentonite-based buffer materials," Canadian Geotechnical Journal Vol. 40, pp. 460-475.

Kuebus, R. and Vaid, Y.P. (1988) "Sand sample preparation- the slurry deposition method," Soils and Foundations, Vol. 28, pp. 107-118.

Lagaly, G. (1989). "Principles of flow of kaolin and bentonite dispersions," Applied Clay Science, Vol. 4, pp. 105-123.

Lagaly, G., and Ziesmer, S. (2003). "Colloid chemistry of clay minerals: the coagulation montmorillonite dispersions," Advanced Colloid and Interface Science, Vol. 100-102, pp. 105-128.

Lambe, T.W., and Whitman, R.V. (1969). "Soil mechanics," Wiley, New York.

Landry, E., Lees, D., and Naudts, A. (2000). "New developments in permeation grouting: Design and evaluation," Concrete International., Vol. 22, No. 8, pp. 47–52.

Laribi, S., Fleureau, J.M., Grossiord, J.L., and Ariguib, N.K. (2006). "Effect of pH on the rheological behavior of pure and interstratified smectite clays," Clay and Clay Minerals, Vol. 54, No. 1, pp. 29-37.

Leong, Y.K. (1988). "Rheology of modified and unmodified Victorian brown coal suspensions," Thesis, Melbourne University, Australia.

Ling, J.T. (1955). “A study of filtration through uniform sand filters,” Proceedings of American Society of Civil Engineering, Vol. 81, pp.1-35.

Liu, J. and Neretnieks, I. (2006). “Physical and chemical stability of the bentonite buffer,” R-06-103, Royal Institute of Technology, Sweden.

Luckham, P., and Rossi, S. (1999). “The colloidal and rheological properties of bentonite suspensions,” Advanced Colloid and Interface Science, Vol. 82, No. 1-3, pp. 43-92.

Mackie, R.I. (1989) “Rapid gravity filtration-towards a deeper understanding,” Filtration and Separation, Vol. 26, pp. 32-35.

Madsen, F.T., and Müller-Vonmoos, M. (1989). “The swelling behavior of clays,” Applied Clay Science. Vol. 4, pp. 143-156.

Mahaut, F., Chateau, X., Coussot, P., Ovarlez, G. (2008). “Yield stress and elastic modulus of suspensions of noncolloidal particles in yield stress fluids,” Journal of Rheology, Vol.52, pp. 287-313.

Markou, I.N., and Atmatzidis, D.K., (2002). “Properties and performance of a pulverized fly ash grout,” Journal of Geotechnical and Geoenvironmental Engineering, Vol.128, pp. 682-691

Malusis, M.A., and Shackelford, C.D. (2002a), “Chemico-Osmotic Efficiency of a Geosynthetic Clay Liner,” Journal of Geotechnical and Geoenvironmental Engineering, Vol. 128, No. 2, pp. 97-106.

Mansur C.I., Postol G., and Salley J.R. (2000). “Performance of relief well systems along mississippi river levees,” Journal of Geotechnical and Geoenvironmental Engineering, Vol. 126, No. 8, pp. 727-738.

Marcotte, D., Marron, J., and Fafard, M. (1994). "Washing of bentonite in laboratory hydraulic-conductivity tests." Journal of Environmental Engineering, Vol. 120, No. 3, pp. 691-698.

Maroudas, A. (1961). “Clarification of suspensions: a study of particle deposition in granular filter media,” Ph.D. dissertation, University of London, London, UK.

Metcafle, R., and Walker (2004). “Bentonite-cement interaction in repository environments,” Proceedings of the international workshop, 14-16 April 2004, Tokyo, NUMO-TR-04-05, Nuclear Waste Management Organization of Japan, Tokyo, pp 27-29.

Metzner, A.B., and Reed, J.C. (1955). “Flow of non-Newtonian fluids-correlation of Laminar, Transition, and Turbulent flow region,.” A.I.Ch.E. Journal, pp. 434-440

Michaels, A., (1958). “Deflocculation of kaolinite by alkali polyphosphates,” Industrial. Engineering Chemistry, Vol. 50, No. 6, pp. 951-958.

Missana, T., and Adell, A. (2000). “On the applicability of DLVO theory to the prediction of clay colloids stability,” Journal of Colloid and Interface Science, Vol. 230, pp. 150-156.

Mitchell, J.K. (1993). “Fundamentals of soil behavior,” 2nd ed. Wiley, New York.

Mittag, J., and Salvidis, S.A., (2003). “The groutability of sands-results from one-dimensional and spherical tests,” Proceedings. of the 3rd International. Specialty Conference on Grouting and Ground Treatment, ASCE, pp. 1372-1382

Mollins, L., Stewart, D., and Cousens, T. (1996). “Predicting the properties of bentonite-sand mixtures,” Clay Minererals. Vol. 31, No. 2, pp. 243-252.

Mourchid, A., Delville, A., Lambard, J., Lecolier, E., and Levitz, P. (1995). “Phase diagram of colloidal dispersions of anisotropic charged particles: equilibrium properties, structure, and rheology of laponite suspensions,” Langmuir, Vol.11, No. 6, pp. 1942-1950.

Muhammad, M. (2004). “Hydraulic, Diffusion, and Retention Characteristics of Inorganic Chemicals in Bentonite,” Ph.D. dissertation, University of South Florida, FL.

Mutch, R.D., R.E. Ash, and J.R. Caputi. (1997). “Contain Contaminated Groundwater,” Chemical Engineering, Vol. 104, No. 5, pp. 114-119.

Nguyen, Q., Akroyd, T., De Kee, D., and Zhu, L. (2006). “Yield stress measurements in suspensions: an inter-laboratory study,” Korea-Australia Rheology. Journal. Vol. 18, No.1, pp.15-24.

Nguyen, Q.D., and Boger, D.V. (1985). “Direct yield stress measurement with the vane method,” Journal of Rheology, Vol. 29, No. 3, pp. 335-347.

Niriella, D., and Carnahan, R.P. (2006).”Comparison study of zeta potential values of bentonite in salt solution,” Journal of Dispersion Science and Technology, Vol. 27, pp. 123-131.

Norrish, K. (1954). “The swelling of montmorillonite," Discussion of Faraday Society, Vol. 18, pp. 120-134.

Olson, R., and Daniel, D. (1981). “Measurement of the hydraulic conductivity of fine-grained soils,” Permeability and Groundwater Contaminant Transport, pp. 18-64.

Ozgurel, H.G., and Vipulanandan, C. (2005). "Effect of grain size and distribution on permeability and mechanical behavior of acrylamide grouted sand," Journal of Geotechnical and Geoenvironmental Engineering, Vol. 131, pp.1457-1465.

Ozkan, S. (2003) "Analytical study on flood induced seepage under river levees," Ph.D. dissertation, Louisiana State University, LO.

Palomino, A. M., and Santamarina, J. C. (2005). "Fabric map for kaolinite: effects of pH and ionic concentration on behavior," *Clays and Clay Mineral.* Vol. 53, No. 3, pp. 211-223.

Pandian, N., Nagaraj, T., and Raju, P. (1995). "Permeability and compressibility behavior of bentonite-sand/soil mixes," ASTM Geotechnical Testing Journal, Vol. 18, No. 1, pp. 86-93.

Parfitt, R., (1978). "Anion adsorption by soils and soil materials," Advanced. Agronomy, Vol. 30, pp. 1-50.

Penner, D., and Lagaly, G. (2001). "Influence of anions on the rheological properties of clay mineral dispersions," Applied. Clay Science Vol. 19, No. 1-6, pp. 131-142.

Permien, T., and Lagaly, G. (1994). "The rheological and colloidal properties of bentonite suspensions in the presence of organic compounds: III. The effect of alcohols of the coagulation of sodium montmorillonite," Colloid Polymer Science, Vol. 272, pp. 1306-1312.

Pearlman (1999). "Subsurface contaminant and monitoring systems: barriers and beyond," U.S EPA, Washington D.C.

Perret, S., Khayata, A., and Ballivya, G. (2000). "The effect of degree of saturation of sand on groutability-experimental simulation," Proceedings of the ICE, Ground Improvement, Vol. 4, pp. 13-22.

Pignon, F., Magnin, A., Piau, J.M., Cabane, B., Lindner, P., and Diat, O. (1997). "Yield stress thixotropic clay suspension: Investigations of structure by light, neutron, and x-ray scattering," Physics Review E 56:3281–3289.

Raffle, J. F., and Greenwood, D.A. (1961). "The relation between the rheological characteristics of grouts and their capacity to permeate soil," Proceedings of the 5th International conference of Soil mechanics and Foundation Engineering, Paris, Vol. 2, pp. 789.

Ramsay, J. D. F., Swanton, S. W., and Bunce, J. (1990). "Swelling and dispersion of smectite clay colloids: determination of structure by neutron diffraction and small-angle neutron scattering," Journal of Chemistry Society Faraday Transactions, Vol. 86, No. 23, pp. 3919-3926.

Ramos-Tejada, M.M., Arrovo, F.J., Peren, R., Duran, J.D.G. (2001). "Scaling behavior of the rheological parameters of montmorillonite suspensions: correlation between interparticle interaction and degree of flocculation," Journal of Colloid and Interface Science, Vol. 235, pp. 245-250.

Rand, B., and Melton, I.E. (1977). "Particle interactions in aqueous kaolinite suspensions," Journal of Colloid and Interface Science. Vol. 60, pp. 308-320.

Reddi, L.N. and Bonala, M.V.S. (1997). "Analytical solution for fine particle accumulation in soil filters," Journal of Geotechnical and Geoenvironmental Engineering, Vol. 123, No. 12, pp. 1143-1152.

Rege, S.D., and Fogler, H.S. (1988). "A network model for deep bed filtration of solid particles and emulsion drops." A.I.Ch.E. Journal, Vol. 34, No, 11, pp. 1761-1771.

Rogers, J. D. and Meehan, R. L. (2008). "Site Characterization and Failure modes in the Paterno Flood in case." Presentation (Personal communication).

Rugg, D. (2010). "Undrained monotonic shear strength of loose saturated sand treated with thixotropic bentonite suspension for soil improvement," M.S. Thesis, The University of Texas at Austin, Austin, TX.

Rumer, R.R. and J.K. Mitchell, (1996). "Assessment of Barrier Containment Technologies A Comprehensive Treatment for Environmental Remedial Application," Product of the International Containment Technology Workshop. National Technical Information Service, PB96-180583.

Ryden, J., and Syers, J. (1975). "Rationalization of ionic strength and cation effects on phosphate sorption by soils," European Journal of Soil Science, Vol. 26, No. 4, pp. 395-406.

Saada, Z., Canou, J., Dormieux, L., Dupla, J.C., and Maghous, S. (2005). "Modeling of cement suspension flow in granular porous media," International Journal for Numerical and Analytical Methods in Geomechanics. Vol. 29, pp. 691-711.

Saak A.W., Jennings, H.M., and Shah, S.P. (2001) "New methodology for designing self-compacting concrete," ACI Materal Journal, Vol. 98, pp. 429-439.

Saiyory, N., Jason, L., Chupin, O., and Hicher, P.Y. (2008), "Modeling and acoustic monitoring of grout propagation in sands," Proceedings of the Institution of Civil Engineers, August, pp. 143-152.

Sakthivadivel, R. (1966). "Theory and mechanisms of filtration of non-colloidal fines through a porous medium," Technical report, HEL 15-5, Hydraulic engineering laboratory, The University of California, Berkeley, CA.

Salgado R., Bandini, P., and Karim, A. (2000) "Shear strength and stiffness of silty sand," Journal of Geotechnical and Geoenvironmental engineering, Vol. 126, pp. 451-462.

Santagata, M., and Santagata, E. (2003). "Experimental investigation of factors affecting the injectability of microcement grouts," Proceedings of the 3rd International Conference, ASCE, Geotechnical special publication 120, pp. 1221-1234.

Santamarina, J., Klein, K.A., Wang, Y.H., Prencke, E. (2002). "Specific surface: determination and relevance," Canandian Geotechnical Journal, Vol. 39, pp. 233-241.

Schramm, L.L., and Kwak, J.C.R. (1982). "Influence of exchangeable cation composition on the size and shape of montmorillonite particles in dilute suspensions," Clay and Clay Minerals, Vol. 30, pp. 40-48.

Schwarz, L.G. and Chirumalla, M. (2007). "Effect of injection pressure on permeability and strength of microfine cement grouted sand." Proceedings of Geo-Denver, Denver, CO. pp. 1-15.

Shomer, I., and Mingelgrin, U. (1978). "A direct procedure for determining number of plates in tactoids of smectite: the Na/Ca case," Clay and Clay Minerals, Vol. 26, pp. 135-138.

Seed, R., Bea, R., Abdelmalak, R., Athanasopoulos-Zekkos, A., Boutwell, G., Briaud, J., Cheung, C., Cobos-Roa, D., Ehrensing, L., and Govindasamy, A. (2008a). "New Orleans and hurricane Katrina. I: Introduction, overview, and the east flank." Journal of Geotechnical and Geoenvironmental Engineering. Vol. 134, No. 5, pp. 701-717.

Sherard J.L., Woodward R.J., Gizienski S.F., and Clevenger W.A. (1963). "Earth and Earth-Rock Dams, Engineering Problems of Design and Construction," John Wiley and Sons, New York.

Sivapullaiah, P. V., Sridharan, A., and Stalin, V. K. (2000). "Hydraulic conductivity of bentonite-sand mixtures," Canadian Geotechnical Journal. Vol. 37, No. 2, pp. 406-413.

Smyth, D., Cherry, J., and Jowett, R. (1995). "Sealable joint steel sheet piling for groundwater pollution control," Proceedings of ER '95: Committed to Results, U.S. Department of Energy, Denver, CO.

Seffe, J.F. (1996). "Rheological methods in food process engineering," 2nd ed. Freeman press, MI.

Soo, H., and Radke, C.J. (1986). "A filtration model for the flow of dilute, stable emulsions in porous media I: Theory," Chemical Engineering Science, Vol. 41, No.2, pp. 263-272.

Spielman, L.A., and Fiztpatrick, J.A. (1973). "Theory for particle collection under London and gravity forces," Journal of Colloid and Interface Science, Vol. 42, No. 3, pp. 607.

Spielman, L.A., and Cukor, P.M. (1973). "Deposition of non Brownian particles under colloidal forces," Journal of Colloid and Interface Science, Vol. 43, No.1, pp. 51.

Sposito, G., and Grasso, D. (1999). "Electrical double layer structure, forces, and fields at the clay-water interface. In: Hsu, J.P. (Ed.), International forces and fields: Theory and Applications," Marcel Dekker, New York, pp.207-249.

Stein, P.C. (1940). "A study of the theory of rapid filtration of water through sand," Ph.D. dissertation, Massachusetts Institute of Technology, Boston, MA.

Stern, O. (1924). "Zur Theorie der Elektrolytischen Doppelschriht," Zeitschrift Electrochem, Vol. 30, pp. 508-516.

Stokes, J.R., and Telford, J.H. (2004). "Measuring the yield behaviour of structured fluids," Journal of Non-Newtonian Fluid Mechanics, Vol.124, pp.137-146.

Studds, P.G., Stewart, D.I., and Cousens, D.W. (1998). "The effects of salt solutions on the properties of bentonite-sand mixtures," Clay Minerals, Vol. 33, pp. 651-660.

Sutter Butte Flood Control Agency, 18, July, 2007 "Flood aware/Flood prepare," <http://www.sutterbutteflood.org>, pp. 1-15.

Tarafda, S., Dey, A., and Gupta, B.S. (1992). " A multiple state stochastic model for deep-bed filtration," Chemical Engineering and Technology. Vol. 15, No.1, pp. 44-50.

Terzaghi, K., and Peck, R. (1967). "Soil mechanics in engineering practice," 2nd ed. John Wiley and sons, New york.

Tchillingarian, G. (1952). "Study of the dispersing agents," Journal of Sediment ary Petrology, Vol. 22, No. 4, pp. 229-233.

The Geological Society of London (2006). "Clay materials used in construction," Geological Society Engineering Geology Special Publication No. 21, London, UK, Ch. 12

Tien, C. (1989). "Granular filtration Aerosols and Hydrosols," Butterworths.

Tombácz, E., and Szerkeres, M. (2004). "Colloidal behavior of aqueous montmorillonite suspensions: the specific role of pH in the presence of indifferent electrolytes," Applied Clay Science, Vol. 27, pp. 75-94.

Tsakiroglou, C.D. and Pyatakes, A.C. (2000), "A new simulator of mercury porosimetry for the characterization of porous materials," Journal of Interface and Colloid Science, Vol. 137, No. 2, pp. 315-339.

Turnbull W.J., and Mansur C.I. (1959). "Investigation of Underseepage-Mississippi River Levees," Transactions, ASCE, Vol. 126, No.1, pp. 1429-1485.

Uhlherr, P.H.T., Guo, J, Tiu, C., Zhang, X.M., Zhou, J.Z.Q, and Fang, T.N. (2005). "The shear-induced solid liquid transition in yield stress materials with chemically different structures," Journal of Non-Newtonian Fluid Mechanics, Vol. 125, pp. 101-119.

U.S. Army Corps of Engineers (1956). TM 3-424, "Underseepage and Its Control, Lower Mississippi River Levees," USACE Waterways Experiment Station, Vicksburg, MS.

US Army Corps of Engineers (2008). "Performance evaluation of the New Orleans and southeast Louisiana Hurricane protection system," Final report.

United States general accounting office (1995). "Midwest flood: information on the performance, effects, and control of levees," GAO/RGED 95-125.

Vogel, H. J., and Roth, K. (2001). "Quantitative morphology and network representation of soil pore structure," Advanced water resources, Vol. 24, No. 3-4, pp. 233-242.

Wilkinson, D. and Willemsen, J.F. (1983). "Invasion and percolation-a new form of percolation theory," Journal of Physics America, Vol.16, No.14, pp.3365-3376.

Wolff T.F. (1987). "Levee Underseepage Analysis for Special Foundation Conditions," Research report prepared for USACE Waterways Experiment Station, Michigan State University, East Lansing, MI.

Wolff, T.F. (2002). "Performance of Levee Underseepage Controls: A Critical Review," USACE Engineer Research and Development Center, ERDC/GSL TR-02-19, Washington, DC.

Yang, N., and Barbour, S. (1992). "The impact of soil structure and confining stress on the hydraulic conductivity of clays in brine environments," Canadian Geotechnical Journal. *CGJOAH*, Vol. 29, No 5.

van Olphen, H. (1977). "An Introduction to Clay Colloid Chemistry," Wiley, New York.

Verwey, E.J.W., and Overbeek, J. Th. G. (1948). "Theory of the stability in lyophobic colloids," Elsevier, Amsterdam, New York, London.

Weiss, A., and Frank, R. (1961). "Űber den bau der gerűste in thixotropen gelen," Z. Naturforsch Vol. 16, pp.141-142.

Zebovitz, S., Krizek, R.J., and Atmatzidis, D.K. (1989). "Injection of fine sands with very fine cement grout," Journal of Geotechnical Engineering, Vol. 115, No. 12, pp.1717-1733.

Zhu, L., Sun, N., Papadopoulos, K., and de Kee, D. (2001). "A slotted plate device for measuring static yield stress," Journal of Rheology Vol. 45, pp.1105-1123.